Partial Volume Correction of 99mTc Oncology SPECT Imaging via Case Specific Resolution Estimation

Rebecca Livingstone Gillen

A dissertation submitted in partial fulfillment of the requirements for the degree of

Doctor of Philosophy

of

University College London.

Institute of Nuclear Medicine, Division of Medicine
University College London

September 10, 2025

I, Rebecca Livingstone Gillen, confirm that the work presented in my thesis is my own. Where information has been derived from other sources, I confirm that this has been indicated in the thesis.

Abstract

This project aimed to develop a practical method to compensate for the detrimental effect of limited spatial resolution in ^{99m}Tc nuclear medicine oncology imaging. Correction for limited resolution is currently not routinely applied in clinical practice, limiting quantitative accuracy.

Literature review identified existing correction strategies, then assessed based on oncology-specific criteria. This found no existing method ideal for oncology. Specifically, many existing correction methods assume that resolution is invariant, which is not a valid assumption for SPECT imaging. Two methods were selected for further investigation.

Key factors affecting SPECT resolution were investigated by simulating SPECT acquisition and reconstruction for simple digital phantoms. Practical experiments demonstrated that assuming invariant resolution could introduce inaccuracies in correcting for the effects of limited resolution.

Case-specific resolution was estimated using the perturbation method, and subsequently incorporated into correction algorithms. This was tested using a range of datasets including simple digital phantoms and computerised anthropomorphic models - with images generated by analytical simulation. Quantitative accuracy improved for correction algorithms incorporating case-specific resolution.

Realistic test datasets developed based on clinical data were used with Monte Carlo software to simulate image acquisition. Two correction algorithms, used with perturbation, were compared with a conventional correction method. Results demonstrated that the Single Target Correction (STC) method with perturbation performed as well as the conventional, Recovery Coefficient (RC), method for

Abstract 4

regional quantification, with the added advantages of producing an image and capturing heterogeneity within the object of interest.

Further work in this area, including assessment of other factors which contribute to quantitative accuracy of quantitative SPECT imaging is required. The work in this thesis could potentially contribute to the practical implementation of correction for the detrimental effect of limited spatial resolution, moving towards images which can more accurately aid the diagnosis, monitoring and treatment of oncology patients.

Impact Statement

Nuclear medicine is an imaging modality which provides information about the function of the body. This functional information is a unique advantage not available from anatomical imaging such as CT. 3D Nuclear Medicine images can be acquired using a technique called SPECT (Single Photon Emission Computed Tomography). As well as visual interpretation, quantitative measurements from SPECT images can be used in a wide range of applications. This includes multiple uses in cancer imaging. Measurements can be used to aid diagnosis, assessing progression or response to treatment, or for treatment planning.

A key disadvantage of SPECT compared to, for example, CT or MRI imaging is that SPECT images are significantly blurrier (inferior spatial resolution). This blurriness affects images visually, but also causes inaccuracies when SPECT images are used to measure the function of small objects. This is known as the Partial Volume Effect (PVE).

There is currently no agreement on the best method to correct for the PVE in cancer imaging. The most frequently used method for correction of the PVE is simplistic and makes several assumptions which may not be valid in all cases. This thesis aimed to develop an improved method for PVE correction by estimating spatial resolution on a case-by-case basis.

This work could benefit the health of the general population as a step towards improving the accuracy of oncology SPECT. This could help to diagnose cancer, or identify cancer spread, earlier and more reliably. Treatment pathways could be personalised for individual patients, depending on response to treatment evaluated using follow-up imaging.

Nuclear Medicine imaging can be used to assess response to a range of therapies, in particular, the evaluation of the safety and efficacy of Molecular Radiotherapy (MRT). MRT targets cancer cells using similar uptake pathways as used for Nuclear Medicine imaging. SPECT could be used to identify patients who could benefit from MRT, plan their treatment, check its effectiveness and ensure that damage to healthy organs at risk remains as low as possible. The accuracy of all of these applications could be improved with more accurate PVE corrections.

Findings and conclusions from the work of this thesis have been disseminated to clinical and university colleagues via oral presentations and posters at national and international conferences. Interesting and useful discussions following these presentations demonstrated engagement with the topic. Findings have also been published in a peer-reviewed paper in the journal of EJNMMI Physics.

The research community utilising software for reconstruction and Monte Carlo simulation employed in this thesis will benefit from the progress made towards working with both software systems in tandem. This software connection could help future researchers explore the topic of Partial Volume Correction as well as a wide range of other topics in SPECT imaging.

The aim of this thesis is that the findings and conclusions could help to guide further research on Partial Volume Correction and improve the accuracy of quantitative Nuclear Medicine imaging for the benefit of patients.

Acknowledgements

Firstly, I would like to acknowledge the National Physical Laboratory who provided funding for this PhD studentship via the Industrial Strategy Challenge Fund and the National Measurement Strategy.

I would like to thank everyone who was involved in my supervisory team throughout this project; Prof. Brian Hutton, Dr. Sarah McQuaid, Prof. Kris Thielemans and Dr. Ana Denis-Bacelar. The time you all took to share your expertise and the many helpful discussions have been invaluable. Thanks also to those in the office and the wider INM department who create a supportive, positive and inspiring environment to work in. In particular, thanks to Dr. Kjell Erlandsson and Dr. Ben Thomas for their knowledge of all things to do with partial volume correction, and help with technical aspects of software. Thanks to Elise, Ludovica and Richard for sharing their experience during the early stages of the PhD. For the moral support when we were all going through it together - thanks to Robbie, Ashley and Alex! Also to Francesca, Sam (especially with SIMIND stuff) and Nicole. Thank you to Daniel for help with STIR, and Harry for being my PVC peer and the useful chats about RC. I'd like to also thank Prof. Michael Ljungberg for input into the work with SIMIND.

A big thank you to all my colleagues in Glasgow for their interest in the project, practical (and often emotional!) support. Especially to Dr Alison Bolster, Gillian, Carolyn, and Sarah. I feel privileged to continue to work with you all.

I genuinely would not have got to the point of submitting this thesis without the immense support from my friends and family. Thank you for your continual love and encouragement, which means so much to me. To my 'wee' siblings, Scott and Eilidh, thank you for consistently looking out for their big sister. To my Mum, thank you for everything that you do for me - as well as absolutely everyone else. A very special thank you, Dad (the original Dr G), for being wise enough to warn me of the difficulties of the PhD and being kind enough to help me through it. A million thank yous to Stuart, who has been the most incredible support in PhD and in life. Let's get this wedding planned now, pal! Thank you all for sticking by me.

Finally I'd like to acknowledge the anonymous patients scanned at the Nuclear Medicine department at Glasgow Royal Infirmary for allowing their images to be used for research.

UCL Research Paper Declaration Form:

referencing the doctoral candidate's own published work(s)

- 1. For a research manuscript that has already been published (if not yet published, please skip to section 2):
 - (a) What is the title of the manuscript?

Towards accurate partial volume correction in ^{99m}Tc oncology SPECT: perturbation for case-specific resolution estimation

(b) Please include a link to or doi for the work:

https://ejnmmiphys.springeropen.com/articles/10.1186/s40658-022-00489-5

(c) Where was the work published?

European Journal of Nuclear Medicine and Molecular Imaging Physics

(d) Who published the work?

Springer Open

(e) When was the work published?

05 September 2022

(f) List the manuscript's authors in the order they appear on the publication:

Rebecca Gillen, Kjell Erlandsson, Ana M. Denis-Bacelar, Kris Thielemans, Brian F. Hutton & Sarah J. McQuaid

(g) Was the work peer reviewed?

Yes

(h) Have you retained the copyright?

Yes

(i) Was an earlier form of the manuscript uploaded to a preprint server (e.g. medRxiv)? If 'Yes', please give a link or doi

No If 'No', please seek permission from the relevant publisher and check the box next to the below statement:

I acknowledge permission of the publisher named under 1d to include in this thesis portions of the

publication named as included in 1c.

2. For a research manuscript prepared for publication but that has not yet been published (if already published, please skip to section 3):

(a) What is the current title of the manuscript?

(b) Has the manuscript been uploaded to a preprint server 'e.g.

medRxiv'?

If 'Yes', please please give a link or doi:

(c) Where is the work intended to be published?

(d) List the manuscript's authors in the intended authorship order:

(e) Stage of publication:

3. For multi-authored work, please give a statement of contribution cover-

ing all authors (if single-author, please skip to section 4):

RG carried out data analyses and drafted the manuscript. All authors participated in the interpretation of the data. All authors read and approved the final manuscript.

4. In which chapter(s) of your thesis can this material be found? Chapter 5

e-Signatures confirming that the information above is accurate (this form should be co-signed by the supervisor/ senior author unless this is not appropriate, e.g. if the paper was a single-author work):

Candidate: Rebecca Gillen

Date: 30/01/2024

Supervisor/Senior Author signature: Sarah McQuaid

Date:06/04/2025

	UCL	Resear	ch Paper I	Declaration Form	Ģ
1	Intr	oductio	n		44
	1.1	Backg	round and	Motivation	44
	1.2	Object	ive		45
	1.3	Structu	are and Ch	apter Outlines	45
2	Prin	ciples o	of Quantita	ative Nuclear Medicine in Oncology	48
	2.1	Molec	ular Radio	therapy	48
	2.2	Nuclea	ar Medicin	e Imaging	49
	2.3	Gamm	a Camera	Systems	49
		2.3.1	Gamma (Camera Detector Components	50
			2.3.1.1	Collimator	50
			2.3.1.2	Scintillation Crystal	50
			2.3.1.3	Light Guide and PMTs	51
			2.3.1.4	Electronics	52
			2.3.1.5	Image Digitisation	52
		2.3.2	Correction	ons Applied to Raw Image Data	52
		2.3.3	Novel Ga	amma Camera Design	53
	2.4	SPECT	Γ-CT Syste	ems	53
	2.5	3D Im	age Recon	struction	53
		2.5.1	Filtered 1	Back Projection	54
		2.5.2	Iterative	Reconstruction	54
			2.5.2.1	Maximum Likelihood Expectation Maximisation .	56

Contents	12
----------	----

			2.5.2.2	Ordered Subsets Expectation Maximisation	57
	2.6	Applic	ations of C	Quantitative SPECT in Oncology	57
		2.6.1	Diagnosis	s and Staging	57
		2.6.2	MRT Tre	atment Planning	58
		2.6.3	Dosimetr	y	59
		2.6.4	Follow-u	p Imaging	60
		2.6.5	Quantitat	ive Metrics	61
	2.7	Limita	tions to Ac	ecuracy in Quantitative SPECT	61
		2.7.1	Attenuati	on	62
			2.7.1.1	Attenuation Correction	62
		2.7.2	Scatter		63
			2.7.2.1	Scatter Correction	63
		2.7.3	Motion		64
		2.7.4	Segmenta	ation	65
		2.7.5	Registrati	ion	65
		2.7.6	Cross-sys	stem quantification	66
		2.7.7	Measurer	ment Uncertainty	66
		2.7.8	Limited S	Spatial Resolution	67
			2.7.8.1	The Partial Volume Effect	68
			2.7.8.2	Partial Volume Correction	70
	2.8	Thesis	Scope .		70
3	Part	ial Volu	me Corre	ction for Oncology SPECT Imaging	72
	3.1	Aims .			72
	3.2	Existin	g PVC Tec	chniques	72
		3.2.1	PVC Rev	riew Papers	72
			3.2.1.1	PET PVC vs SPECT PVC	73
		3.2.2	Categorie	es of PVC Implementation	73
			3.2.2.1	Techniques for reducing the PVE by improving	
				resolution	74
			3.2.2.2	Projection based vs Image based techniques	74

		3.2.2.3	Segmentation based vs segmentation free tech-	
			niques	74
		3.2.2.4	Region-based vs voxel-based techniques	75
		3.2.2.5	Other PVC techniques	76
	3.2.3	Literatur	e Review Summary	77
3.3	Develo	ping crite	ria to assess PVC methods for oncology SPECT	78
	3.3.1	Shape of	VOI	78
	3.3.2	Segment	ation and use of other image data	79
	3.3.3	Uniform	ity	79
	3.3.4	Resolution	on	80
	3.3.5	Artefacts		80
	3.3.6	Voxelwis	se evaluation	81
	3.3.7	Uncertai	nty estimation	81
	3.3.8	Practical	Considerations	81
	3.3.9	Summar	y of Proposed Criteria	82
3.4	Using	Oncology	SPECT Criteria to assess existing PVC methods	83
	3.4.1	In-recons	struction Techniques to Improve Resolution	83
		3.4.1.1	Resolution Modelling	83
		3.4.1.2	Reconstruction with prior information	84
	3.4.2	Regional	Mean Value Correction Methods	85
		3.4.2.1	Recovery Coefficient	85
		3.4.2.2	Geometric Transfer Matrix	87
		3.4.2.3	Local Projection	88
		3.4.2.4	Local Background Correction	90
	3.4.3	Voxelwis	se methods, where segmentation is required	92
		3.4.3.1	Videen/Meltzer Method	92
		3.4.3.2	Single Target Correction	93
	3.4.4	Voxelwis	se, Segmentation-Free Methods	95
		3.4.4.1	Iterative Deconvolution	96
	3 4 5	Method 1	Evaluation against Oncology SPECT Criteria	97

			3.4.5.1	Shortlisted methods for further study and devel-	
				opment	9
			3.4.5.2	Possible Areas for Method Development 9	ç
			3.4.5.3	Scope of Testing	(
			3.4.5.4	Test Datasets	(
			3.4.5.5	Bone SPECT/CT as test data	1
			3.4.5.6	Tektrotyd SPECT/CT as test data 10	3
	3.5	Conclu	usions		5
4	Asse	essment	of key fa	ctors affecting SPECT resolution variability and	
	the i	impact	on the PV	E 10	(
	4.1	Backg	round		6
	4.2	Aims .			7
	4.3	Existin	ng work .		7
	4.4	Genera	al use of S	ΓIR in simulation-based testing 10	8
		4.4.1	Generation	ng Input Data with STIR	8
		4.4.2	STIR SP	ECT System Model	8
			4.4.2.1	Definition of Collimator in STIR	ç
		4.4.3	STIR Re	construction	2
	4.5	Simula	ation-based	Testing of Variation in SPECT Spatial Resolution 11	2
		4.5.1	Methods		3
			4.5.1.1	Simulated Phantoms and Attenuation Maps 11	3
			4.5.1.2	Determination of FWHM values	4
		4.5.2	Results		6
			4.5.2.1	Effect of position in FOV	6
			4.5.2.2	Effect of reconstruction parameters	7
			4.5.2.3	Effect of attenuation	8
			4.5.2.4	Effect of non-uniform activity distribution 12	1
		4.5.3	Discussion	on	3
			4.5.3.1	Reconstruction parameters	3
			4532	Attenuation 12	4

	1 7
Contante	13
Contents	1.7

		4.5.3.3	Non-uniform activity distribution	
		4.5.3.4	Limitations	
	4.5.4	Conclusion	ons	
4.6	Bias es	stimate due	e to PVC application with invariant PSF 126	
	4.6.1	Aims .		
	4.6.2	Methods		
		4.6.2.1	Phantom Generation	
		4.6.2.2	Convolution	
		4.6.2.3	RC calculation	
		4.6.2.4	Bias Calculation	
	4.6.3	Results		
		4.6.3.1	Recovery Coefficients	
		4.6.3.2	Bias due to applying incorrect RC 131	
	4.6.4	Discussion	on	
	4.6.5	Conclusio	ons	
4.7	Phantom-based Testing of Spatial Variation of the PVE			
	4.7.1	Backgrou	and	
	4.7.2	Aims .		
	4.7.3	Methods		
		4.7.3.1	Equipment	
		4.7.3.2	Phantom set-up	
		4.7.3.3	Acquisition and Reconstruction	
		4.7.3.4	Data Analysis	
	4.7.4	Results		
		4.7.4.1	Effect on Detector Orbit	
		4.7.4.2	Visual detectability	
		4.7.4.3	Quantitative assessment	
	4.7.5	Discussion	on	
	4.7.6	Conclusio	ons	
4.8	Chapte	er 4 Conclu	ısions	

5	Use of Perturbation to Measure Spatial Resolution, and the Application			n			
	to P	PVC					
	5.1	Backg	round and	Aim	. 145		
	5.2	Pertur	bation for	PSF Measurement	. 146		
		5.2.1	Previous	studies using perturbation	. 146		
	5.3	Metho	ds		. 147		
		5.3.1	Phantom	Generation	. 147		
			5.3.1.1	Simple Geometric Phantoms	. 147		
			5.3.1.2	Anthropomorphic Phantoms	. 149		
		5.3.2	Simulati	on of Projection Data	. 151		
		5.3.3	Perturba	tion	. 153		
		5.3.4	Reconstr	ruction	. 154		
		5.3.5	PSF Cha	racterisation	. 154		
		5.3.6	Assessm	ent of PSF Accuracy	. 156		
		5.3.7	Partial V	folume Correction with STC	. 157		
		5.3.8	Lesion Q	Quantification using Regional Mean Values	. 158		
	5.4	Result	s		. 158		
		5.4.1	PSF estin	mation with perturbation	. 158		
			5.4.1.1	PSF variation with reconstruction update and po-			
				sition in FOV	. 158		
			5.4.1.2	PSF variation with lesion contrast and size	. 160		
			5.4.1.3	Effect of Point Position Within a Lesion on PSF			
				measurement	. 162		
			5.4.1.4	PSF variation with surrounding activity distributio	n162		
			5.4.1.5	Checking accuracy of perturbation-estimated PSF	167		
		5.4.2	PVC Res	sults	. 167		
			5.4.2.1	Simple Phantom	. 167		
			5.4.2.2	Anthropomorphic Phantoms	. 170		
	5.5	Discus	ssion		. 174		
5.5.1 Limitations			176				

Contents	17

	5.6	Conclu	ision		178	
6	Mon	onte Carlo Simulation of Clinically Relevant Test Datasets 180				
	6.1	Aim .			180	
	6.2	Backg	round		181	
		6.2.1	Monte C	Carlo Simulation	181	
		6.2.2	Clinicall	y Realistic Test Data	181	
	6.3	Metho	ds		182	
		6.3.1	SIMIND	simulation parameter definition	182	
		6.3.2	SIMIND	Set-up Validation	182	
			6.3.2.1	Detector position and motion	183	
			6.3.2.2	Planar Spatial Resolution	185	
			6.3.2.3	Energy Spectra	186	
			6.3.2.4	Planar Sensitivity	187	
		6.3.3	Use of S	IMIND with STIR software	187	
			6.3.3.1	Accepted Data Types	188	
			6.3.3.2	Coordinate Systems and Orientation	189	
			6.3.3.3	Units, Naming Conventions and Header Structure	189	
			6.3.3.4	Definition of Attenuation	189	
		6.3.4	Develop	ment of digital phantoms based on clinical data	191	
			6.3.4.1	Clinical source data	191	
			6.3.4.2	Preparation of patient data	192	
			6.3.4.3	Patient dataset A	195	
			6.3.4.4	Patient dataset B	196	
			6.3.4.5	Patient dataset C	196	
			6.3.4.6	Patient dataset D	198	
			6.3.4.7	Patient dataset E	199	
			6.3.4.8	Insertion of synthetic lesions	200	
		6.3.5	Generati	on of GT test datasets	201	
			6.3.5.1	Data preparation for SIMIND	201	
			6.3.5.2	SIMIND simulation	201	

		6.3.5.3	Reconstruction of Simulated data 202
6.4	Result	s	
	6.4.1	SIMIND	Set-up Validation
		6.4.1.1	Detector position and motion 202
		6.4.1.2	Image Orientation
		6.4.1.3	Planar Spatial Resolution 205
		6.4.1.4	Energy Spectra
		6.4.1.5	Planar Sensitivity
	6.4.2	Clinicall	y Realistic Activity Distributions with lesions 209
		6.4.2.1	Case 1: Spherical Lesion in liver (Patient Data A) 209
		6.4.2.2	Case 2: Spherical Lesion in liver (Patient Data B) 210
		6.4.2.3	Case 3: Spherical Lesion in liver (Patient Data C) 212
		6.4.2.4	Case 4: Spherical Lesion in liver (Patient Data D) 212
		6.4.2.5	Case 5: Spherical Lesion in liver (Patient Data E) 213
		6.4.2.6	Case 6: Non-Spherical Lesion in Bowel (Patient
			data A)
		6.4.2.7	Case 7: Non-Spherical Lesion in liver (Patient
			data B)
		6.4.2.8	Case 8: Non-Spherical Lesion in liver (Patient
			data C)
		6.4.2.9	Case 9: Non-Spherical Lesion in lung (Patient
			data D)
	6.4.3	SIMIND	Simulation of GT test datasets
		6.4.3.1	Radius of Rotation review
		6.4.3.2	Comparison of SIMIND and Clinical Projection
			Data
6.5	Discus	ssion	
	6.5.1	Monte C	Carlo Validation
		6.5.1.1	Planar Spatial Resolution Validation 218
		6.5.1.2	Energy Spectra Comparison

Contents	19
Contents	19

		6.5.2	Test Data	aset Generation
	6.6	Conclu	isions	
7	Test	ing of P	VC algor	ithms 220
	7.1	Aim .		
	7.2	Metho	ds	
		7.2.1	Test Data	asets
		7.2.2	PVC me	thods
			7.2.2.1	Single Target Correction (STC)
			7.2.2.2	Iterative Deconvolution using Richardson-Lucy
				(RL)
			7.2.2.3	Recovery Coefficient (RC)
		7.2.3	Methods	for Analysis
			7.2.3.1	Visual Assessment
			7.2.3.2	Voxel-based analysis
			7.2.3.3	Region-based analysis
	7.3	Result	s	
		7.3.1	Spherica	1 Lesions
			7.3.1.1	Visual Assessment
			7.3.1.2	Quantitative Assessment
		7.3.2	Non-Sph	nerical Lesions
			7.3.2.1	Visual Assessment
			7.3.2.2	Quantitative Assessment
		7.3.3	Regional	Mean Value Results Summary
	7.4	Discus	ssion	
		7.4.1	Recovery	y Coefficient Performance
		7.4.2	Richards	on-Lucy with Perturbation Performance 239
		7.4.3	Single Ta	arget Correction with Perturbation Performance 240
		7.4.4	Limitatio	ons
			7.4.4.1	Absolute Quantification of Monte-Carlo Simu-
				lated Data

_	
Contents	20

			7.4.4.2 Recovery coefficient calculation and application .	240
		7.4.5	Further work	241
	7.5	Conclu	isions	241
8	Gene	eral Coi	nclusions, Limitations, and Future Directions	243
	8.1	Overal	l Conclusions	243
	8.2	Discuss	sion	244
		8.2.1	Reconstruction for quantitative assessment	244
			8.2.1.1 Matrix Size	245
			8.2.1.2 Use of Resolution Modelling in Reconstruction .	245
		8.2.2	Limitations and Further Work	247
			8.2.2.1 Influence of registration and segmentation	248
			8.2.2.2 Application to other radionuclides	248
		8.2.3	Practicalities of implementing PVC on clinical data	249
	8.3	Summa	ary	250
Ap	pend	ices		251
A	Deta	il of PV	C Method Scoring Based on Novel Criteria	251
В	Use	of STIR	2 Software	259
C	Use	of SIMI	IND Software	264
D	SIM	IND ST	TIR connection	267
E	IRA	S Appli	cation and Ethical Approval	280
Bil	bliogr	aphy		283

List of Figures

2.1	Schematic showing the basis of an iterative reconstruction algo-	
	rithm. Figure reproduced from Zaidi et al. [2006] with permission	
	from Springer Nature (Licence number 5981880433174)	55
2.2	Diagram demonstrating the PVE on a circular source with uniform	
	activity in a cold background. Maximum measured activity is re-	
	duced, and some counts are detected outside of the true source	
	boundary. This figure was originally published in JNM. M. Soret	
	et al. Partial-Volume Effect in PET Tumor Imaging. J Nucl Med.	
	2007;6:932-956. ©SNMMI [Soret et al., 2007]	69
3.1	Diagram demonstrating segmentation of compartments used for the	
	LP method where there are $J=2$ compartments in the local region of	
	interest (lesion and local background), and the remainder is used to	
	calculate a global background term. Reproduced with permission	
	from Southekal et al. [2012] (licence ID 1588756-1)	88
3.2	Diagram illustrating the relevant regions used for the LB method in	
	2D. Black = 'true' object, light grey = spill-out region, dark grey =	
	background region. The blue voxels are used to compensate for the	
	effect that background activity has on the red voxel [Hofheinz et al.,	
	2012]	91
3.3	Flow chart demonstrating the steps involved in the iterative Single	
	Target Correction (STC) partial volume correction method	94

3.4	PVC method and criteria summary matrix, demonstrating suitable (green) and unsuitable (red) aspects of each method. Scoring has been defined as: $0 = \text{Doesn't}$ meet criteria at all, $1 = \text{Meets}$ criteria in very limited cases, $2 = \text{Partially meets}$ criteria, $3 = \text{Meets}$ criteria in most cases, $4 = \text{Meets}$ criteria in almost all cases, $5 = \text{Entirely meets}$ criteria. The full table can be found in Appendix A and acronyms are defined at the beginning of this document.	. 98
4.1	Plot of mass attenuation coefficient values for lead (from NIST data) vs energy. The dotted line is the fitted data, allowing a value for 140 keV to be calculated	. 111
4.2	Distance from collimator face vs resolution (FWHM) for the Mediso system using LEHR collimators. The graph shows; straight line indicating the collimator resolution R_c as calculated using equation 2.7, values for the system resolution R_s based on equation 2.6. These system resolution data points were used to fit parameters used for STIR simulation based on equation 4.2. A check was made against a measured system resolution value at approximately 10cm distance	. 111
4.3	Examples of digital phantoms and attenuation maps used to investigate how resolution can vary in SPECT imaging. (a) Elliptical cylinder with point sources, (b) Non-uniform activity distribution, (c) Uniform attenuation map, (d) Non-uniform attenuation map	. 113
4.4	(a) Axial slice through elliptical phantom, reconstructed using 33 OSEM iterations (6 subsets) with RM off. Inset shows an example of planar section used for 2D Gaussian fitting, (b) Example of PSF profile, in the radial direction, with resulting Gaussian fit	. 114
4.5	Illustration of tangential, axial and radial directions which will be used for FWHM measurements of the PSF	. 116

4.6	FWHM measurements from a uniform elliptical phantom recon-	
	structed to 33 OSEM iterations without using RM. Error bars based	
	on the Gaussian fit are not visible on this graph	117
4.7	Graphs demonstrating variation of sigma values (1 pixel = 1.5 mm)	
	with number of reconstruction updates. Reconstructions without	
	RM, and with RM are shown in (a) and (b), respectively. Values	
	were measured for a point 8 cm from the centre of a uniformly	
	attenuating elliptical cylinder. X-axis is number of updates (where	
	6 updates = 1 full iteration)	118
4.8	Graphs demonstrating the effect on resolution in each direction for	
	different positions within the uniform elliptical phantom. Recon-	
	struction was performed using OSEM with 200 updates, without	
	RM, with 2D RM and with 3D RM. Error bars based on the Gaus-	
	sian fit are not visible on these graphs	119
4.9	Appearance of the uniform elliptical cylinder with a non-uniform	
	attenuation map, reconstructed without RM (top) and with 2D RM	
	(bottom)	120
4.10	Transaxial slice through reconstructed non-uniform activity distri-	
	bution data (input data shown in Figure 4.3 b). Reconstruction was	
	performed with no RM and with 200 OSEM updates. The point at	
	the left of the ellipse is close to two hot areas, and the point on the	
	right is not expected to be affected by these areas	121
4.11	Plot showing the variation of FWHM in each direction with update	
	number, for reconstructions performed with 2D RM. Results are	
	shown for the point close to the hot areas in the phantom in Figure	
	4.10, and for the point away from the hot areas in the same phantom.	122

4.12	An example of the Gibbs-type ringing artefact introduced by apply-
	ing RM at 33 OSEM iterations (6 subsets) to a point 12cm from the
	centre of a uniform cylinder. The original voxel value was 1000.
	The Gaussian shape shown for the tangential profile of the PSF re-
	constructed with 2D RM is not a good fit
4.13	Phantoms, with a range of lesion sizes and TBRs, used to estimate
	inaccuracy due to application of PVC with the assumption of invari-
	ant resolution
4.14	Diagram demonstrating the process of calculating the 'central' and
	'specific' recovery coefficients (RC), which are used for evaluat-
	ing the bias incurred when performing PVC with the assumption of
	invariant resolution
4.15	Recovery coefficients, as calculated based on lesions of a range of
	sizes and TBRs, convolved using two different kernels
4.16	Plots of Recovery Fraction (RF) for a range of 'lesion' diameters
	and TBRs. Circular points represent the uncorrected RF of lesions
	convolved with the specific PSF. The green line represents the RF
	of lesions corrected using the 'specific' RC (i.e. perfect correction).
	Crosses represent the RF of lesions corrected using the 'central' PSF. 132
4.17	Plot demonstrating the percentage bias incurred from applying PVC
	with RC values based on the PSF at the centre of the FOV 133
4.18	Photographs of the set up of NEMA phantoms with two spheres at
	the isocentre (top row), and the resulting reconstructed SPECT/CT
	data (bottom row). The central spheres shown are the 13 mm di-
	ameter sphere (left hand side images), and the 28 mm sphere (right
	hand side images)

4.19	Comparison of the orbit of detectors with the NEMA phantom in two different positions along the x-axis (i.e. position 1 had one sphere in the centre of the Field of View (FOV), position 2 moved a different sphere to the centre of the Field of View). Radar plot shows the projection number around the circumference, and the position of the detector relative to the centre of the FOV for each projection angle.	138
4.20	Comparison of the phantom set up with the 10 mm sphere in the centre of the FOV (left) and moved 11.4 cm laterally along the x-axis (right), reconstructed using the clinical protocol with RM	138
4.21	Mean Recovery Coefficient curves for the six spheres, acquired at the image isocentre, and 11.4 cm from the centre. VOIs were drawn based on the size and position of the spheres on the registered CT data. Data presented includes images reconstructed using the clinical protocol, including RM, and without RM.	139
4.22	Maximum Recovery Coefficient curves for the six spheres, acquired, reconstructed and analysed as per Figure 4.21	140
5.1	Images showing representative slices of the simple geometrical phantom, showing the two different lesion positions, the three different TBRs, and examples of the lesion radii used in this study	148
5.2	Images showing representative slices of the simple geometrical phantom, with points in different position relative to the lesion of interest.	149

5.3	XCAT phantom (GT) showing activity distribution set up to represent a bone metastasis in the femoral head. The top row shows the	
	dataset generated with activity within the bladder, the bottom row	
	shows the dataset generated assuming an empty bladder. CT data	
	generated with XCAT is shown overlayed with the activity data. A	
	'hot metal' colour scale is used where white corresponds to high-	
	est activity, through yellow, orange, red and black corresponding to	
		- 1
	lowest activity)]
5.4	XCAT phantom (GT) showing activity distribution set up to repre-	
	sent a Tektrotyd scan with a uniform lesion in the liver. CT data	
	generated with XCAT is shown overlayed with the activity data.	
	The top row shows a lesion with $TBR = 4$ (Krenning score of 3).	
	Lower row shows a lesion with $TBR = 6.25$ (Krenning score of 4).	
	A 'hot metal' colour scale is used where white corresponds to high-	
	est activity, through yellow, orange, red and black corresponding to	
	lowest activity	52
5.5	XCAT phantom (GT) showing activity distribution set up to repre-	
	sent a Tektrotyd scan with a necrotic lesion in the liver. CT data	
	generated with XCAT is shown overlayed with the activity data. A	
	'hot metal' colour scale is used where white corresponds to high-	
	est activity, through yellow, orange, red and black corresponding to	
	lowest activity	53
5.6	2D Gaussians were reviewed with contour lines in order to allow a	
	visual check of fit, including the theta parameter	55
5.7	Diagram visualising the process used to assess the accuracy of the	
	perturbation-estimated PSF	56

5.8	FWHM measurements in each direction vs reconstruction update number (10 updates = 1 full iteration) measured in a) central lesion without noise, b) off-centre lesion without noise, c) central lesion with noise and d) off-centre lesion with noise. The perturbation point was positioned in the centre of a 36 mm radius lesion and the lesion TBR was 10 in all cases shown. Error bars relate to the standard deviation in the fitted FWHM parameters but are too small to be seen clearly on noise-free data	. 159
5.9	Graphs demonstrating the effect of lesion parameters of a) lesion contrast and b) lesion size on tangential FWHM measurements for selected reconstruction updates in noise-free images of the simple elliptical phantom. The point of measurement was in a lesion, 8 cm from the centre of the FOV. When varying the lesion TBR, the radius was set to 36 mm. When varying the lesion radius, the TBR was set to 10	. 160
5.10	Graphs demonstrating the effect of lesion contrast on tangential FWHM measurements for selected reconstruction updates in noisy images of the simple elliptical phantom. The point of measurement was in a 36 mm radius lesion, 8 cm from the centre of the FOV	. 161
5.11	Plots show FWHM measurements vs reconstruction update number (10 updates = 1 full iteration) from noise-free data, where the perturbation point was positioned centrally in the FOV, but at different positions relative to the centre of a 36mm radius lesion (lesion TBR = 10) as shown in Figure 5.2 (a) - (c).	. 163

5.12	FWHM measurements in each direction vs reconstruction update
	number as measured in uniform lesions within anthropomorphic
	phantoms for noise-free data in an XCAT activity distribution simu-
	lating a) a bone scan and b) a Tektrotyd scan. The perturbation point
	was positioned in the centre of each spherical lesion. The bone scan
	lesion was positioned within the femoral head, adjacent to the blad-
	der, and the Tektrotyd lesion was positioned within normal liver 164
5.13	Ribs-like phantom used to assess the effect of orbit and activity dis-
	tribution on convergence behaviour (shown in the graph in (c)) 165
5.14	FWHM measurements in each direction vs reconstruction update
	number as measured in the femoral head lesion of the bone scan,
	with high activity within the bladder
5.15	RRMSE results for the 36 mm radius lesion, positioned 8 cm from
	the isocentre in the noise-free simple phantom. Results are shown
	for two different contrast settings, for perturbation-estimated PSF
	and a non-specific PSF
5.16	a) Regional mean values (RMVs) measured for a lesion in the sim-
	ple cylindrical phantom with 36 mm radius, TBR = 10, positioned
	centrally in FOV, for different image reconstruction update num-
	bers. Note that the uncorrected noise-free and noisy datasets over-
	lay each other. b) Deviation in RMV from ground truth (in %)
	following STC with perturbation-estimated PSF or the non-specific
	PSF, for off-centre lesions and a range of lesion sizes. All lesions
	had TBR=10, and all images used 200 reconstruction updates 169
5.17	a) - c) from left to right; ground truth, uncorrected and corrected
	images, in the transaxial plane, through the centre of a 36 mm radius
	lesion within the the simple phantom using noise-free data. d) - f)
	from left to right; local region around the lesion, zoomed in, on
	ground truth, uncorrected and corrected data

3.18	Noise-free images, in the transaxial plane, of the ACAT bone scan
	phantom dataset. (a) is the uncorrected image reconstructed with
	200 updates, (b) is the local region around the lesion in the uncor-
	rected image, (c) is the local region around the lesion GT data (used
	for segmentation), and (d) is the post-PVC images after correction
	with 10 STC iterations
5.19	Noise-free images, in the transaxial plane, of the uniform lesion in
	the liver of the XCAT Tektrotyd scan phantom datasets. (a) is the
	uncorrected image reconstructed with 200 updates, (b) is the local
	region around the lesion in the uncorrected image, (c) is the local
	region around the lesion GT data (used for segmentation) and (d) is
	the post-PVC images after correction with 10 STC iterations 171
5.20	Noise-free images, in the transaxial plane, of the non-uniform lesion
	in the liver of the XCAT Tektrotyd scan phantom datasets. (a) is the
	uncorrected image reconstructed with 200 updates, (b) is the local
	region around the lesion in the uncorrected image, (c) is the local
	region around the lesion GT data (used for segmentation), and (d)
	is the post-PVC images after correction with 10 STC iterations 172
5.21	Regional Mean Values before and after STC correction, compared
	with Ground Truth, for noise-free data and 200 reconstruction up-
	dates, for the three different liver lesions investigated within the
	Tektrotyd XCAT dataset. The value for the spleen is also demar-
	cated with a line demonstrating that the uncorrected RMV of uni-
	form lesion 2 is lower than the spleen, but the ground truth and
	post-STC corrected RMV is actually greater than the spleen. Data
	corrected with STC based on a non-specific PSF is also included
	and demonstrates a consistent over-correction compared with GT 173

6.1	Experimental set up for system resolution measurements made us-	
	ing line sources acquired on Siemens Symbia system. The detectors	
	were moved such that acquisitions were made at a range of source	
	to detector distances	86
6.2	Data used and linear fits either side of HU = 0, allowing CT data to	
	be converted to density for use in SIMIND	90
6.3	From left to right: the interfile sinogram (for a slice in the middle of	
	the body) of clinical Tektrotyd data acquired using an energy win-	
	dow centred on the photopeak with a Symbia SPECT/CT system,	
	the anterior view projection image, the posterior view projection	
	image	93
6.4	From left to right: the interfile sinogram (for a slice in the mid-	
	dle of the body) of clinical Tektrotyd data acquired using an energy	
	window centred 22 keV lower than the photopeak with a Symbia	
	SPECT/CT system, the anterior view projection image, the poste-	
	rior view projection image	94
6.5	From left to right: transaxial, coronal and sagittal slices through an	
	example patient dataset showing (a) unsmoothed, and (b) smoothed	
	data	95
6.6	Flowchart outlining the steps used for the preparation of GT test	
	datasets, and the subsequent use of these for analysis of PVC methods.19	97
6.7	STIR reconstruction of Patient Data A, fused with CT, which forms	
	the background for GT dataset Cases 1 and 6	98
6.8	STIR reconstruction of Patient Data B, fused with CT, which forms	
	the background for GT dataset Cases 2 and 7	98
6.9	STIR reconstruction of Patient Data C, fused with CT, which forms	
	the background for GT dataset Cases 3 and 8	99
6.10	STIR reconstruction of Patient Data D, fused with CT, which forms	
	the background for GT dataset Cases 4 and 8	99

6.11	STIR reconstruction of Patient Data E, fused with CT, which forms
	the background for GT dataset Case 5
6.12	Results from measuring the distance for the LEHR and LEGP collimators are shown as points. The green line shows the expected distance based on the sum of the radii shown on the Patient Positioning Monitor (PPM). Approximate measurement error on each point was 3 mm, however error bars are too small to be seen here. 203
6.13	Plots of Radius of rotation vs projection angle for acquisition of a NEMA phantom acquired with the Siemens Symbia SPECT-CT, and simulated in SIMIND using a counter clockwise rotation starting at 180°
6.14	Review of projection images, comparing real projection images acquired using the Symbia gamma camera (top row) and the simulated projection images generated using SIMIND with a rotation set to Counter Clockwise, starting at 180 degrees (bottom row) 205
6.15	Resulting images of the rods used to measure the FWHM at different distances from the detector produced by the Symbia system as viewed on Hermes
6.16	Example images generated in SIMIND, used to assess the planar system resolution of MC simulated images. 6.16a also shows region selected on ImageJ used for plotting line spread profiles 206
6.17	Example profiles through the acquired line sources as measured on Symbia and SIMIND, with a range of distances between test object and collimator face. The Gaussian fits based on parameters optimised by Excel Solver are shown as lines in each plot 207

6.18	System resolution (in FWHM) variation with distance shown for	
	real data, SIMIND data and STIR system model, compared with	
	the expected system resolution (according to equation 2.6). Mea-	
	surements made at a range of distances, using line sources ac-	
	quired on Siemens Symbia (blue points) are compared with SI-	
	MIND measurements (green points). The linear resolution approxi-	
	mation made by STIR software is shown as a black line (from equa-	
	tion 4.2)	208
6.19	Bland-Altman plot showing mean spatial resolution as measured in	
	SIMIND simulations and measurements from a real Symbia gamma	
	camera. Measurements are based on images of five rods. Error bars	
	are derived from the standard deviation of the average FWHM from	
	the five rods	209
6.20	Energy spectrum for ^{99m} Tc SIMIND simulation of example dataset	
	1 of Tektrotyd data, overlayed with a spectrum acquired on the	
	Siemens Symbia gamma camera of a Tektrotyd scan patient. Count	
	data are normalised to the maximum value of each spectrum	210
6.21	SIMIND simulation for the assessment of planar sensitivity	210
6.22	Sensitivity profiles	211
6.23	Data of test case 1; spherical lesion inserted in the liver of Patient	
	dataset A. These data were used as GT data and were input to SI-	
	MIND for simulation. Activity distribution displayed fused with	
	CT	211
6.24	Data of test case 2; spherical lesion inserted in the liver of Patient	
	dataset B. These data were used as GT data and were input to SI-	
	MIND for simulation. Activity distribution displayed fused with	
	CT	211

6.25	Data of test case 3; spherical lesion inserted in the liver of Patient
	dataset C. These data were used as GT data and were input to SI-
	MIND for simulation. Activity distribution displayed fused with
	CT
6.26	Data of test case 4; spherical lesion inserted in the liver of Patient
	dataset D. These data were used as GT data and were input to SI-
	MIND for simulation. Activity distribution displayed fused with
	CT
6.27	Data of test case 5; spherical lesion inserted in the liver of Patient
	dataset E. These data were used as GT data and were input to SI-
	MIND for simulation. Activity distribution displayed fused with
	CT
6.28	Data of test case 6; non-uniform and non-spherical lesion inserted
	in the bowel area of Patient dataset A. These data were used as GT
	data and were input to SIMIND for simulation. Activity distribution
	displayed fused with CT
6.29	Data of test case 7; non-spherical and highly heterogenous lesion
	inserted in the liver of Patient dataset B. These data were used as GT
	data and were input to SIMIND for simulation. Activity distribution
	displayed fused with CT
6.30	Data of test case 8; non-spherical and highly heterogenous lesion
	inserted in the liver of Patient dataset C. These data were used as GT
	data and were input to SIMIND for simulation. Activity distribution
	displayed fused with CT
6.31	Data of test case 9; non-spherical and heterogenous lesion inserted
	in the right lung of Patient dataset D. These data were used as GT
	data and were input to SIMIND for simulation. Activity distribution
	displayed fused with CT

6.32	Review of standard deviation of voxel values in a uniform area of
	the same size, comparing clinical acquisition to SIMIND simula-
	tion, for patient dataset A
7.1	Example RRMSE evaluation for Case 3, for images with PVC using
	RL applied up to 500 RL iterations (a) and comparing STC and RL
	for up to 10 iterations (b)
7.2	Screengrabs from AMIDE showing VOIs positioned on the NEMA
	phantom used for RC calculation. Left to right: transaxial, coronal
	and axial planes
7.3	Curve fit for NEMA phantom data, using all seven imaged spheres,
	to produce the mean RC curve
7.4	Example images for Case 2 including GT, uncorrected, STC cor-
	rected and RL corrected spherical lesion. Images in the Left column
	show transaxial plane of whole image FOV. The other images show
	transaxial plane images of the local region around the lesion 226
7.5	PVC corrected lesion images of Case 2, shown in the Axial (left),
	Coronal (centre) and Sagittal (right) planes. Top row: STC cor-
	rected lesion. Middle row: RL corrected lesion, Bottom row: lesion
	with voxel values replaced by RC-corrected regional mean values
	to produce pseudo-RC image
7.6	Residual images, in the transaxial plane, comparing the STC-
	corrected data to the Ground Truth (GT) for each STC iteration in
	Case 2. Values are expressed as percentages, relative to the GT le-
	sion value, and the scale ranges from -100% of GT (corrected voxel
	value overestimates the voxel value by 100%) to 100% (corrected
	voxel value underestimates the GT voxel value by 100%)

7.7	Residual images, in the transaxial plane, comparing the RL-	
	corrected data to the GT for RL iterations 1-7 and selected higher	
	RL iterations in Case 2. Values are expressed as percentages, rel-	
	ative to the GT lesion value, and the scale ranges from -100%	
	(corrected voxel value overestimates the voxel value by 100%) to	
	100% (corrected voxel value underestimates the GT voxel value by	
	100%)	28
7.8	Graph showing the Relative Root Mean Square Error (RRMSE) (in	
	scaled voxel value) for Cases 1-5 (uniform, spherical lesions) for	
	uncorrected data, images produced by STC and RL, and a pseudo-	
	RC-corrected image	29
7.9	Corrected lesion TBR for Cases 1 - 5 (spherical lesions)	3C
7.10	Graph showing the percentage deviation from Ground Truth TBR	
	for spherical lesions in Cases 1 - 5 after application of PVC by	
	different methods	31
7.11	Example images for Case 7 including GT, uncorrected, STC cor-	
	rected and RL corrected non-spherical, heterogenous, lesion. Im-	
	ages in the Left column show transaxial plane of whole image FOV.	
	The other images show transaxial plane images of the local region	
	around the lesion	32
7.12	Profiles through the long axis of the transaxial slice for the lesion	
	included in Case 7, showing profiles for uncorrected data, scaled	
	ground truth data, data corrected using STC and data corrected us-	
	ing RL	32
7.13	PVC corrected lesion images of Case 7, shown in the Axial (left),	
	Coronal (centre) and Sagittal (right) planes. Top row: STC cor-	
	rected lesion. Bottom row: RL corrected lesion	3

7.14	Residual images, in the transaxial plane, comparing the STC-
	corrected data to the GT for each STC iteration in Case 7. Values
	are expressed as percentages, relative to the GT lesion value, and
	the scale ranges from -100% (corrected voxel value overestimates
	the voxel value by 100%) to 100% (corrected voxel value underes-
	timates the GT voxel value by 100%)
7.15	Residual images, in the transaxial plane, comparing the RL-
	corrected data to the GT for RL iterations 1-7, and selected higher
	RL iterations in Case 7. Values are expressed as percentages, rel-
	ative to the GT lesion value, and the scale ranges from -100%
	(corrected voxel value overestimates the voxel value by 100%) to
	100% (corrected voxel value underestimates the GT voxel value by
	100%)
7.16	Graph showing the RRMSE for Cases 6 - 9 (non-spherical, non-
	uniform lesions) for uncorrected data, images produced by STC and
	RL, and a pseudo-corrected image for RC
7.17	Graph showing the corrected lesion TBR for Cases 6 - 9 (non-
	spherical, non-uniform lesions)
7.18	Graph showing the percentage deviation from Ground Truth TBR
	for non-spherical, non-uniform lesions in Cases 6 - 9 after applica-
	tion of PVC by different methods
7.19	Box plot showing the median, minimum, maximum and interquar-
	tile range (IQR) of the percentage deviation from Ground Truth
	TBR for lesions in Cases 1 - 9 after application of PVC by dif-
	ferent methods. Points lying outwith 1.5 x IQR are represented by
	small circles

List of Tables

4.1	FWHM results for point sources positioned 8cm from the centre;
	for a uniform ellipse, a non-uniform ellipse with a point away from
	and a point close to hot regions. All from data reconstructed with
	200 OSEM updates
5.1	A summary of different lesions examined using the uniform ellipti-
	cal phantom
6.1	Key parameters used to define the Siemens Symbia Intevo Bold sys-
	tem with LEHR collimators on SIMIND software. The right hand
	column references the position within the SIMIND input file used
	to define a specific feature
6.2	Key differences between STIR and SIMIND software conventions 188
6.3	Summary of total counts in projection data acquired in clinical Tek-
	trotyd cases using the Siemens Symbia SPECT/CT System at Glas-
	gow Royal Infirmary
6.4	Reconstruction parameters used to reconstruct clinical Tektrotyd
	data, in preparation for inserting synthetic lesions
6.5	Summary of SD in uniform area of projection data acquired; com-
	paring clinical data and SIMIND simulation

List of Acronyms

AC Attenuation Correction

AI Artificial Intelligence

CDR Collimator-detector Response

CRC Contrast Recovery Coefficient

CF Calibration Factor

CT Computed Tomography

CZT Cadmium zinc telluride

DEW Dual-energy Window

DVH Dose Volume Histogram

EARL EANM Research Ltd

FBP Filtered Back Projection
FLAB Fuzzy locally adaptive Bayesian
FOV Field of View
FWHM Full-width at half maximum
FWTM Full-width at tenth maximum
GT Ground Truth
GTM Geometric Transfer Matrix
pGTM perturbation based GTM

GRI Glasgow Royal Infirmary

HDP Hydroxydiphosphonate

IR Iterative Reconstruction

IEC International Electrotechnical Commission

HU Hounsfield Unit

iY iterative Yang method
itD iterative Deconvolution
LB Local Background
LEHR Low Energy High Resolution
LP Local Projection
MAP Maximum a Posteriori
MC Monte Carlo
MDP Methyl diphosphonate
MIRD Medical Internal Radiation Dose
MDT Multidisciplinary Team meeting
MGM Müller-Gärtner Method
MLEM Maximum Likelihood Expectation Maximisation

MRI Magnetic Resonance Imaging

MRT Molecular Radiotherapy MTC Multi-Target Correction **NEMA** National Electrical Manufacturers Association **NET** Neuroendocrine tumour NM Nuclear Medicine OAR Organ at Risk **OSEM** Ordered Subsets Expectation Maximisation **PCA** Principal Component Analysis **PET** Positron Emission Tomography PVC Partial Volume Correction PVE Partial Volume Effect **PSF** Point Spread Function

PMT Photomultiplier Tube

PPM Patient Positioning Monitor PRRT peptide receptor radionuclide therapy **PSMA** prostate specific membrane antigen **RBV** Region-Based Voxelwise RC Recovery Coefficient **RL** Richardson-Lucy **ROI** Region of Interest **RoR** Radius of Rotation **RM** Resolution Modelling **RRMSE** Relative Root Mean Square Error

RMV Regional Mean Value

SC Scatter Correction

SD Standard Deviation

SPECT Single Photon Emission Computed Tomography

STC Single Target Correction

STIR Software for Tomographic Image Reconstruction

SUV Standardised Uptake Value

TAC Time activity curve

TBR Target to Background Ratio

TEW Triple-energy Window

VC Van Cittert

VOI Volume of Interest

XCAT Extended cardiac-torso phantom

Chapter 1

Introduction

1.1 Background and Motivation

The key strength of Nuclear Medicine imaging is the capability of providing information on the function of organs, tumours and other structures in the body. The main drawback, in comparison to structural imaging such as Computed Tomography (CT) or Magnetic Resonance Imaging (MRI), is the limited spatial resolution. This limited spatial resolution not only detrimentally affects the image appearance qualitatively, but can lead to quantitative inaccuracies - this is known as the Partial Volume Effect (PVE). The PVE results in reduced quantitative accuracy, particularly for small objects. Underestimates of 20-40% have been reported [Shcherbinin and Celler, 2011], and larger errors are possible depending on imaging modality, activity, and size of object.

The use of quantitative Single Photon Emission Computed Tomography (SPECT) imaging in oncology has wide ranging potential applications, from diagnosis to dosimetry to evaluation of treatment response [Erlandsson et al., 2012b, Zhao et al., 2018]. The utility of quantification depends on the accuracy and precision of the quantitative measurements from the image. The PVE limits the accuracy of these measurements and therefore a correction method is required which is suitable for practical implementation in oncology SPECT.

1.2 Objective

The main objective of this work is to assess potential for improving quantitative accuracy in ^{99m}Tc oncology SPECT imaging through the application of a practical Partial Volume Correction (PVC) algorithm.

A review of the literature is performed to identify and explore existing PVC methods. Existing methods are critically appraised, including consideration of practicalities of implementation, and potential for applying novel adaptations to improve on existing weaknesses. Algorithms with novel adaptation to incorporate case-specific resolution measurements are tested in situations relevant to oncology SPECT imaging with ^{99m}Tc. Complexity of test datasets range from simplistic geometrical phantoms to realistic Monte Carlo (MC) generated datasets based on patient data. Performance of the novel adapted algorithms are compared with the uncorrected data, known ground truth images, and the currently accepted "standard" PVC method.

1.3 Structure and Chapter Outlines

Chapter 2 provides a background, including the principles of Nuclear Medicine (NM) imaging. This includes a focus on aspects which limit the accuracy of quantification, in particular the limited spatial resolution. Applications of quantitative SPECT in oncology are outlined and the concept of the PVE is introduced.

Chapter 3 describes PVC methods which have been utilised in previous research, critically appraising them for their suitability for oncology SPECT imaging. A set of criteria is designed to identify properties of algorithms which are appropriate for practical application in oncology SPECT. The review of existing methods from the literature includes a description of the method, an assessment of the benefits, drawbacks, and assumptions made, in comparison to the oncology SPECT criteria. The literature review demonstrates that there is no consensus on the optimal method for PVC in oncology. Also, even well established and well accepted methods have limitations and rely on assumptions. The oncology

SPECT criteria are used to identify methods from the literature which are potentially suitable for practical implementation. The criteria also aid identification of known weaknesses in existing PVC algorithms which could be addressed by applying novel adaptations.

Chapter 4 assesses the resolution variation across the Field of View (FOV) in SPECT imaging, and the possible impact on the PVE. The variation in resolution across the FOV is a significant issue in SPECT imaging due to the use of physical collimation. This is relevant since several existing PVC methods assume invariant resolution. In addition to carrying out a literature review, the extent of resolution variation is investigated using simulation [Gillen et al., 2019] and phantom work on a real gamma camera system [Gillen, 2022]. Simulations were also used to assess the potential effect of assuming invariant resolution for PVC, with and without using Resolution Modelling (RM) in the reconstruction.

Chapter 5 proposes a solution to the challenge of spatially variant resolution for PVC in SPECT. Using the perturbation method to estimate the case-specific resolution, a novel implementation of PVC is introduced. The perturbation-based resolution, in terms of the Point Spread Function (PSF), is incorporated into the Single Target Correction (STC) PVC algorithm and applied to geometric and anthropomorphic digital phantoms using analytic simulations [Gillen et al., 2022].

Chapter 6 recognises that evaluation of accuracy of PVC algorithms requires test datasets which represent relevant scenarios for the clinical application. Examples based on real clinical images are used as the basis for generating test datasets. Synthetic lesions, including those with non-spherical shapes and non-uniform activity distribution, are added for a known ground truth. MC simulations of the imaging process are performed. This produces realistic, relevant, test datasets with known ground truth. Validation of the MC simulation is included in this chapter.

Chapter 7 uses the datasets designed in Chapter 6 to assess the STC and Richardson-Lucy (RL) PVC methods using perturbation estimated case-specific resolution, as described in Chapter 5. This assessment determines whether

quantification is improved by utilising the case-specific resolution methods compared with the established and well-accepted Recovery Coefficient (RC) method.

Chapter 8 concludes with an overview of the findings of the work in this thesis. This includes limitations of the current investigation and potential future directions of work in this field. The conclusion also outlines a suggestion for how the findings of this thesis could be implemented in practice.

Chapter 2

Principles of Quantitative Nuclear Medicine in Oncology

Nuclear Medicine (NM) uses radiopharmaceuticals for diagnostic imaging, laboratory tests and Molecular Radiotherapy (MRT).

For both imaging and MRT the radiopharmaceuticals administered to patients are taken up by cells due to physiological or biochemical processes. NM imaging illustrates functional information, and NM therapy is targeted to cancer cells to minimise harm to healthy tissue.

2.1 Molecular Radiotherapy

The use of radionuclides for treatment of cancer began earlier than the development of imaging techniques, when ¹³¹I was used to treat functioning thyroid metastases [Seidlin et al., 1946]. In recent years, there has been an expansion of applications and radiopharmaceuticals used for therapy in oncology [Goldsmith, 2019, Sapienza and Willegaignon, 2019]. Recent analysis demonstrated that, from 2007 to 2021, there has been a 231% increase in MRT treatments given in the UK [Rojas et al., 2023].

Treatments including ¹⁷⁷Lu peptide receptor radionuclide therapy (PRRT) for Neuroendocrine tumours (NETs) and ²²³Ra-Chloride or ¹⁷⁷Lu-prostate specific membrane antigen (PSMA) for metastatic prostate cancer [Parker et al., 2013, Rahbar et al., 2017] are continuing to grow significantly in the UK following strong

evidence from recent clinical trials [Rojas et al., 2023].

Several of the radionuclides used for MRT have gamma photon emissions which mean that they can be imaged. Alternatively, they may have a 'theranostic pair' - i.e. an associated imaging radiopharmaceutical with pharmacokinetics which are assumed to be the same or similar to the therapeutic radiopharmaceutical. Quantitative data based on theranostic images can identify patients who would benefit from MRT, can help to plan treatments (including ensuring Organ at Risks (OARs) are not over-dosed) and can be used to monitor response to treatment [Turner, 2018, Langbein et al., 2019]. Accurate quantitative theranostic imaging could potentially be used to give bespoke treatments, personalised for individual patients [Turner, 2018]. Therefore, it is important that quantitative measurements from SPECT imaging are accurate as they could impact the safety and efficacy of MRT (more detail given in Section 2.6).

2.2 Nuclear Medicine Imaging

The two key items of imaging equipment used in Nuclear Medicine are the Gamma Camera and the Positron Emission Tomography (PET) system. The focus of this work is images acquired using a Gamma Camera. References to PET imaging within this thesis are limited to indicating the difference in spatial resolution between SPECT and PET images, where PET imaging has superior spatial resolution.

2.3 Gamma Camera Systems

Conventional gamma camera design is based on two detectors which can rotate about a fixed gantry. For 2D imaging, detectors may remain in place over one part of the patient for planar images or stay in place while the patient bed travels through the gantry to produce whole-body images. The focus of this thesis is tomographic imaging (Single Photon Emission Computed Tomography (SPECT)) which involves rotating detectors around the patient, acquiring images at different angles and reconstructing these data to create a set of 3D images. This has the advantage of removing the superposition of overlying structures seen on 2D

imaging, improving contrast and facilitating image interpretation.

The work in this thesis is based on a dual detector system using scintillation crystals.

2.3.1 Gamma Camera Detector Components

In this section, components of a conventional dual scintillation crystal system will be described with a focus on aspects which affect quantification, in particular aspects relevant to image resolution or Partial Volume Correction (PVC).

2.3.1.1 Collimator

The collimator is the component of the gamma camera which most significantly limits the resolution of NM images. It is required since radioactive decay produces gamma photons isotropically. The collimator acts within the detection system to create a relationship between the position of decay and the point of detection. Photons travelling in a direction allowed by each collimator hole will reach the detector, while photons approaching from other angles do not contribute to the image. Typically, only about 0.01 % of incident photons travel within the angle of acceptance, contributing to the image [Hutton, 2021]. The sensitivity can be improved, at the cost of reducing the spatial resolution.

A commonly used collimator in NM imaging is known as Low Energy High Resolution (LEHR) which is usually the collimator of choice for SPECT imaging with ^{99m}Tc. Other collimators are designed for high sensitivity (fewer, larger holes) and high energy (fewer, larger, longer holes separated by thicker septa).

Spatial resolution is best when the detector is closest to the object being imaged. This means that, for optimal resolution, the gamma camera heads should be positioned as close to the patient as possible without coming into contact. The relationship between distance and resolution (i.e. the depth dependent-resolution) for a LEHR collimator is described further in Section 2.7.8.

2.3.1.2 Scintillation Crystal

Sodium Iodide doped with Thallium (NaI(Tl)) is the scintillation crystal of choice for conventional gamma camera systems. An important feature of the NaI(Tl)

crystal which affects the spatial resolution is the relatively high atomic number. This makes it more likely for gamma rays to undergo photoelectric absorption than Compton scattering, thus maintaining a correlation between the detection point and the decay position. Doping with Thallium results in an improved light conversion efficiency and also ensures that the wavelength of the visible light is appropriate for the crystal and Photomultiplier Tubes (PMTs).

The optimum thickness of NaI(Tl) is usually between 6 and 13 mm, depending on the energy of photons being imaged. This thickness is a compromise between detection efficiency and spatial resolution, with thicker crystals improving detection efficiency but reducing spatial resolution. The reduced spatial resolution for thicker crystals can be attributed to the light signal spreading out more for thicker crystals prior to being incident on the PMTs [Lawson, 2013].

2.3.1.3 Light Guide and PMTs

The light guide provides optical coupling between the scintillation crystal and the PMTs. A thicker light guide results in better uniformity, but poorer resolution (as for the crystal, due to the spreading of light signal prior to reaching the PMTs). The PMTs are used to convert visible light into an electrical signal and amplify that signal. The signals from the PMTs are analysed based on the magnitude of the signal in an energy selection stage. Signals which correspond to gamma rays of energy outwith the desired range are not used (for example, a low energy signal suggests that the gamma ray photon has been scattered and hence has no valuable positional information). Some scatter, however, will still contribute to the image due to the limited energy resolution, affecting image quality (reduction in contrast) and quantitative accuracy. Correction for scatter is required for accurate quantification (discussed in section 2.7.2.1). The position of the event relative to the photomultiplier tubes can affect the intrinsic resolution. If the light from an incident gamma photon is spread across many PMTs, the uncertainty in positioning that event is greater - resulting in a poorer spatial resolution. Conversely, if the incident gamma photon interacts with the crystal very close to the centre of one PMT, it is difficult to precisely locate the event (i.e. a change in real spatial position has a smaller effect on the change in signal), also resulting in poor spatial resolution. The intrinsic spatial resolution is, therefore, best when the incident signal is midway between PMTs [Lawson, 2013].

2.3.1.4 Electronics

The output from each PMT contributes to determining the position and energy of an event. The sum of the output from all PMTs is proportional to the amount of light produced in the crystal (hence the energy of the detected gamma photon). Event positioning is based on Anger positioning logic. Signals below a certain threshold (i.e. from PMTs far from the event) may be discarded before being positioned in order to reduce the effect of noise.

At this stage, the image data is digitised onto a predefined matrix of pixels for review and further processing.

2.3.1.5 Image Digitisation

The pixel size, along with the spatial resolution of the imaging system [Cherry et al., 2012], will impact the spatial resolution, and could therefore affect quantification. Matrix size also affects the noise which can also impact quantification [Boellaard et al., 2004]. The Nyquist sampling theory stipulates the maximum size of a pixel in order to fully capture image data without losing high spatial frequency information [Cherry et al., 2012]:

$$pixel size = \frac{1}{(2 \times k_{max})}$$
 (2.1)

where k_{max} is the maximum spatial frequency in the image. Put another way, this means that for objects smaller than twice the pixel size, the digitisation process will result in a loss of information, and inaccurate quantification.

2.3.2 Corrections Applied to Raw Image Data

Planar images produced from the gamma camera are not automatically perfectly uniform. A number of factors contribute to this non-uniformity, for which corrections can be applied. Due to the bell-shape of the PMT response function, there is a reduction in response between adjacent tubes. These variations across

the detector are resolved by creating an energy correction map. The shape of the PMT response also affects the signal positioning, which can be corrected for using a linearity correction map. A final uniformity correction is also applied to deal with small residual non-uniformities which may be due to factors including collimator or crystal defects.

It is important for quantitative SPECT data that these corrections are applied accurately to avoid amplifying any artefacts in the reconstruction process.

2.3.3 Novel Gamma Camera Design

Currently, most gamma cameras in clinical settings consist of dual-detector scintillation crystal-based systems, as described above. However, the use of direct conversion with Cadmium zinc telluride (CZT) detectors is growing in popularity. In particular, the smaller dimension of CZT detectors have enabled the use of novel gamma camera geometry with multiple small detectors covering 360° around the patient, allowing improved contouring around the patient. This design, along with the properties of the CZT detectors, allows for improved sensitivity (therefore potentially reduced noise) and spatial resolution compared with the conventional dual-detector NaI(Tl) set-up [Desmonts et al., 2020].

2.4 SPECT-CT Systems

Hybrid imaging refers to the combination of functional information from emission imaging with structural imaging (typically Computed Tomography (CT)) providing anatomical information. Over the past two decades, SPECT-CT systems have become commercially available [Van den Wyngaert et al., 2020]. Structural information, including electron density from CT, can be useful when applying corrections for e.g. attenuation and scatter (see Section 2.7), facilitating more accurate SPECT quantification.

2.5 3D Image Reconstruction

The information recorded in SPECT imaging consists of "projection" images acquired at different angles around the patient. These "projection" images

corresponds to histograms of the count distribution on the detector. In first approximation, the value at each pixel depends on the activity in the Field of View (FOV) integrated over the line parallel to the collimator holes (albeit these data are noisy and affected by attenuation, scatter and imperfect collimation). This includes activity within the patient, and any activity outwith the patient (within the FOV). These projections can be displayed in a stack of sinograms, where each slice is represented by a 2D array containing projection data. An image reconstruction algorithm is required to transfer the data from this 'projection space' sinogram into 2D slices in 'image space'.

2.5.1 Filtered Back Projection

The most common analytic image reconstruction algorithm is called Filtered Back Projection (FBP). Images produced by FBP are limited in their accuracy since the simple line-integral model on which they are based cannot account for physical factors such as attenuation or the depth-dependent resolution intrinsic to imaging with a collimator within the reconstruction [Qi and Leahy, 2006]. Due to this significant limitation for quantitative SPECT, it is not used in this thesis.

2.5.2 Iterative Reconstruction

Iterative Reconstruction (IR) methods involve making an initial estimate of the activity distribution, simulating the acquisition process (commonly referred to as "forward projection"), then updating the estimation by comparing the projection estimates with the actual sinogram, as shown in Figure 2.1.

This process is repeated until a certain number of iterations have been completed, or until some other stopping criteria has been met. IR aims to find the best estimate of the true source activity distribution, f, given a set of projection data, p. The forward projection step can be described with equation 2.2:

$$\bar{\mathbf{p}}_i = \sum_j \mathbf{a}_{ij} \mathbf{f}_j \tag{2.2}$$

where $\bar{\mathbf{p}}_i$ represents the expected measurement within the projection data, \mathbf{a}_{ij} is the system matrix which describes the emission and detection process for the

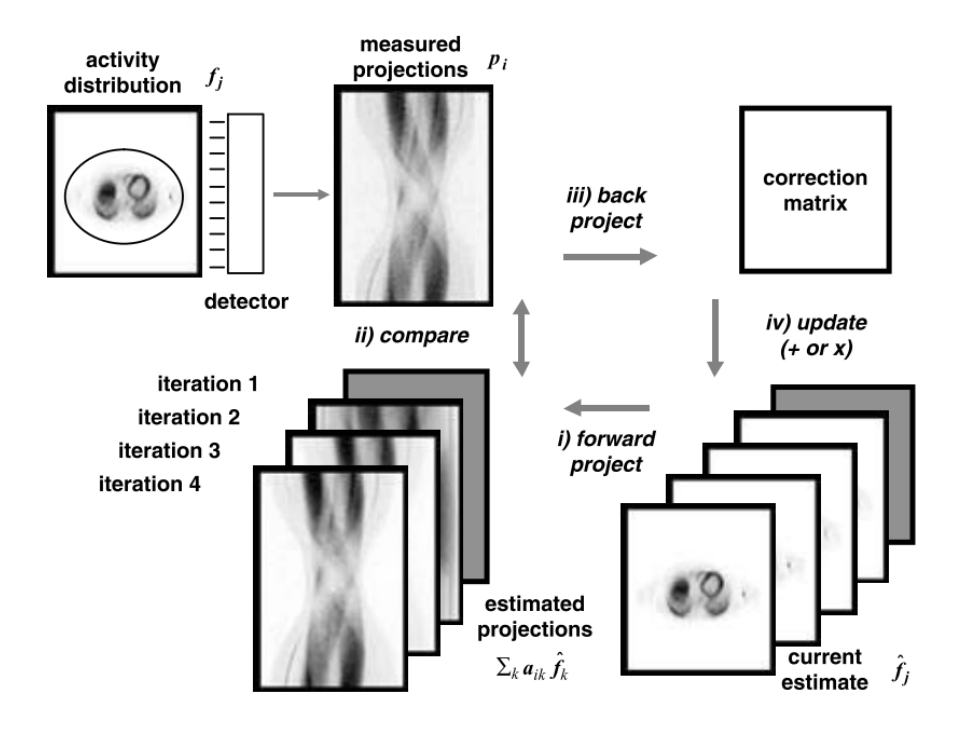


Figure 2.1: Schematic showing the basis of an iterative reconstruction algorithm. Figure reproduced from Zaidi et al. [2006] with permission from Springer Nature (Licence number 5981880433174).

specific imaging system, and \mathbf{f}_j represents a voxel from which the pixel value \mathbf{p}_i originates.

The noise in PET and SPECT emission data can be modelled as Poisson distributed. This Poisson model means that the probability of measuring \mathbf{p}_i counts when the expected measurement is $\bar{\mathbf{p}}_i$ can be expressed as:

$$\operatorname{prob}[\mathbf{p}_{i}|\bar{\mathbf{p}}_{i}] = \frac{e^{\bar{\mathbf{p}}_{i}}(\bar{\mathbf{p}}_{i})^{\mathbf{p}_{i}}}{\mathbf{p}_{i}!}$$
(2.3)

An advantage of IR over analytical algorithms like FBP is that characteristics of the image acquisition system can be modelled in the forward and back projectors, allowing corrections for attenuation, scatter and the distance dependent collimator-detector response to be applied within the reconstruction (see further detail in Section 2.7). Additional prior information can also be incorporated in IR algorithms to improve the quality of the reconstructed image [Qi and Leahy, 2006]. A post-reconstruction filter can also be used to manage the noise levels which can be problematic when IR algorithms are run for high numbers of iterations. Overall,

IR methods produce images which are quantitatively more accurate than those produced by FBP.

The main disadvantage of IR compared with analytical reconstruction methods is the computational expense. This is significantly less problematic now, compared with previous years when computing power was more limited.

Many different iterative reconstruction methods have been described in the literature, with more recent algorithms incorporating Artificial Intelligence (AI) or Machine Learning. In their review Qi and Leahy [2006] identify key distinctions between different algorithms. Algorithms can be categorised by the choice of cost function (including how the data is modelled, and/or a regulariser or smoothing function if used within reconstruction), the optimisation procedure (i.e. how the cost function is minimised or maximised), and the computational cost (i.e. the number of iterations required, which is determined by the rate of convergence). For this thesis, the focus will remain on the most commonly used IR algorithms currently in clinical use; Maximum Likelihood Expectation Maximisation (MLEM) and Ordered Subsets Expectation Maximisation (OSEM).

2.5.2.1 Maximum Likelihood Expectation Maximisation

Given the Poisson model of noise, the likelihood of acquiring the count distribution of the projection data, P, given the current estimate of the source activity distribution, f, can be expressed based on p_i , f_j , and the system matrix a_{ij} . Maximising the likelihood of this expression provides the most likely emission data given the measured projection data.

To determine the Maximum Likelihood (ML) solution, the approach used most commonly is Expectation Maximisation (EM) [Qi and Leahy, 2006].

The MLEM equation can be expressed as [Shepp and Vardi, 1982]:

$$f_j^{\text{new}} = \frac{f_j^{\text{old}}}{\sum_l a_{lj}} \sum_i a_{ij} \frac{p_i}{\sum_k a_{ik} f_k^{\text{old}}}$$
(2.4)

This describes the two steps involved in MLEM; first the expected projections are estimated by forward projecting the current estimate through the system matrix,

then the current estimate is updated to maximise the likelihood (based on comparing the measured and estimated projections, back-projecting this and multiplying the current estimate by this ratio).

2.5.2.2 Ordered Subsets Expectation Maximisation

OSEM is a useful, clinically validated, mechanism to accelerate the MLEM algorithm [Hudson and Larkin, 1994, Hutton et al., 1997, Qi and Leahy, 2006]. OSEM considers an ordered subset of projection data for each iteration. The subset size (or the number of subsets), and the number of iterations can be varied by the user. More projections per subset will speed up the reconstruction compared with MLEM. Provided that the subset size is not too small and the number of updates is not too high, the images obtained by MLEM and OSEM are very similar [Zaidi et al., 2006]. OSEM is the widely accepted standard method of reconstructing clinical SPECT data, and this method will be used for reconstruction throughout this project.

2.6 Applications of Quantitative SPECT in Oncology

While quantitative SPECT is a relatively new technology, there are several potential promising clinical applications in oncology [Dickson et al., 2019]. These include diagnosis, staging, planning of MRT, MRT dosimetry and follow-up using sequential imaging. The preferred metric for quantification may depend on the application and a brief description of possible metrics is included in Section 2.6.5.

2.6.1 Diagnosis and Staging

Diagnosis of cancer and staging disease using SPECT imaging is largely performed by visual assessment. The accuracy of the visual assessment may be limited by the specificity of the study. Quantitative information could potentially assist with enabling more accurate diagnosis and staging using SPECT scans. Radionuclide bone scans using ^{99m}Tc labelled to a diphosphonate (usually Methyl diphosphonate (MDP) or Hydroxydiphosphonate (HDP)) are one of the most common scans performed in clinical Nuclear Medicine departments - often performed as part of routine staging for several different types of cancer [Van Den Wyngaert et al.,

2016]. They are sensitive studies which highlight areas of osteoblastic activity. This activity could be due to degenerative changes, trauma, or metastatic disease. The presence or absence of uptake alone cannot specify the nature of the physiology or pathology - therefore the specificity of a conventional whole body, planar, bone scan has been considered to be a limitation. SPECT-CT allows lesions to be localised using the CT component, which can help with accuracy in reporting [De Schepper et al., 2019]. There is also a potential benefit of utilising quantification to aid diagnosis, however more work is required in order to derive clinically relevant numerical thresholds [Ross et al., 2019].

2.6.2 MRT Treatment Planning

As mentioned in Section 2.1, MRT is a rapidly growing area. The use of theranostic pairs can provide information for treatment planning before the first fraction of therapy is delivered. One example of this is the use of ^{99m}Tc Tektrotyd imaging to identify patients with Neuroendocrine tumour (NET) which are somatostatin receptor positive, and would therefore be candidates for peptide receptor radionuclide therapy (PRRT). A semi-quantitative metric known as the Krenning score can be used for Tektrotyd or ¹¹¹In Octreotide images to determine whether a patient would benefit from PRRT [Krenning et al., 1999]. The Krenning score, which compares lesion uptake to normal liver uptake, may be impacted by the limited resolution if the lesion size is small compared with the reconstructed spatial resolution. Further detail on the Krenning score can be found in Section 3.4.5.6.

There are several papers in the literature which compare PET and SPECT imaging for identifying NETs. However, in general they do not attempt to correct for the limited resolution, which is a more significant issue for SPECT than PET. PET tracers were found to be more suitable for the in vivo identification of NETs [Poletto et al., 2022]. Quantification of small lesions, in particular, is more accurate in ⁶⁸Ga Dotatate PET than ¹¹¹In Octreotide SPECT [Hope et al., 2019]. Another study comparing ^{99m}Tc Tektrotyd to ¹⁸F FDG PET [Saponjski et al., 2021] found a difference in true positive identification rate between the imaging techniques - especially for small lesions. This also suggests that the Partial Volume Effect of

limited spatial resolution is a limiting factor.

Given the rate of growth for MRT, it could be important to consider utilisation of quantitative SPECT imaging as a more accessible technology than PET [Dickson et al., 2019]. Comparing the accuracy of PET and SPECT imaging for identification of patients who could benefit from PRRT would be fairer with the application of an appropriate correction for limited spatial resolution.

2.6.3 Dosimetry

Dosimetry of MRT procedures is important for the evaluation and assurance of efficacy and safety of the treatment. Calculation of absorbed dose to lesions and also OARs can be performed. While not being performed universally, a survey based on data from 2020-22 and 27 countries demonstrated that 84% of centres surveyed perform some form of dosimetry calculation [Peters et al., 2023].

Dosimetry calculations are complex, involving multiple stages of measurement and calculation. The Medical Internal Radiation Dose (MIRD) schema is a well established framework for the calculation of absorbed dose to a region [Loeevinger and Berman, 1968]. MIRD describes how the mean absorbed dose to a target region can be calculated based on the activity in another region. This must account for the type of radiation, biological properties of organs, and the cumulated activity within the region (based on a Time activity curve (TAC)).

An extension to the MIRD strategy is to produce a voxelwise 3D map of absorbed dose distribution using dose-point kernels [Giap et al., 1995, Graves et al., 2019].

A recent article notes that clinical implementation of dosimetry has been limited due to a lack of consensus on methodologies for calculation of the multiple factors involved [Gustafsson and Taprogge, 2023]. Different methods for data collection (e.g. how many time points, how activity is measured) and fitting the TAC can produce different results, despite testing the same radiopharmaceutical and organ [Gustafsson and Taprogge, 2023]. Quantification of objects in SPECT feed in to this time-activity curve and dosimetry calculation. Accuracy in dosimetry is also challenged by the range of different radionuclides used, and the range of size

and shapes of objects considered. These factors affect the extent of the impact of the limited spatial resolution (more in Section 2.7.8.1).

It has been highlighted that in order to derive accurate activity concentration measurements for dosimetry, management of the limited spatial resolution of nuclear medicine images by finding a robust solution for Partial Volume Effect (PVE) correction is key [Marquis et al., 2025]. The issue of managing the limited spatial resolution is also raised in terms of uncertainty estimation - in particular for the variability that partial volume correction can contribute to dosimetry calculations [Gustafsson et al., 2015, Gear et al., 2018]. It has also been noted that the understanding of the relationship between absorbed dose to tissues, and the response to MRT is limited by the effect of the resolution of SPECT studies [Marquis et al., 2023].

2.6.4 Follow-up Imaging

Sequential imaging can be used to monitor the efficacy of an intervention. By comparing images acquired weeks or months apart, clinicians can assess how disease has responded to, for example, MRT or chemotherapy. Quantitative SPECT could aid the identification of lesions which are less avid after treatment - demonstrating response to the treatment. Alternatively, in the absence of intervention, quantification of lesions increasing in avidity or new lesions could also provide useful clinical information to guide further management. Follow-up imaging with quantitative PET-CT is widely used, and one study has found a strong correlation between Standardised Uptake Value (SUV) measured with PET and SPECT for prostate and breast cancers, concluding that quantitative SPECT imaging could be useful for follow-up imaging [Arvola et al., 2019].

There are a number of confounding factors which make comparing quantitative measurements from images at different time points difficult or unreliable. These factors include those related to different body conditions at those time points. For example, body habitus, body positioning for imaging and variable physiological uptake in neighbouring organs (bladder, bowel). Technical factors including administered activity and equipment used for imaging could also impact

quantification. Several of these confounding factors could have an effect of the resolution of the reconstructed image - and therefore impact the extent of the detrimental effect of the partial volume effect. Correcting accurately for this effect could potentially reduce variability in quantification for some of the factors which are impossible or not practical to control.

2.6.5 Quantitative Metrics

In quantitative PET, SUV metrics are most often used. The SUV converts the measured activity concentration to a measure of uptake by normalising to the patient weight and administered activity. The activity concentration is usually derived from the counts measured from a region or volume selected by the user and a measured Calibration Factor (CF). There are different definitions of SUV metric, including SUV $_{max}$, SUV $_{mean}$ and SUV $_{peak}$ (including different interpretations of SUV $_{peak}$ [Vanderhoek et al., 2012]), each with different advantages and limitations. While SUV metrics are widely used in diagnosis and staging with PET-CT imaging, they are not yet in clinical practice for quantitative SPECT imaging. Work has been performed to differentiate between normal uptake and metastatic NET lesions from 99m Tc EDDA/HYNIC-TOC (Tektrotyd) SPECT-CT in terms of SUV $_{max}$ [Reilly et al., 2021]. However, this work does not take into account the effect of the limited spatial resolution on quantification.

For certain diagnostic scans, relative metrics may be relevant (for example the ratio between lesion uptake to normal physiological liver uptake forms the basis of the Krenning score used for NET diagnosis - more detail is given in Section 3.4.5.6).

Quantitative SPECT for dosimetry requires absolute quantification, for example in terms of Bq/cc (or similar). However there is debate over whether this should be evaluated per voxel or on a whole region basis [Chiesa et al., 2019] (discussed further in Section 3.2.2.4).

2.7 Limitations to Accuracy in Quantitative SPECT

In addition to the detrimental effect of limited spatial resolution, the PVE, which is the focus of this thesis (see Section 2.7.8.1 for full description), there are other

factors which could limit the accuracy of quantitative SPECT.

A key contributor to the accuracy of quantitative SPECT is the calculation of a cross-calibration factor between the radionuclide calibrator and gamma camera. The accuracy of this depends on the activity measured by the radionuclide calibrator, which should be traceable back through the calibration chain to a primary standard. Nationally for the UK this primary standard is held at the National Physical Laboratory. It is recommended that the radionuclide calibrator is accurate to within 5% of the primary standard [Gadd et al., 2006]. This $\pm 5\%$ accuracy will also apply to measurements made of activities administered to patients, which may also contribute to calculations for quantification.

Several other factors, such as attenuation and scatter, have well-accepted methods for correction. Unlike these other factors, there is currently no consensus on the optimal method for correction of the PVE in oncology imaging. Practical challenges which can limit accurate quantification include mis-registration or imperfect segmentation of the object(s) of interest. While these are related to the PVE, registration and segmentation are established fields of study in their own right. Optimisation of attenuation, scatter and motion correction tools, and techniques for registration and segmentation fall outwith the scope of this project.

2.7.1 Attenuation

Gamma photons interacting with matter within the patient may be scattered to the point where they are not detected. This has the effect of a non-uniform activity profile across a uniform activity distribution. Different materials have different attenuation coefficients, with bone being more attenuating than water. A rough calculation demonstrates that approximately 70% of photons originating from the centre of a human head could be attenuated [Gillen et al., 2015]. If not corrected for, this will affect quantification in SPECT imaging [Hutton et al., 2011].

2.7.1.1 Attenuation Correction

Simple attenuation correction, assuming the entire body consists of the same material, can be performed using the Chang method [Chang, 1978]. The availability

of a registered CT dataset can improve the accuracy of attenuation correction [Chang, 1978, Ljungberg, 2018].

Due to the difference in energies between the CT photons and the SPECT photons, some scaling for the transmission of photons is required. Care must also be taken when using a CT scan with contrast agents, or if the patient has metal implants, as this may introduce artefacts.

2.7.2 Scatter

If Compton Scattering occurs within the patient at a small enough angle, scattered photons may still pass through the collimator holes and be detected. There may also be scatter within the detector itself. Scattered photons may account for 30–40% of the photons detected in the photopeak [Hutton et al., 2011]. The effect of scattered photons contributing to the image is "blurring and haziness of the observed projections, [which] reduces reconstructed contrast and introduces significant uncertainty in quantification of the underlying activity distribution" [Hutton et al., 2011].

2.7.2.1 Scatter Correction

A simple form of Scatter Correction (SC) can be performed using Chang Attenuation Correction (AC) by setting broad beam (lower) attenuation coefficient. This doesn't incorporate any spatially variable correction.

Energy windows acquired at the same time as the photopeak can be used to perform Dual or Triple-energy Window (TEW) scatter correction. Scaling the scatter image appropriately gives an estimate of the contribution from scatter, SE, as per equation 2.5 for a triple energy scatter estimate [Hutton et al., 2011]:

$$SE = \left(\frac{C_l}{w_l} + \frac{C_u}{w_u}\right) \times \frac{w_p}{2} \tag{2.5}$$

where C_l and C_u are the counts in the lower and upper windows, respectively, w_l , w_u and w_p are the widths of the lower, upper and peak energy windows. For a dual energy window correction C_u is set to zero.

Monte Carlo (MC) scatter correction algorithms are now more commonplace

due to improved computational potential. Advanced MC algorithms can also incorporate a correction for septal penetration [Liu et al., 2008] or modelling of the response of the detector and collimator [Sohlberg and Kajaste, 2012].

2.7.3 Motion

Patients may also move during SPECT acquisition. This could be due to cardiac motion, breathing, or less predictable motion due to being uncomfortable. Motion during the SPECT acquisition could lead to blurring of the image (a temporal partial volume effect [Erlandsson et al., 2012a]) or other artefacts. In addition, any motion between the SPECT and the CT acquisitions may result in a mis-registration between the two datasets and therefore may affect the accuracy of attenuation and scatter correction if CT is used for these.

Motion could be accounted for in the acquisition, reconstruction or analysis. Cardiac motion is, in general, rhythmic and predictable. This allows an ECG trace to acquire gated data over hundreds of cardiac cycles. Gated data combines images taken at the same phase of a heartbeat and the combined images can be looped in sequence to form a representative cardiac cycle. Respiratory motion could also be corrected for by gating using hardware devices, or by data driven software methods [Walker et al., 2020, Frood et al., 2018]. These methods tend to be employed in PET imaging more than SPECT, and the issue of motion has been studied less for quantitative SPECT for MRT compared with other SPECT applications such as cardiac imaging [Gustafsson and Taprogge, 2023].

In general (with the exception of respiratory or cardiac motion) it is better to prevent or reduce motion in acquisition, rather than correcting for it. This can be achieved by immobilisation devices, ensuring that patients are comfortable and utilising a trade off between acquisition time (i.e. noise) and the likelihood of patient motion. Raw data can be reviewed following the scan to assess for motion, and repeat acquisitions performed if the extent of motion is likely to result in non-diagnostic images.

2.7.4 Segmentation

A full assessment of segmentation falls outwith the scope of this work. However, as key PVC techniques including Recovery Coefficient (RC) and Single Target Correction (STC) require segmentation, a brief overview of the development of segmentation methodology is given here for completeness (with reference made to a Symposium "Functional Volume Segmentation - State of the Art" presented at the 2019 EANM conference [Hatt, 2019]).

Initially, functional volumes were delineated entirely manually. This could be done based on anatomical images such as CT or MRI. Manual delineation is subject to inter-operator variation, time consuming and not practical to perform for many volumes of interest. From the mid 1990's the use of thresholding techniques was explored, based on the relative pixel values around a volume of interest. This technique is faster than entirely manual methods, but no onesize-fits-all segmentation method using thresholding was found. Optimisation of parameters used for thresholding are required for specific imaging equipment and reconstruction settings (in particular the noise levels in images is influential) [Hatt et al., 2011]. The late 2000's utilised statistical ("stochastic") techniques, such as Fuzzy locally adaptive Bayesian (FLAB) or clustering methods [Foster et al., 2014]. These have been shown to be more accurate and repeatable than the simpler thresholding methods, in particular for small objects [Hatt et al., 2011]. However, there remains uncertainty in segmentation - in particular for small volumes. Recent work has focussed on automatic techniques, not requiring user intervention [Hatt et al., 2017]. AI and Machine Learning (ML) may prove to be be useful for registration and segmentation applications in the future. However, this requires further work, including the production of reliable training datasets. Further discussion of AI in PVC can be found in Section 3.2.2.5.

2.7.5 Registration

The importance of registration between functional and anatomical images depends on the use of the anatomical dataset in PVC and/or segmentation. Depending on the technique, segmentation, however, may require a registered anatomical dataset.

2.7.6 Cross-system quantification

In addition to correcting for intra-system factors, there are also effects which depend on the imaging system which could result in differences in quantification. This means that if the same patient or phantom is scanned on two different SPECT-CT systems, the measurements may be different. Efforts to harmonise systems, and standardise measurements, are important for multi-centre trials [Dickson et al., 2022, Peters et al., 2020]. There is a well established European accreditation programme for ¹⁸F-FDG PET-CT, known as EANM Research Ltd (EARL) [Kaalep et al., 2018]. A similar programme is now underway for ¹⁷⁷Lu SPECT-CT, motivated by the recent rapid growth of MRT using ¹⁷⁷Lu [EARL and EANM, 2022]. Work has also demonstrated the feasibility of standardising SPECT-CT quantification with ^{99m}Tc, provided that acquisition and reconstruction protocols are carefully standardised [B Peters et al., 2019].

2.7.7 Measurement Uncertainty

Given the known sources of error which limit the accuracy, repeatability and precision of quantification in SPECT, it is important to consider measurement uncertainty. Uncertainties allow data to be interpreted and used appropriately.

In phantoms, the accuracy of quantitative SPECT has been estimated at around 5% for activity concentration evaluation [Willowson et al., 2018, Shcherbinin et al., 2008]. The accuracy is likely to be poorer in patients as there are multiple parameters which are not as easy to control as in phantom studies.

For the application of dosimetry, specifically, each process contributing to the dosimetry chain will have an uncertainty associated with it. Each individual uncertainty contribution should be propagated for the calculation of absorbed dose. This includes measurements of count rate, calibration factor, calculation of area under a TAC, delineation of the volume of interest, the choice of scaling factor, and any corrections applied [Gear et al., 2018]. Guidance has been published by EANM to help to standardise the calculation of uncertainties for dosimetry [Gear et al., 2018].

The limited spatial resolution of SPECT images (and the correction for this)

has been identified as one of the most important sources of uncertainty, particularly for small volumes of interest [Gustafsson et al., 2015].

2.7.8 Limited Spatial Resolution

2D Spatial Resolution

In planar imaging with a gamma camera, the spatial resolution measures the level of detail of a radionuclide distribution that the gamma camera can reproduce. This is often measured in terms of the Full-width at half maximum (FWHM) of a line source. The system resolution R_s depends on both the collimator resolution $R_c(d)$ (which depends on the distance from the collimator, d) and the intrinsic resolution R_i by:

$$R_s = \sqrt{(R_c(d)^2 + R_i^2)}$$
 (2.6)

The intrinsic resolution is somewhat limited by scattering in the crystal, but the main limitation is due to the statistical fluctuations in the number of light photons detected by the PMTs and, in turn, the number of electrons that the PMTs produce (i.e. limited by the electronics). The overall system resolution is also affected by the collimator resolution which depends on the collimator design, and the distance from the source, d, by equation 2.7 [Cherry et al., 2012]:

$$R_c(d) = \frac{D(l_{eff} + d)}{l_{eff}} \tag{2.7}$$

where D is the diameter of the collimator holes, and l_{eff} is the effective collimator hole length by equation 2.8 [Cherry et al., 2012]:

$$l_{eff} = l - 2\mu^{-1} \tag{2.8}$$

where μ is the attenuation coefficient of the material the collimator is constructed from (usually lead).

3D Spatial Resolution in SPECT imaging

SPECT imaging is based on multiple 2D images acquired at different angles.

Detector motion may be set up to follow a fixed Radius of Rotation (RoR) meaning that the detectors are at a constant distance from the centre of the FOV. However, more commonly in clinical imaging the detectors move in and out to ensure that they are as close as possible to the patient at each rotation in order to optimise the collimator resolution (i.e. minimising the distance parameter d). In addition to the factors which affect 2D spatial resolution, the angular sampling, and reconstruction settings also influence the reconstructed SPECT resolution. The depth-dependence of the collimator resolution means that, for SPECT imaging, the PSF will depend on the position in the FOV.

The spatial resolution of an imaging system, characterised by the image of a point source, the Point Spread Function (PSF), can be described with the FWHM. The PSF can often be modelled as Gaussian in shape with a typical FWHM on the order of 10-20 mm for SPECT imaging (depending on radionuclide, collimators used, radius of rotation and reconstruction technique) [Ryu et al., 2019]. In comparison, the FWHM associated with PET resolution is approximately 3-5 mm, with less variation in resolution across the FOV as PET imaging does not require collimators and the detectors are in fixed positions. Both SPECT and PET resolution are significantly poorer than the sub-mm resolution which can be achieved with modern CT or MRI systems.

2.7.8.1 The Partial Volume Effect

Consequences of the limited spatial resolution can be referred to as the PVE. The PVE occurs when an object partially fills the sensitive volume of the detection system [Hutton and Osiecki, 1998], where the sensitive volume is the volume defined by the resolution of the detection system from which emitted photons would be detected at a given detector location [Erlandsson et al., 2012b]. When this occurs, activity which originates from the object can be detected outside of the true boundary. In the simple case of a hot object in a non-active background, the result of this 'spillover' is that the apparent activity within the object is reduced, and the size of the object appears larger as demonstrated in Figure 2.2.

Measurements of uptake, for objects of dimensions approaching 2-3 times the

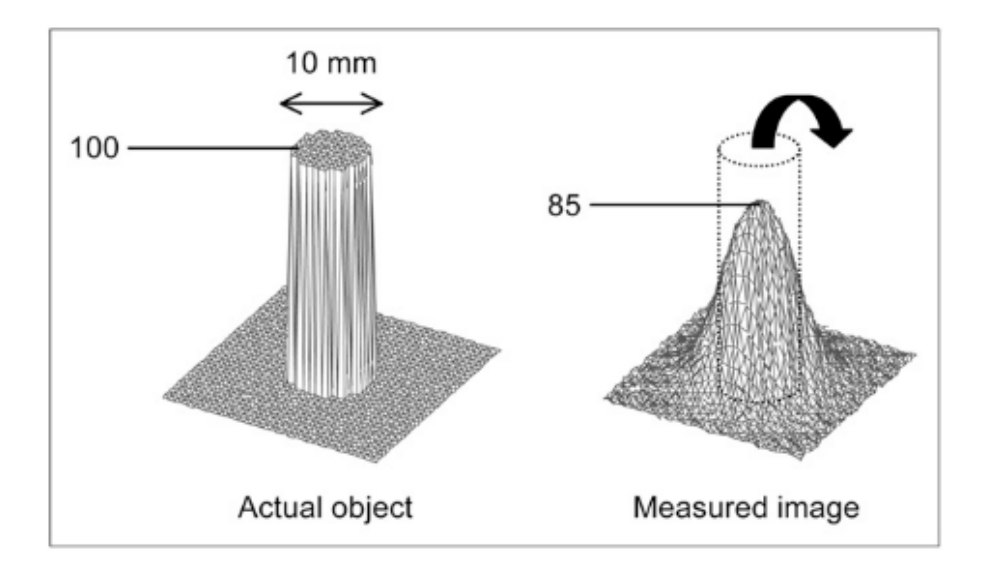


Figure 2.2: Diagram demonstrating the PVE on a circular source with uniform activity in a cold background. Maximum measured activity is reduced, and some counts are detected outside of the true source boundary. This figure was originally published in JNM. M. Soret et al. Partial-Volume Effect in PET Tumor Imaging. J Nucl Med. 2007;6:932-956. ©SNMMI [Soret et al., 2007]

FWHM are affected [Bettinardi et al., 2014], and the extent of the effect is increased for smaller objects. The impact is generally greater for uptake metrics involving the mean rather than the maximum value. This occurs because, for mean uptake values, more voxels included in the measurement are affected by the effect of the limited spatial resolution. Maximum uptake values tend to be less affected because the single highest voxel value may still capture part of the peak signal. This has been discussed in terms of SUV, where "the maximum SUV in the lesion... has been found to be less affected by PVE than mean SUV" [Bettinardi et al., 2014]. The shape of the object is also related to the extent of the effect, with the key parameter being the 'compactness' of the object; objects which are more compact suffering less from the PVE [Finocchiaro et al., 2019].

Simple cases with a zero background, result only in spill-out. However, 'spill-in' to a region will be present if the background is non-zero and this will also affect the apparent uptake [Akerele et al., 2020]. Objects with a high activity compared with the surroundings (i.e. a high Target to Background Ratio (TBR)) demonstrate more apparent activity reduction than objects with a lower contrast since there is relatively less spill-in to compensate for the spill-out [Soret et al., 2007].

Several of these factors can change for the same lesion between sequential images acquired with gaps of days or weeks, and therefore would be important to consider when performing follow-up studies.

There are actually two components to the PVE; "spill-over" (including spill-in and spill-out) due to the blurring of the imaging system, and the "tissue fractionation effect". This second component occurs due to image sampling as, in principle, a single voxel could contain multiple types of tissue [Erlandsson et al., 2012a]. The tissue-fraction effect is the key PV component in CT or MRI images. However, due to the relatively poorer resolution, the spillover aspect of the PVE dominates in NM imaging and is the main focus for correction in SPECT data. The tissue-fraction effect will not be discussed further in this thesis.

2.7.8.2 Partial Volume Correction

The PVE leads to quantitative and qualitative inaccuracies in Nuclear Medicine imaging. Therefore, a correction method is sought to improve the accuracy, which is the focus of this project. Existing correction methods are discussed in depth in Section 3.2.

2.8 Thesis Scope

The main focus of this thesis will be oncology SPECT imaging with ^{99m}Tc. There are several reasons for investigating the PVE in SPECT, rather than PET. A major factor is that the PVE has potential to affect quantitative SPECT data more than PET due to the lower spatial resolution. In addition, as discussed in Section 2.6, there are multiple potential applications of quantitative SPECT, including the rapidly developing area of MRT. As quantitative SPECT is still a developing technique, there is a potential opportunity for novel work to influence clinical practice. Pragmatically, SPECT imaging is globally more accessible than PET due to the lower cost of SPECT imaging equipment and ease of radiopharmaceutical production [Dickson et al., 2022].

There are several reasons to motivate the focus of oncology imaging. There is more published work on PVC for other clinical applications such as neurology

and cardiology. In neurology and cardiology, the size, shape and position of the objects of interest are more predictable, with less variability compared with tumours or metastases which could in theory occur anywhere in the body, having any shape or size (position, shape and size all impact the PVE). This thesis focusses on imaging with ^{99m}Tc in the first instance. Due to the number of variables possible in addressing the PVE, the practical approach for initial investigation was to concentrate on a radionuclide which is straightforward to image. However, to be useful for oncology SPECT, any PVC algorithm should be suitable for use with a range of radionuclides, including those used for MRT, which may be more challenging to image due to higher energy/septal penetration. While not covered in this work, investigation of other radionuclides would be a useful area for further study.

Chapter 3

Partial Volume Correction for Oncology SPECT Imaging

3.1 Aims

As described in Section 2.7.8.1, the Partial Volume Effect (PVE) can result in visual and quantitative inaccuracies in Nuclear Medicine imaging.

This chapter aims to describe types of existing PVE correction methods from the literature. As current literature demonstrates a lack of consensus on the optimal method for Partial Volume Correction (PVC) in oncology, this chapter also aims to develop a set of oncology SPECT-specific criteria to allow critical assessment of existing methods. Finally, this chapter aims to use the criteria to select a subset of existing PVC methods for further description and investigation of suitability for practical application in oncology SPECT imaging with ^{99m}Tc.

3.2 Existing PVC Techniques

Over 20 different PVC strategies which had been applied to PET and SPECT imaging were identified in the literature.

3.2.1 PVC Review Papers

Several review papers giving overviews of the PVE in Nuclear Medicine imaging have been published [Soret et al., 2007, Erlandsson et al., 2012b, Bettinardi et al., 2014, Thomas et al., 2016, Cysouw et al., 2016, 2017, Alavi et al., 2018, Jomaa

et al., 2018]. Clinical applications highlighted in these reviews include neurology and cardiology in addition to oncology. Many methods have been proposed and applied in brain and cardiac imaging [Erlandsson et al., 2012b]. In contrast to brain and cardiac imaging, the lack of consensus regarding the optimal PVC method for oncology is noted in multiple reviews [Soret et al., 2007, Cysouw et al., 2016, 2017, Alavi et al., 2018].

3.2.1.1 PET PVC vs SPECT PVC

All reviews except one [Erlandsson et al., 2012b] discuss PET imaging only, reflecting the relatively more widespread use of quantification in PET compared with SPECT imaging. However, the benefits of PVC in SPECT imaging, specifically in oncology, are potentially significant. Several radionuclides used in planning and delivery of molecular radiotherapy have emissions which can be imaged using a gamma camera, but not a PET system. This enables posttherapy SPECT data to be used for dosimetry calculations [Rahmim and Zaidi, 2008, Bailey and Willowson, 2014, Ljungberg, 2018, Dickson et al., 2019]. In addition, since SPECT imaging has comparatively poorer spatial resolution than PET there is potential for a greater improvement in quantitative accuracy by applying PVC to SPECT images. Due to differences in the imaging systems, some of the assumptions in existing PVC algorithms that may be valid for PET imaging may not be appropriate for PVC of SPECT data. Specifically, the use of collimators in SPECT imaging results in a variation in resolution across the Field of View (FOV). This is investigated in Chapter 4.

3.2.2 Categories of PVC Implementation

Methods to reduce or correct for the Partial Volume Effect may be implemented during reconstruction or post-reconstruction (i.e. to projection data or image data). Methods may or may not need object segmentation information. Corrected data may be in the form of a Regional Mean Value (RMV), or the correction may be applied on a voxel-by-voxel basis. The advantages and disadvantages of each of these approaches will be described in the following sections.

3.2.2.1 Techniques for reducing the PVE by improving resolution

Reduction of the extent of the PVE can be achieved by improving the resolution as part of the reconstruction algorithm. While not strictly a PVC method, since there will be a residual PVE, they could potentially be used in tandem with other methods. However, compensation for resolution in the reconstruction can result in artefacts [Nuyts, 2014].

3.2.2.2 Projection based vs Image based techniques

The main advantage of methods performed based on projection data (i.e. within the reconstruction) is that they do not require input of information regarding the image resolution. In addition, there is less need for case-specific user input of other parameters (with the exception of the choice of reconstruction settings). However, in-reconstruction methods will usually require more iterations to reach convergence and therefore reconstruction can be slower. In addition, at high iterations, Gibbs artefacts can be introduced at high contrast edges which detrimentally affect the appearance and quantitative accuracy of the image [Nuyts, 2014].

In clinical practice, reconstruction is most often performed with proprietary software provided by the imaging system vendor, or a third party. Therefore, implementation of techniques which require adjustments to clinically validated reconstruction algorithms would depend on collaboration with the vendor. Projection-based methods, applied in-reconstruction, could incorporate higher resolution information from anatomical data, but non-concordance between anatomical and functional data could introduce artefacts. Image-based methods are generally faster and simpler to implement, and could be applied to any reconstructed SPECT data set (regardless of imaging system or reconstruction software).

3.2.2.3 Segmentation based vs segmentation free techniques

Several PVC techniques incorporate anatomical information into the correction algorithm. The first step of this is to define a Volume of Interest (VOI). Segmentation of this VOI could be based on the emission image itself, or could be defined using higher resolution images such as CT or MRI. Regions can be

defined manually or using automated or semi-automated methods. If emission data are used, due to the limited resolution and resulting blurred edges, it may be necessary to use a threshold to define the border of a VOI. Different thresholds will result in VOIs of different sizes (or shapes), and there is currently no consensus on a thresholding level [Foster et al., 2014]. If anatomical data are used, the edges of objects are clearer due to the superior resolution, however the structural edges may not necessarily match the metabolically active volume. In addition, it is difficult to guarantee perfect registration between the emission data and CT or MRI data. Mis-registration will be more prominent for small objects or lesions which will be affected most by the PVE [Carnegie-Peake et al., 2022]. Non-automated segmentation methods which require user input are easy to implement and intuitive, however, will increase the inter- and intra-user variability, and may be time consuming if segmentation of multiple regions is required. Clearly, segmentation could be important for determining the optimal PVC method in oncology as the choice of segmentation technique could impact the PVC result [Foster et al., 2014]. This is particularly relevant when considering the practical application of PVC to realistic clinical data, rather than digital or physical phantoms where segmentation is generally more reliable.

As noted in Section 2.7, further study and optimisation of segmentation techniques falls outwith the scope of this thesis, however a brief overview is given in Section 2.7.4.

Segmentation free techniques, on the other hand, do not require the definition of VOIs. This means that they are independent of any other image dataset and don't require any manual input which could introduce variability. However, without any information regarding the boundary of the object of interest, it is very difficult to achieve full correction using segmentation-free methods [Erlandsson et al., 2012a].

3.2.2.4 Region-based vs voxel-based techniques

PVC methods may produce an image of the corrected data, with voxelwise correction, or may output a single RMV only. The best option is likely to depend on the application, but this choice is non-trivial. There is ongoing debate as to whether

voxelwise data is preferred to a mean regional value for dosimetry [Chiesa et al., 2019]. A 2023 survey including multiple types of Molecular Radiotherapy (MRT) found that evaluation over the whole region is the most commonly used image-based metric compared with 3D voxel-based dosimetry for most types of therapy [Peters et al., 2023]. Recently published guidance states that mean absorbed dose at an organ or sub-organ level should be calculated [Stokke et al., 2024]. This guidance also states that, additionally, dose calculations at the voxel level may be given, provided that robust methods for error reduction are in place.

Advantages of a voxelwise correction include the potential for demonstrating inhomogeneity within a region, and the ability to generate Dose Volume Histograms (DVHs). However, the uncertainties associated with single voxel analysis are large compared with regional mean value analysis Tran-Gia et al. [2020]. If it was required, voxel-level registration would be extremely challenging. If corrections were put in place such that voxel-based correction could produce quantitatively accurate images, however, the noise vs resolution trade-off for quantitative images may not be suitable for visual assessment. This could be overcome by producing different reconstructed datasets; for visual assessment and for quantitative analysis.

Current practice does not generally utilise voxel-based corrections, given the challenges mentioned above. However, it was considered important to examine PVC methods which allow voxelwise correction as this could add clinical value in future applications. This could include dosimetry calculations for heterogenous lesions, including potentially creation of dose-volume histograms [Chiesa et al., 2019].

3.2.2.5 Other PVC techniques

A recent development in nuclear medicine involves incorporating new technologies such as Artificial Intelligence (AI) and Machine Learning (ML). Many projects in this area of work have been published in the past 2-3 years and may not have been comprehensively tested. The majority of the literature reviewed for this thesis was published before the "explosion of AI" in nuclear medicine. For this reason, AI/ML PVC techniques have not been investigated in the current thesis. A brief overview

has been included here for completeness.

Several recent reviews include examples of applications of AI/ML in Nuclear Medicine. The most frequently cited applications related to oncology are in segmentation, denoising (or enabling the use of lower administered activity), dosimetry, and improving resolution in the reconstruction [Seifert et al., 2021, Arabi et al., 2021, Cheng et al., 2021, Decuyper et al., 2021, Visvikis et al., 2022, Lopes et al., 2025]. These review papers generally do not explicitly mention correction for the PVE using AI/ML, however the PVE is noted in the context of making segmentation more challenging [Visvikis et al., 2022, Lopes et al., 2025] or in the context of superior resolution reducing the extent of the PVE [Arabi et al., 2021, Cheng et al., 2021].

Some research on for utilising AI/ML for strategies to correct for PVE has been published recently. Examples include PVC for post MRT SPECT imaging [Leube et al., 2024b], and a concurrent PVC and denoising technique [Mohammad-Saber et al., 2024] in PET.

3.2.3 Literature Review Summary

PVC in Nuclear Medicine is an active field of study, with new PVC algorithms being developed on an ongoing basis. Review of the literature including significant bodies of work proposing, assessing and validating different PVC methods has been useful for identifying key features of a range of methods. However, to the author's knowledge there is still no consensus on the optimal practical PVC method for oncology SPECT.

Given the range of characteristics of existing PVC methods, it is not obvious which of these methods would be most suitable, or could be suitable with some adaptation, for application in oncology SPECT imaging. Reviewing the literature made it clear that developing a set of criteria would be necessary to assess existing PVC methods for their suitability in oncology SPECT. A set of novel criteria was developed based on information in previous literature and the author's practical experience in clinical nuclear medicine imaging.

3.3 Developing criteria to assess PVC methods for oncology SPECT

Since an 'ideal' PVC method will be specific to the application, the first stage of this project aimed to define a set of criteria for the 'ideal' PVC method specifically for oncology SPECT. These criteria will facilitate assessment of existing methods, and the production of a shortlist of algorithms meriting further investigation. Comparing existing algorithms to the ideal criteria will also enable the identification of limitations or disadvantages of existing algorithms which could be improved for the application of oncology SPECT by introducing some novel adaptation.

All existing PVC methods have assumptions, advantages and limitations which affect their suitability for application in oncology SPECT. Oncology SPECT has specific challenges which may result in reduced accuracy or reliability in PVC (some of which do not apply in other commonly studied areas such as neurology, cardiology or PET). In addition, it is important to consider whether the application of PVC would be practicable in routine clinical practice.

This section details specific considerations of oncology SPECT images which, if not fulfilled, could limit accurate and reliable application of PVC. Therefore, these constitute the foundation of the criteria for a suitable PVC method for oncology SPECT.

3.3.1 Shape of VOI

The first aspect of oncology imaging which can challenge PVC algorithms is that lesions can be a wide range of shapes and sizes. In addition, since lesion shape and size may change between sequential images, the extent of the PVE may change. This has a potential confounding effect e.g. for monitoring treatment response. If a lesion decreases in size, the extent of the PVE will be greater, so a decrease in uptake may be observed even if the metabolic activity has not changed [Soret et al., 2007].

Criterion 1. The PVC method should not assume a specific shape for the volume of interest

3.3.2 Segmentation and use of other image data

Another challenge is the definition of VOIs by segmentation. Some segmentation techniques utilise higher resolution anatomical imaging modalities such as CT or MRI. However, with these methods there is a possibility of non-concordance between anatomical shape (as seen on CT or MRI) and the region of functional uptake. There are a range of possible reasons for this, including mis-registration, non-functional areas, metabolically active lesions which are not visualised on anatomical imaging, or microscopic spread of the lesion which is undetectable by current imaging technology.

Criterion 2. The PVC method should not depend on segmentation based on anatomical images (CT or MRI)

A possible reason for mis-registration between SPECT and CT data is due to the different effect on motion between the SPECT acquisition and the relatively short CT acquisition. Motion, including unavoidable motion due to breathing, during SPECT acquisition can also result in artefacts such as blurring objects of interest. These reasons, amongst others, mean that segmentation is unlikely to be perfect. Therefore, any PVC technique should be robust to inevitable errors in segmentation due to registration or motion.

Criterion 3. The PVC method should be robust to errors in registration, motion and segmentation

3.3.3 Uniformity

Uptake in lesions or other areas of interest may be non-uniform. Lesions may be functionally heterogenous. Larger lesions, in particular, may demonstrate a necrotic core.

Criterion 4. The PVC method should not assume uniformity in the functional region of interest

Due to spill-in, the apparent uptake within a volume of interest can be affected by uptake in surrounding areas. The surrounding background in oncology imaging is not necessarily uniform or zero (PVC methods applied to brain imaging can assume zero uptake in the cerebrospinal fluid). For oncology, there are several organs including the bladder, bowel and spleen, in which the activity can vary over time. This could could affect the apparent activity of nearby lesions in sequential scanning due to different levels of spill-in.

Criterion 5. The PVC method should not assume a uniform (or zero) background

3.3.4 Resolution

Cancer primaries and metastases may be located in almost any area of the body, and therefore almost any position in the image FOV. For example, imaging of the abdominal region covers a relatively large FOV. This should be factored in for oncology imaging, but may not be as important considering the relatively limited FOV in cardiac or neurology imaging. The reason that this may be important is that the resolution of reconstructed SPECT data can vary across the field of view [Kappadath, 2011], and this could therefore affect the extent of the PVE. The resolution, described by the Point Spread Function (PSF), can also depend on factors such as surrounding activity distribution and reconstruction parameters.

Another factor to consider is the shape of the PSF, in particular for radionuclides with high energy emissions such as those used that may be used in MRT oncology applications. For some radionuclides, significant penetration can be expected through the collimator septa, which can create non-Gaussian PSF shapes.

Criterion 6. The PVC method should not assume a known, or invariant, resolution (PSF)

3.3.5 Artefacts

Controlling noise is an important aspect to factor in to any correction methods. As SPECT images can already suffer from high levels of noise - in particular post-therapy images acquired for dosimetry at late time points where activity will be lower. Therefore, any PVC techniques which are known to increase noise, or

introduce any other artefacts which may affect image interpretation, should be used with caution.

Criterion 7. The PVC method should not amplify noise or introduce other artefacts

3.3.6 Voxelwise evaluation

The debate, discussed in Section 3.2.2.4, regarding whether region based or voxel based values are preferred for dosimetry is ongoing. Therefore, in order to future-proof for use of voxelwise data, it is preferred that the PVC method used in oncology imaging allows for this. Another advantage of producing a voxel-by-voxel correction is that an image can be produced for visual interpretation - potentially including useful clinical information about the distribution of activity within a the volume of interest.

Criterion 8. The PVC method should produce a voxelwise correction (rather than a single regional mean value)

3.3.7 Uncertainty estimation

It has been noted in Section 2.7.7 that evaluation of the uncertainty associated with a measurement is important for appropriate interpretation. This is true for the uncertainty associated with partial volume corrected data.

Criterion 9. The PVE method should enable evaluation of uncertainty on corrected value(s)

3.3.8 Practical Considerations

As discussed previously, segmentation can be challenging. This is true, to an extent, in all Nuclear Medicine imaging. However, neurology and cardiology imaging focus on organs which are largely predictable and reproducible in shape. This allows the use of PVC methods utilising templates for ease of segmentation - potentially of the entire image. This is not a solution which is possible for oncology imaging (except perhaps for dosimetry of Organs at Risk (OARs)). Manual segmentation of the entire image is time consuming, subject to inter-

operator variability and may be error prone. In oncology, lesions and metastases can occur anywhere in the body and the extent of the imaging FOV is likely to be greater than in neurology or cardiac applications.

Criterion 10. The PVC method should not depend on segmentation of the entire image

For practical adoption into clinical use, the PVC method would need to be straightforward for the end user. Complex methods involving multiple stages of user input would have more opportunity to introduce errors or variations. A simple, quick, solution for PVC would be preferable.

Criterion 11. The PVC method should be simple and practical to implement (without requiring time-consuming user input)

3.3.9 Summary of Proposed Criteria

A summary of the novel set of criteria developed as part of this research is included here for ease of reference and to enable a comparison between detail in the sections above and Figure 3.4.

To be suitable for use in oncology SPECT imaging, the PVC method should:

- 1. Not assume a specific shape for the volume of interest
- 2. Not depend on segmentation based on anatomical images (CT or MRI)
- 3. Be robust to errors in registration, motion and segmentation
- 4. Not assume uniformity in the functional region of interest
- 5. Not assume a uniform (or zero) background
- 6. Not assume a assume known, or invariant, resolution (PSF)
- 7. Not amplify noise or introduce other artefacts
- 8. Produce a voxelwise correction
- 9. Enable evaluation of uncertainty on corrected value(s)

- 10. Not depend on segmentation of the entire image
- 11. Should be simple and practical to implement

3.4 Using Oncology SPECT Criteria to assess existing PVC methods

As discussed in Section 3.2.2, there are benefits and drawbacks for different categories of PVC methods. There is no clear optimal combination of categories for application in oncology SPECT. Utilising the developed criteria aids assessment of which existing methods could potentially be most suitable. This section includes description and discussion of the advantages, disadvantages and limitations of existing methods which may be promising candidates for application in oncology SPECT.

3.4.1 In-reconstruction Techniques to Improve Resolution

This category of methods which can be incorporated into the image reconstruction algorithm, with the aim to reduce the impact of the PVE by improving the resolution.

3.4.1.1 Resolution Modelling

Resolution Modelling (RM), also known as collimator-detector response modelling in SPECT or PSF modelling in PET refers to incorporating a model of effects which degrade resolution into the reconstruction process by improving the accuracy of the system model [Tsui et al., 1994]. This has the effect of improving the resolution [Rahmim et al., 2013], however the resolution will remain spatially variant [IAEA, 2014]. An improved system model could instead be used to suppress noise, depending on the number of reconstruction iterations used [Nuyts, 2014]. RM is implemented in many commercial clinical systems [Erlandsson et al., 2012b]. The key disadvantage to RM is that edge artefacts (often known as Gibbs ringing artefacts) may be observed. This is because complete recovery is not possible due to the loss of high spatial frequency information at acquisition. The severity of the artefacts can be reduced by using a lower iteration number, and/or aim for

partial correction by using an underestimated PSF [Nuyts, 2014]. It has been noted that when RM is applied, there is not complete correction for the PVE. Therefore, further correction is required which may be made more challenging due to uncertainties in reconstructed resolution [Hutton et al., 2006]. The magnitude of these uncertainties may be increased if artefacts have been introduced to the reconstructed image. Reconstructing with RM can also reduce convergence speed and change the noise structure of the reconstructed image [Rahmim et al., 2013].

Despite the uncertainties caused by RM artefacts, it may still be valuable to consider RM as part of the solution for PVC due to the commercial availability and ease of immediate implementation in clinical practice. In particular, the advantage of improving uniformity of resolution across the FOV may be advantageous. This is explored further in Chapter 4.

3.4.1.2 Reconstruction with prior information

Another possible in-reconstruction solution is to utilise prior information to improve resolution. This prior information can be based on anatomical images, assuming that areas of functional uptake are correlated on CT or MRI images. These solutions generally penalise the reconstruction to encourage solutions to be smooth within regions, while allowing high contrast to remain at boundaries between regions, thus maintaining sharp edges while controlling noise. Prior information can either be used for re-parameterisation (e.g. using kernels) or regularisation (by the Bayesian Maximum A Posteriori (MAP) or penalised likelihood framework) [Bland et al., 2019]. Segmentation of anatomical imaging is not always necessary; kernels may be used which group regions together based on similarity in MRI signal [Bowsher et al., 2004]. Another kernel-based strategy involves the use of a hybrid kernel which incorporates both high-resolution data and emission data (known as hybrid kernel expectation maximisation, HKEM [Deidda et al., 2019, Marquis et al., 2021]). Use of prior information in addition to RM has been shown to improve quantification in tumour imaging [Alessio et al., 2005].

It was noted that many of these techniques have been applied to brain imaging [Soret et al., 2007, Erlandsson et al., 2012b], which generally has better

concordance between emission and anatomical imaging, and registration is usually more straightforward. The main drawback of these methods is the sensitivity to mis-registration and the potential to suppress detail, e.g. small tumours, which are visible on the emission image but not on the anatomical image.

3.4.2 Regional Mean Value Correction Methods

One of the first PVC techniques proposed, the Recovery Coefficient (RC) method [Hoffman et al., 1979], is a simple post-reconstruction, region-based method which returns a mean value for a single region. For correction of multiple regions, the Geometric Transfer Matrix (GTM) method [Rousset et al., 1998] is well-established for PVC in brain imaging. Other methods which apply a correction to an entire region include the Local Projection (LP) method [Moore et al., 2012] and the Local Background (LB) method [Hofheinz et al., 2012].

3.4.2.1 Recovery Coefficient

The RC method is conceptually the simplest implementation of PVC. Its simplicity contributes to the prevalence of RC implementation in oncology [Soret et al., 2007]. However, there are many underlying assumptions to this method - many of which could be invalid. The RC method usually assumes spherical regions with uniform uptake and also assumes that the true region size is known. There are also implicit assumptions that the resolution is the same as for the conditions under which the RC value was measured, and that the true lesion Target to Background Ratio (TBR) is the same as was used for phantom acquisition.

The RC method applies a size-specific multiplicative factor based on the ratio of measured activity concentration, C', to true activity concentration, C. At its most basic, for hot lesions in a cold background, it can be calculated as per equation 3.1 [Hoffman et al., 1979]:

$$RC = \frac{C'}{C} \tag{3.1}$$

However, equation 3.1 is strictly only valid for objects in a cold background, as it only models spill-out, not spill-in. An alternative to the basic RC equation is

the Contrast Recovery Coefficient (CRC) [Gnesin et al., 2016], which is sometimes known as the Hot Contrast Recovery Coefficient, Q_H , as it accounts for a non-zero background:

$$Q_{H} = \frac{\frac{a_{c,sph}}{a_{c,bkg}} - 1}{\frac{A_{c,sph}}{A_{c,bkg}} - 1}$$
(3.2)

where $a_{c,sph}$ and $a_{c,bkg}$ are the measured activity concentration within the sphere and background, respectively. $A_{c,sph}$ and $A_{c,bkg}$ are the true activity concentration within sphere and background, respectively.

Unless it is explicitly stated, it is not always clear whether the application of RC accounts for background or spill-in. Regardless of specific equation used, the Recovery Correction factor is usually derived from measurements made on International Electrotechnical Commission (IEC) National Electrical Manufacturers Association (NEMA) phantom images with spheres filled with a known activity. RC measurement data can be fitted to a function, allowing RC values to be calculated for objects with any volume (i.e. not just those included in a standard NEMA phantom). Another point of variation in implementation of the RC method is the choice of function for this fitting, but the most frequently uses is an empirical two-parameter logistic function [Gear et al., 2018]:

$$f_{RC}(v) = \left(1 + \left(\frac{a}{v}\right)^b\right)^{-1} \tag{3.3}$$

where v is the sphere volume in ml, and a and b are fitting parameters. However, this fit may not be valid for objects of a greater volume than those in a standard NEMA phantom. A review of the use of RC in post-therapy SPECT imaging (using 123 I and 177 Lu), based on NEMA phantom measurements concluded that RC was insufficient for correcting SPECT images unless larger spheres were included in the RC curve model [Gear et al., 2019].

In addition to the volume of the object of interest, the RC factor depends on the specific system and radionuclide used, as well as the TBR, acquisition settings and reconstruction parameters. However, measurement of the true region size or true

TBR in order to identify the appropriate factor is challenging since both values are affected by the PVE.

Conventional, phantom-based RC methods are limited in that they are valid for spherical lesions only, despite the original publication which proposed the method considering a range of shapes [Hoffman et al., 1979]. Non-spherical lesions have been considered for ¹³¹I SPECT data [Dewaraja et al., 2001], where a greater PVE was noted for non-spherical structures (up to a 40% difference), for ^{99m}Tc and ¹⁷⁷Lu SPECT using 3D printed inserts representing organs of different shapes [Robinson et al., 2016] and for ¹⁷⁷Lu SPECT data [Finocchiaro et al., 2019] where RC curve models were found to depend on the region shape. A recent MIRD publication also notes the limitation of the assumption of sphericity and has worked towards developing an RC-based method which accounts for object shape in terms of the volume-to-surface area (V/SA) ratio, and the object to background ratio [Marquis et al., 2025]. Additional drawbacks of phantom-based RC methods include experimental error in phantom filling and set up. It has been shown through experiment and simulation that the configuration of spheres within the phantom can impact the recovery curve [Armstrong, 2019, Leube et al., 2024a]. Nonphantom based RCs could be derived which account for non-spherical geometries by convolution of the object with the system PSF [Erlandsson et al., 2012b], however this then requires an estimation of the PSF.

Despite the clear limitations, this is the method of choice in practice, and is simple to implement. Therefore, it would be useful to include this method in testing as a comparator for assessing the performance of alternative methods.

3.4.2.2 Geometric Transfer Matrix

The use of the GTM method requires segmentation of the entire image, usually based on a CT or MRI dataset. Each segment is then, in turn, convolved with a known PSF to generate a matrix of 'cross-talk' factors between the different segmented regions. This produces corrected mean values for each region; assuming a constant PSF and that every region has a uniform activity concentration.

Variants of the GTM method such as perturbation-based GTM (p-GTM,

[Du et al., 2005]) and symmetric GTM (s-GTM, [Sattarivand et al., 2012]) have also been proposed. However, the requirement to segment the entire image is a significant limitation in oncology.

3.4.2.3 Local Projection

PVC methods have been proposed which operate in the projection domain, based on segmentation performed in the image domain. Early work required the segmentation of the entire image [Huesman, 1984], but another proposed correction method avoids this issue [Moore et al., 2012]. The method, known as LP, works by segmenting J compartments (where J is typically a small number depending on the local background) in a local region around the lesion or object of interest. The aim is to calculate the corrected activity concentration for each region, C_j . It is recommended that the segmentation is performed based on a registered high resolution anatomical image, followed by down sampling the data to match the SPECT resolution.

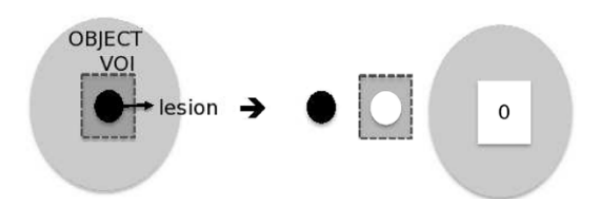


Figure 3.1: Diagram demonstrating segmentation of compartments used for the LP method where there are J=2 compartments in the local region of interest (lesion and local background), and the remainder is used to calculate a global background term. Reproduced with permission from Southekal et al. [2012] (licence ID 1588756-1).

Example compartments are shown in Figure 3.1. Taking one compartment, j, at a time, the voxels within the compartment are assigned a uniform value = 1. This binary region is then forward projected using the system model to produce ideal projections of each compartment ($p_{j=1}$ and $p_{j=2}$ for Figure 3.1). Separately, the local region defined around the lesion of interest is set to = 0 and that mask is applied to reconstructed SPECT data to leave the 'global background' (note that this is dependent on the reconstruction parameters used, including iteration number, k). This is then forward projected to get the projection of the global background $g_{out}^{(k)}$.

Measured projections, λ , can be described for each projection ray, i as:

$$\lambda_{i} = \sum_{j=1}^{J} C_{j} p_{ij} + g_{out,i}^{(k)}$$
(3.4)

Where C_j is the unknown activity concentration of compartment j. Since this technique utilises projection data, Poisson statistics can be used to model the probability of obtaining n_i counts in detector pixel, i, given the expected projections λ_i , as above. Maximising the log likelihood by taking the derivatives with respect to each of the C_j values, generates a set of J equations which can be simultaneously solved to get PV corrected mean activity estimates for the activity concentration in each compartment, C_j^{corr} .

The paper originally proposing this method uses simulated multiple pinhole micro SPECT lesion data using ^{99m}Tc [Moore et al., 2012]. The method was subsequently applied to a full clinical system, again by simulation, as part of an investigation to optimise lesion detection and quantification [McQuaid et al., 2011]. LP has been evaluated in comparison to the perturbation based GTM (pGTM) method [Du et al., 2005], where the key advantage of the LP method is that segmentation is not required for the entire image. LP was found to have improved or equal accuracy and precision compared with GTM [Southekal et al., 2012].

This method claims to compensate for "tissue partial volume and spillover" effects [Moore et al., 2012], but there is no correction for the tissue fraction effect, other than at lesion edges. This is due to the segmentation based on a higher resolution image. Artefacts may be introduced at high iterations or at areas of high contrast due to the requirement to model resolution within the system model (see Section 3.4.1). The studies referenced above were all performed on simulations of uniform spheres. The method assumes uniformity, but could theoretically be applied to non-spherical regions. An attempt to model non-uniform uptake (i.e. radially varying to reflect central necrosis) found that precision was worse, but accuracy was improved with a non-uniform model compared with the assumption that the uptake was uniform [Southekal et al., 2011]. Further development of the

LP method has been attempted by incorporating the correction into an iterative reconstruction process [Cal-González et al., 2015, 2018a], for the application of quantitative PET imaging of coronary plaques rather than oncology SPECT. It is not clear if there is a significant advantage gained by incorporation into the reconstruction for PET coronary plaque imaging [Dekemp et al., 2018], except potentially the application of motion correction which could be a significant issue in cardiac studies [Cal-González et al., 2018b].

The main limitations of the LP method are; the assumption of uniformity within each compartment and the requirement for high-resolution data which are perfectly correlated and registered with the emission data. Nevertheless, the method is relatively simple and would be fast to implement since segmentation throughout the whole image is not required. It has been demonstrated to be reasonably robust to 'moderate' inaccuracies in segmentation and registration [Southekal et al., 2012], and does not assume a specific PSF.

3.4.2.4 Local Background Correction

A method designed to correct for spill-out from hot lesions in a colder background using a defined background region was proposed [Hickeson et al., 2002] and extended for application in 3D [Bundschuh et al., 2010]. These methods are limited in that the background region surrounding the lesion is assumed to be uniform, which is not always the case. A LB method (also referred to as the 'model free' method) was developed, which was based on the defined background concept but which does not assume homogeneity throughout the entire background region [Hofheinz et al., 2012]. This method aims to calculate the corrected activity concentration averaged over the region of interest, C_{ROI}^{corr} .

The LB method operates in 3D and requires segmentation of the 'true' object boundary. Segmentation gives the volume of the 'true region', V_{ROI} and the uncorrected activity concentration, C_{ROI}^{uncorr} . Segmentation could be based on CT or MRI data or, as in the paper proposing the method, based on the emission image [Hofheinz et al., 2012]. As shown in Figure 3.2, an inner shell (known as the spill-out region, sp) is then defined around the true object boundary with width equal to

the Full-width at half maximum (FWHM). The authors state that by the edge of the spill-out region (i.e. 1 FWHM from the edge of the true region), the signal has dropped to background level to within about 0.5%. External to the spill-out region is an outer shell (known as the background region) which is defined as a width of 2.5 FWHM around the inner shell.

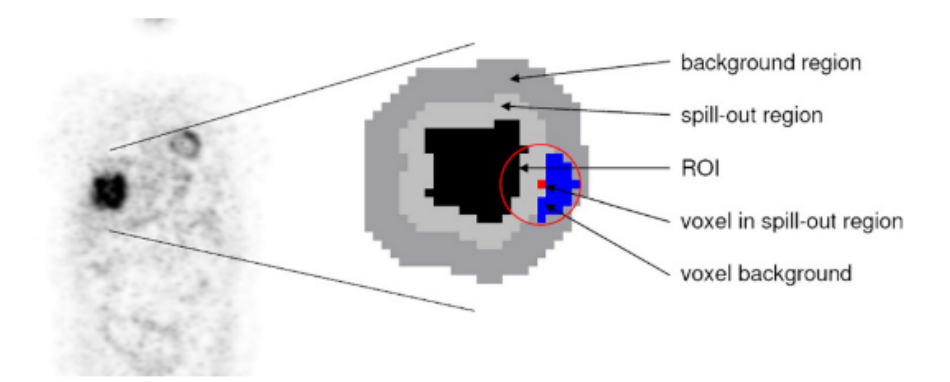


Figure 3.2: Diagram illustrating the relevant regions used for the LB method in 2D. Black = 'true' object, light grey = spill-out region, dark grey = background region. The blue voxels are used to compensate for the effect that background activity has on the red voxel [Hofheinz et al., 2012].

This method was tested on anthropomorphic digital phantoms, based on real lesions, and was found to perform better than methods which assumed a homogeneous background for the whole lesion [Hofheinz et al., 2012]. Results from using this method were also found to be comparable to Resolution Modelling and iterative Deconvolution [Hoetjes et al., 2010]. It has been implemented in several oncology studies, including for ¹⁸F-FDG PET lung lesion imaging [Salavati et al., 2015], ⁹⁰Y microsphere PET imaging [Van Den Hoven et al., 2016], and ¹⁸F-FDG PET liver lesion imaging [Samim et al., 2017].

The most significant limitation of this method is that it does not appear to be able to correct for spill-in if there is a contribution from a region external to the ROI which is of higher activity. Also, it depends on knowledge of the resolution, but it is stated that this is a relatively weak dependence (compared with e.g. iterative deconvolution), with precision only required to the size of a voxel. As with other methods which rely on segmentation, the results of PVC depend on the reliability of the segmentation method which in turn can depend on the contrast and noise levels

[Hofheinz et al., 2012].

3.4.3 Voxelwise methods, where segmentation is required

The methods described in Section 3.4.2 produce a single value; the mean for the region of interest. However, methods have been developed to correct regions on a voxel-by-voxel basis.

3.4.3.1 Videen/Meltzer Method

This technique was first proposed for 2D regions in brain imaging in 1988 [Videen et al., 1988] before it was extended to 3D volumes [Meltzer et al., 1990]. It was later simplified based on an assumption that the activity concentration fluctuates by only a small amount about a mean value [Meltzer et al., 1999].

The Videen/Meltzer method involves segmenting the region of interest and generating a binary image from this (i.e. region voxels = 1, other voxels = 0). Convolving this binary image with the PSF produces a correction image, consisting of what are effectively voxelwise Recovery Coefficients. In this simple case, the background is assumed to be zero which is unlikely to be true in oncology. Despite correcting on a voxel by voxel basis, the method depends on the assumption that any non-uniformity is small compared with the mean value so may not be appropriate for heterogeneous objects. Nevertheless, the strategy of generating a voxelwise correction map forms the basis for other corrections, such as the Müller-Gärtner Method (MGM) which incorporates spill-over from multiple regions and has been implemented successfully in brain imaging [Müller-Gärtner et al., 1992], and the Multi-Target Correction (MTC) method which repeats the MGM for multiple compartments to build up a corrected image [Erlandsson et al., 2006]. However, both the MGM and the MTC require segmentation of the entire image which is impractical in oncology imaging.

Other voxelwise corrections include the Yang method which also generates a pixel-by-pixel correction map based on the ratio between the real image and a simulated 'pure' image with negligible FWHM, and also requires segmentation of the whole image, knowledge of the PSF and knowledge of the relative regional

mean activity values [Yang et al., 1996]. Developments of this method to avoid the requirement of relative regional mean information include Region-Based Voxelwise (RBV) which is a combination of GTM, to get relative regional mean values, and Yang so that voxelwise correction is still achieved [Thomas et al., 2011]. Another variant, known as iterative Yang (iY) works by iteratively improving the image estimate, starting with regional mean values in the original uncorrected image and usually requires only a few (3-5) iterations [Erlandsson et al., 2012b].

Despite successful application in brain imaging, due to the requirement of segmenting the entire image, none of the above methods are appropriate for oncology, but their description demonstrates the development of the voxelwise correction technique.

3.4.3.2 Single Target Correction

The Single Target Correction (STC) method, first proposed by Erlandsson and Hutton in 2014 [Erlandsson and Hutton, 2014], also known as 'Single Region Voxelwise' correction, corrects for both spill-in and spill-out to both the background and the region of interest.

Application of STC involves segmenting a single region of interest (aka the target). Corrections for spill-in and spill-out are applied to both the region and the surrounding background. Requirements for this method include knowledge of the PSF and segmentation of the volume of interest. The process is demonstrated as flow diagram in Figure 3.3.

The STC algorithm is outlined in the following stages:

- 1. Start with uncorrected data
- 2. Segment the 'target' of interest
- 3. Apply a voxelwise spill-in correction to the target by subtraction of a voxelwise term, derived in a similar way to the Videen/MGM (no assumption of uniformity)
- 4. Apply a spill-out correction to the target by dividing by a recovery coefficient term (assumes that the target is uniform)

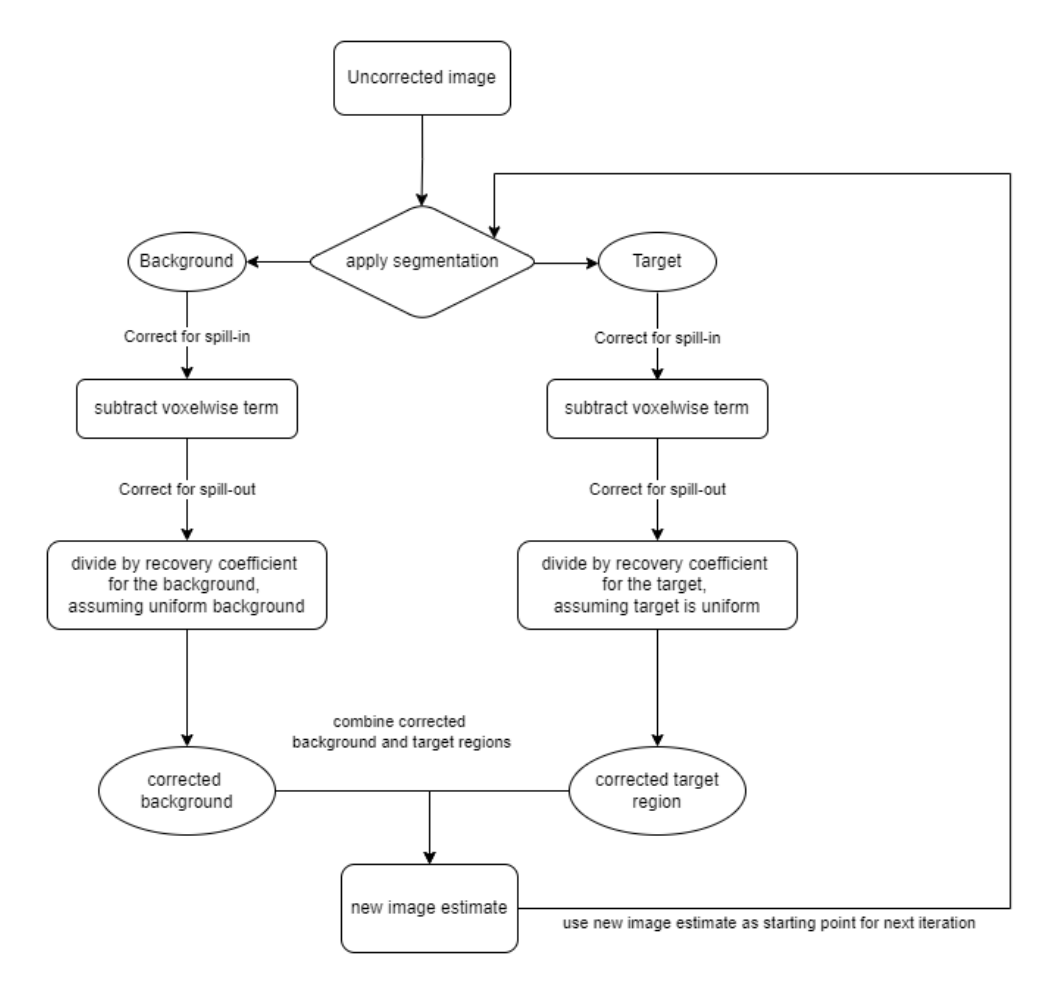


Figure 3.3: Flow chart demonstrating the steps involved in the iterative Single Target Correction (STC) partial volume correction method.

- 5. Correcting the background for spill-in (subtracting a voxelwise term, as above)
- 6. Correcting the background for spill-out (dividing by a recovery coefficient term for the background, assuming uniform background)
- 7. Combine the corrected target and the corrected background region to produce a new image estimate
- 8. Repeat from step 2 with new image estimate

This method has been applied to non-oncology applications. It has been used for PVC when evaluating the myocardium to blood ratio where the STC technique was compared to an iterative deconvolution method, and the iterative Yang method

(iY) method in terms of accuracy and precision [Erlandsson and Hutton, 2014]. Results showed that the STC method demonstrated better accuracy and precision than the iterative deconvolution method, and 'not quite as good' accuracy, but improved precision, compared with iY [Erlandsson and Hutton, 2014]. Another paper has used STC to derive an image-based arterial input function for dynamic PET imaging [Sari et al., 2017].

An advantage of the STC method in the oncology setting is that segmentation is required only for a single region, as opposed to requiring segmentation of the entire image as per other segmentation-based voxelwise PVC methods. In addition, the STC method returns voxelwise corrected images, as opposed to simply regional mean value data. This is achieved despite assuming uniformity within the region for performing spill-out correction, as no assumptions regarding the uniformity are required for performing spill-in correction. It provides the benefits of voxelwise correction, such as demonstrating heterogeneity. Corrected images, e.g. with improved edge definition, may be useful in visual lesion detection, provided that segmentation is performed accurately.

A key limitation of this method is that an accurate estimate of the PSF is required. It has been shown that the result depended on the PSF value used [Sari et al., 2017]. STC appears to be relatively straightforward to implement, and may be a viable option for a voxelwise correction method to investigate further. However, it is currently untested in an oncology setting.

3.4.4 Voxelwise, Segmentation-Free Methods

A key limitation of the above methods is the requirement to define the region of interest (and sometimes other regions), this means that the effectiveness of these methods can depend on the type of segmentation technique used. However, there have been segmentation-free methods proposed which avoid this issue. Segmentation-free methods generally aim to improve the spatial resolution of images, thus reducing the impact of the PVE, rather than aiming to return a corrected regional mean value.

3.4.4.1 Iterative Deconvolution

The general form of iterative Deconvolution (itD) algorithms involves iteratively updating an image estimate based on a difference image. The difference image is derived from comparing the actual acquired image, *I*, to the image estimate convolved with a known PSF.

Evaluating the difference image and performing the update can be done in different ways. Two of the main implementations of itD are the Richardson-Lucy (RL) algorithm [Richardson, 1972, Lucy, 1974] and the Van Cittert (VC) algorithm [Biemond et al., 1990, Carasso, 1999]. The Richardson-Lucy method assumes a Poisson noise model and operates on the basis of maximum likelihood, so updates are calculated by dividing the estimate by the acquired image to get the difference image (equation 3.5):

$$I_{corr}^{n+1} = I_{corr}^{n} \times \alpha \left[\frac{I}{(I_{corr}^{n} * PSF)} \right]$$
 (3.5)

The VC method assumes a Gaussian noise model and operates by Least-Squares, so updates are calculated by subtracting the estimate from the acquired image to get the difference image (equation 3.6):

$$I_{corr}^{n+1} = I_{corr}^{n} + \alpha [I - (I_{corr}^{n} * PSF)]$$

$$(3.6)$$

In equations 3.5 and 3.6, α is a weighting factor which is typically close to 1 [Erlandsson et al., 2012b].

The key benefit of itD techniques is that segmentation is not required. Therefore the results are not subject to errors or uncertainty introduced during registration or segmentation. However, noise is amplified at increasing iteration numbers. Therefore, full recovery is usually not achieved since, in practice, the iterative process is usually stopped early to manage noise levels. Regularisation solutions have been proposed with the aim of reducing the noise amplification. These include total variation [Tohka and Reilhac, 2008], wavelet-based denoising [Boussion et al., 2009], and HYPR denoising which has been used with itD

in dynamic data [Golla et al., 2017, Cysouw et al., 2019]. Another drawback of the itD techniques is that the resolution is usually assumed to be known and invariant. Performing deconvolution with a spatially variant resolution may be computationally expensive, but a method has been proposed to speed up processing using Principal Component Analysis (PCA), assuming that the variation in resolution across the FOV is known [Irace et al., 2016]. An alternative solution is correcting based on the PSF at a specific position in the FOV. This has been tested for Positron Emission Tomography (PET) [Barbee et al., 2010]. The requirement of known PSF remains.

A small number of NM studies have used an implementation of itD which operates without full knowledge of the PSF. Semi-blind deconvolution only needs the form of the PSF specified (e.g. Gaussian) and therefore can be used if the width is not known [Li et al., 2017a]. Blind deconvolution can be implemented without information on either the shape or the parameters of the PSF [Mignotte and Meunier, 2000, Wu et al., 2017]. However, with each of these techniques there are other fitting parameters which need to be selected (e.g. which control the smoothness of the image and PSF [Li et al., 2017a]). One implementation of blind deconvolution, applied in cardiac SPECT/CT requires a registered high resolution anatomical image which, as discussed previously, may not be exactly concordant with the emission data [Wu et al., 2017]. It is also possible to combine application of itD to a single region, with a region-based method. Simulation work investigating this demonstrated promising results [Thomas et al., 2016].

Given the advantages of segmentation-free application, it may be advantageous to study iterative deconvolution further for application in oncology. The RL method has been shown to demonstrate lower bias, compared with the VC method [Tohka and Reilhac, 2006, Thomas et al., 2016], and therefore will be the implementation of itD used for futher work in this thesis.

3.4.5 Method Evaluation against Oncology SPECT Criteria

Twenty of the methods identified in the literature were scored based on the criteria listed in Section 3.3.9 to assess suitability for application in oncology SPECT.

Methods were assigned scores from 0-5 for each criteria point. Meeting desirable criteria perfectly would give a score of 5, and the presence of undesirable properties would score 0. The theoretical 'ideal' method would score 5/5 for every item in the criteria list. An average score across all 11 criteria was calculated for each PVC method. Figure 3.4 summarises the scores for the PVC methods for each criteria. The rationale for each method, per criteria, is included in Appendix A.

				Undesirable qualities (Y=0, N=5)												
				Desirable qualities (N=0, Y=5)												
				Assumption of VOI shape?	Requires use of higher resolution data (e.g. CT or MRI)?	Robust to small changes/errors in segmentation or registration?	Assumes uniformity in region(s)?	Assumes zero background?	Assumes known and invariant PSF?	Amplifies Noise or Introduces Artefacts?	Produces voxelwise correction?	Evaluate uncertainty on final value(s)?	Easy/simple implementation?	Segmentation of entire image required?	Total/55	Mean/5
Post recon methods	Partition-based		RC	0	5	3	0	1	1	5	0	1	4	5	25	2.27
		VOI mean	GTM	5	2	2	0	5	1	5	0	0	1	0	21	1.91
			sGTM	5	2	3	0	5	1	5	0	0	1	0	22	2.00
			pGTM	5	2	2	0	5	1	5	0	0	1	0	21	1.91
			LP	5	4	3	1	5	5	4	0	3	4	4	38	3.45
			LB	5	4	3	2	5	1	3	0	0	4	4	31	2.82
			VID	5	5	3	2	0	0	5	4	0	4	4	32	2.91
			MGM	5	2	3	2	3	0	5	4	0	4	3	31	2.82
			STC	5	5	3	4	5	0	5	5	0	4	5	41	3.73
			Yang	5	2	3	2	4	1	5	5	0	2	0	29	2.64
			RBV	5	2	3	3	5	1	5	5	0	3	0	32	2.91
			iY	5	5	3	3	5	1	5	5	0	4	0	36	3.27
	Enhancement	Voxelwise	itD	5	5	5	5	5	0	1	5	0	5	5	41	3.73
			itD + reg	5	5	4	4	5	0	3	5	0	4	3	38	3.45
			(semi-)blind itD	5	2	5	5	5	3	1	5	0	3	5	39	3.55
L .			multiresolution	5	5	2	5	5	0	1	5	0	4	5	37	3.36
Pod	ᇤ		RM	5	5	5	5	5	5	1	5	0	4	5	45	4.09
In-recon methods	Image		recon + reg priors	5	0	2	4	5	5	3	5	0	1	3	33	3.00
			recon + kernel priors	5	0	3	4	5	5	3	5	0	2	3	35	3.18
≐			HKEM	5	1	3	4	5	4	2	5	0	4	5	38	3.45

Figure 3.4: PVC method and criteria summary matrix, demonstrating suitable (green) and unsuitable (red) aspects of each method. Scoring has been defined as: 0 = Doesn't meet criteria at all, 1 = Meets criteria in very limited cases, 2 = Partially meets criteria, 3 = Meets criteria in most cases, 4 = Meets criteria in almost all cases, 5 = Entirely meets criteria. The full table can be found in Appendix A and acronyms are defined at the beginning of this document.

Figure 3.4 demonstrates that none of the existing methods in the literature meet all of the criteria for the ideal PVC method for oncology SPECT. The framework,

however, assists in the identification of a shortlist of viable options which may work well in oncology SPECT following some adaptation to mitigate against existing limitations.

3.4.5.1 Shortlisted methods for further study and development

From the methods identified in the literature and scored against the criteria, a shortlist of three methods for further study and development was produced. The shortlisted methods were selected on the basis of the highest mean score. The three methods with the highest scores were:

- Resolution Modelling mean score 4.09/5 (in-reconstruction, returns voxelwise correction, currently commonly implemented in routine clinical reconstruction)
- Iterative Deconvolution mean score 3.73/5 (post-reconstruction, returns voxelwise correction)
- Single Target Correction mean score 3.73/5 (post-reconstruction, region-based, returns voxelwise correction)

This shortlist of three methods includes methods which encompass different categories (as identified in italics in the list above). This enables comparison between different categories of method. Another comparison will be with the RC method, as is the most widely used method in clinical practice (despite the relatively low score based on the criteria).

3.4.5.2 Possible Areas for Method Development

The criteria matrix allowed identification of aspects of the shortlisted methods which scored lowest, acting as a guide for aspects that could be improved by novel adaptation.

The RM method is known to enhance the resolution rather than fully correcting for the PVE and therefore could be used in combination with other methods. Another key disadvantage is the potential introduction of Gibbs artefacts. The use of the RM method going forward in this thesis will be contingent on these artefacts not affecting quantitative accuracy.

An assumption of a known, and positionally invariant, PSF is a key limitation of both the STC, and itD methods. A case-specific PSF could potentially be estimated using a technique known as perturbation [Stamos et al., 1988, Du et al., 2005]. In the case of iterative deconvolution, it may prove to be more practical to focus on a local area rather than trying to correct for the whole image since accounting for spatially variant PSF is challenging.

Finally, the criteria matrix demonstrates that most methods are lacking in the evaluation of uncertainty in the PVC corrected value. It will be important to understand how the uncertainty from each method could be estimated.

3.4.5.3 Scope of Testing

The theoretical 'ideal' PVC method would recover the exact ground truth; i.e. produce a voxelwise correction which is completely accurate and precise, with no assumptions required. The 'ideal' method would also be entirely robust to misregistration and segmentation errors, and would be applicable to all situations (i.e. all applications from diagnosis to dosimetry, all imaging systems and settings, all disease sub-types, all anatomical positions). However, this is practicably unrealistic and some compromises must be made.

The intended scope of this project is to evaluate the shortlisted methods which could theoretically be used in a wide range of scenarios. In addition, the project aims to develop an understanding of the limitations of each method. While work in this thesis is limited to ^{99m}Tc SPECT imaging, findings will be helpful in directing further study towards a solution which can be demonstrated to be successful for a range of radionuclides used in oncology SPECT.

3.4.5.4 Test Datasets

Following initial implementation, the shortlisted methods will be assessed using simple digital phantoms to verify that the algorithm performs as expected. Further testing will explore the the effect of different parameters (if relevant), and any novel adaptations intended to improve the PVC performance. The methods will also be

applied to more complex digital phantoms, with complexity levels approaching realistic patient data. Examples of ^{99m}Tc SPECT clinical data which would be useful for the basis of realistic test datasets include bone scans and Tektrotyd scans (both routine clinical studies, with examples of potential applications given in Section 2.6, and described further in Sections 3.4.5.5 and 3.4.5.6).

A combination of test datasets will be required to ensure that PVC methods are challenged with test conditions which encompass a range of possible clinical scenarios. The test data must include a range of region shapes and sizes in a range of positions in the FOV. The lesions and surrounding areas should include different levels of heterogeneity, with a range of TBRs. The most realistic dataset would be patient studies, which may include examples of a range of tumour conditions and images with motion artefacts which are imperfectly registered. However, a key limitation of patient data is the lack of ground truth. Physical phantom studies avoid this issue since the ground truth is known (to 5-10% accuracy, limited by the radionuclide calibrator). However, there are also inherent issues in physical phantom studies which are crucial for the assessment of the PVE, namely that objects in typical geometric phantoms have 'cold'/non-active walls [Hofheinz et al., 2010]. Physical phantoms also generally do not represent the complexity seen in patients in terms of activity and attenuation distribution. Physical phantoms are also limited in the flexibility in terms of the different positions and conditions that can be tested. Simulations, including Monte Carlo (MC) simulations, would be a useful compromise in generating datasets with realistic conditions where the ground truth is known. It is possible to use MC simulations of real patient data, with the incorporation of a 'synthetic' lesion, for which the ground truth can be known.

3.4.5.5 Bone SPECT/CT as test data

Radionuclide bone scans utilising ^{99m}Tc-labelled diphosphonates are a sensitive imaging study which can provide valuable information on a range of processes involving bone remodelling, including malignant diseases [Van Den Wyngaert et al., 2016]. There has been interest in quantification in bone scans since the 1990's [Brenner et al., 1997]. A key drawback of bone scans is the relatively low

specificity. The specificity of planar studies can be improved by acquiring SPECT or SPECT/CT. There are a range of potential applications for which quantification could improve specificity and confidence in reporting SPECT bone scans [Ross et al., 2019].

Due to the ubiquitous nature of bone scans, and the potential applications described below, bone SPECT was selected as a relevant source of test data for assessing PVC algorithms.

Diagnosis and prognosis

Assessment of the prognosis of patients with cancer depends on whether the disease has metastasised. This can be assessed with a bone scan, but it can be difficult to discriminate between bone metastases and degenerative changes. An assessment of Standardised Uptake Value (SUV) in SPECT/CT bone studies of patients with prostate cancer demonstrated a significant difference between bone metastases and normal vertebrae or degenerative changes [Kuji et al., 2017].

One of the issues limiting the utilisation of quantification in bone SPECT/CT is normal range. Work is ongoing in this respect, reviewing SUVs and absolute quantification in the normal lumbar vertebrae [Cachovan et al., 2013].

Monitoring treatment response

Monitoring response to treatment has been identified as a potential application for quantitative bone SPECT/CT [Van Den Wyngaert et al., 2016].

A strong correlation between the standard, validated method of quantitative ¹⁸F-NaF PET for assessing longitudinal studies, and quantitative SPECT has been demonstrated in metastatic breast and prostate cancer [Arvola et al., 2019]. Both benign and malignant lesions were included in the assessment. Arvola et al. [2019] also note that SPECT studies will be more affected by the PVE than in PET, which affects the SUV. Following on from this work, comparing baseline and follow-up studies for patients with breast cancer notes that quantitative SPECT has the potential to improve standardisation of evaluation (also make it more robust), and is could be used with PERCIST criteria already in use for PET imaging [Gherghe et al., 2023].

3.4.5.6 Tektrotyd SPECT/CT as test data

^{99m}Tc EDDA/HYNIC-TOC (Tektrotyd) scans are used to assess somatostatin receptor-positive Neuroendocrine tumours (NETs). Tektrotyd scans could potentially be used in multiple stages of the NET patient pathway including diagnosis, treatment planning, dosimetry, and assessing response to treatment. Tektrotyd SPECT studies have been selected as the basis for test datasets since the accurate application of PVC to these studies could be important for several quantitative applications, described below.

The Krenning Score

The semi-quantitative Krenning score, mentioned in Section 2.6.2, can be used to assess NET disease [Krenning et al., 1999]. The basis of the score is an assessment of the uptake in lesions relative to the uptake in the liver and uptake in spleen. Higher scores indicate more intense lesion uptake. A score of 3 indicates lesion uptake higher than liver, and a score of 4 indicates lesion uptake higher than liver and spleen.

However, the Krenning score was originally formulated for planar imaging using ¹¹¹In, and has been extrapolated for use in 3D imaging such as PET [Park et al., 2021]. In addition, there may be inter-operator variability in comparing lesions to normal liver. For these reasons, there is interest in reviewing Tektrotyd studies with quantitative SPECT [Reilly et al., 2021].

Diagnosis and prognosis

In addition to visual review of NET lesions in Tektrotyd studies, the Krenning score has been shown to correlate with disease progression [Saponjski et al., 2021]. As the extent of the PVE depends on multiple factors including the size, contrast and position within the FOV, accurate application of PVC would improve lesion and position independence when quantifying uptake and determining prognosis.

Treatment planning

A Krenning score of 3 or 4 indicates that patients will respond better to a type of MRT known as peptide receptor radionuclide therapy (PRRT) [Krenning et al., 1999]. It follows, therefore, that accurate quantification of NET lesions and

metastases adds confidence to the planning of the treatment pathway which will be most beneficial for an individual patient. Since the PVE limits the accuracy of quantification, especially for smaller lesions, it could be interesting to re-evaluate the performance of Tektrotyd scans (compared with e.g. PET scans) when accurate PVC is applied. PET has become the standard for pre-PRRT patient selection, despite "few formal data to support the use of SSTR PET over ¹¹¹In-pentetreotide scintigraphy" [Park et al., 2021]. However, the application of appropriate PVC could improve the performance of Tektrotyd SPECT data compared with PET - especially for small lesions.

Dosimetry

Post-PRRT imaging for dosimetry can be performed using the emissions from the therapeutic ¹⁷⁷Lu. Early studies used planar imaging, but more often dosimetry is now based on imaging protocols involving SPECT (either sequential SPECT studies, or using a combination of SPECT and planar data) [Gleisner et al., 2022, Jackson et al., 2020]. A recent recommendation paper for ¹⁷⁷Lu dosimetry states that the PVE is relevant in most cases, including for Organs at Risk (OARs), for example, the kidneys [Gleisner et al., 2022].

There may be scope for personalising the administered activity, to ensure each patient gets the greatest benefit in terms of highest tumour absorbed dose with limiting dose to OARs [Prete et al., 2017]. Appropriate PVC for lesions and OARs will be important to ensure the accuracy of absorbed dose calculations.

While the work on this thesis focusses on ^{99m}Tc, it is intended that methods should be applicable to other radionuclides, and therefore to post therapy dosimetry. The distribution of activity is expected to be similar in ¹⁷⁷Lu post therapy imaging compared with ^{99m}Tc Tektrotyd as both show areas of somatostatin receptor uptake. Therefore, we expect that any conclusions drawn using test data based on ^{99m}Tc imaging should also be applicable to ¹⁷⁷Lu imaging of NETs, provided that the relative spatial resolution is accounted for. ¹⁷⁷Lu images will have a poorer spatial resolution than ^{99m}Tc, and therefore the extent of the PVE is expected to be greater in post-therapy imaging, and so application of PVC could be even more important

than quantification in diagnostic radionuclides.

Monitoring treatment response

Tektrotyd SPECT/CT is noted to be a valuable tool for staging and follow-up of patients NETs [Sergieva et al., 2016]. Sequential Tektrotyd scans used to monitor response to MRT can demonstrate changes to the size and avidity of the same lesion. These changes can confound quantification due to the different extent of the PVE. Accurate application of PVC could reduce the impact of this effect.

3.5 Conclusions

This chapter explored the existing techniques for PVC in the literature. The lack of an optimal method for PVC in oncology SPECT highlighted the need to compare existing methods to identify those which could be promising for this application. A novel set of criteria that a PVC method should fulfil to be suitable for oncology SPECT was developed. This criteria aided critical assessment of existing methods; allowing a shortlist of promising methods to be formed and highlighting areas of weakness for further development.

The methods shortlisted, RM, itD (using RL) and STC will be explored further throughout this thesis, and compared with the RC method.

Chapter 4

Assessment of key factors affecting SPECT resolution variability and the impact on the PVE

4.1 Background

As discussed in Section 3.2, many existing PVC methods require information about the resolution of reconstructed images [Erlandsson et al., 2012b], usually in the form of a Point Spread Function (PSF). In SPECT, resolution can depend on factors including position in the Field of View (FOV), image acquisition and reconstruction parameters (including application of Resolution Modelling (RM), post-reconstruction filtering and number of iterations), and patient-specific factors such as activity distribution and attenuation. However, the potential extent of this variability in spatial resolution is not well appreciated.

The application of a spatially variable PSF in the Partial Volume Correction (PVC) process is computationally complex. It is important to assess the magnitude of the errors (if any) associated with assuming the simpler solution of a spatially invariant PSF to justify this complexity. The main aim of this chapter is to assess the magnitude of these errors when applying PVC in oncology SPECT imaging.

4.2. Aims 107

4.2 Aims

This chapter describes experiments using simulation and real phantom data aiming to:

- Investigate how SPECT resolution varies under different conditions, including the application of RM and a range of reconstruction iteration numbers.
- Estimate the impact on quantification due to applying PVC with the assumption of invariant resolution.

4.3 Existing work

The differences in resolution for different positions and for different OSEM iteration settings has been previously studied for point sources acquired on a Siemens Symbia T SPECT/CT system [Kappadath, 2011]. This work concluded that radial and tangential resolution varied depending on distance from the centre of the FOV, that the PSF was anisotropic and that the resolution depends on the number of OSEM updates used. These conclusions are generally well accepted, however the possible extent of the difference in PSF is perhaps less widely appreciated.

Recovery of activity concentration measurements, depending on position in FOV, has been studied using a NEMA phantom on a Siemens Intevo 6 system [Armstrong, 2019]. This study found that varying the locations of the spheres within the phantom (i.e. within the FOV) detrimentally affected the reproducibility of activity concentration recovery. This can be attributed to the difference in Partial Volume Effect (PVE) due to different positions in the FOV

However, some effects are less predictable. These include patient-specific aspects such as different body shapes, locations of high and low-attenuating material, and the distribution of activity within the image. How these factors affect the PSF has been studied less compared with the effect of the position in the FOV. Kappadath [2011] studied resolution at different lesion Target to Background Ratios (TBRs), however the effect of distribution of activity was not investigated.

4.4 General use of STIR in simulation-based testing

Software for Tomographic Image Reconstruction (STIR) [Thielemans et al., 2012, Marti-Fuster et al., 2013b] is Open Source software, used widely in tomographic imaging. It is useful for research as it can be used for generating input datasets, performing SPECT simulations to generate projection/sinogram data, and reconstructing these simulations using a range of algorithms. Example parameter files, and examples of commands used to run STIR are included in Appendix B.

The benefits of performing testing based on computer simulations include defining exact Ground Truth (GT) values, and the ability to control a range of factors in order to investigate one specific variable at a time.

4.4.1 Generating Input Data with STIR

STIR can be used to generate input emission and attenuation datasets for simulation based on pre-defined shapes. These shapes can be combined, subtracted, overlaid and rotated to create a range of phantom geometries. Detail of how this was used for the work in this chapter is given in the Methods section 4.5.1.1.

4.4.2 STIR SPECT System Model

STIR was used to forward project phantom data to produce sinogram data. This projection can be done based on a system matrix which has different options for modelling the effects of attenuation and spatially varying resolution [Marti-Fuster et al., 2013a]. Calculation of attenuation can be performed using a "Simple" model (where the integral of attenuation coefficients is performed along one line between the detector pixel and the image voxel, assuming attenuation is the same across the whole Collimator-detector Response (CDR) function), or a "Full" model (where the integration is done along a line per pixel along the width of the CDR). The CDR can be modelled in three different ways:

- RM off (geometric projection only)
 - Simplest option
 - Computationally fastest and least memory required

- No modelling based on collimator parameters only affected by projection of the square pixel on to the detector
- Less accurate than other options
- RM applied in 2D (transaxial plane only)
 - Compromise in complexity between no RM and RM in 3D
 - Collimator detector response modelled as a 1D Gaussian distribution
 - Models in-plane PSF, but each slice is independent
 - Less accurate than 3D RM
- RM applied in 3D (interactions across the volume)
 - Computationally slowest and most memory required
 - Collimator detector response modelled as a 2D Gaussian distribution
 - Models cross-plane PSF, accounting for interactions between slices
 - More accurate than other options

In this chapter, forward projections incorporating attenuation and collimator-detector response were simulated in 3D using a system model representing acquisition of ^{99m}Tc emission data with a Mediso Anyscan system, with LEHR collimators, using 180 projections over 360° and a 25cm circular Radius of Rotation (RoR).

4.4.2.1 Definition of Collimator in STIR

STIR defines the PSF of collimator-detector response as a Gaussian with the width, represented by the standard deviation, σ , varying with distance from the collimator. Note that σ is related to the Full-width at half maximum (FWHM) by:

$$FWHM = 2\sqrt{2\ln(2)}\sigma \tag{4.1}$$

The STIR model assumes a linear relationship between resolution and distance from collimator face as per Equation 4.2:

$$\sigma(d) = \text{slope} \times d + \sigma_0 \tag{4.2}$$

[Thielemans et al., 2023]

where d is the distance in cm from the collimator face. The *slope* and σ_0 parameters are specific to the system and collimator being modelled, and when defined appropriately will account for the system resolution (R_s) . Using existing data, values for *slope* and σ_0 were derived by fitting a linear equation to expected values for the system resolution, R_s (defined by equation 2.6, based on the intrinsic resolution, R_i , and collimator resolution, R_c).

The intrinsic resolution, R_i , is routinely measured at acceptance testing and the FWHM was reported to be 2.8 mm for the Mediso Anyscan system (corresponding to a σ_0 of 0.79 mm) based on acceptance tests performed by a Mediso engineer in 2018.

The collimator resolution R_c was calculated for a range of distances as per equation 2.7. The values required for equation 2.7; hole diameter, D, and hole length, l, were taken from the Mediso Anyscan equipment manual [Mediso]. The effective hole length from equation 2.8 was calculated using the NIST X-Ray Mass Attenuation Coefficients for lead, μ https://physics.nist.gov/PhysRefData/XrayMassCoef/ElemTab/z82.html. Since the NIST data does not specify a mass attenuation coefficient for lead at 140 keV, the data for energies in the range of 88 - 400 keV was fitted (see Figure 4.1. From this, the attenuation coefficient for lead at 140 keV was calculated to be 2.81 mm⁻¹) (based on the density of lead of 11.35 g/cm³ [Hubbell and Seltzer, 1996]).

Using the calculated value of l_{eff} , and equation 2.7, the collimator resolution, R_c was calculated and is shown in Figure 4.2. The system resolution, R_s , also shown in Figure 4.2, incorporates the the intrinsic resolution according to equation 2.6.

The accuracy of the fitted parameters was verified by comparing the fitted line to a measurement of the planar system resolution at approximately 10cm from the collimator surface, acquired as part of the Mediso acceptance testing (FWHM = 7.1 mm).

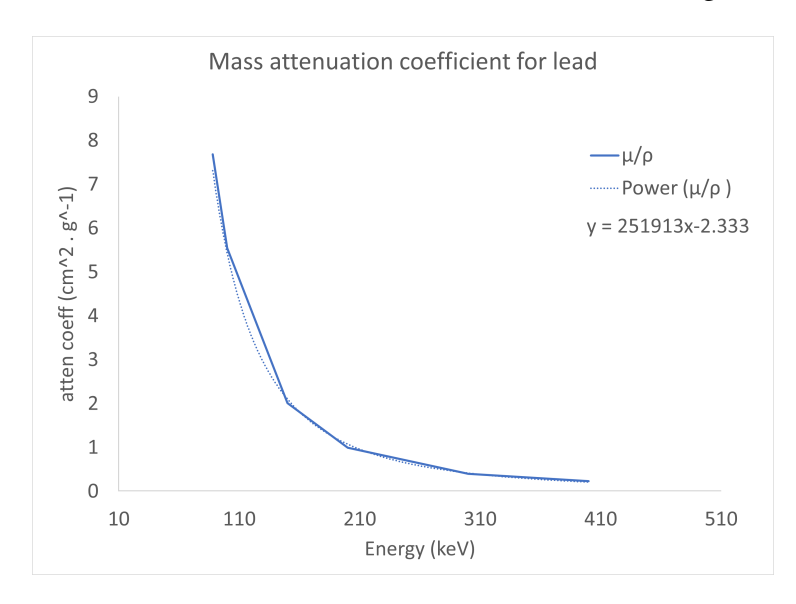


Figure 4.1: Plot of mass attenuation coefficient values for lead (from NIST data) vs energy. The dotted line is the fitted data, allowing a value for 140 keV to be calculated.

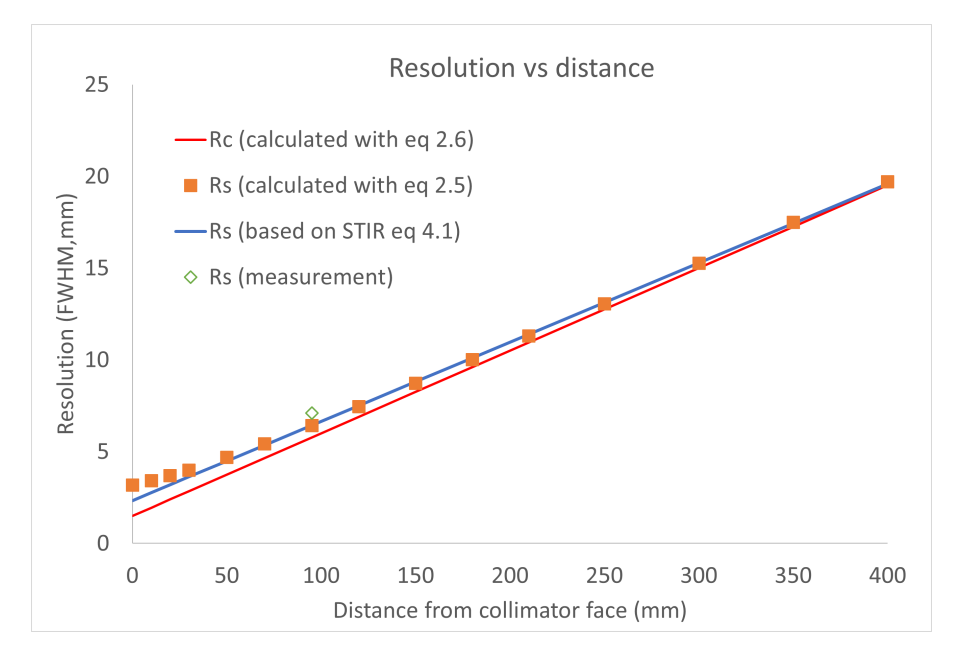


Figure 4.2: Distance from collimator face vs resolution (FWHM) for the Mediso system using LEHR collimators. The graph shows; straight line indicating the collimator resolution R_c as calculated using equation 2.7, values for the system resolution R_s based on equation 2.6. These system resolution data points were used to fit parameters used for STIR simulation based on equation 4.2. A check was made against a measured system resolution value at approximately 10cm distance.

A straight line fit to the distance vs system resolution data is shown in Figure 4.2. This was fitted to the linear range, using values in distance range 5-40cm.

Resulting fit parameters for the STIR collimator model (equation 4.2) were *slope* = 0.18, σ_0 = 0.1 cm (with σ_0 calculated based on a FWHM value of 0.23 cm and equation 4.1).

4.4.3 STIR Reconstruction

STIR was used to reconstruct projection data using OSEM up to 198 updates (33 iterations, with 6 subsets). Images were saved for review every 10 updates. Reconstructions were performed using the full range of RM options available in STIR (i.e. geometric, 2D and 3D PSF modelling) and with simple attenuation correction.

4.5 Simulation-based Testing of Variation in SPECT Spatial Resolution

In this section, a series of experiments were designed to vary one of the following parameters at a time (keeping the remaining parameters the same);

- Position of test object in FOV
- Reconstruction settings
 - Number of total updates
 - Use of RM
- Uniformity of attenuation map
- Activity distribution

The use of simulations rather than real phantom data can minimise other factors which can introduce variation. For example, a calibration factor used to convert pixel value to activity concentration is not required, and specifications of positions and intensities can be set and reproduced exactly. Simulation-based testing also allows the definition of known Computed Tomography (CT) values.

4.5.1 Methods

4.5.1.1 Simulated Phantoms and Attenuation Maps

STIR was used to generate digital cylindrical and elliptical cylinder phantoms, with single voxel 'point sources' in a range of positions within the phantom. Attenuation maps were also generated. When imaging is simulated and projection data is reconstructed, each of the point sources will produce a PSF, indicating the resolution under specific imaging conditions. Transaxial slices illustrating the design of digital phantoms are shown in Figure 4.3.

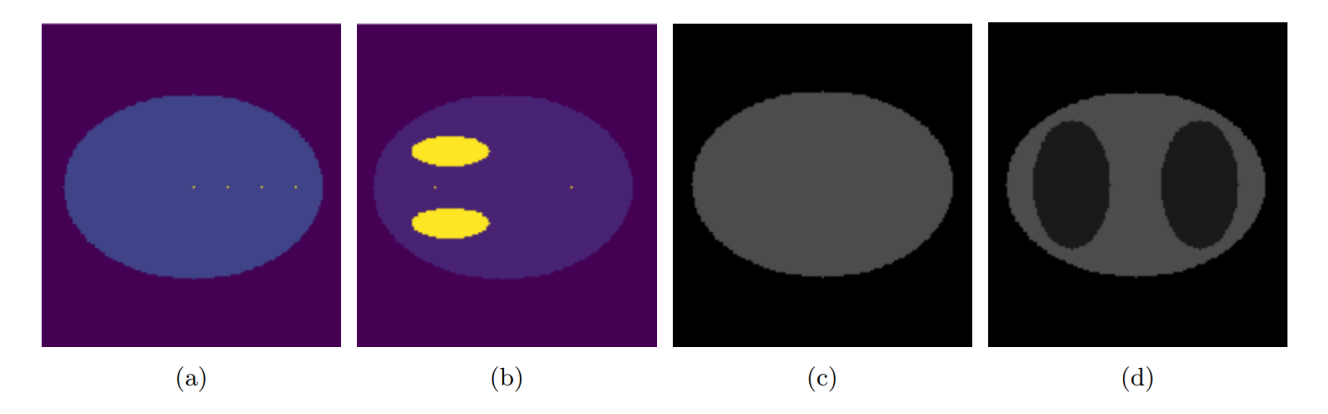


Figure 4.3: Examples of digital phantoms and attenuation maps used to investigate how resolution can vary in SPECT imaging. (a) Elliptical cylinder with point sources, (b) Non-uniform activity distribution, (c) Uniform attenuation map, (d) Non-uniform attenuation map.

The cylinder phantoms were set up with a diameter of 30.0 cm and length of 5.1 cm. The diameter was chosen to represent the cross-sectional dimensions of a realistic patient (or physical phantom). The length is shorter than a comparable real phantom since a longer phantom would increase processing time, without providing any additional information about resolution variation across the FOV. The elliptical cylinder phantoms were also set up with a length of 5.1cm. The major diameter of the elliptical cylinder was 30.0 cm, and the minor diameter was 21.6 cm. This setup resulted in a cross section close in dimension to an elliptical Jaszczak phantom [Data Spectrum, 2025].

Digital phantoms of both shapes were generated with uniform activity distribution and single-voxel point sources with TBR= 1000:1 at 4 cm intervals

from the centre (Figure 4.3 (a)). In addition, an elliptical phantom with two hot areas (TBR = 20:1) and point sources 8 cm left of centre and 8 cm right of centre was constructed (Figure 4.3 (b)). Uniform attenuation maps were generated with attenuation coefficient of $0.15 \, \mathrm{cm}^{-1}$ to represent $^{99\mathrm{m}}$ Tc in water, Figure 4.3 (c)), and also with non-uniform attenuation incorporating two regions approximating lungs where the attenuation coefficient was set to $0.05 \, \mathrm{cm}^{-1}$ (Figure 4.3 (d)). Phantoms were generated on a $256 \times 256 \times 64$ matrix, with isotropic 1.5mm voxels. This voxel size was sufficiently small to ensure that the NEMA criteria for measuring the spatial resolution was met (i.e. FWHM > 3 pixels wide [National Electrical Manufacturers Association (NEMA), 2001]).

The generated phantoms were simulated using STIR as described in Section 4.4.2. The resulting sinograms were reconstructed using STIR as described in Section 4.4.3. Figure 4.4 (a) is an example of a reconstructed dataset, for the phantom shown in Figure 4.3 (a) and attenuation map shown in Figure 4.3 (c).

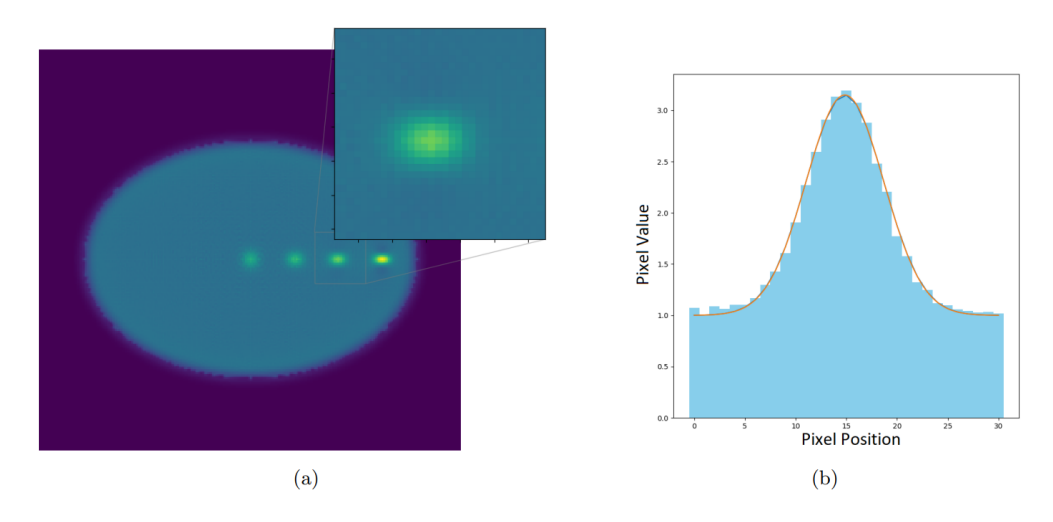


Figure 4.4: (a) Axial slice through elliptical phantom, reconstructed using 33 OSEM iterations (6 subsets) with RM off. Inset shows an example of planar section used for 2D Gaussian fitting, (b) Example of PSF profile, in the radial direction, with resulting Gaussian fit.

4.5.1.2 Determination of FWHM values

The inset of Figure 4.4 (a) shows the Region of Interest (ROI) which defines the data used to measure resolution in the reconstructed images. 2D Gaussians were fitted using three 2D slices through the reconstructed data (i.e. the x-y, x-z and

y-z planes), through the centre of the reconstructed PSF. The 2D Gaussian fit was performed according to Equation 4.3:

$$f(x,y) = Ae^{-\left(\frac{(x-x_o)^2}{2\sigma_x^2} + \frac{(y-y_o)^2}{2\sigma_y^2}\right)} + \text{offset}$$
 (4.3)

where A is the amplitude of the Gaussian peak, σ_x and σ_y indicate the standard deviations, indicating the width of the curve, in each direction and (x_o, y_o) is the centre point of the Gaussian. The offset parameter was set to the known background value.

Fitting was performed using SciPy in Python [The SciPy community, 2019]. This uses a non-linear least squares curve fitting to fit a Gaussian, according to equation 4.3, to the 2D PSF data. An initial guess for parameters A, (x_o, y_o) , σ_x , and σ_y was input to the fitting algorithm. The algorithm returns optimised values of each parameter such that the sum of the squared residuals of the data minus the fit is minimised. In addition to the optimised parameters, the function also returns an estimate of the covariance of the optimised parameters, from which the variance and, in turn, the standard deviation error on each parameter was calculated.

Each slice gave values for two of the radial, tangential and axial directions, and the FWHM values for each direction were averaged over two slices (i.e. two slice directions). The fitted data was overlayed with actual pixel values and the fit was visually reviewed in each case. An example of a fitted profile, overlayed on measured pixel values is shown in Figure 4.4 (b). Uncertainties were approximated based on estimated covariance of the optimised parameters given by the Python curve fitting function.

As the SPECT resolution should not be assumed to be isotropic, the FWHM was evaluated in the radial, axial and tangential directions individually. These directions are illustrated, relative to a phantom in a SPECT system in Figure 4.5. In this figure, the direction of the bed axis is along the z-axis, the y-axis would be from posterior to anterior, and the x-axis would be the patient's right to left side.

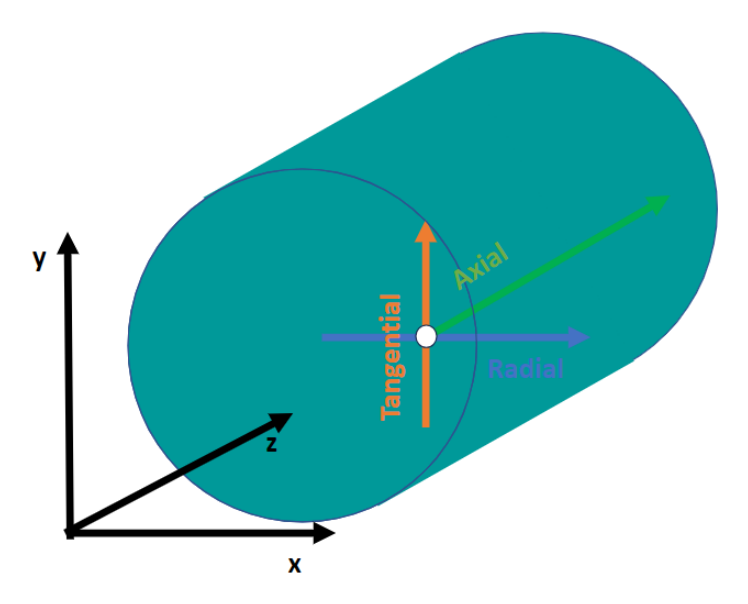


Figure 4.5: Illustration of tangential, axial and radial directions which will be used for FWHM measurements of the PSF.

4.5.2 Results

FWHM values were assessed to evaluate variation in resolution due to position in FOV, reconstruction parameters, attenuation and activity distribution. Unless otherwise specified, results refer to measurements from images reconstructed using OSEM with 33 iterations and 6 subsets (i.e. 198 updates).

4.5.2.1 Effect of position in FOV

Results demonstrate that FWHM values depend on position in the FOV. Resolution also depends on the direction of measurement. Results demonstrating this are presented in Figure 4.6 for the uniform elliptical cylinder, simulated with a uniform attenuation map.

Figure 4.6 demonstrates anisotropy in the PSF which depends on position along the x-axis; the radial, tangential and axial FWHM were within 3% of each other at the centre. However, the tangential and radial FWHM differed by 45% at a position 12cm from centre. The tangential resolution FWHM values were most affected by the position. Comparing the tangential FWHM at the central position (FWHM = 13.6 mm \pm 0.2 mm) and a position 12cm from the centre (FWHM = 7.0 mm \pm 0.1 mm) demonstrates variation by 48%. The FWHM as measured in the radial direction was least affected by the effect of the position along the x-axis.

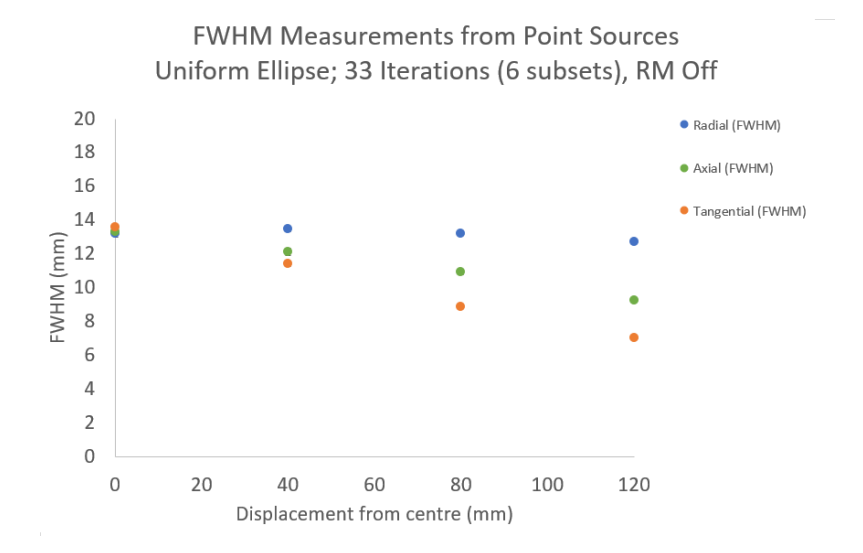


Figure 4.6: FWHM measurements from a uniform elliptical phantom reconstructed to 33 OSEM iterations without using RM. Error bars based on the Gaussian fit are not visible on this graph.

4.5.2.2 Effect of reconstruction parameters

Results demonstrate that the resolution varies depending on number of updates and whether or not RM is applied. Figure 4.7 (a) shows resolution measurements in each direction vs the number of updates when RM is not used. In each of the three directions, the width of the PSF is larger for early iterations, but reaches a steady value by approximately 100 updates, suggesting that reconstruction to convergence has been achieved. Figure 4.7 (b) demonstrates resolution measurements in each direction vs the number of updates when reconstruction is performed using RM in 3D. In comparison to Figure 4.7 (a), the PSF in each of the directions is wider for the first 10-20 updates. In addition, the resolution values have not yet reached stable values, suggesting that convergence is slower when RM is applied. Reconstruction was performed to a fixed number of updates, rather than aiming for convergence (in particular for the RM data) since Ordered Subsets Expectation Maximisation (OSEM) may converge to a limit cycle rather than a single solution [Twyman et al., 2019].

The expected benefit of reconstructing with RM is an improvement in resolution across the FOV. FWHM values in each direction for images reconstructed without RM, compared with images reconstructed with 2D RM and 3D RM, are



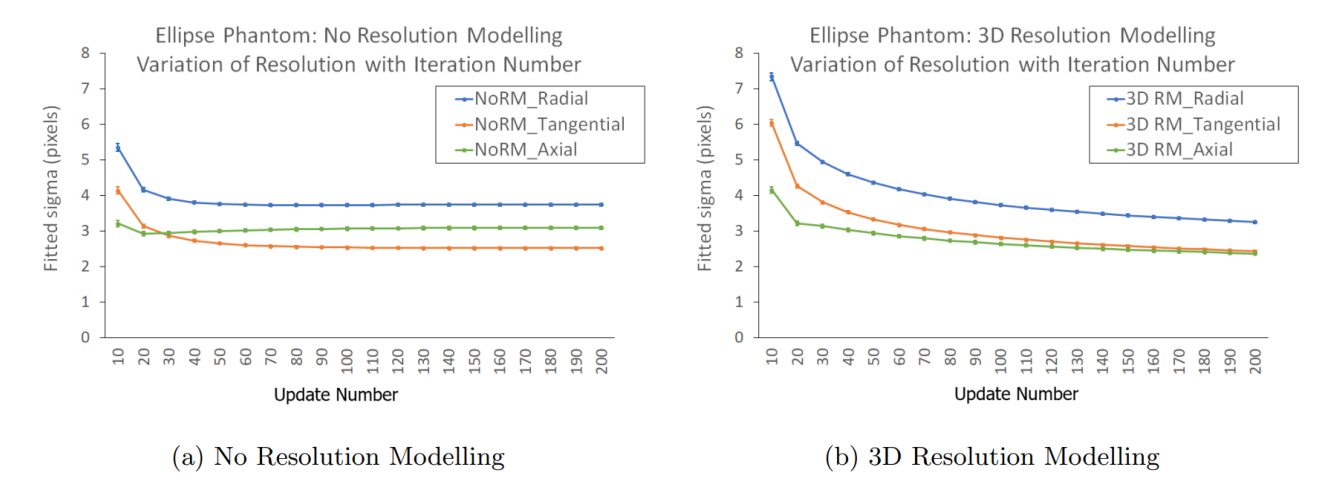


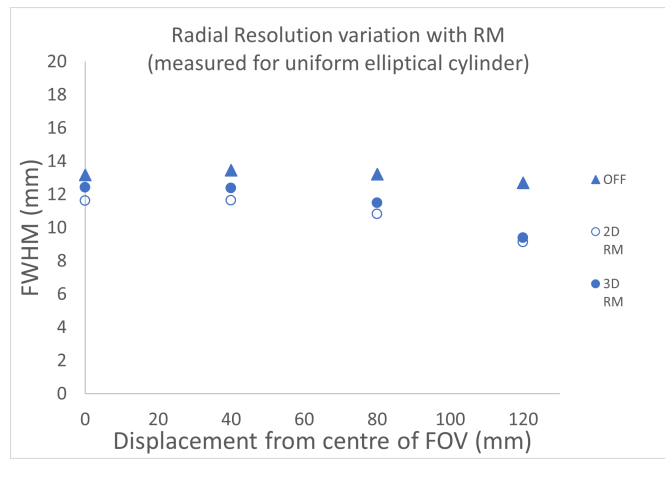
Figure 4.7: Graphs demonstrating variation of sigma values (1 pixel = 1.5 mm) with number of reconstruction updates. Reconstructions without RM, and with RM are shown in (a) and (b), respectively. Values were measured for a point 8 cm from the centre of a uniformly attenuating elliptical cylinder. X-axis is number of updates (where 6 updates = 1 full iteration).

shown in Figure 4.8 for four different positions in the FOV.

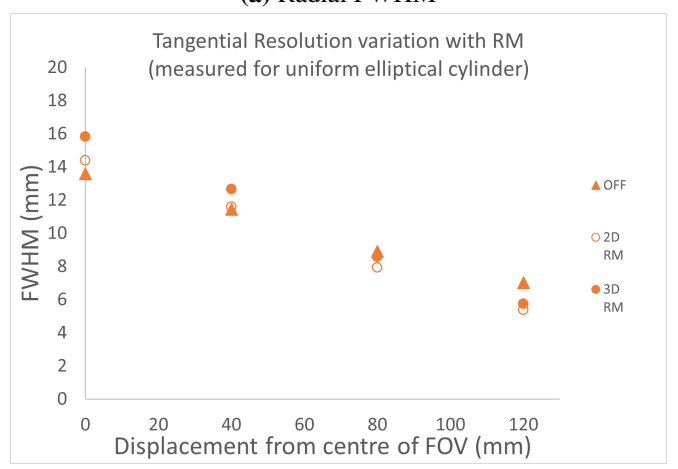
These results show that the application of RM improved the resolution in radial and axial directions of the uniform elliptical cylinder phantom. However, the tangential FWHM was larger for the central position (0 cm displacement from centre) when reconstructed with RM, and RM only improved the resolution for points positioned more than 8 cm off-centre. The application of RM did not remove the resolution dependance on position in FOV. In fact, difference between the radial and tangential FWHM values at 12cm compared with the centre position was greater when 2D and 3D RM was applied, compared with no RM. For the axial direction, the difference in axial FWHM between the 12cm and central positions was greater for data reconstructed with 3D RM compared with no RM. Anisotropy in the PSF remained despite the application of RM.

4.5.2.3 Effect of attenuation

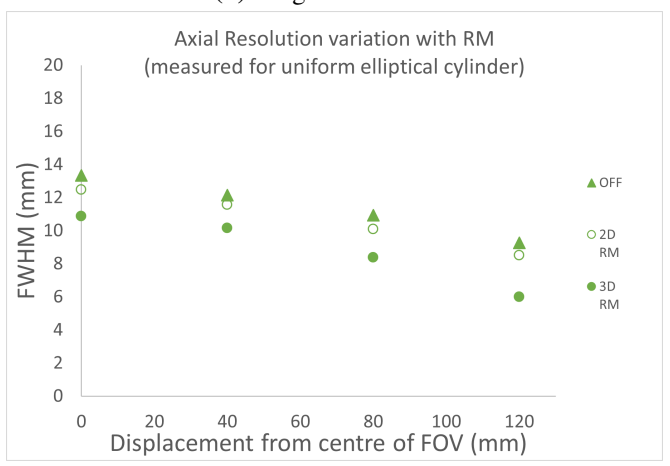
Objects of different shapes will have different attenuating properties at different projection angles. The effect of phantom shape on the resolution was investigated by reviewing FWHM measurements at specific positions within the FOV in a uniform cylinder compared with in a uniform elliptical cylinder. The resulting



(a) Radial FWHM



(b) Tangential FWHM



(c) Axial FWHM

Figure 4.8: Graphs demonstrating the effect on resolution in each direction for different positions within the uniform elliptical phantom. Reconstruction was performed using OSEM with 200 updates, without RM, with 2D RM and with 3D RM. Error bars based on the Gaussian fit are not visible on these graphs.

FWHM values were consistent, regardless of the shape of the phantom, to within 2%.

In addition to the shape, there may be variation within the attenuation coefficients of materials within a phantom or patient, resulting in non-uniform attenuation. This is important to consider for oncology SPECT, where lesions could be anywhere in the body. There are other applications, e.g. neuro imaging, where an assumption of uniform attenuation may be more appropriate. To explore the effect of a non-uniform attenuation map, the elliptical cylinder phantom was simulated using a simplified approximation of an attenuation map with lung-like shapes of low attenuation material (see Figure 4.3 d). The top left image of Figure

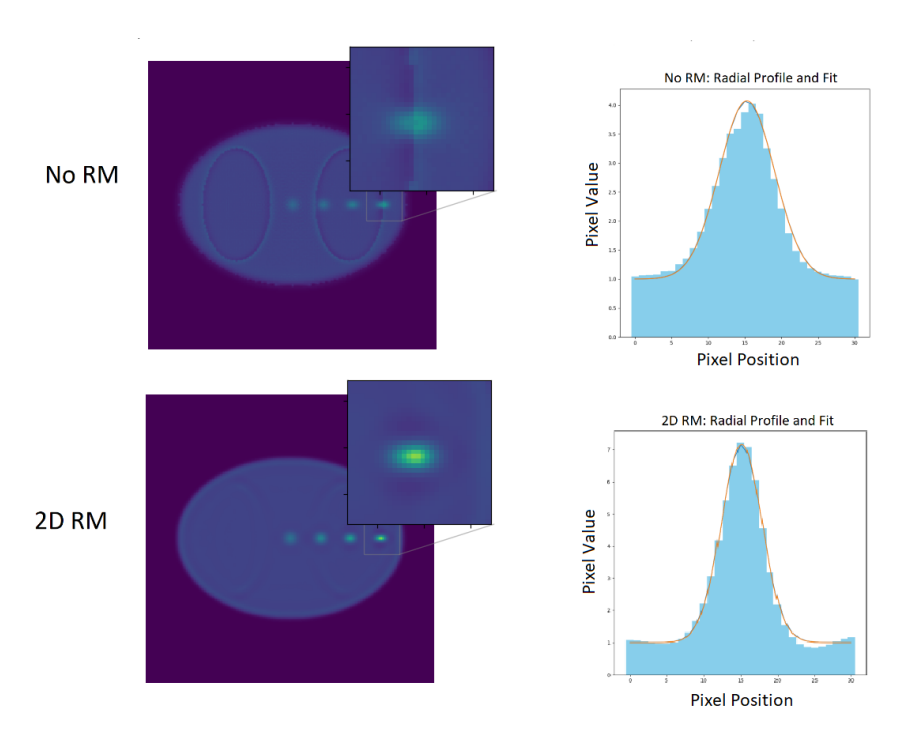


Figure 4.9: Appearance of the uniform elliptical cylinder with a non-uniform attenuation map, reconstructed without RM (top) and with 2D RM (bottom).

4.9 shows artefacts at the boundaries between areas of high and low attenuation when reconstruction is performed in STIR without using RM. This is consistent with findings from previous work [Marti-Fuster et al., 2013a]. The artefacts reduced when 2D RM was applied (bottom left image of Figure 4.9). The artefacts affect the shape of the profile, and the Gaussian fit of the no RM data is poorer than the fit to data with 2D RM is applied. Points positioned away from

these artefacts demonstrated consistent resolution measurements compared with the elliptical cylinder simulated with uniform attenuation to within 6% when no RM is used.

4.5.2.4 Effect of non-uniform activity distribution

The phantom shown in Figure 4.3 b) was reconstructed with and without RM. An example reconstructed transaxial slice is shown in Figure 4.10.

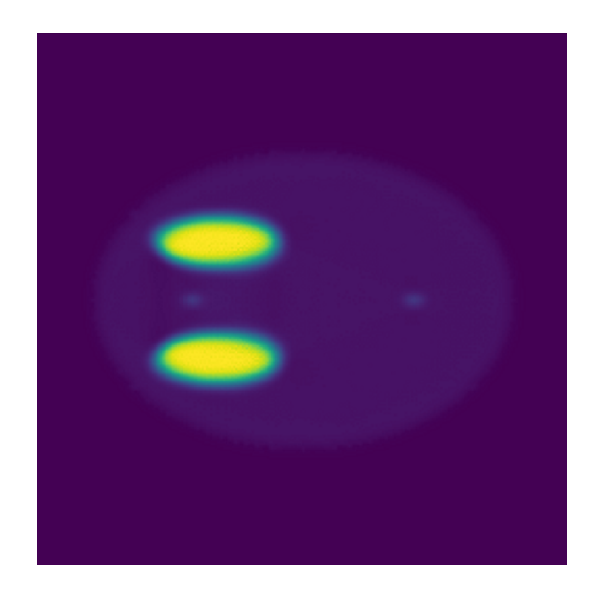


Figure 4.10: Transaxial slice through reconstructed non-uniform activity distribution data (input data shown in Figure 4.3 b). Reconstruction was performed with no RM and with 200 OSEM updates. The point at the left of the ellipse is close to two hot areas, and the point on the right is not expected to be affected by these areas.

The measured resolution at the two different points (one close to the hot regions, and one away from the hot regions) is illustrated vs update number in Figure 4.11 (for 2D RM). FWHM measurements for the two points, reconstructed with 200 updates, and with RM on and off are summarised in Table 4.1. Comparing results from the two points demonstrates how high activity areas close to the point of interest can affect the resolution. In the table, these results are additionally compared with values measured for the same point in the FOV within the uniform elliptical phantom (i.e. no hot areas impacting the PSF).

The point located close to the hot regions demonstrated poorer radial resolution than the point with the same displacement from centre in the uniform elliptical

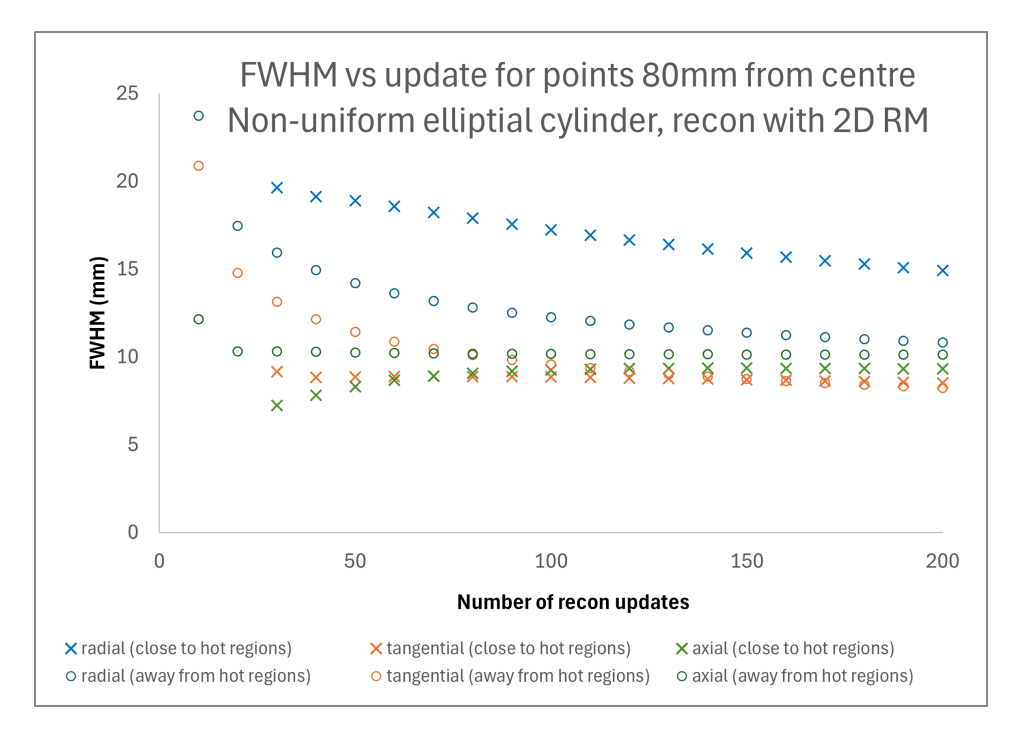


Figure 4.11: Plot showing the variation of FWHM in each direction with update number, for reconstructions performed with 2D RM. Results are shown for the point close to the hot areas in the phantom in Figure 4.10, and for the point away from the hot areas in the same phantom.

	FWHM Measurements (mm) at Points 80mm offset from centre													
			Resolution Modelling Off						2D Resolution Modelling On					
Phantom Type		Radial	Std Dev	Tang- ential	Std Dev	Axial	Std Dev	Radial	Std Dev	Tang- ential	Std Dev	Axial	Std Dev	
Uniform Ellipse		13.22	0.13	8.91	0.10	10.93	0.15	10.82	0.10	7.93	0.08	10.08	0.11	
Non- uniform Activity Ellipse	away from hot regions	13.41	0.14	8.86	0.10	10.93	0.16	10.83	0.10	8.24	0.09	10.13	0.11	
	close to hot regions	13.88	0.28	9.05	0.16	9.75	0.13	14.91	0.21	8.52	0.15	9.32	0.14	

Table 4.1: FWHM results for point sources positioned 8cm from the centre; for a uniform ellipse, a non-uniform ellipse with a point away from and a point close to hot regions. All from data reconstructed with 200 OSEM updates.

cylinder. This difference depending on activity distribution was greater when reconstruction using 2D RM was performed (38% larger FWHM), compared with no RM (5% larger FWHM). The differences were also compared with iteration number as images were produced every 10 updates between 10 and 200 updates. Greater differences were observed at low iteration numbers (i.e. less than 50

updates) compared to later iterations (around 200 updates) which can be seen in Figure 4.11. The point located away from the hot regions in the same phantom agreed with the uniform elliptical cylinder to within 1% in all directions for non-RM reconstructions, and to within 4% for reconstructions with 2D RM. The effect of neighbouring activity distribution on resolution has also been shown in simulations of a phantom with spherical inserts [Leube et al., 2024a] - also demonstrating more of an effect when RM is applied.

4.5.3 Discussion

4.5.3.1 Reconstruction parameters

RM was expected to improve the resolution (as discussed in Section 3.4.1.1), however the results presented in this section suggest that this is not universally true. In addition, the resolution remained spatially variant throughout the FOV. The likely reason for these effects is a reduced convergence rate when RM is used. More iterations may be required to improve resolution beyond that of a non-RM reconstruction, or to reduce the difference in measured PSF depending on position in the FOV. However, increasing number of iterations increases the reconstruction time, will amplify noise and can also worsen "Gibbs" ringing artefacts if RM is used [Dewaraja et al., 2012]. Artefacts as a result of the application of RM were observed in this investigation and an example is shown in Figure 4.12, where the bottom row shows the PSF image and profiles through it in the radial and tangential directions when reconstructed with 2D RM in STIR. The ringing artefact can be seen most clearly in the tangential profile of the 2D RM reconstructed data. Figure 4.12 also shows a small artefact when RM was not applied. This could be attributed to STIR reconstruction without RM which still involves some interpolation which will introduce some degree of resolution recovery.

The findings related to the effect of the reconstruction parameters on the PSF will be helpful in informing the choice of reconstruction settings (namely number of updates and whether or not to use RM) for other tests performed in this thesis. The key drawbacks of the use of RM include the introduction of Gibbs artefacts, requirement of more updates to see any benefit in terms of improved resolution, and

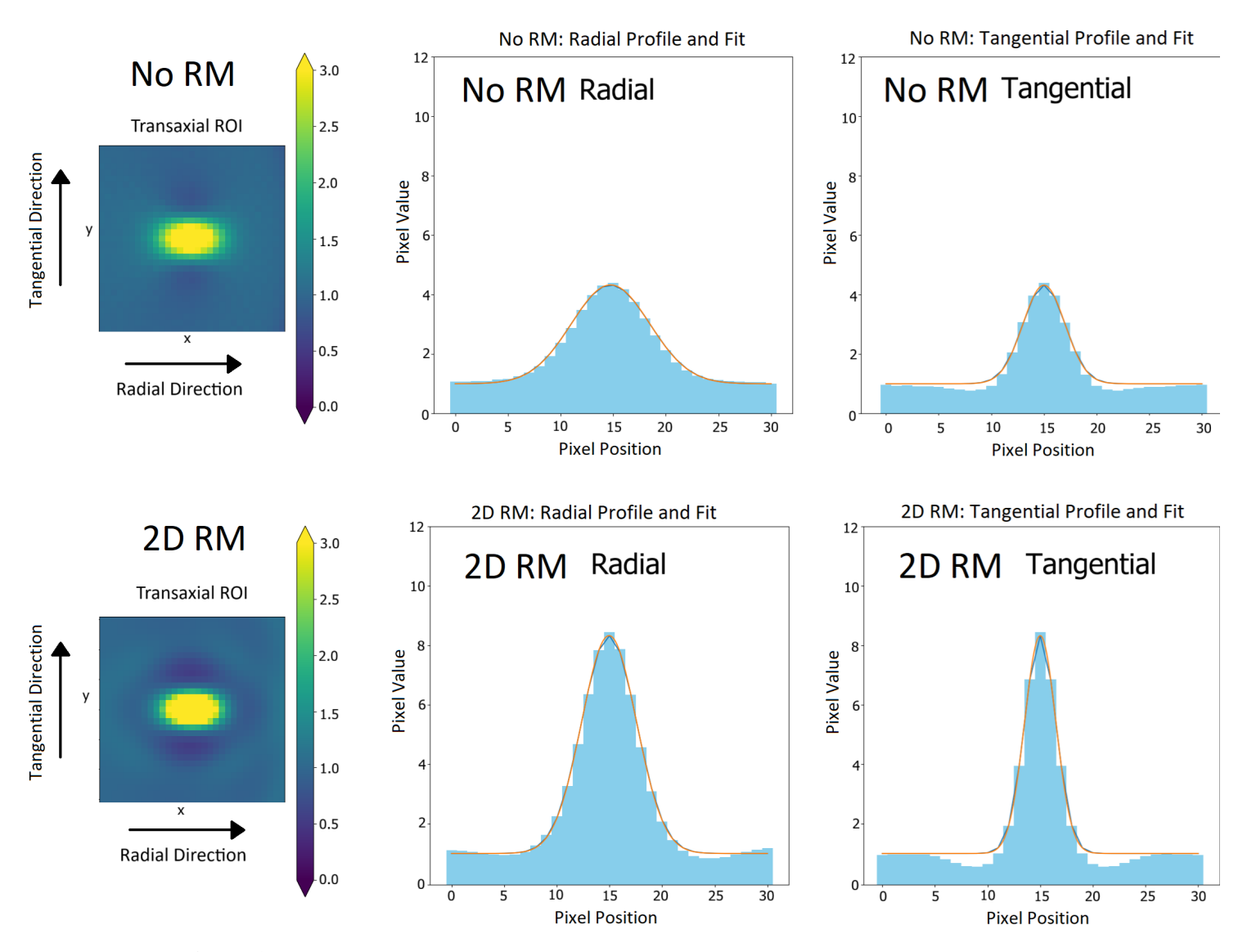


Figure 4.12: An example of the Gibbs-type ringing artefact introduced by applying RM at 33 OSEM iterations (6 subsets) to a point 12cm from the centre of a uniform cylinder. The original voxel value was 1000. The Gaussian shape shown for the tangential profile of the PSF reconstructed with 2D RM is not a good fit.

increased variability in PSF depending on the activity distribution in the proximity of the position of interest (the latter two points could possibly be attributed to unpredictable convergence behaviour when RM is used). RM was also not able to remove the variability of the PSF with position in the FOV, or make the PSF isotropic.

4.5.3.2 Attenuation

This investigation did not find a significant difference between resolution measurements for phantoms of different shapes. However, this may be because the cross-sections of the cylinder and elliptical cylinder are similar. A more pronounced shape difference may have demonstrated a larger effect. In addition to investigating uniformly attenuated shapes, lung-like areas of low attenuation were incorporated into the elliptical cylinder. This also demonstrated agreement to within 6% of the uniformly attenuating dataset, provided that points were not positioned in areas affected by reconstruction artefacts present when RM was not applied.

4.5.3.3 Non-uniform activity distribution

The results from this investigation with simulated data demonstrate that the activity distribution affects the resolution, as the point which was close to the two hot regions (in Figure 4.3 (b)) demonstrated a poorer radial resolution. This may be due to the slower convergence rate expected at points close to high activity areas [Liow and Strother, 1993]. The direction that the resolution is most detrimentally affected by proximity to hot areas may depend on the orientation of the hot areas, i.e. if they had been positioned to the left and right of the point of interest (rather than the set up tested; above and below) then a deterioration in the tangential resolution may be expected.

4.5.3.4 Limitations

Limitations of this simulation investigation include the use of a smaller voxel than is typically used clinically. All simulations were performed noise-free. If Poisson noise had been added to the simulations, this would have been more realistic and would have enabled study of noise amplification with increasing number of updates. Simulations were performed without scatter, therefore assuming the application of a perfect scatter correction in the reconstruction. All simulations were based on a circular-orbit acquisition at a single radius of rotation, which is not likely to be the set-up used in clinical practice for oncology SPECT imaging. In addition, the attenuation properties of the patient bed were not included in the simulation.

Further work is required to study resolution variation in more realistic clinical scenarios. Monte Carlo modelling could be a useful tool for further investigation.

Finally, the characterisation of resolution using only FWHM measurements is a limitation. The additional measurement of Full-width at tenth maximum (FWTM) would inform more about the shape of the curve, which could be important for radionuclides other than ^{99m}Tc.

Despite the above limitations, the results from this section demonstrate that the potential variation in resolution in SPECT imaging could impact quantification, and this merits further study. In addition, these initial simulation studies give a useful indication of experimental variables to be explored, and guidance for reconstruction settings to use for future investigations.

4.5.4 Conclusions

The simulation work performed in Section 4.5 demonstrated that the use of RM was problematic in that artefacts were introduced, the PSF was found to vary more depending on activity distribution, and more reconstruction updates were required in order to reliably improve resolution. Attenuation was not found to impact resolution measurements, provided that attenuation correction artefacts were not present in the image.

Results from this section have demonstrated that, in order to apply an accurate PV correction, a position-specific and patient-specific estimate of the PSF is more reliable when derived from data reconstructed without RM. A targeted approach to PVC, using a case-specific correction, would obviate the need to use RM to reduce the PVE by improving the resolution.

4.6 Bias estimate due to PVC application with invariant PSF

4.6.1 Aims

As demonstrated in Section 4.5, resolution depends on imaging conditions and specific position of the object of interest. Therefore, it is important to estimate the

impact that applying PVC has on the quantification of small lesions when resolution is assumed invariant. The aim of the present section is to determine, by simulation, the possible bias incurred in applying PVC assuming invariant resolution.

4.6.2 Methods

4.6.2.1 Phantom Generation

A set of digital phantoms were generated in STIR. Each of these phantoms incorporated small spherical 'lesions', positioned off-centre, in an elliptical cylinder containing uniform background activity. Phantoms each had a single 'lesion', and different phantoms covered a range of lesion diameter and TBR values. In each case, the position of the lesion was 12 cm from the centre of the FOV. Example images of the digital phantoms used for this investigation are shown in Figure 4.13.

4.6.2.2 Convolution

Phantoms were convolved with two different Gaussian kernels, where kernel parameters were based on measurements performed in Section 4.5.:

- Kernel based on the PSF from a position 12 cm from the centre of an elliptical phantom, assuming OSEM reconstruction with 200 updates and no RM. This will be referred to as the 'specific' kernel since it is specific to the lesion position, phantom, and imaging conditions.
 - Specific $FWHM_{radial} = 12.7 \text{ mm}$
 - Specific $FWHM_{tangential} = 7.0 \text{ mm}$
 - Specific $FWHM_{axial} = 9.3 \text{ mm}$
- Kernel based on the PSF from the centre of a cylindrical phantom, assuming OSEM reconstruction with 200 updates and no RM. This will be referred to as the 'central' kernel
 - Central $FWHM_{radial} = 13.2 \text{ mm}$
 - Central $FWHM_{tangential} = 13.2 \text{ mm}$
 - Central $FWHM_{axial} = 13.5 \text{ mm}$

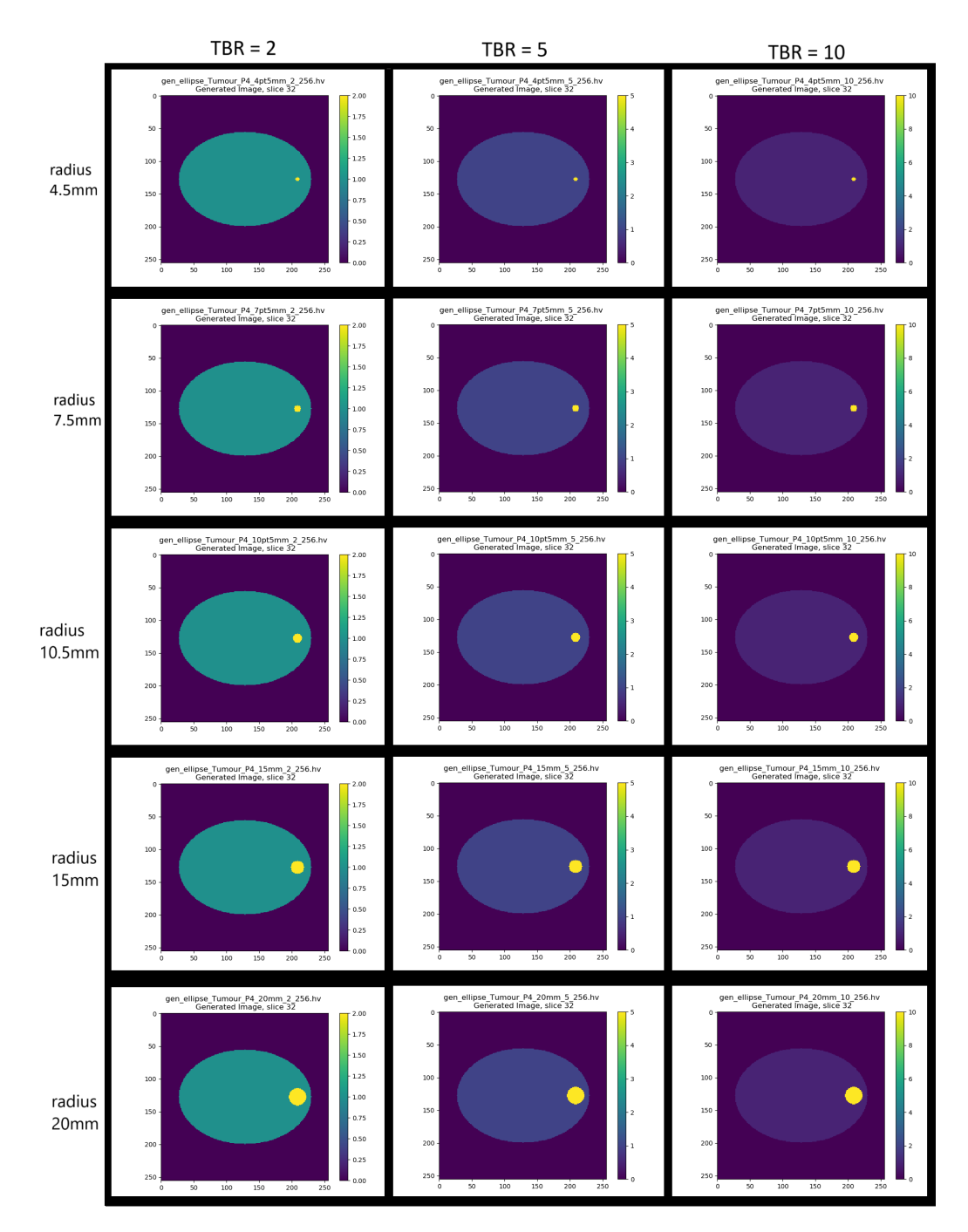


Figure 4.13: Phantoms, with a range of lesion sizes and TBRs, used to estimate inaccuracy due to application of PVC with the assumption of invariant resolution.

A summary of the convolution process is shown in Figure 4.14.

4.6.2.3 RC calculation

The Recovery Coefficient (RC) was calculated by comparing the total value within the known volume of the lesion pre- and post-convolution; representing the GT and

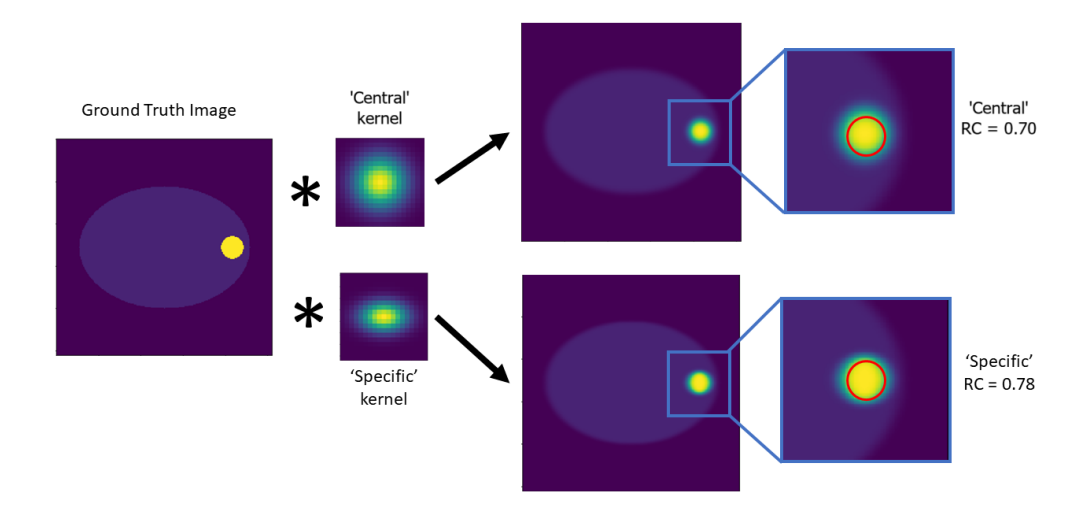


Figure 4.14: Diagram demonstrating the process of calculating the 'central' and 'specific' recovery coefficients (RC), which are used for evaluating the bias incurred when performing PVC with the assumption of invariant resolution.

uncorrected lesion uptake, respectively.

The RC calculation was performed as per equation 3.1 (described in Section 3.4.2.1) and is replicated in equation 4.4 for ease of reference:

$$RC = \frac{C'}{C} \tag{4.4}$$

where C' is the number of counts in the known volume of the lesion measured from the convolved dataset, and C is the number of counts in the known volume of the lesion in the Ground Truth dataset.

This can then be used to generate a corrected number of counts as per equation 4.5:

$$C_{corr} = \frac{C'}{RC} \tag{4.5}$$

4.6.2.4 Bias Calculation

To calculate any bias that would be introduced by performing PVC with an inappropriate PSF, a Recovery Fraction (RF) value, indicating the bias relative to the known Ground Truth, was calculated as per equation 4.6

$$RF = \frac{C_{corr}}{GT} \tag{4.6}$$

where C_{corr} represents a measure of the counts in the lesion, which could be uncorrected counts, counts corrected by the specific RC, or counts corrected by the central RC. RF values less than 1 indicate an underestimate of the GT, and RF values greater than 1 indicate an overestimate.

The RF of uncorrected data is equivalent to the specific RC since $C_{\text{specific}} = C_{\text{uncorr}}$:

$$RF_{Uncorr} = \frac{C_{uncorr}}{GT} = \frac{C_{specific}}{GT} = RC_{Specific}$$
 (4.7)

The RF based on data corrected using the central RC simplifies to a ratio of the specific RC to the central RC:

$$RF_{CentralCorr} = \frac{C_{CentralCorr}}{GT} = \frac{\frac{C_{uncorr}}{RC_{central}}}{GT} = \frac{C_{specific}}{GT \times RC_{central}} = \frac{\frac{C_{specific}}{GT}}{RC_{central}} = \frac{RC_{Specific}}{RC_{central}}$$

$$(4.8)$$

From equation 4.5, we can see that correcting the lesion counts from the convolved dataset with the RC derived from the same dataset will give a perfect correction, i.e.:

$$RF_{SpecificCorr} = \frac{\frac{C_{specific}}{GT}}{\frac{C_{specific}}{GT}} = \frac{RC_{Specific}}{RC_{Specific}} = 1$$
 (4.9)

Since the RF is the ratio of RCs from each convolved image, it represents the bias in the corrected value relative to the ground truth.

4.6.3 Results

4.6.3.1 Recovery Coefficients

Recovery Coefficients were calculated for the images convolved with the specific and central kernels. Results are shown in Figure 4.15. For all TBRs and all lesion radii, the central kernel RC is lower than the specific RC. This implies that if correction is applied with the central RC, the data will be over-corrected.

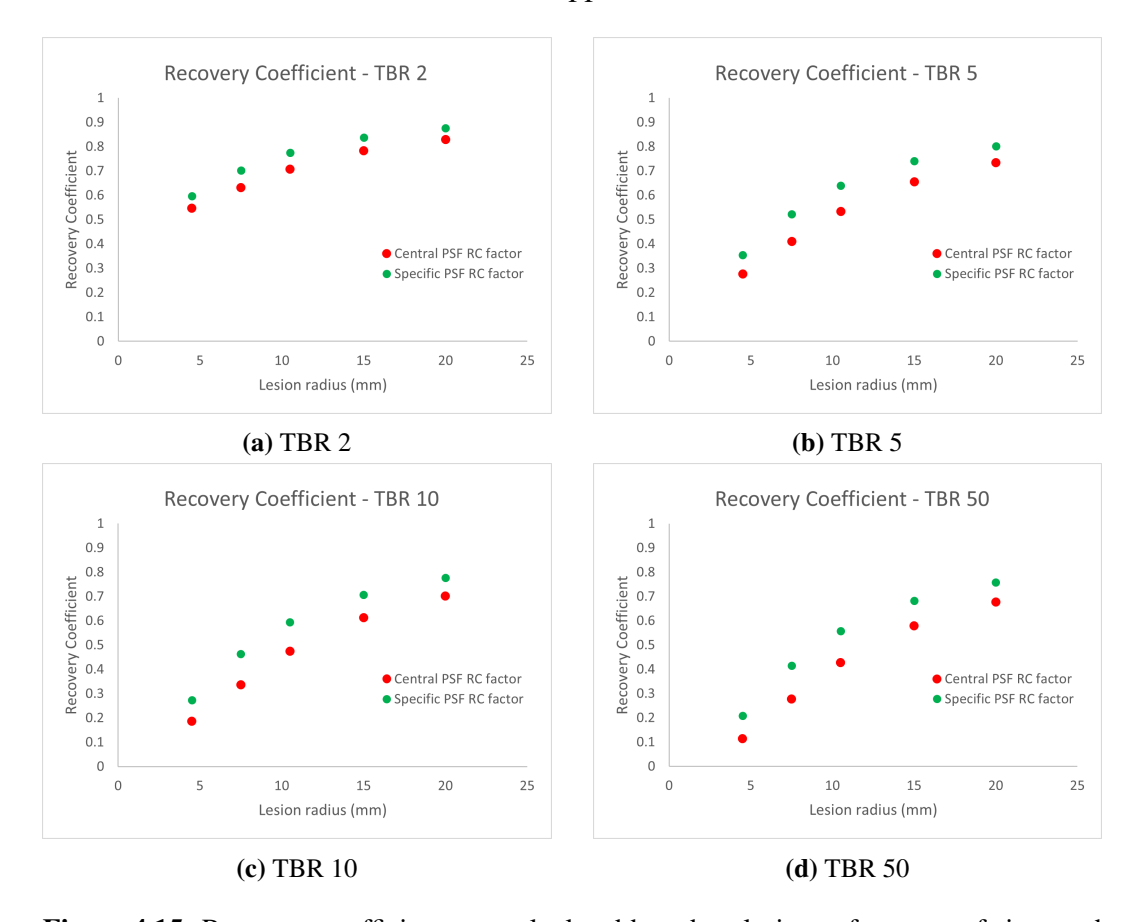


Figure 4.15: Recovery coefficients, as calculated based on lesions of a range of sizes and TBRs, convolved using two different kernels.

4.6.3.2 Bias due to applying incorrect RC

Figure 4.16 plots the RF values for lesions of diameter 0.9 cm, 1.5 cm, 2.1 cm, 3 cm and 4 cm, each with TBRs of 2:1, 5:1 and 10:1. The results demonstrate that the use of a 'central' PSF for PVC introduces a bias which depends on lesion diameter and tumour to background ratio (TBR).

In this case, since the 'central' PSF was wider than the 'specific' PSF, the values were over-corrected. A maximum bias of 47% greater than ground truth was measured for the smallest sphere (diameter 0.9 cm) at the largest TBR (10:1) in the range tested. The bias was less than 12% for lesions of any size with TBR of 2:1, and less than 13% for lesions of any TBR with diameter of 4 cm.

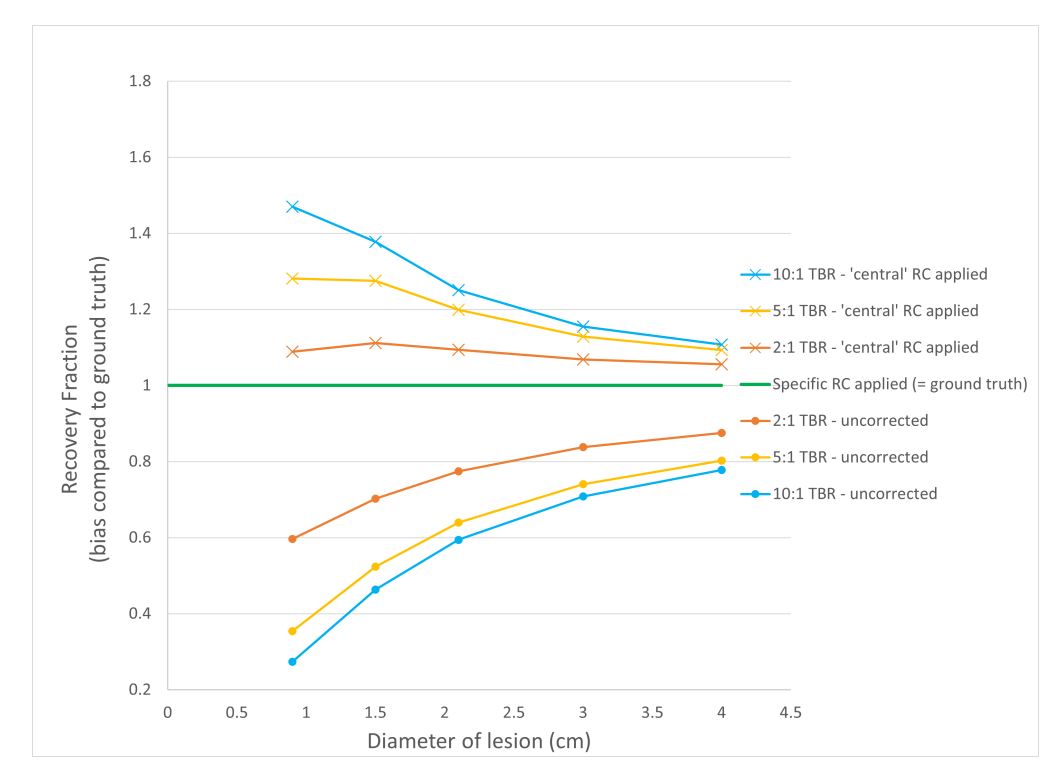


Figure 4.16: Plots of Recovery Fraction (RF) for a range of 'lesion' diameters and TBRs. Circular points represent the uncorrected RF of lesions convolved with the specific PSF. The green line represents the RF of lesions corrected using the 'specific' RC (i.e. perfect correction). Crosses represent the RF of lesions corrected using the 'central' PSF.

4.6.4 Discussion

The observation that there is a greater bias for smaller lesions is intuitive since the impact of the PVE is greater for smaller objects. The observation that the bias is greater for higher TBRs may be less intuitive, but can be attributed to the compensating effect of spill-in from the background being relatively small compared with situations with a lower contrast between target and background.

The conclusions drawn from this simple test are limited to the specific case studied; i.e. a 12 cm difference between PSF measurement positions. The rationale behind this was to replicate the position that a SPECT resolution measurement may be made during system QC tests (i.e. the centre of the FOV). However, this may be a worst-case scenario and the position difference between the centre and the position of interest is likely to be smaller than 12 cm in many cases. The use of a 'standard' PSF reflecting the resolution at the radius that NEMA spheres are positioned at

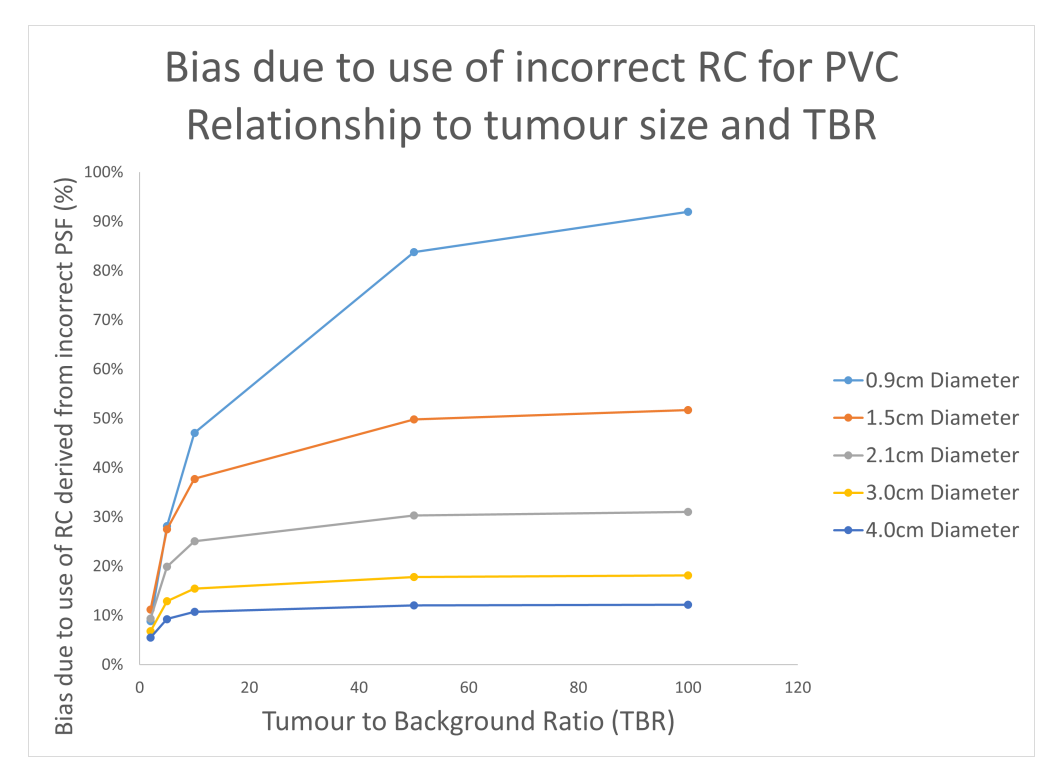


Figure 4.17: Plot demonstrating the percentage bias incurred from applying PVC with RC values based on the PSF at the centre of the FOV.

during phantom acquisition of RC values may have been more representative (since phantom RC measurements make an implicit assumption that the resolution across the FOV is the same as at the radius of the spheres, or is invariant across the FOV).

Results also demonstrated the importance of TBR, in addition to size, in applying PVC, which is often overlooked when applying RC based on phantom data as it is impractical to acquire NEMA phantom data at every possible TBR, and knowledge of the ground truth TBR is not feasible.

It should be noted that the convolution approach used to estimate the spread due to limited spatial resolution is an approximation for the full simulation and reconstruction of the 'lesions' in different positions. Convolution was used due to the relative improvement in computational speed (<1 minute per dataset for convolution, compared with >90 hours per dataset for simulation and reconstruction of 256 matrices). The accuracy of this approximation was validated by simulating and reconstructing images for the 20 mm radius lesion and TBR = 10:1. The resulting bias values agreed with the convolution method to within 1%.

4.6.5 Conclusions

Results from the simulations in this section have demonstrated that applying PVC using an invariant spatial resolution will result in quantitative inaccuracies. The extent of the quantitative bias will depend on the size of the lesion and the TBR.

4.7 Phantom-based Testing of Spatial Variation of the PVE

4.7.1 Background

Simulation work in section 4.6 demonstrated a potentially significant variation in quantification (up to 47 %) due to spatial dependence of the PVE in SPECT imaging. However, due to the limitations of simulation work, real phantom data is required to support the conclusions. Limitations of the simulation work performed in this chapter include the assumptions made in setting up the system model, not including scatter in the simulation and not including noise in the simulation. However, test conditions are difficult to replicate in a physical phantom due to possible errors in positioning, phantom filling and higher noise levels. In addition, imaging true 'point' sources for PSF estimation is challenging as, in general, fillable phantoms have Perspex walls and a finite volume.

Rather than replicating with point sources, NEMA phantom data, acquired on a SPECT/CT system, will be used to assess whether the conclusions of the simulation work can be corroborated with real phantom data.

A previous study using a NEMA phantom observed up to 35 % spatial variation in the activity concentration recovery, used for PVE correction, as a result of different sphere configurations within NEMA phantom [Armstrong, 2019]. This study noted that the variation in clinical images is likely underestimated. However, this previous study did not isolate the effect of sphere position in the FOV from other factors, including variation in attenuation and variation in surrounding activity distribution due to position within the phantom body.

4.7.2 Aims

The present investigation aims to systematically assess the spatial dependence of the PVE using a NEMA phantom imaged on a SPECT/CT system.

4.7.3 Methods

4.7.3.1 Equipment

Acquisitions were performed on a Siemens Symbia Intevo Bold SPECT/CT system using LEHR collimators. A NEMA phantom was filled with ^{99m}Tc using a TBR of 10:1. This contrast level was selected as representative of a typical clinical TBR, and to allow comparison with previous studies (e.g. [Armstrong, 2019] and simulation work in the previous section).

4.7.3.2 Phantom set-up

The NEMA phantom was used for this experiment due to its non-symmetrical shape, to give different information in addition to the simulations using the cylinder and elliptical cylinder phantoms.

Rather than the conventional use of the NEMA phantom using all 6 spheres, only two spheres were filled and imaged for any one set of images. Each pair of spheres was imaged twice. As shown in Figure 4.18, the first images were acquired with the phantom positioned on the scanner bed with one sphere at CT isocentre, the second set of images were acquired with other sphere in the pair at the isocentre. This results in a 11.4 cm lateral position change along the x-axis of the resulting image. This distance is well within the range of possible separation between two lesions in the same patient. CT LASERs were used to aid the set-up and positioning. It was expected that the resolution would be poorer for the sphere imaged at the centre, based on simulation results.

Three filling and scanning sessions enabled image acquisition of all 6 spheres positioned both in-centre and off-centre. This allowed RC curves, including all sphere sizes, to be generated for both positions. Note that due to time restrictions in the use of clinical equipment, the phantom TBR varied from 6.1 (for the 10 mm and 22 mm diameter spheres) to 10.1 (for the 13 mm and 28 mm diameter

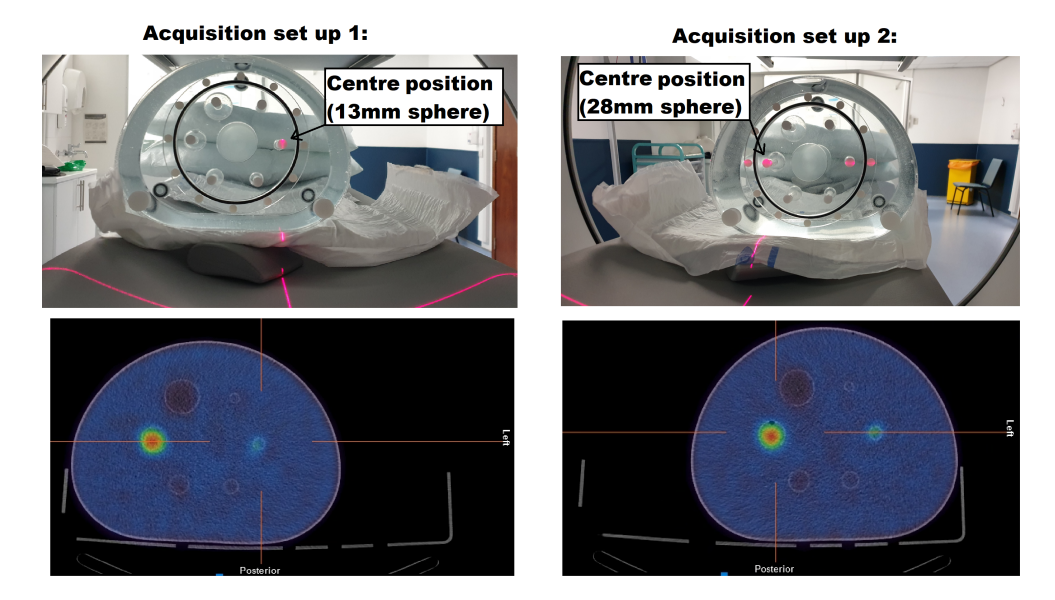


Figure 4.18: Photographs of the set up of NEMA phantoms with two spheres at the isocentre (top row), and the resulting reconstructed SPECT/CT data (bottom row). The central spheres shown are the 13 mm diameter sphere (left hand side images), and the 28 mm sphere (right hand side images).

spheres) (TBR was 8.4 for 17 mm and 37 mm spheres). These TBRs were confirmed using samples taken from stock dilution used for sphere filling and the background tank after acquisition. The samples were measured using an autogamma counter to confirm the activity concentration ratio. These TBRs are in the same range as was used in the previous work referenced [Armstrong, 2019].

4.7.3.3 Acquisition and Reconstruction

Images were acquired using a clinical scanning protocol for Tektrotyd SPECT/CT. This was a non-circular orbit with 120 projections, using body contouring, on a 128×128 matrix, energy window was $140~\text{keV}\pm7.5\%$. The acquisition protocol was adjusted to stop on counts, rather than time per projection, in order to improve consistency in total counts between individual acquisitions. Total counts acquired, averaged over all 6 acquisitions was 24.45(0.08) million counts.

Reconstruction was performed using Hermes software, and parameters typically used for the clinical Tektrotyd studies; OSEM, (8 iterations, 15 subsets, CT Attenuation Correction, Monte Carlo Scatter Correction, Resolution Modelling and a 10 mm Gaussian post filter). Images were reconstructed onto a 128×128

matrix (4.795 mm voxels). A second set of reconstructions without Resolution modelling was also performed.

4.7.3.4 Data Analysis

Spherical VOIs around the hot spheres were segmented using Hermes software based on the sphere volume and position seen on the registered CT data.

The Contrast Recovery Coefficient (CRC) was calculated for each sphere in both positions (using equation 3.2).

4.7.4 Results

4.7.4.1 Effect on Detector Orbit

The impact of moving the phantom on the orbit of the detectors can be assessed by reviewing the position of the detectors for each projection angle. This is shown in Figure 4.19.

Figure 4.19 demonstrates that the orbit of the detectors was affected only slightly, in the anterior section of the detector orbit, by the shift of the NEMA phantom. It is not expected that this small difference in orbit will impact the resolution, in comparison with the position in the FOV.

4.7.4.2 Visual detectability

In addition to assessment of quantitative accuracy, it is important to note that in clinical practice patient images are almost always reported based on visual assessment.

It was observed that the visual detectability of the smallest sphere depended on how the phantom was positioned. When the 10 mm diameter sphere was positioned at centre, the sphere could not be seen - the expected position is indicated by an arrow on Figure 4.20.

When the phantom was shifted such that the 10 mm sphere was 11.4 cm along the x-axis, the sphere can be seen, albeit subtly. The images were acquired to the same number of counts and reconstructed using the same settings, suggesting that this visual difference is due to the inferior resolution at the centre of the FOV (rather than being attributed to a noise or convergence difference). The other sphere in the

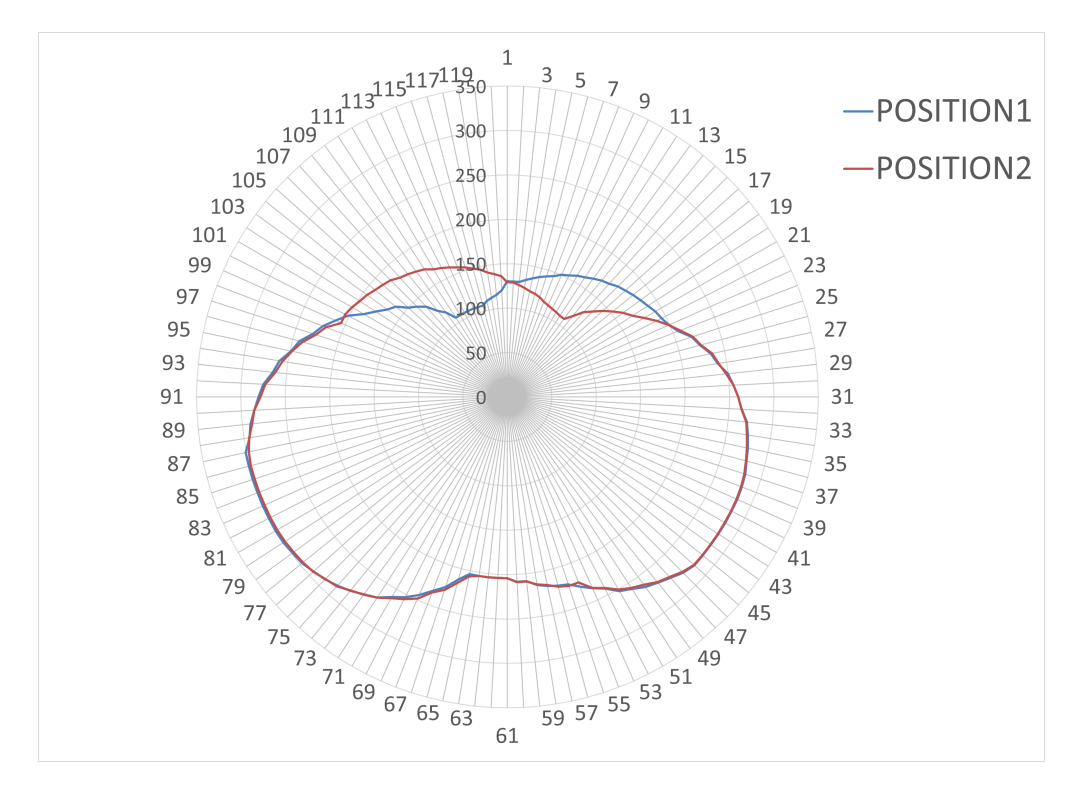


Figure 4.19: Comparison of the orbit of detectors with the NEMA phantom in two different positions along the x-axis (i.e. position 1 had one sphere in the centre of the FOV, position 2 moved a different sphere to the centre of the Field of View). Radar plot shows the projection number around the circumference, and the position of the detector relative to the centre of the FOV for each projection angle.

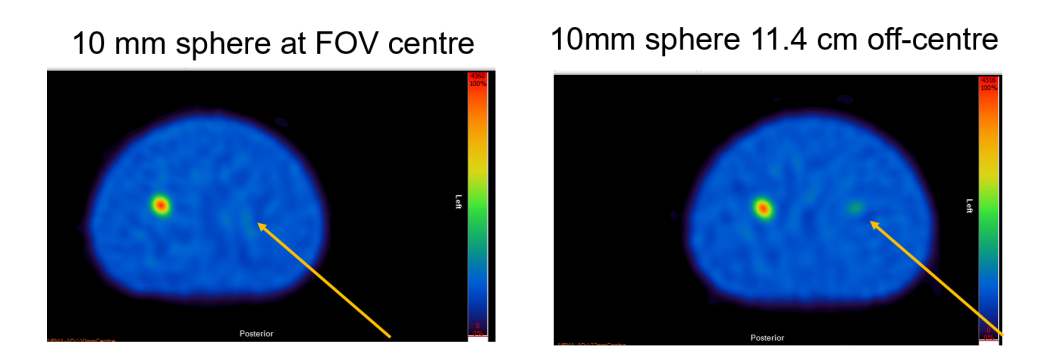


Figure 4.20: Comparison of the phantom set up with the 10 mm sphere in the centre of the FOV (left) and moved 11.4 cm laterally along the x-axis (right), reconstructed using the clinical protocol with RM.

phantom shown in Figure 4.20 has a diameter of 22 mm, and the visual perception is relatively unaffected.

4.7.4.3 Quantitative assessment

Mean Recovery Coefficient

The mean RC curve for data reconstructed using the clinical parameters (i.e. with RM) is presented in Figure 4.21. The position in the FOV affects the RC most for the 10 mm diameter and 13 mm diameter spheres, reflecting visual observations. For data reconstructed with RM, changing position has less of an impact for spheres of diameter 17 mm and above compared with the smaller two spheres.

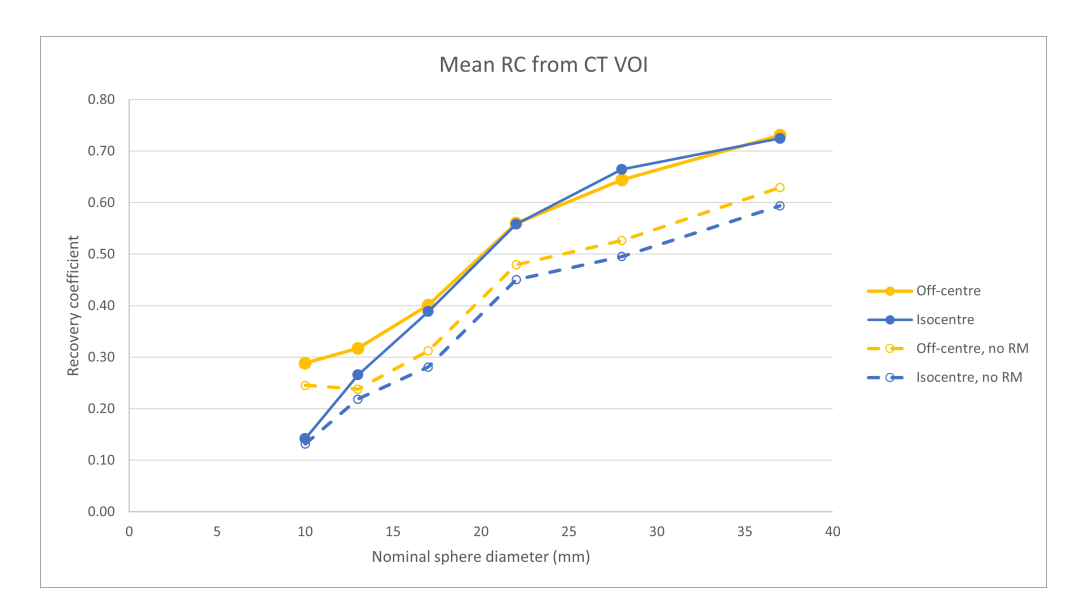


Figure 4.21: Mean Recovery Coefficient curves for the six spheres, acquired at the image isocentre, and 11.4 cm from the centre. VOIs were drawn based on the size and position of the spheres on the registered CT data. Data presented includes images reconstructed using the clinical protocol, including RM, and without RM.

Reconstruction without RM results in mean RC plots which are further from complete recovery (i.e. further below RC = 1) than data reconstructed without RM. For all sphere sizes, the off-centre RC curve is higher than the isocentre RC curve. This is a small, but relatively consistent, difference for all sphere sizes except the smallest sphere, where the positional difference is greater.

Maximum Recovery Coefficient

Maximum activity concentration recovery is the metric presented in [Armstrong, 2019], however since this is based on a single value it can depend on noise in the image. The benefit of using the maximum RC as a metric is that the

dependence on VOI selection is reduced. Figure 4.22 shows RCmax results for images reconstructed with and without RM.

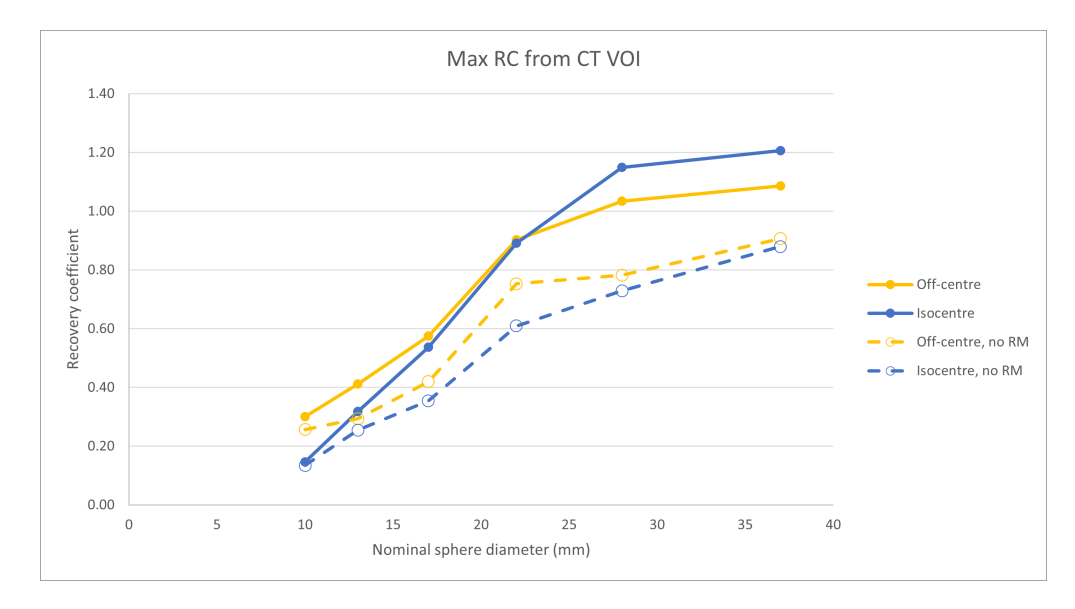


Figure 4.22: Maximum Recovery Coefficient curves for the six spheres, acquired, reconstructed and analysed as per Figure 4.21.

A key, expected, difference between the RCmax and RCmean plots is that the values are higher for RCmax, overshooting 1 for the two largest spheres.

The RCmax plots for data reconstructed without RM follow a similar trend to the RCmean in that there is a small, relatively consistent difference depending on position where the off-centre RC is higher than the isocentre for all sphere sizes. However, for the RCmax data reconstructing using RM, the off-centre RC is greater than the isocentre RC for the smaller spheres, and lower for the larger spheres. This was not expected, given that the central position is expected to have inferior resolution.

Difference in RC due to position

Previous phantom work with varying position of NEMA spheres demonstrated a 32-35% variation in the maximum activity concentration recovery depending on position, for the three largest spheres [Armstrong, 2019]. The present experiment, which aimed to separate the effect of a positional change within the FOV from other factors, determined that the maximum difference in RCmax due to the position was 29%, a similar magnitude to that found in previous work.

The range of RC difference values for RCmax data is greater than that for RCmean data, possibly due to the relatively greater effect of noise on the RCmax metric. The difference between the central and off-centre position in RCmean is less than 5% for all except the two smallest spheres when data are reconstructed with RM. The RCmean values from images reconstructed without RM demonstrate a relatively more consistent difference, for all spheres except the smallest.

4.7.5 Discussion

The difference in RC curves, depending on position, was smaller than expected based on conclusions drawn from simulation work (see e.g. Figure 4.15). However, a key difference between the simulation and phantom experiments is the reconstruction software and settings used. Reconstruction of the simulation data was performed using STIR, and reconstruction of the phantom data was performed in Hermes using reconstruction settings which included a 10 mm postreconstruction Gaussian filter. Certain reconstruction settings, in particular the smoothing filter, may contribute to reducing the difference in resolution across the FOV, compared with simulation work. The utility of a smoothing filter in clinical applications is largely for assistance with visual interpretation, however it is generally not beneficial for quantification. In addition, the system model used for simulation and reconstruction of the simulation data was based on a different gamma camera system to the one used for the NEMA phantom acquisition. This means that the collimators are made differently, which could have an impact on the system resolution at different distances. Another difference between phantom work and simulation work is and the orbit of detectors which was circular in simulation work and non-circular in NEMA phantom acquisition. In order to remove this variable, future simulation work should incorporate non-circular orbits. A final difference between simulation and phantom work is the presence of cold perspex walls in the NEMA spheres. Simulation datasets do not include this cold wall, which better replicates the clinical reality of a lesion in tissue.

Previous phantom work involved three configurations of spheres within the phantom [Armstrong, 2019]; this changes attenuation within the NEMA phantom

for each sphere. Similar work involved simulating 720 different configurations, noting variation between configurations increased when reconstruction was performed with RM [Leube et al., 2024a]. Current work aimed to isolate the resolution variation effect from the attenuation and any other differences which may be introduced. To do this, the symmetry along the centre of NEMA was utilised, and the phantom was moved along the x-axis by translation only (no rotation) to ensure that scatter and attenuation should be similar in each position.

The effect of reconstructing with RM can be seen in Figures 4.21 and 4.22. For RC_{mean}, for the larger spheres, the effect of spatially variable resolution is reduced which can be seen since the RC curves for different positions are overlapping for most spheres. However, this is not the case for the two smallest spheres. This means that RM does not remove the effect of a spatially varying PSF for small objects which are most affected by the PVE. The RC_{max} data demonstrate that RM has a different impact on spheres of different sizes. This variation introduced by RM will not necessarily be consistent across patients with different activity distributions (since convergence rates in different areas of the image could be different). This supports the conclusion drawn in Section 4.5.3 that the use of RM could introduce challenges for accurate application of PVC.

A limitation of the phantom work presented in this section is that no errors or uncertainties were calculated. Previous NEMA acquisitions have demonstrated repeatability with an order of magnitude of \pm 10 % [Shearer et al., 2024]. Another limitation is the variability in TBRs between different acquisitions. However, all TBRs were in a clinically realistic range, and no systematic differences are noted in results. Due to limitations on time available on clinical imaging systems, only one set of acquisitions was images for each phantom and sphere configuration. Ideally, more repeats would have been acquired which may indicate whether differences observed, particularly in visual interpretation, are due to random noise fluctuations.

Further work on this phantom experiment could involve repeating the acquisition on different systems, or using different reconstruction methods. However, comprehensive work published previously demonstrates the finding that

equipment and reconstruction settings can impact RC curves [B Peters et al., 2019], and so repetition of this work is not necessary. We can however, conclude that for a phantom-acquired RC curve to be applied accurately, it should be specific to the imaging system, and reconstruction settings used.

4.7.6 Conclusions

This phantom study has demonstrated that areas of poorer resolution within the FOV result in reduced detectability of small lesions. Quantification of objects smaller than 17 mm in diameter appears to be affected by the variation in resolution observed when the position in the FOV is changed.

4.8 Chapter 4 Conclusions

Testing performed with computer simulated data demonstrated that resolution cannot be considered spatially invariant in SPECT. The PSF depends on imaging conditions, including reconstruction method. Variation in the FWHM of more than 40% is possible, depending on imaging conditions, position in FOV and direction of measurement.

PVC applied to simulated data with the assumption of spatial invariance incurred biases of between 10-47% compared with the ground truth. The magnitude of the bias depends on imaging conditions, and lesion characteristics such as size, position and contrast with background.

Imaging using a gamma camera and NEMA phantom demonstrates that the extent of the PVE, characterised by evaluating the mean RC, depends on position by 1.3-29.3%, for all spheres larger than 11 mm in diameter, depending on the reconstruction parameters. For the smallest NEMA sphere, the difference is between 87 and 100%.

For both simulated and phantom studies, the use of RM was found to introduce variability in the resolution, which depends on multiple factors. Therefore, measurement of the PSF, specific to patient, position, and reconstruction is required for accurate PVC whether or not RM is applied. For the application of oncology SPECT, it will be important to incorporate a case specific resolution estimate into

the PVC algorithm. A method for doing this is discussed in Chapter 5.

Chapter 5

Use of Perturbation to Measure Spatial Resolution, and the Application to PVC

This chapter is based on a previously published paper [Gillen et al., 2022].

5.1 Background and Aim

The variation of spatial resolution in SPECT imaging is not usually considered when applying Partial Volume Correction (PVC). However, as demonstrated in Chapter 4, the assumption of invariant resolution may result in quantitative inaccuracy in PVC corrected data. Therefore, if the PVC method of choice requires knowledge of the Point Spread Function (PSF), measuring the case-specific PSF could improve the accuracy of PVC corrected images.

The main aim of this chapter is to investigate whether the use of a technique known as perturbation could be used to measure the PSF in order to improve the accuracy in application of PVC. The use of perturbation for PSF estimation will be tested in computer simulated scenarios commonly encountered in clinical SPECT oncology imaging, such as bone scans and Tektrotyd imaging.

5.2 Perturbation for PSF Measurement

The perturbation method, first demonstrated in 1988 [Stamos et al., 1988], involves adding projections of a small noise-free source to sinogram data, creating a "perturbed" dataset. Following reconstruction, the original reconstructed image is subtracted from the image reconstructed using the perturbed dataset. If a point source is used as the perturbation, the resulting difference image represents the PSF for that specific imaging case (i.e. the specific position in Field of View (FOV), reconstruction settings, and activity distribution). This means that perturbation could allow case-specific, i.e. patient-specific PSF measurement.

5.2.1 Previous studies using perturbation

The perturbation method has been used to demonstrate, through simulations, that the PSF is object dependent for maximum likelihood reconstruction algorithms for SPECT [Stamos et al., 1988]. Further simulation work on maximum likelihood reconstruction, using a small Gaussian perturbation, concluded that the measured PSF was dependent on the object size and the number of iterations used in the reconstruction [Liow and Strother, 1993]. Perturbation has also been used in physical data to evaluate the resolution of a novel SPECT system [Erlandsson et al., 2009], and to investigate the effect of using resolution modelling in the reconstruction of a SPECT brain phantom, compared with a simple uniform cylinder phantom [Badger and Barnden, 2014].

For reliable PSF measurement, point source contrast (intensity compared with background) should be small enough to avoid artificial enhancement due to the non-linearities in the reconstruction algorithm. A study on the acceptable point source contrast required for stable Full-width at half maximum (FWHM) values found a threshold of 0.1 (i.e. the reconstructed peak intensity of the point source with background should be less than 110 % of the background activity) [Gong et al., 2016]. This threshold was adhered to in the present study.

Previous research on perturbation for resolution measurement has covered a range of equipment, simulation and experimental work, on simple and complex datasets including geometric phantoms and anthropomorphic cardiac and brain

phantoms [Stamos et al., 1988, Liow and Strother, 1993, Erlandsson et al., 2009, Badger and Barnden, 2014, Gong et al., 2016, Li et al., 2017b]. This includes work which uses perturbation in combination with Geometric Transfer Matrix (GTM) in brain SPECT imaging [Du et al., 2005]. However, none of the previous investigations have systematically challenged the perturbation method in oncology SPECT. This chapter examines the use of perturbation for PSF estimation in phantoms with different lesion sizes, contrasts, and positions - including both simple geometric phantoms and more complex anthropomorphic phantoms.

5.3 Methods

5.3.1 Phantom Generation

Sets of simple geometric phantoms and anthropomorphic datasets were generated. Simple geometric phantoms were generated in STIR, and anthropomorphic phantoms were generated using Extended cardiac-torso phantom (XCAT) software [Segars et al., 2018]. Generated datasets in image space are referred to as the Ground Truth (GT).

5.3.1.1 Simple Geometric Phantoms

The simple geometrical phantoms consisted of a uniform elliptical cylinder (major radius = 152 mm, minor radius = 108 mm, length = 216 mm) on a 128×128 matrix with 4 mm³ voxels. Uniform spheres of higher intensity were added to this uniform background to represent hot lesions in a non-zero background.

Examples of the types of simple geometric phantom used are shown in Figure 5.1. The different cases examined are summarised in Table 5.1.

For all datasets specified in Table 5.1, the point source used for PSF estimation was positioned centrally within the lesion. In addition to this central position, the effect of non-central point position within a lesion was studied. This is important to explore because, in practice, the exact position of the centre of a lesion may not be known. To perform these non-central PSF measurements, the point position remained at the centre of the FOV and the centre of a 36 mm radius lesion, with Target to Background Ratio (TBR) = 10, was moved relative to the point along the

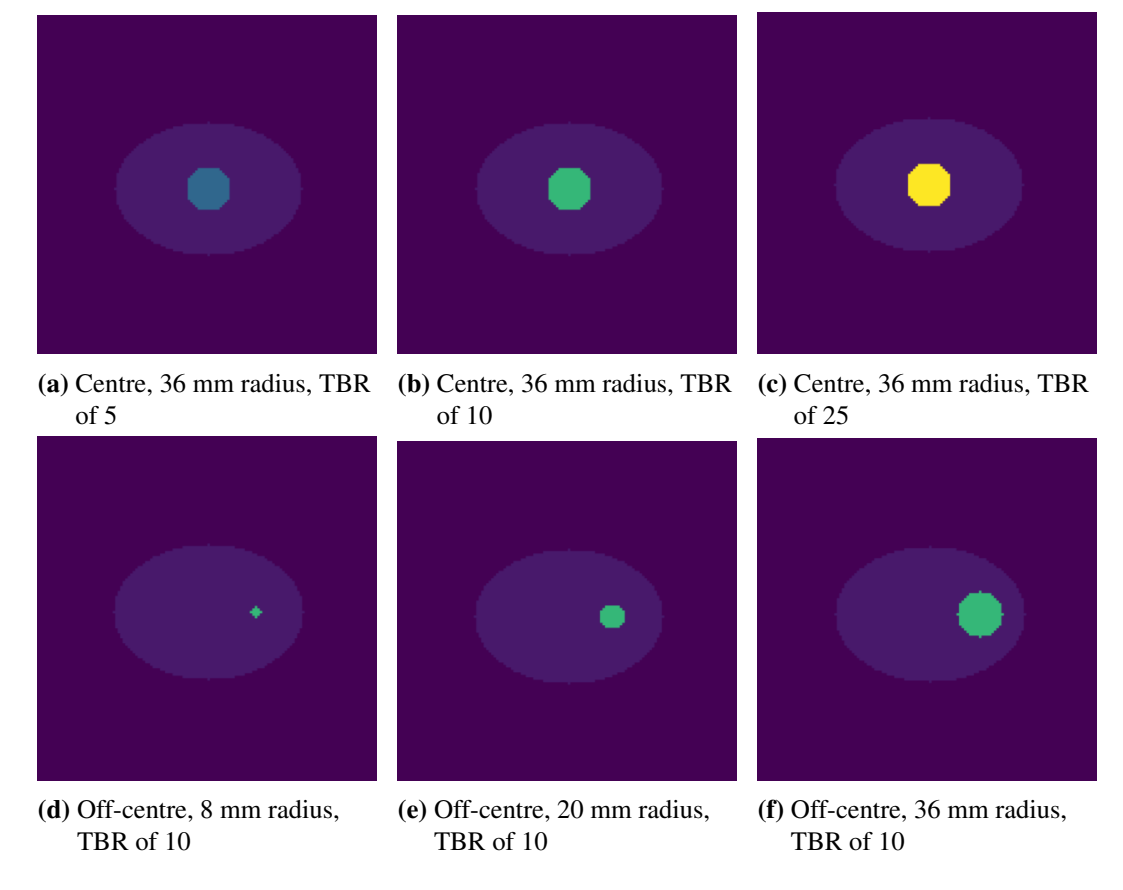


Figure 5.1: Images showing representative slices of the simple geometrical phantom, showing the two different lesion positions, the three different TBRs, and examples of the lesion radii used in this study.

Lesion Positions	Isocentre
	8 cm from isocentre
Lesion Radii	8 mm
	12 mm
	20 mm
	28 mm
	36 mm
Lesion TBRs	5
	10
	25

Table 5.1: A summary of different lesions examined using the uniform elliptical phantom

horizontal axis, as shown in Figure 5.2.

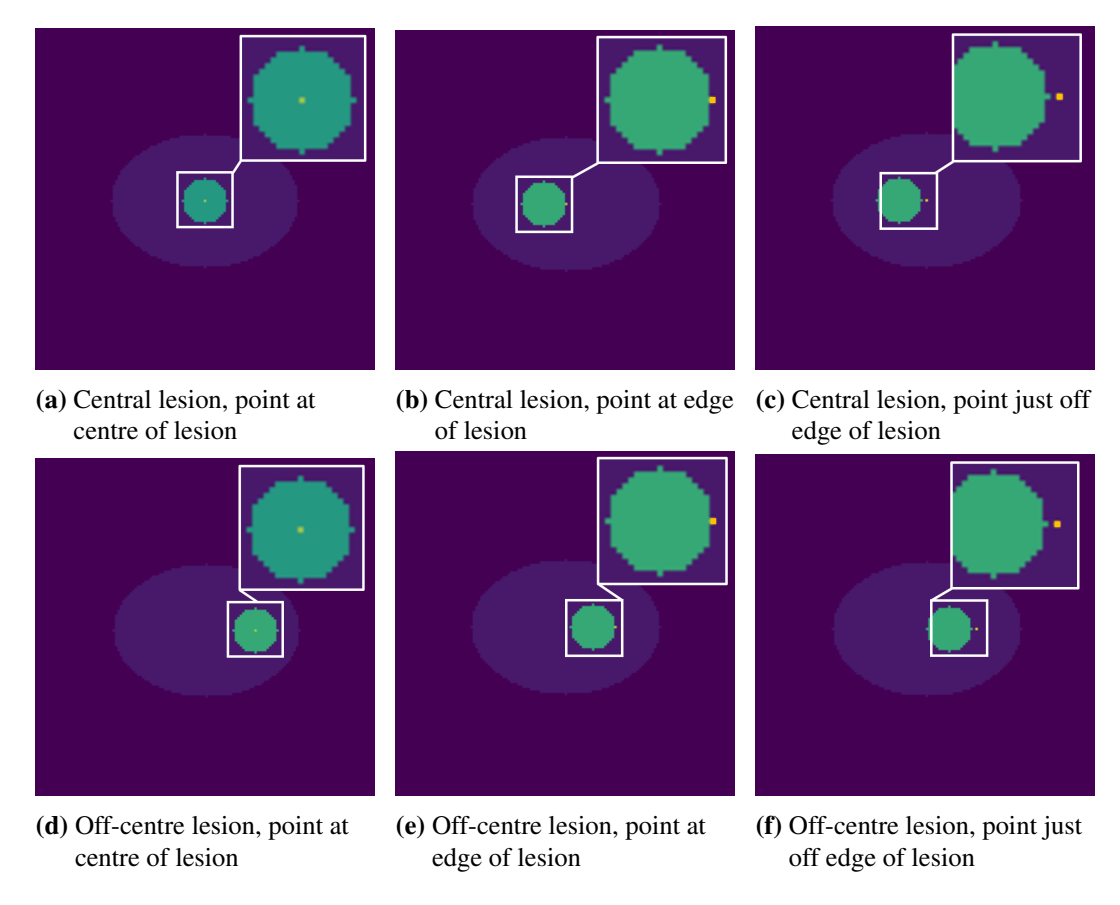


Figure 5.2: Images showing representative slices of the simple geometrical phantom, with points in different position relative to the lesion of interest.

The experimental set-up shown in Figure 5.2 is designed to decouple the effect of the measurement position in the FOV from the effect of the point position within a lesion. Measurements at the lesion centre (Figures 5.2 a) and d)) were compared with a point positioned at the edge voxel of the lesion (Figures 5.2 b) and e)), and a point positioned just outside of the lesion edge, 2 voxels (8 mm) away (Figures 5.2 c) and f)).

5.3.1.2 Anthropomorphic Phantoms

Parameters of the XCAT phantom were adjusted to generate digital phantoms which approximately replicated two common types of clinical ^{99m}Tc SPECT studies. The first phantom was designed with the appearance of a typical ^{99m}Tc phosphate scan for bone imaging. The other phantom was developed to replicate a ^{99m}Tc EDDA/HYNIC-TOC (Tektrotyd) scan used to assess neuroendocrine tumours

(more detail on Tektrotyd imaging is given in Section 3.4.5.6). XCAT phantoms were generated on 256×256 matrices with 2.2 mm^3 voxels. The rationale for using a matrix with smaller voxels for phantom generation than is used for image reconstruction was to attempt to reduce digitisation effects (which would not occur in a real clinical situation where the emission source, i.e. the patient, is not voxelised).

Bone scan XCAT Phantom

The activity distribution for the bone imaging scenario was generated with a small non-zero non-bone-specific background. The range of the generated bone scan phantom was from lumbar spine to the proximal end of the femoral shaft - including the pelvis. Datasets with and without activity in the bladder were generated. Spherical lesions with diameter of 15 mm were added in the right iliac fossa and the right femoral head. Example ground truth XCAT generated images of bone scans are shown in Figure 5.3. Lesion intensity was set to be five times as intense as normal bone, based on average measurements in normal bone and metastases from 5 clinical bone SPECT datasets.

Tektrotyd scan XCAT Phantom

The Tektrotyd case was generated with physiological uptake in the spleen, liver, bowel and urinary tract, including kidneys (relative organ intensities were within ranges observed in published data [Reilly et al., 2021]).

The range of the generated Tektrotyd scan was from mid thorax to bladder. Lesions with different characteristics were added within the liver. Lesions of uniform uptake, diameter 30 mm, with two different intensities relative to normal liver were investigated (TBR = 4, and TBR = 6.25). In the case of the TBR = 6.25 lesion, it is also notable that this is 20% more intense than spleen (the Krenning score, based on relative uptake in lesion, liver and spleen is described in Section 3.4.5.6). Example images of the two sets of XCAT generated Tektrotyd data, with the two different lesion intensities, are shown in Figure 5.4.

In addition to the uniform lesions, a lesion with non-uniform uptake pattern was generated to simulate a lesion with a necrotic core. The non-uniform lesion

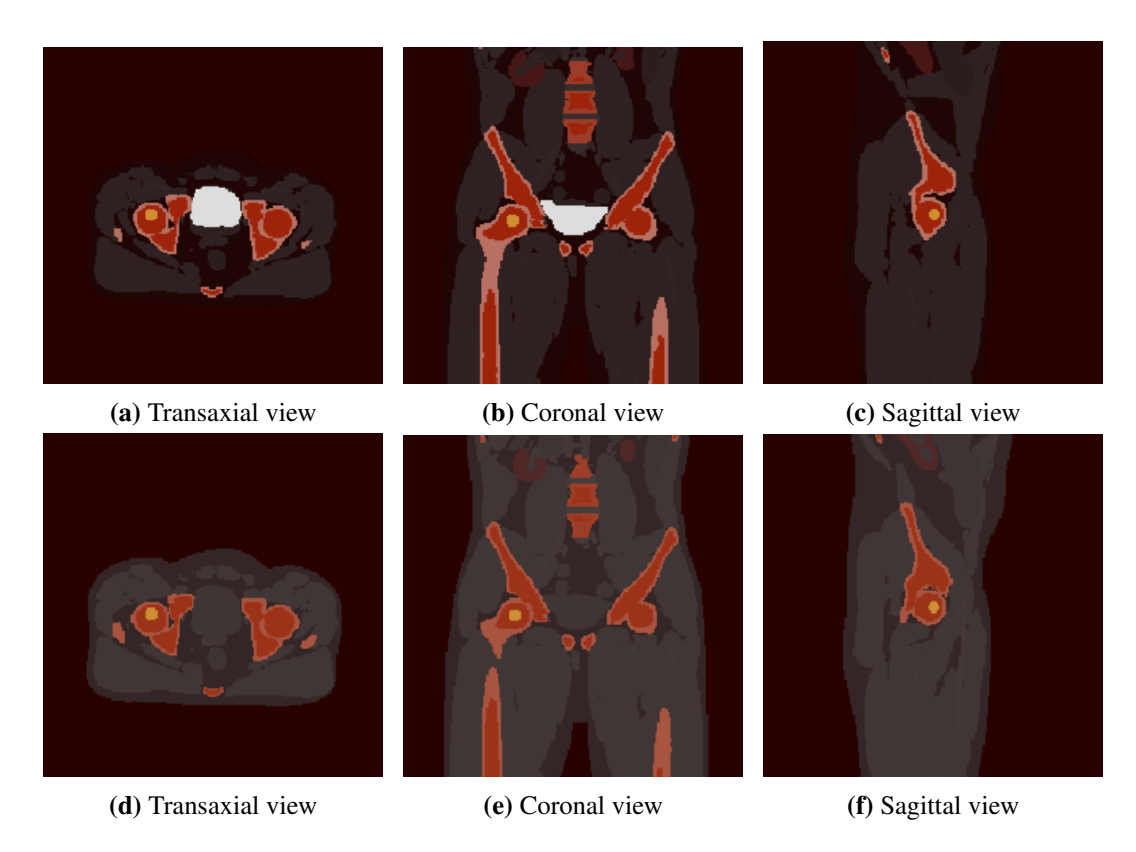


Figure 5.3: XCAT phantom (GT) showing activity distribution set up to represent a bone metastasis in the femoral head. The top row shows the dataset generated with activity within the bladder, the bottom row shows the dataset generated assuming an empty bladder. CT data generated with XCAT is shown overlayed with the activity data. A 'hot metal' colour scale is used where white corresponds to highest activity, through yellow, orange, red and black corresponding to lowest activity.

had an outer diameter of 44.4 mm, and an inner volume of lower intensity with diameter 22 mm. Example images showing the non-uniform lesion can be seen in Figure 5.5.

5.3.2 Simulation of Projection Data

STIR was used to forward project the generated phantom datasets described above, including the "full" model of attenuation and with 3D PSF modelling [Marti-Fuster et al., 2013a] (refer to Section 4.4.2 for description of attenuation model). The system model was designed to represent imaging of ^{99m}Tc using parameters based on the information available about LEHR collimators for a SPECT system (Anyscan Trio, Mediso, Laborcutca 3. H-1037 Budapest Hungary) (description of the system can be found in Section 4.4.2). Sinograms were generated without scatter or noise.

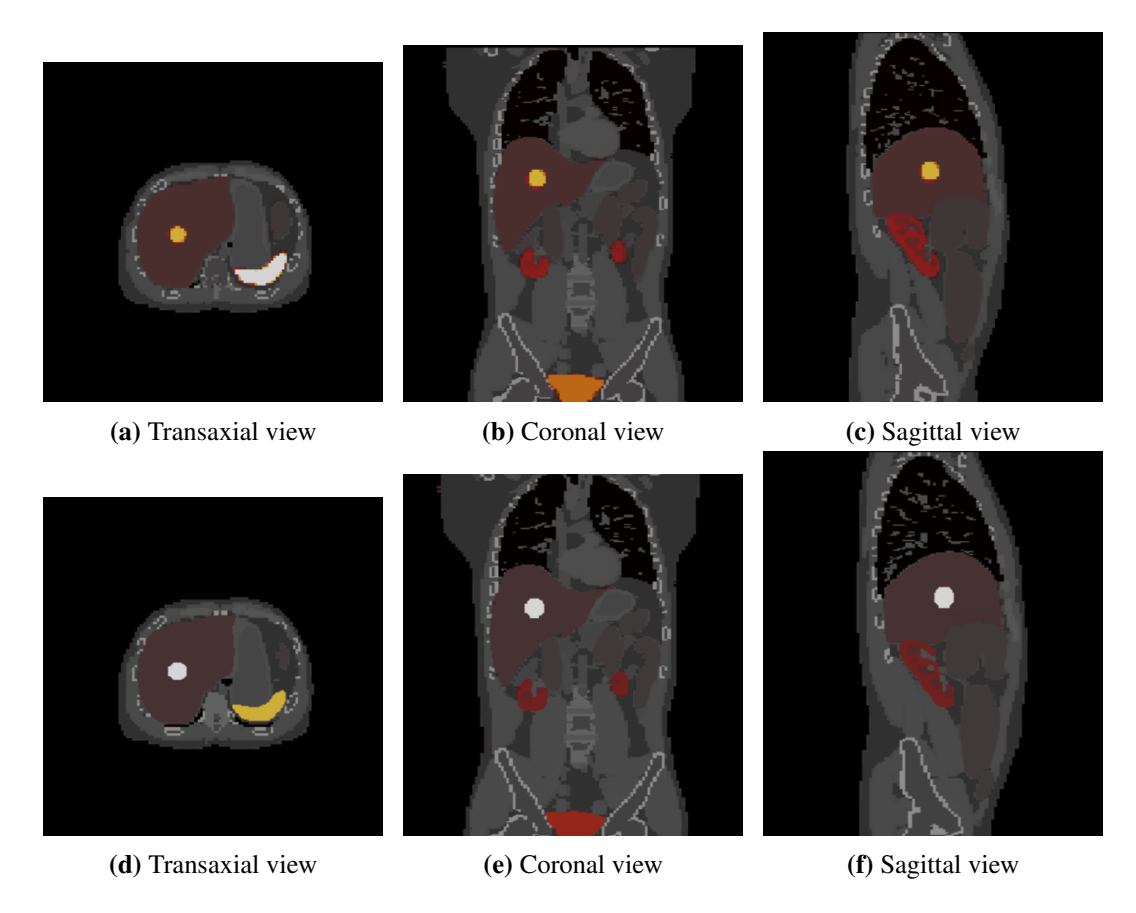


Figure 5.4: XCAT phantom (GT) showing activity distribution set up to represent a Tektrotyd scan with a uniform lesion in the liver. CT data generated with XCAT is shown overlayed with the activity data. The top row shows a lesion with TBR = 4 (Krenning score of 3). Lower row shows a lesion with TBR = 6.25 (Krenning score of 4). A 'hot metal' colour scale is used where white corresponds to highest activity, through yellow, orange, red and black corresponding to lowest activity.

Further to noise-free data, additional noisy datasets were produced with the use of a STIR utility to add Poisson noise.

Simulation of the forward projection was performed using an elliptical orbit (major axis radius = 250 mm, minor axis radius = 175 mm) with 120 projections onto a matrix of 128×128 isotropic pixels, 4.4 mm² in dimension. An elliptical orbit was used for anthropomorphic data in order to escalate the clinical realism from a circular orbit. An elliptical orbit is a step towards an orbit defined by contouring detector position for individual patients.

Total counts (i.e. the sum of all projections) in the simple phantom and bone scan datasets were set to approximately 5×10^6 . This is typical of total counts, and

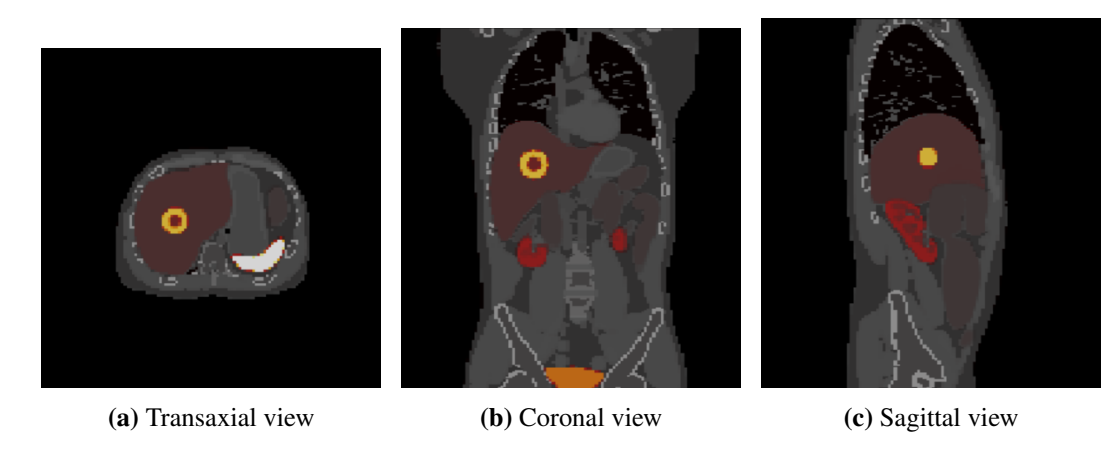


Figure 5.5: XCAT phantom (GT) showing activity distribution set up to represent a Tektrotyd scan with a necrotic lesion in the liver. CT data generated with XCAT is shown overlayed with the activity data. A 'hot metal' colour scale is used where white corresponds to highest activity, through yellow, orange, red and black corresponding to lowest activity.

therefore Poisson noise levels, seen in clinical SPECT bone scan imaging. Total counts for Tektrotyd imaging datasets were set to approximately 22×10^6 , again reflecting typical clinical studies. Typical count data of clinical studies was derived from an audit of patients at Glasgow Royal Infirmary (GRI) Nuclear Medicine department.

The components of the simple geometrical phantom (i.e. the background elliptical phantom, and a range of lesions of different positions and sizes) were forward projected separately and the resulting sinograms combined. Projecting as separate components allowed the sinograms of the lesion data to be scaled to achieve the different TBRs detailed in Table 5.1. Projection data using 120 projections were generated for the simple phantom based on a circular orbit with a radius of rotation of 26 cm and 120 projections. Projection data were produced using a matrix of 128 × 128 isotropic pixels, 4.0 mm² in dimension.

The generated XCAT phantoms and separate lesions were forward projected and the resulting sinograms combined as above.

5.3.3 Perturbation

Point sources, consisting of activity in a single voxel, were generated. Noise free sinograms of the point source were simulated using STIR in the same way as

the phantoms described above. These sinograms were then scaled such that the intensity of the reconstructed point source was less than 10 % of the intensity of the underlying voxel in the reconstructed image [Gong et al., 2016]. Reconstructions of the non-perturbed data were subtracted from reconstructions of the perturbed data to produce an image of the reconstructed PSF, indicating the situation-specific resolution. For the elliptical cylinder phantom, the perturbation points were positioned in two different positions in the FOV; the isocentre and 8 cm from the isocentre. In the anthropomorphic phantoms, the perturbation points were generated to match the position at the centre of each lesions.

5.3.4 Reconstruction

Reconstructions with and without the added perturbation point source were performed using identical parameters. Reconstruction was performed in STIR, using OSEM with 10 subsets and 20 iterations (200 updates in total). The "simple" attenuation model option in STIR was used in the reconstruction (refer to Section 4.4.2 for description of this model). This model of attenuation is not as accurate as the "full" model [Marti-Fuster et al., 2013a] used for simulating the sinogram data. This difference between simulation and reconstruction was designed to align with the reality of clinical situations where attenuation correction may be imperfect. Resolution Modelling was not applied in reconstruction due to the disadvantages such as ringing artefacts and increased variance discussed in Chapter 4.

5.3.5 PSF Characterisation

The reconstructions without the added point source were subtracted from the reconstructions of data with the added perturbation point source. 2D Gaussians were fitted to the resulting PSF in each orthogonal plane as described in Section 4.5.1.2. The method of fitting was advanced from the previous chapter, fixing the offset of the Gaussian to zero, as the subtracted data would always have zero background. Another development was made to the 2D Gaussian fitting, in order to allow for points which are positioned off-axis as the Gaussian would not be orthogonal to the horizontal axis. To account for rotation of the 2D Gaussian

from the horizontal axis an angle parameter, θ , was introduced into the Gaussian fit according to Equation 5.1:

$$f(x,y) = Ae^{-(a(x-x_o)^2 + 2b(x-x_o) \times (y-y_o) + c(y-y_o)^2)}$$
(5.1)

where A is the amplitude of the Gaussian peak, σ_x and σ_y indicate the standard deviations. The known centre point of the Gaussian was a fixed parameter (x_o, y_o) , as before. Parameters, incorporating the angular information θ , a,b and c are defined as:

$$a = \left(\frac{\cos^2(\theta)}{2\sigma_x^2}\right) + \left(\frac{\sin^2(\theta)}{2\sigma_y^2}\right) \tag{5.2}$$

$$b = \frac{-\sin(2\theta)}{4\sigma_x^2} + \frac{2\theta}{4\sigma_y^2} \tag{5.3}$$

$$c = \left(\frac{\sin^2(\theta)}{2\sigma_x^2}\right) + \left(\frac{\cos^2(\theta)}{2\sigma_y^2}\right) \tag{5.4}$$

The value of θ was calculated based on the geometry of the known position of the point within the image, and fixed to that value for fitting ($\theta = 0$ for points on the axes). This was checked visually by reviewing contour lines and fitted profiles, as in the example shown in Figure 5.6. FWHM values for the radial, tangential and axial directions were calculated based on the average of values from two planes.

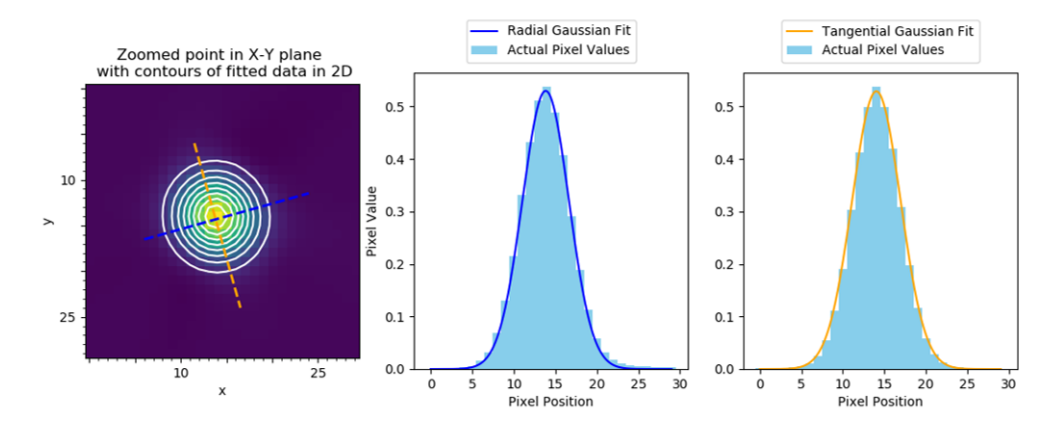


Figure 5.6: 2D Gaussians were reviewed with contour lines in order to allow a visual check of fit, including the theta parameter

The FWHM values measured in different imaging situations were compared to examine dependence on parameters including reconstruction iteration (specifically whether PSF changes between sequential update images were smooth or unpredictable), lesion size and TBR, position in FOV, and surrounding activity distribution.

5.3.6 Assessment of PSF Accuracy

An assessment of the accuracy of the perturbation-estimated PSF, independent of any effects due to the PVC algorithm used, was required. This was done by comparing reconstructed noise-free images to images generated by convolving the input GT data with a 3D Gaussian. Two different Gaussians were used for convolution; the first was equivalent to the perturbation-estimated PSF, the second represented a PSF as measured from the centre of the FOV. The analysis process is summarised in Figure 5.7.

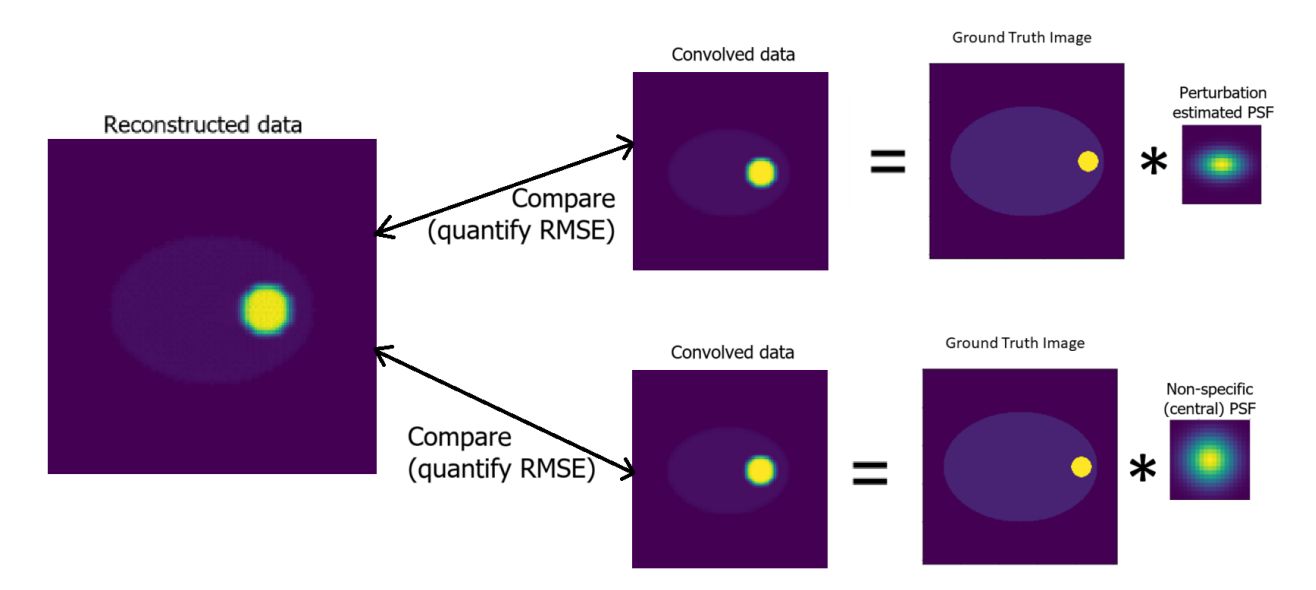


Figure 5.7: Diagram visualising the process used to assess the accuracy of the perturbation estimated PSF.

It is expected that the GT data convolved with the perturbation estimated PSF would more accurately match the reconstructed data than the GT convolved with the PSF measured at the centre of the FOV, provided that the perturbation-estimated PSF is an accurate estimate of the case-specific and position specific resolution. To

quantify how well the two convolved images matched the reconstructed image, the Relative Root Mean Square Error (RRMSE) (%) was calculated over a local volume around the lesion as follows:

RRMSE =
$$\frac{\sqrt{\frac{1}{N}\sum_{i=1}^{N}(R_i - C_i)^2}}{\mu_{GT}} \times 100\%$$
 (5.5)

where N is the number of voxels in the local volume, R_i is the voxel value at position i in the reconstructed image, C_i is the voxel value at position i in an image of the GT convolved with the perturbation-estimated PSF, and μ_{GT} is the mean value of the local volume of the GT image. The RRMSE was also calculated for reconstructed images compared with the GT convolved with a non case-specific PSF. For this work, the non-specific PSF used was one measured at the centre of the FOV. This non-specific PSF was chosen since this may be the only position where the PSF is measured in practice. The RRMSE was calculated for images saved every 10 OSEM updates (between 10 and 200 updates).

5.3.7 Partial Volume Correction with STC

PVC was applied to the reconstructed datasets using the Single Target Correction (STC) method, described fully in Section 3.4.3.2. STC applies a Partial Volume correction, incorporating both spill-in and spill-out, to a single object and allows for non-uniformity within the target object. This method was used as it utilises information regarding the resolution, which can be estimated using perturbation. In addition, it was assessed to be one of the methods which could potentially be suitable for application in oncology (see Section 3.4.5.1).

In this work, STC was applied by segmenting the lesion based on the generated image. Ten STC iterations were used and a non-negativity constraint was imposed. The application of STC was tested in this work using a range of STC iterations for both the simple phantom and the XCAT phantom. A sufficient number of iterations in both cases was found to be 10, in agreement with previous work [Sari et al., 2017].

158

Regional Mean Values (RMVs) of the lesion before and after PVC were assessed. The RMV was calculated as the mean over all voxels within the known volume of the lesion (as determined from the GT data). PVC was performed with STC using the perturbation-estimated PSF. PVC was also performed with STC using the non-specific PSF, as described above, in order to study the effect of PSF on quantification.

Application of PVC to XCAT data involved first resampling the emission image (128×128 voxels) to match the Ground Truth image (256×256 voxels), prior to PSF estimation, and before segmentation.

5.4 Results

5.4.1 PSF estimation with perturbation

5.4.1.1 PSF variation with reconstruction update and position in FOV

As expected based on simulations with point sources presented in Chapter 4, perturbation estimated FWHM values depended on the direction of measurement (radial, tangential or axial) and depended on the location of measurement point in the FOV. Figure 5.8 shows the perturbation based FWHM measurements in each direction varying with number of reconstruction update, for noisy and noise-free data. These measurements were made in the simple geometrical phantom using a point source positioned centrally within a 36 mm radius lesion. The lesion was positioned at two different positions in the FOV. The results for the lesion at the centre of the FOV (as per Figure 5.2 a)) are shown in graphs in Figures 5.8a) and 5.8c). The results for the lesion 8 cm away from the isocentre, along the horizontal axis (as per Figure 5.2 d)) are shown in graphs in Figures 5.8b) and 5.8d).

At 200 updates, the perturbation-estimated FWHM values in each direction depend on the position of measurement in the FOV. In addition, the PSF measured at the central point is roughly isotropic as the radial, tangential and axial FWHM

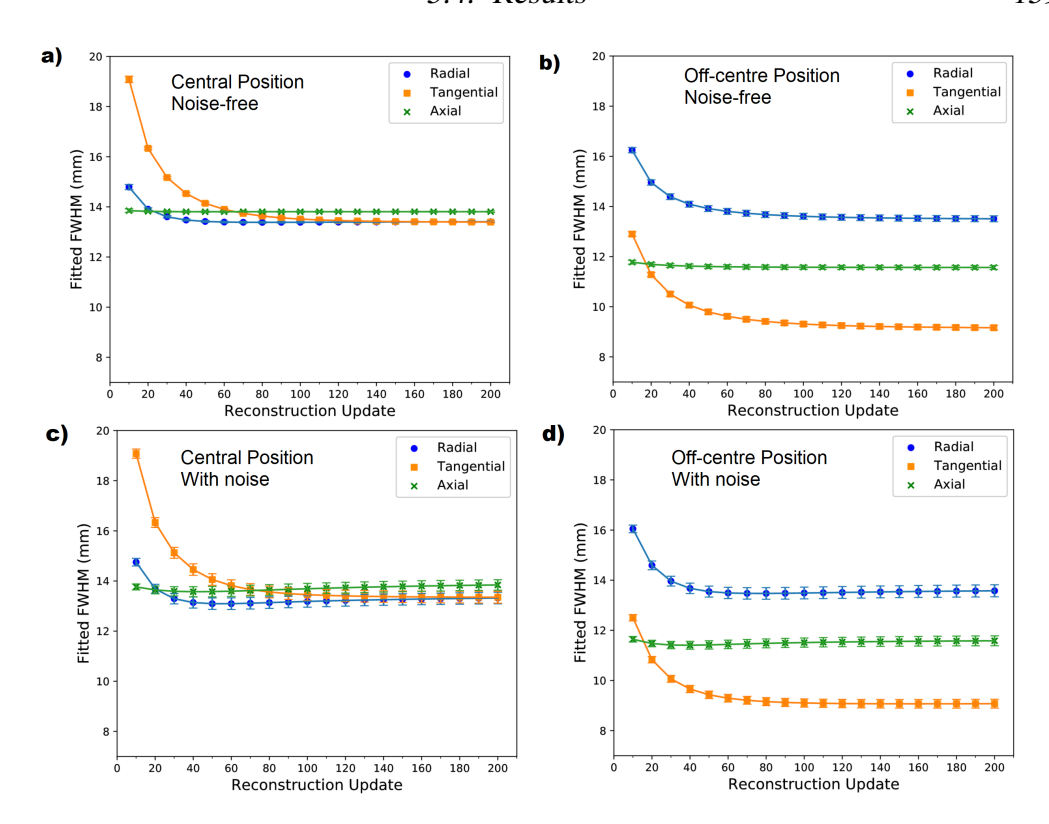


Figure 5.8: FWHM measurements in each direction vs reconstruction update number (10 updates = 1 full iteration) measured in a) central lesion without noise, b) offcentre lesion without noise, c) central lesion with noise and d) off-centre lesion with noise. The perturbation point was positioned in the centre of a 36 mm radius lesion and the lesion TBR was 10 in all cases shown. Error bars relate to the standard deviation in the fitted FWHM parameters but are too small to be seen clearly on noise-free data.

values are within 3 % of 13.4 mm in both noisy and noise-free data (note that this is close to the finding in Section 4.5.2.1 that FWHM is isotropic in the central position to within 3% of 13.6 mm)). The PSF at the off-centre position is anisotropic; the radial FWHM is 13.51 ± 0.11 mm, the axial is 11.57 ± 0.08 mm, and the tangential is 9.16 ± 0.09 mm at 200 updates for noise-free data. Measurements from noisy images of the off-centre point at 200 iterations agree to within 1% of noise-free FWHM values, and within 1 Standard Deviation (SD) of the noise-free FWHM measurements in each direction (where the SD is calculated from the fitting of Gaussian used to characterise the FWHM, as described in Section 4.5.1.2).

5.4.1.2 PSF variation with lesion contrast and size

Figure 5.9 demonstrates how lesion contrast (chart a) and lesion size (chart b) affect the perturbation-estimated tangential FWHM measurements, depending on reconstruction update. These measurements were made for noise-free data in the simple elliptical phantom (shown in Figure 5.2 d)). Tangential FWHM values are presented here. Radial FWHM values demonstrate a similar pattern, and Axial FWHM values are consistent to within 1% regardless of number of iterations, TBR or lesion size.

The perturbation-estimated tangential FWHM depends on the TBR of the lesion, i.e. differences are noted between measurements made at TBRs of 5, 10 and 25, but only for images reconstructed using less than 100 OSEM updates. This is also true for different lesion sizes (radii of 8, 20, and 36 mm were tested). For images reconstructed with 100 or more updates, the FWHM measurements were consistent to within 2.0 % for different lesion sizes and contrasts in noise free data, for measurements made at the same position in the FOV at 200 updates.

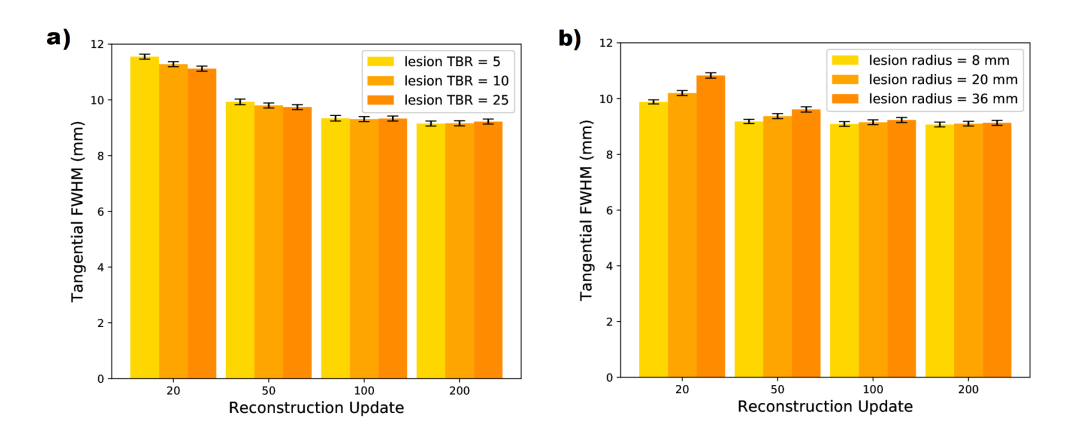


Figure 5.9: Graphs demonstrating the effect of lesion parameters of a) lesion contrast and b) lesion size on tangential FWHM measurements for selected reconstruction updates in noise-free images of the simple elliptical phantom. The point of measurement was in a lesion, 8 cm from the centre of the FOV. When varying the lesion TBR, the radius was set to 36 mm. When varying the lesion radius, the TBR was set to 10.

In noise-free data, for 20 updates, the tangential FWHM measurement was found to vary from 11.12 ± 0.09 to 11.55 ± 0.09 mm depending on the lesion TBR. Comparing TBR = 10 to the TBR = 5 and the TBR = 25 data demonstrates

differences of greater than 2 SDs. Beyond 100 updates, the tangential FWHM measurement was within 1 SD of 9.3 mm for all lesion contrasts. For 200 updates the tangential FWHM was within 1 SD of 9.2 mm for all lesion contrasts.

For noisy data, measuring the tangential FWHM in images with a lesion TBR of 5 was found to be within 2 SD of TBR = 10 and TBR = 25 measurements for low reconstruction updates. This difference was greater than 2 SD above around 100 reconstruction updates. This is shown in Figure 5.10. This may be due to higher Poisson noise due to lower counts in the lesion with TBR = 5 (the background was constant between all image datasets).

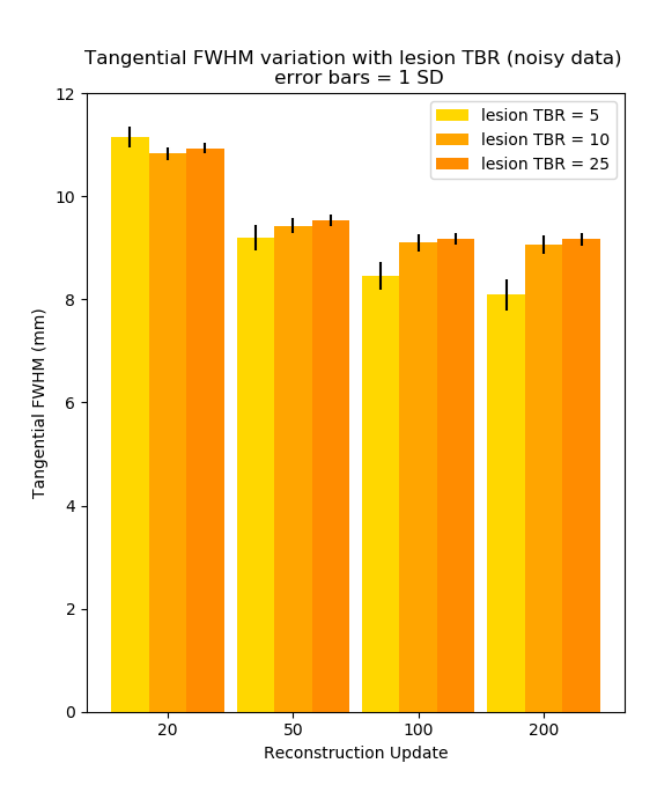


Figure 5.10: Graphs demonstrating the effect of lesion contrast on tangential FWHM measurements for selected reconstruction updates in noisy images of the simple elliptical phantom. The point of measurement was in a 36 mm radius lesion, 8 cm from the centre of the FOV.

Noise-free data demonstrated increased variability in FWHM for different lesion sizes when measurements were made in images reconstructed with fewer updates. Measurements made in images reconstructed with 100 updates, or more, were all within 1 SD of each other.

5.4.1.3 Effect of Point Position Within a Lesion on PSF measurement

The effect of point position within a lesion was studied in the simple geometrical phantom, with point positions shown in Figure 5.2. Noise-free FWHM measurements are shown in Figure 5.11. These results show that the tangential FWHM measurements differed for different point positions relative to the lesion centre. Compared with the point at the centre, the point at the edge of the lesion had comparatively higher tangential FWHM values at early iterations (below about 100 updates), but by 200 updates, the values agreed well. However, for the point outside the lesion edge the tangential FWHM was still higher than the measurement made at the centre of the lesion for all image updates. Adding noise to these images resulted in increased uncertainty in the PSF fitting, resulting in larger errors, but no significant change in FWHM values. While the effect of point position was studied only for a single lesion size and TBR, the results are expected to be representative, provided that the intensity of the perturbation point is chosen appropriately.

5.4.1.4 PSF variation with surrounding activity distribution

The simple geometrical phantom, used as the background activity distribution for perturbation-estimated PSF results above, is useful for demonstrating the effect of varying different parameters such as reconstruction settings and lesion characteristics. However, this simple phantom is not a good approximation of real clinical data. The surrounding activity distribution will impact convergence. Therefore, PSF measurements in anthropomorphic datasets such as those in Figures 5.3, 5.4, and 5.5 are a step towards investigating perturbation estimated PSF in a realistic clinical activity distribution.

Comparing perturbation estimated FWHM values at 200 updates in Figures 5.12 and Figures 5.8 a) and c) demonstrated that absolute FWHM values measured in the anthropomorphic datasets in each direction are all smaller than those measured at the central position in the simple geometrical phantom set-up.

This superior resolution can be explained by the closer proximity to the simulated detector face due to the lesion position being further from the centre of the FOV and due to the non-circular orbit which enables detectors to be positioned



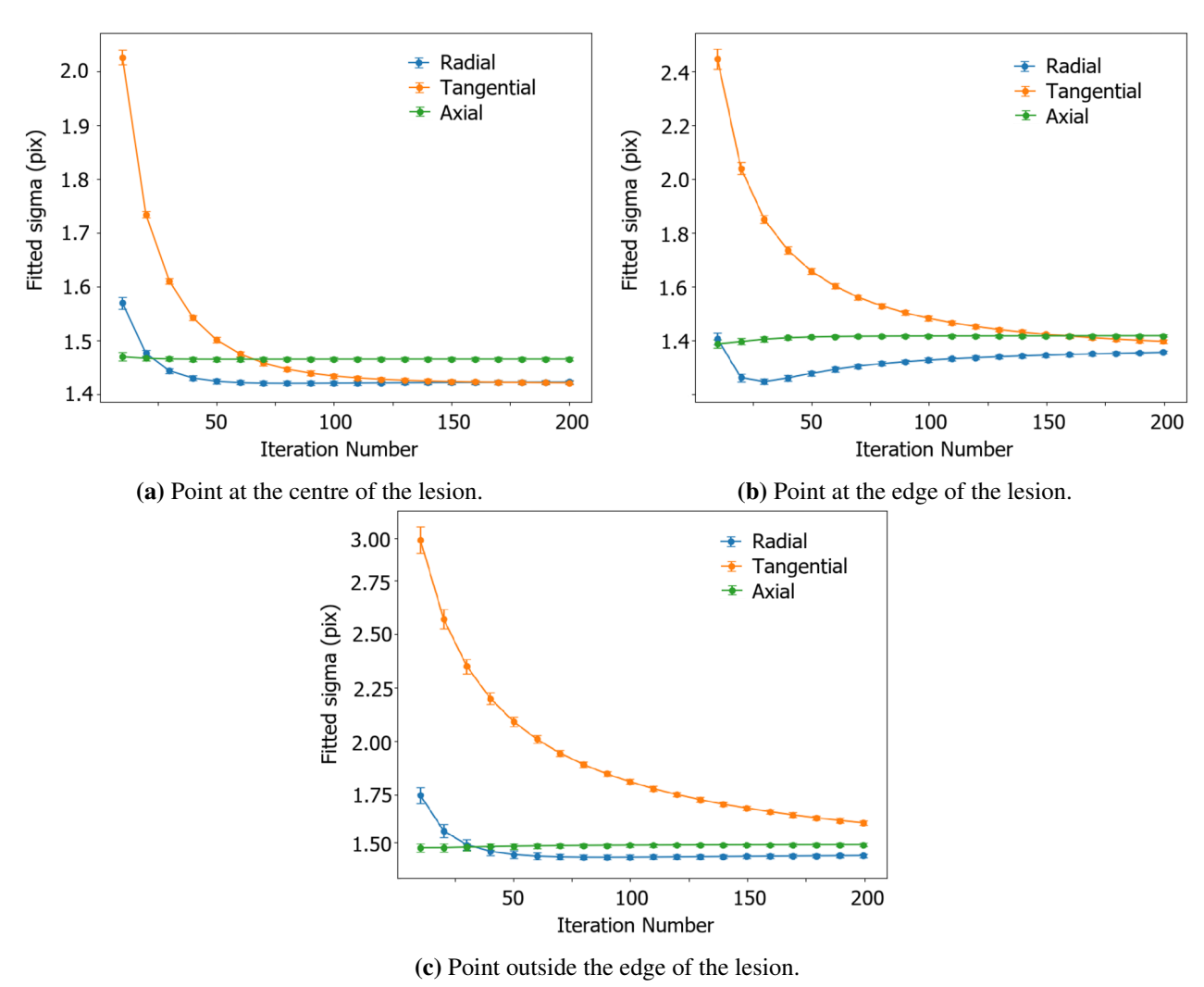


Figure 5.11: Plots show FWHM measurements vs reconstruction update number (10 updates = 1 full iteration) from noise-free data, where the perturbation point was positioned centrally in the FOV, but at different positions relative to the centre of a 36mm radius lesion (lesion TBR = 10) as shown in Figure 5.2 (a) - (c).

closer to the surface of the object being imaged. Adding Poisson noise had only a very small effect on the measured FWHM values.

A dependence on the number of reconstruction updates used in the image was observed - in particular for the Tektrotyd activity distribution dataset. FWHM results are shown in Figure 5.12.

This dependence on update number had also been observed for measurements made in the simple dataset. A difference between the simple and anthropomorphic activity distributions is that a relatively constant FWHM value is reached at a lower

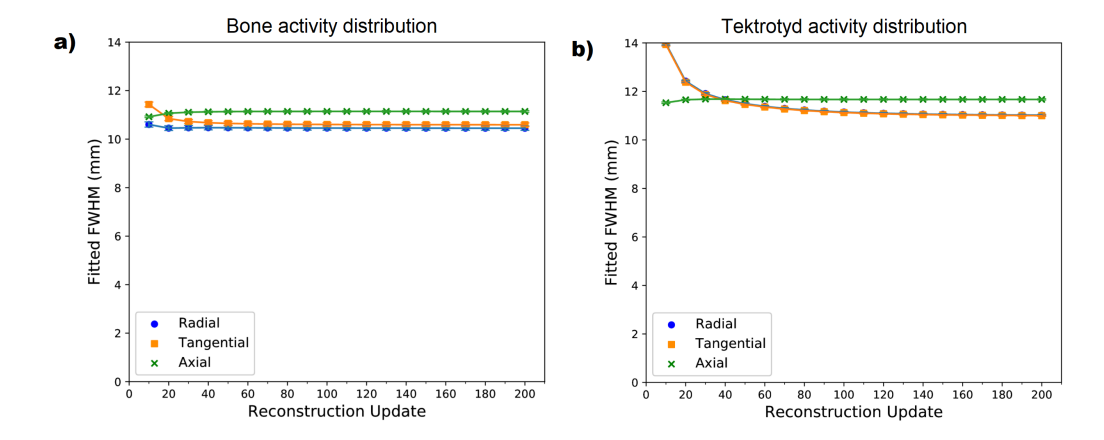


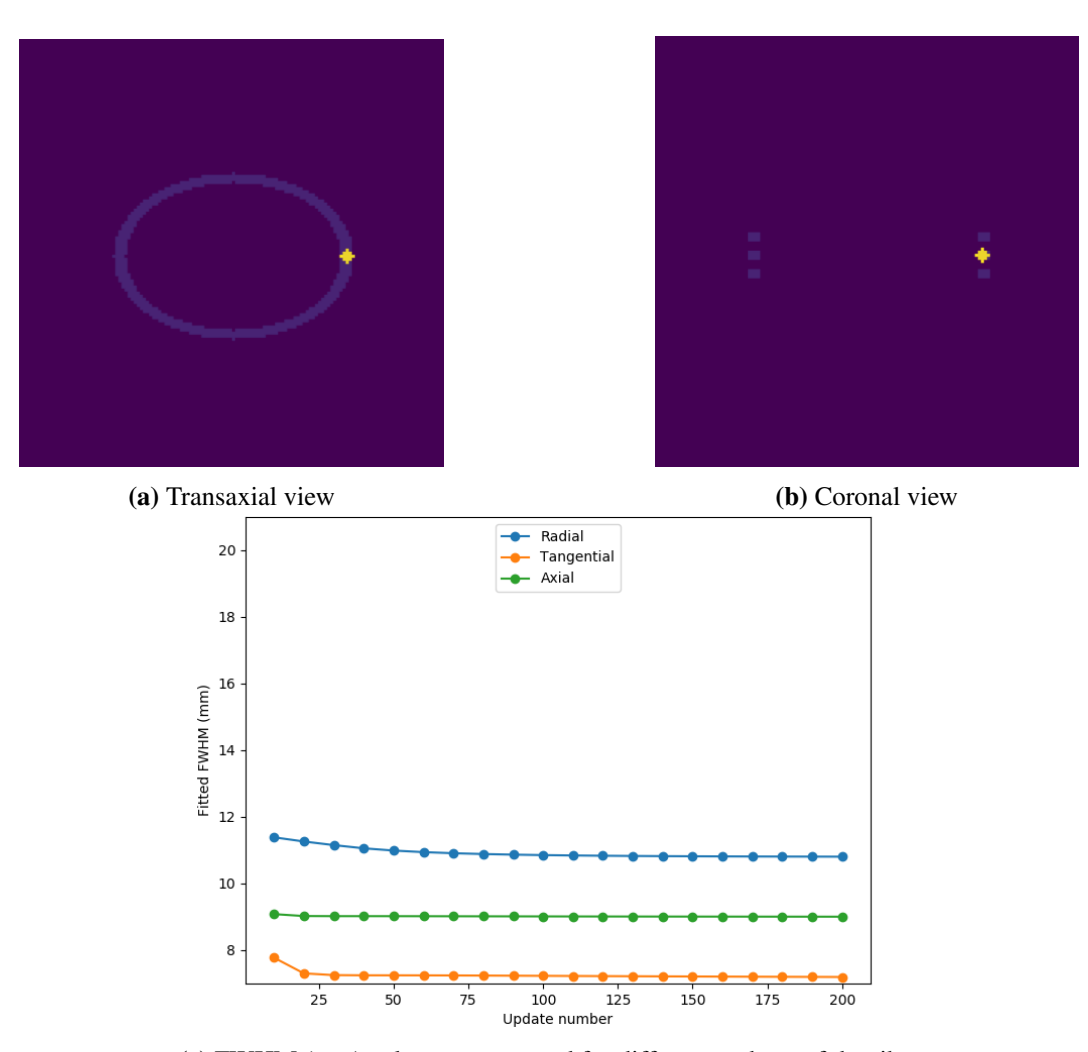
Figure 5.12: FWHM measurements in each direction vs reconstruction update number as measured in uniform lesions within anthropomorphic phantoms for noise-free data in an XCAT activity distribution simulating a) a bone scan and b) a Tektrotyd scan. The perturbation point was positioned in the centre of each spherical lesion. The bone scan lesion was positioned within the femoral head, adjacent to the bladder, and the Tektrotyd lesion was positioned within normal liver.

number of updates in the anthropomorphic phantoms compared with what was observed for the simple phantom - this can be seen by comparing data in Figure 5.12 with the plots in Figure 5.8.

PSF variation with reconstruction update number was observed to be reduced for the anthropomorphic phantoms when compared with the simple cylinder phantom. A possible explanation for this difference in behaviour is the difference in surrounding activity distribution. The lesions of interest within the anthropomorphic phantoms, in particular the XCAT bone phantom lesion, are surrounded by more low activity voxels compared with the simple phantom lesion. An additional contribution may be the relative magnitudes of the FWHM values which are lower in the anthropomorphic phantom cases.

This was explored further by simulating a lesion within a uniform ring, with the same external dimensions as the standard simple phantom (see e.g. Figure 5.1), but with the inner volume voxel values set to zero - shown in Figure 5.13. This gives a sparser activity distribution compared with the standard simple phantom. This design results in an activity distribution similar to a bone scan (of eg. thorax area), but with an external shape and size identical to the simple geometrical phantom.

5.4. Results 165



 $\mbox{(c)}$ FWHM (mm) values as measured for different updates of the ribslike phantom

Figure 5.13: Ribs-like phantom used to assess the effect of orbit and activity distribution on convergence behaviour (shown in the graph in (c)).

Simulation was performed using a circular orbit, in order to match the acquisition simulated for the standard simple phantom. However, in the phantom shown in Figure 5.13a, the lesion was positioned further from the centre of the FOV (resulting in improved resolution). The variation of FWHM with update number demonstrated relatively unchanging values at an earlier update number compared with the standard simple phantom. Since both were acquired with a circular orbit, this supports the hypothesis that the difference in convergence observed is likely due to the surrounding activity distribution and/or the size of the PSF, rather than the detector orbit.

Activity within bladder

A variation in activity distribution that can commonly be seen between sequential scans is the presence or lack of activity within the bladder. This is most often seen in clinical bone scan studies, in particular for prostate cancer staging. The effect of this on PSF measurement using perturbation was examined by comparing XCAT bone scan data with and without activity in the bladder. Input images are shown in Figure 5.3 where (a) - (c) shows activity within the bladder and (d) to (f) shows no activity within the bladder. Figure 5.14 shows FWHM values for activity within the bladder, which can be compared to Figure 5.12 a) showing FWHM for no bladder activity. In the case of the full bladder, the bladder activity was set to 15 times that of normal bone. Comparing these data to the zero activity bladder results shows a difference of less than 1.7 % between FWHM values for images reconstructed with more than 50 updates. Images reconstructed with fewer updates demonstrated up to 6.4 % difference in measured FWHM value between the empty bladder and full bladder activity distributions

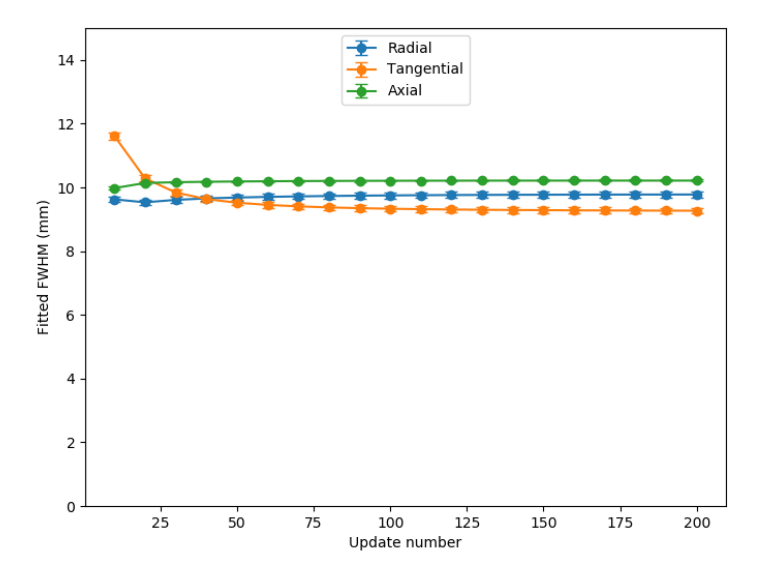


Figure 5.14: FWHM measurements in each direction vs reconstruction update number as measured in the femoral head lesion of the bone scan, with high activity within the bladder.

Overall the results in this section demonstrate that the perturbation-estimated PSF is not significantly affected by high activity structures nearby, as long as sufficient updates are performed in the reconstruction.

5.4.1.5 Checking accuracy of perturbation-estimated PSF

The accuracy of the perturbation-estimated PSF data was assessed by evaluating the difference between reconstructed images and ground truth images convolved with a PSF, as described in Section 5.3.6.

As shown in Figure 5.15, a consistently lower RRMSE was demonstrated when convolution was performed using the perturbation-estimated PSF, compared with convolution using a non-specific PSF for the simple geometrical phantom. This was the case for all images except those reconstructed with fewer than 20 updates. The RRMSE assessment was performed for a range of lesion diameters and lesion contrasts. Figure 5.15 shows a subset of situations tested.

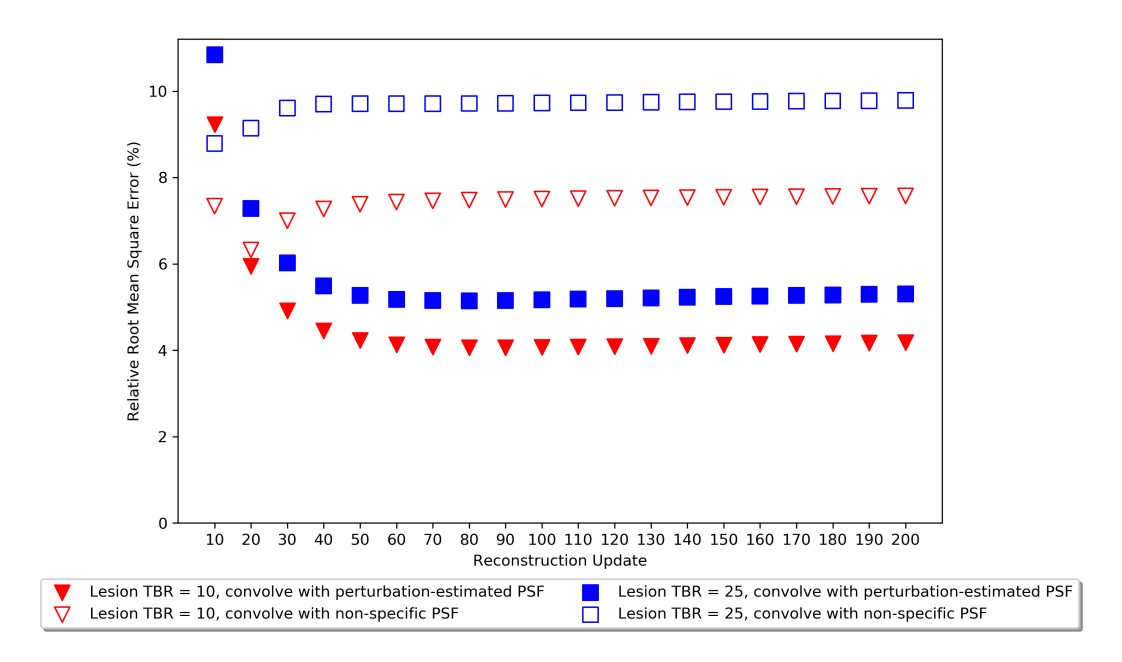


Figure 5.15: RRMSE results for the 36 mm radius lesion, positioned 8 cm from the isocentre in the noise-free simple phantom. Results are shown for two different contrast settings, for perturbation-estimated PSF and a non-specific PSF

5.4.2 PVC Results

5.4.2.1 Simple Phantom

The lesion Regional Mean Values (RMVs) were found to be closer to the GT when PVC with the STC algorithm was applied using a perturbation-estimated PSF, compared with uncorrected data. This was the case for all reconstruction updates,

for all lesion sizes, positions and lesion TBRs examined.

Figure 5.16 a) shows corrected and uncorrected regional mean values, compared with Ground Truth (GT), for a 36 mm radius lesion (TBR=10) positioned at the centre of the FOV for different numbers of reconstruction updates. Noisy and noise-free RMVs measured in uncorrected images were very similar, as expected. Uncorrected RMVs underestimated the GT by between 17 % and 23 %. PVC corrected noise-free images, using a perturbation-estimated PSF, result in RMVs within 0.7 % of ground truth in images reconstructed with more than 40 updates (within 0.4 % for more than 100 updates). For noisy data, some reduction in accuracy is seen compared with corrected noise free data. However, corrected noisy RMVs are closer to the GT than uncorrected data (within 2.8 % of Ground Truth for images reconstructed with more than 20 updates).

Figure 5.16 b) demonstrates the deviation of the RMV from GT before and after applying PVC with STC for a range of lesion sizes within the simple phantom. Results are shown for noise-free images reconstructed with 200 updates, for offcentre lesions with TBR=10. Uncorrected data demonstrated underestimation of the RMV by between 19.4 % and 58.0 % compared with the GT. The largest deviation from ground truth was observed for the smallest lesion - as expected since smaller lesions are more affected by the PVE. Following the application of STC with the perturbation-estimated PSF, the corrected RMV agreed with the ground truth to within 3.6 % for all lesion sizes. The residual post-correction bias was lower for larger lesions compared with the smallest lesions investigated. RMVs following the application of STC using a non-specific PSF were also calculated. In this case (where the lesions were positioned off-centre), the non-specific PSF used was one measured at the centre of the FOV. The non-specific PSF used was wider than the perturbation-estimated PSF, and was therefore expected to over-correct the RMV. STC using this non-specific PSF overestimated the RMV compared with the ground truth by between 10.4 % to 63.0 %. The largest overestimation was observed for the smallest lesion.

Example post-STC images are shown in Figure 5.17c) and f) demonstrating

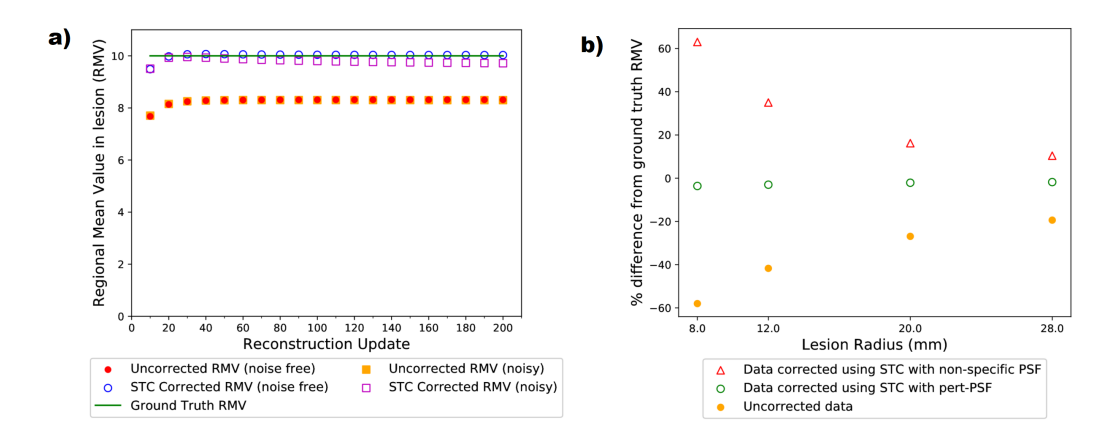


Figure 5.16: a) Regional mean values (RMVs) measured for a lesion in the simple cylindrical phantom with 36 mm radius, TBR = 10, positioned centrally in FOV, for different image reconstruction update numbers. Note that the uncorrected noise-free and noisy datasets overlay each other. b) Deviation in RMV from ground truth (in %) following STC with perturbation-estimated PSF or the non-specific PSF, for off-centre lesions and a range of lesion sizes. All lesions had TBR=10, and all images used 200 reconstruction updates.

that STC produces images with improved edge definition around the lesion of interest.

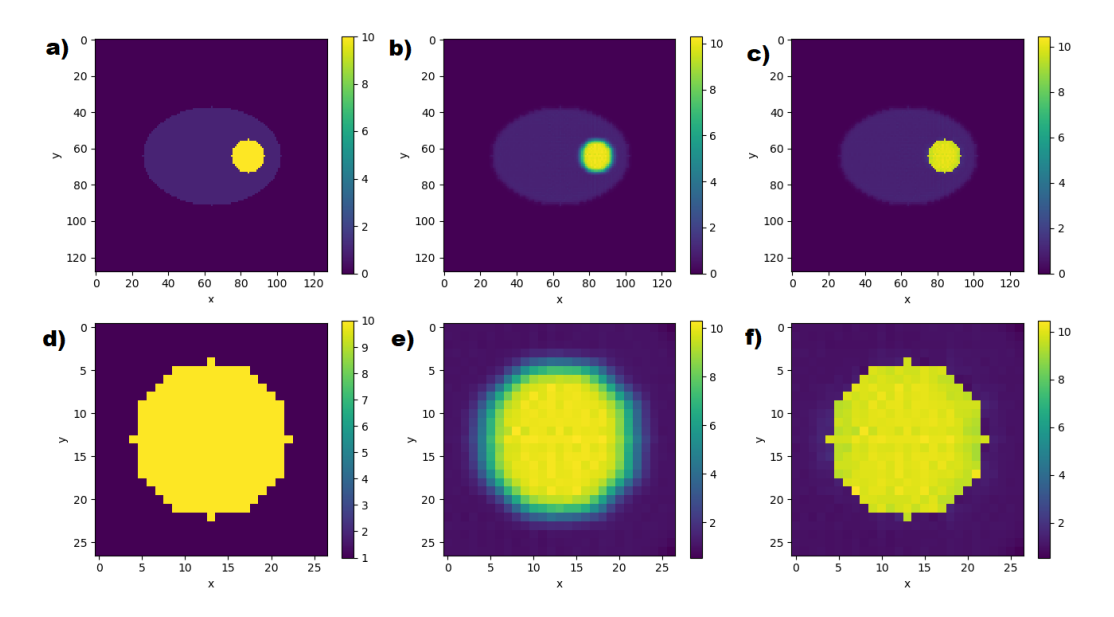


Figure 5.17: a) - c) from left to right; ground truth, uncorrected and corrected images, in the transaxial plane, through the centre of a 36 mm radius lesion within the the simple phantom using noise-free data. d) - f) from left to right; local region around the lesion, zoomed in, on ground truth, uncorrected and corrected data.

5.4.2.2 Anthropomorphic Phantoms

Images of uncorrected and corrected transaxial slices through the centre of lesions in different positions within XCAT anthropomorphic phantoms are shown in Figures 5.18, 5.19 and 5.20.

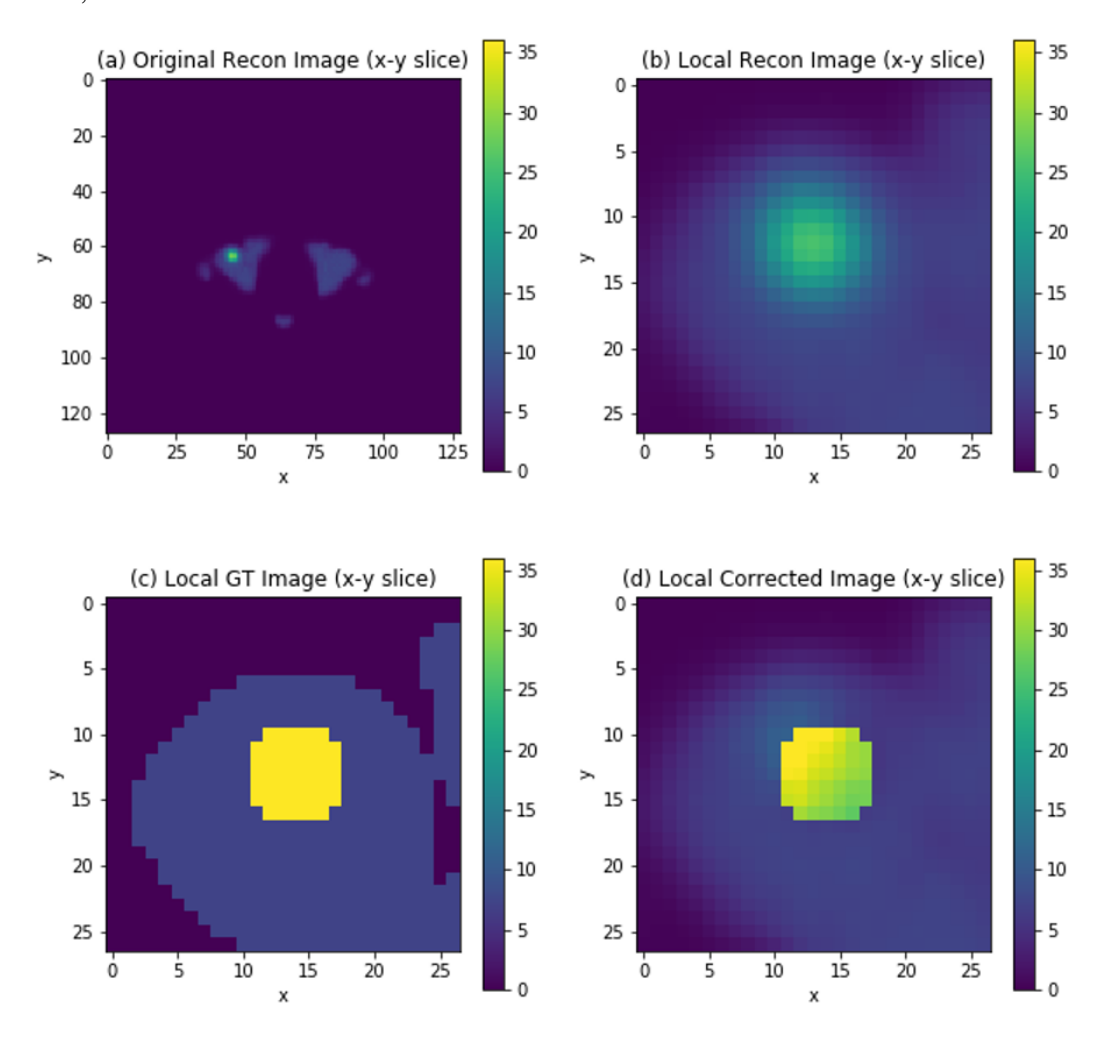


Figure 5.18: Noise-free images, in the transaxial plane, of the XCAT bone scan phantom dataset. (a) is the uncorrected image reconstructed with 200 updates, (b) is the local region around the lesion in the uncorrected image, (c) is the local region around the lesion GT data (used for segmentation), and (d) is the post-PVC images after correction with 10 STC iterations.

As seen in the simple phantom, STC correction improves the edge definition, and also the quantitative accuracy for the XCAT lesions.

For the bone lesion shown in Figure 5.18, the uncorrected RMV underestimates the GT value by between 47.7 % and 50.6 %, depending on the reconstruction update number. Applying PVC using the perturbation-estimated PSF and 10 STC

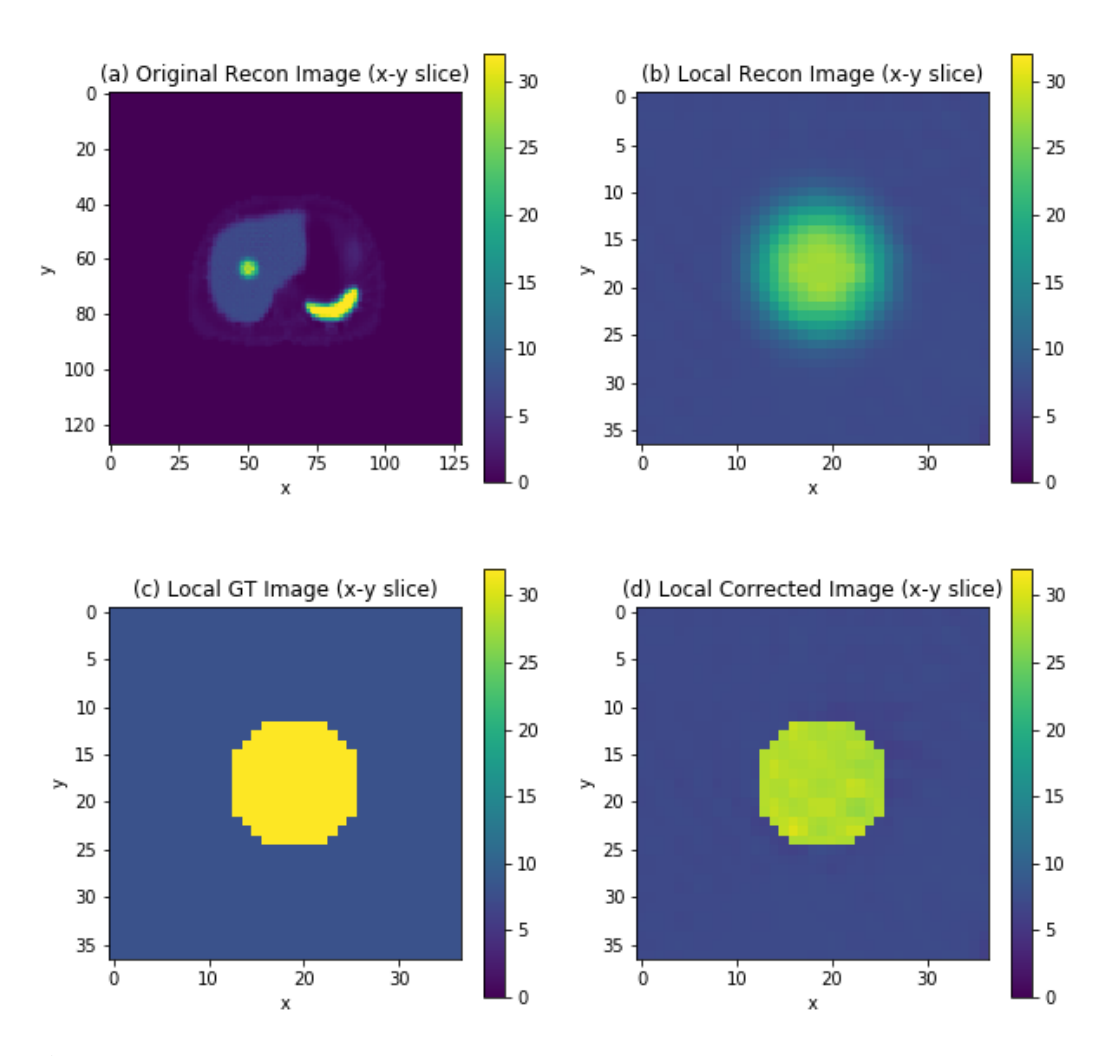


Figure 5.19: Noise-free images, in the transaxial plane, of the uniform lesion in the liver of the XCAT Tektrotyd scan phantom datasets. (a) is the uncorrected image reconstructed with 200 updates, (b) is the local region around the lesion in the uncorrected image, (c) is the local region around the lesion GT data (used for segmentation) and (d) is the post-PVC images after correction with 10 STC iterations.

updates resulted in corrected RMV within 1.6 % of the ground truth for images reconstructed with more than 100 reconstruction updates. Applying PVC using a non-specific PSF resulted in an overestimation of the lesion RMV of up to 61.1 % more than the GT.

For the uniform Tektrotyd liver lesion shown in Figure 5.19, the RMV measured from the uncorrected image underestimates the true value by between 26.6 % and 35.6 %, depending on the reconstruction update number. For noisy data the true value was underestimated by 26.8 % - 36.5 % Applying PVC using

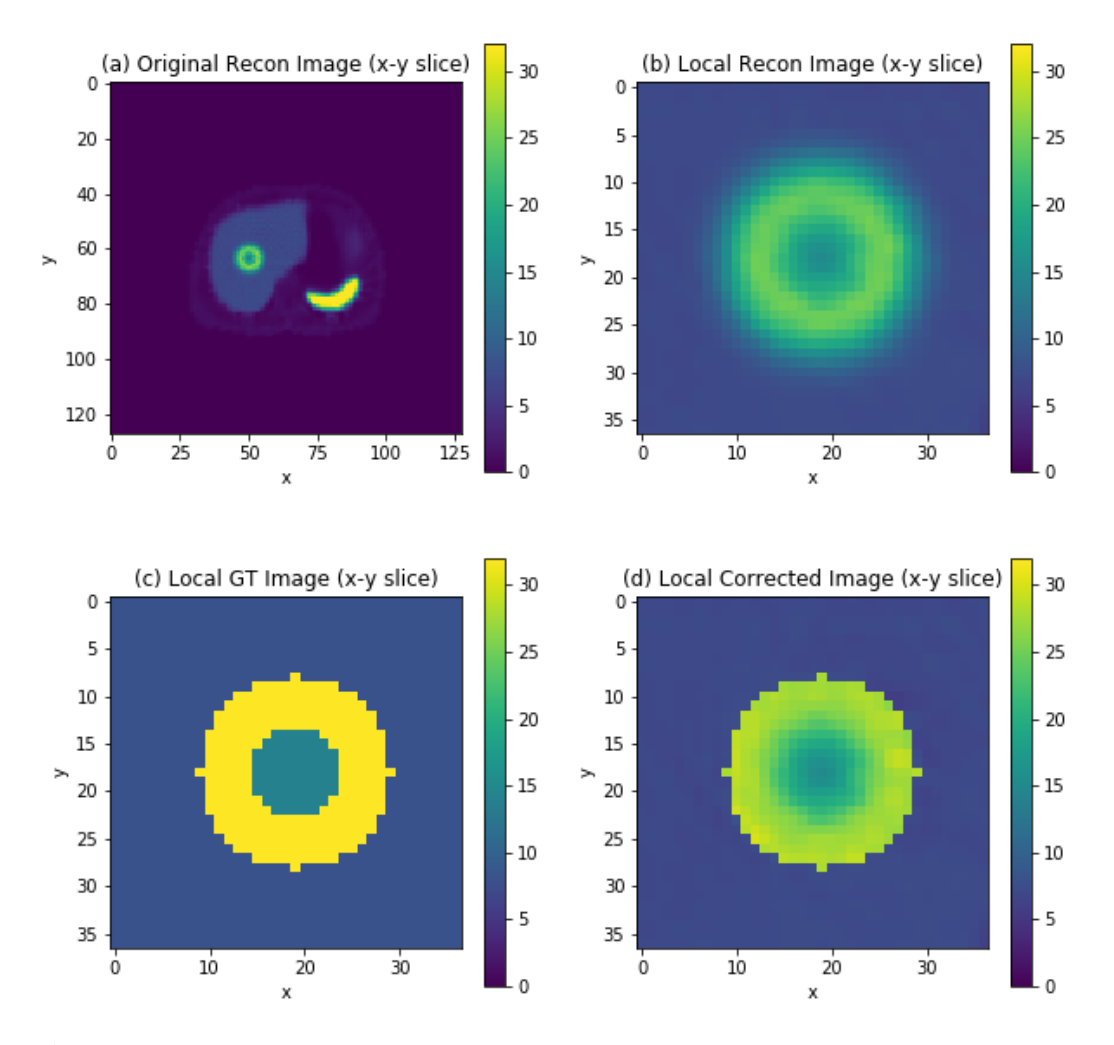


Figure 5.20: Noise-free images, in the transaxial plane, of the non-uniform lesion in the liver of the XCAT Tektrotyd scan phantom datasets. (a) is the uncorrected image reconstructed with 200 updates, (b) is the local region around the lesion in the uncorrected image, (c) is the local region around the lesion GT data (used for segmentation), and (d) is the post-PVC images after correction with 10 STC iterations.

the perturbation-estimated PSF and 10 STC iterations resulted in corrected RMV within 1.3 % of the ground truth for images reconstructed with more than 100 reconstruction updates for both noisy and noise-free data. Another uniform lesion, in the same position with a TBR = 6.25 (rather than TBR = 4), underestimated the true value by 29.7 % - 36.8 % for noise-free data and between 30.3 % - 37.4 % for noisy data. Corrected RMVs for both noisy and noise-free data were within 1.4 % of the true value.

For the non-uniform Tektrotyd liver lesion shown in Figure 5.20, uncorrected

RMVs were between 19.1 % and 25.3 % for noise-free data and between 20.3 % and 26.1 % for noisy data. Following PVC, the RMVs were within 1.9 % for both noisy and noise-free data.

Pre- and post-correction RMVs from the noise-free Tektrotyd datasets are shown in Figure 5.21 for 200 reconstruction updates and 10 STC iterations demonstrating the improvement in RMV accuracy compared with ground truth for corrected data, provided that a case-specific PSF is used within the STC algorithm.

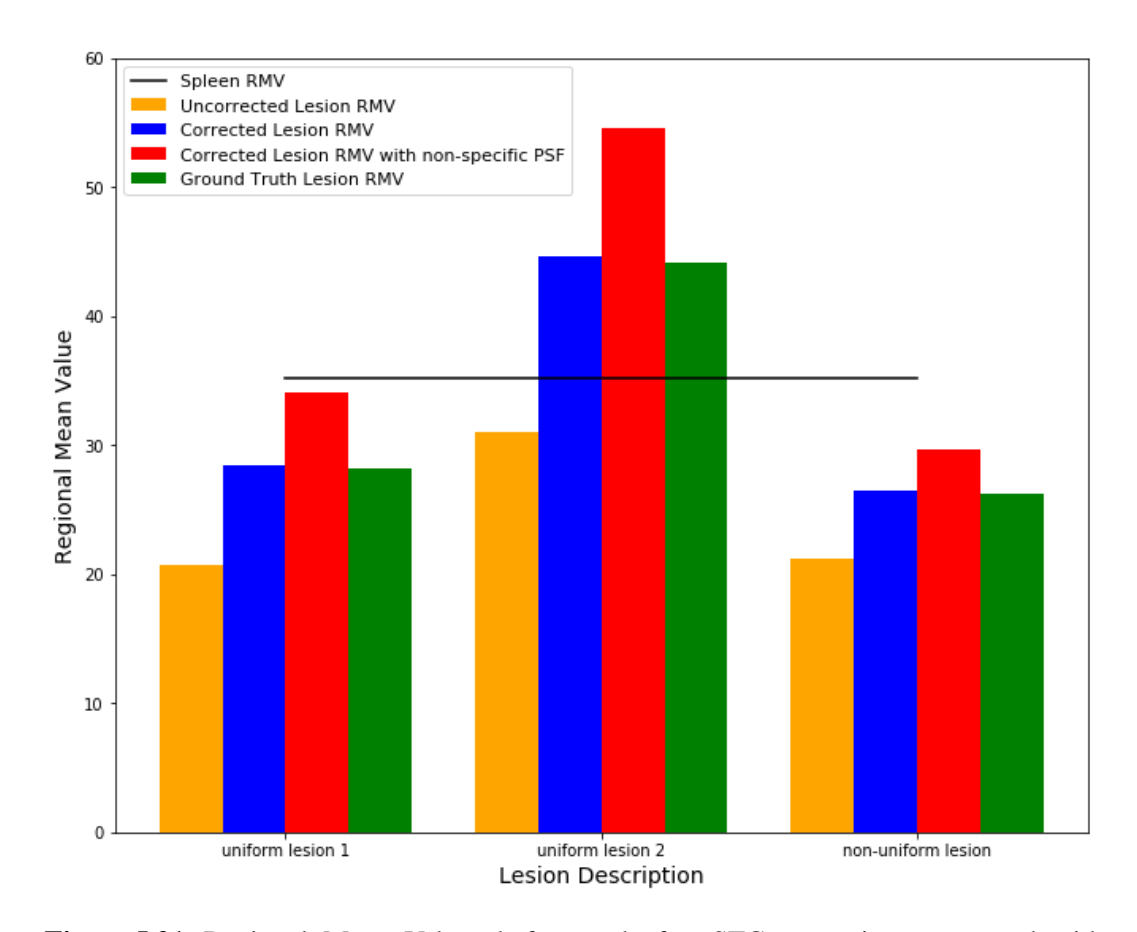


Figure 5.21: Regional Mean Values before and after STC correction, compared with Ground Truth, for noise-free data and 200 reconstruction updates, for the three different liver lesions investigated within the Tektrotyd XCAT dataset. The value for the spleen is also demarcated with a line demonstrating that the uncorrected RMV of uniform lesion 2 is lower than the spleen, but the ground truth and post-STC corrected RMV is actually greater than the spleen. Data corrected with STC based on a non-specific PSF is also included and demonstrates a consistent over-correction compared with GT.

5.5 Discussion

Results presented in this chapter demonstrate that perturbation, using a single voxel point source, can be used to evaluate the impact of a variety of factors commonly encountered in clinical practice on the PSF. This indicates that accurate application of any PVC algorithm requiring information on the PSF likely requires a case-specific measurement.

One factor included in the 'case-specific' description is the number of updates used in the reconstruction. The PSF was found to depend on the reconstruction update number. In each case investigated with the simple geometrical phantom, a minimum of approximately 100 reconstruction updates (10 OSEM iterations with 10 subsets) are required for FWHM values in each direction to become approximately stable with iteration number. However, the convergence rate also depends on the size and contrast of objects of interest; larger objects of higher contrast will converge faster than small, low contrast objects. From the shape of the plots in Figure 5.8, it is possible to see that the FWHM measurements could continue to change with number of reconstruction updates beyond 200 - in particular the tangential direction at the off-centre position, albeit at a significantly slower rate than is seen at earlier updates. Given this slow variation at higher updates, between 100 and 200 reconstruction updates could be a reasonable recommendation as it is a compromise between consistency in reconstruction and processing time. Another factor to consider is that noise increases with higher iterations, and this could detrimentally impact the precision of quantitative measurements.

Further support to a potential recommendation to ensure sufficient reconstruction updates are used for quantitative images is given in the results of the experiment comparing zero and non-zero activity within the bladder of the XCAT phantom. Here, a difference was seen when comparing otherwise identical images when images were reconstructed with fewer than 50 updates. For higher updates, the perturbation-estimated PSF was virtually independent of the presence of activity within the bladder.

Results presented in Section 5.4.1.2 indicate that factors such as lesion contrast

and intensity can also impact the PSF estimation if fewer than 100 reconstruction updates are used (for example, see Figure 5.9). The range of reconstruction updates this applies to includes reconstruction settings typically used in clinical practice. For example, international guidance recommends 24-50 updates, and notes the need to balance noise and resolution [Van Den Wyngaert et al., 2016]. Lesions may change in size and tracer avidity (therefore TBR) throughout a course of treatment, and this can confound quantification since the extent of the PVE will vary due to these changes. Reconstructing with fewer than 100 OSEM updates may introduce variability in the PSF measurement which in turn may impact the accuracy of the applied PVC.

Figure 5.8 shows that the standard deviation values on FWHM measurements are greater for earlier reconstruction updates. This suggests a higher level of uncertainty in the 2D Gaussian fits for images reconstructed with low numbers of iterations compared with more iterations. For increased confidence in the fit of the PSF, and to reduce the dependence of FWHM measurement on iteration number, lesion size, and contrast, data presented here suggests that at least 100 updates should be used for reconstruction.

The accuracy of corrected images depends on both the accuracy of the PVC method and the accuracy of the resolution measurement. Therefore, residual bias in regional mean values may not be solely due to limitations of the perturbation method – they may be due to limitations of the STC method. An example of this is the apparent gradient introduced across the uniform lesion as seen in Figure 5.18. This effect was most obvious in this particular case where the activity distribution is an extreme example (i.e. the lesion is very close to the boundary of a bone and soft tissue interface). This may have contributed to the gradient, the appearance of which has emphasised by the nature of the colour scale. Exhaustive tests were performed to confirm that this was not due to upsampling and confidence in the technique in general is supported by the quantitative accuracy of the regional mean value. The perturbation method will be tested using the other PVC methods on the shortlist in Chapter 7. However, the RRMSE analysis did demonstrate lower error when the

image was convolved with a perturbation-estimated PSF versus a non-specific PSF, acting as a check of the suitability of the perturbation method independent of the PVC method.

One advantage of the STC method for partial volume correction is the production of a corrected image, rather than assuming uniformity across the lesion and assigning a single value across the region. Since some stages of the STC correction include voxelwise correction, the heterogeneity of the lesion could be retained. This is demonstrated in Figure 5.20 which shows the STC method applied to a non-uniform lesion with uptake pattern typical of a lesion with a necrotic core.

5.5.1 Limitations

One limitation of the simulations performed in this chapter is that the system models and software used for generating sinograms and for reconstructing were very similar (with the exception the precision to which the attenuation and PSF were modelled). This does not replicate the "real life" situation accurately, where the system model used for reconstruction is an approximation of the physical gamma camera used for acquisition. To test the potential significance of this limitation, a preliminary investigation using simulations with non-matched system models was performed. Initial results showed that the estimated PSF depends on the system model used to simulate imaging of the point source (i.e. used to generate the sinogram of the perturbation source).

A limitation of the perturbation technique is the practicalities of generating the perturbation point in clinical practice. A possible suggestion could be to use a measured point source - ensuring that the geometry and conditions for generating the sinogram of the perturbation source exactly matched that of the acquisition of patient data. However, a significant disadvantage of this is the requirement to make a measurement at every position of interest for the final PVC. In addition, the measurement would not match the patient-specific attenuation and scatter situation. There would be experimental errors also in the production of a point source. Therefore, work to assess the required accuracy of the system model, such as validation of resolution at different distances under different scatter and attenuation

conditions, would be beneficial to guide the assessment of the suitability of using a simulated perturbation source. Alternatively, the point source could be generated through Monte Carlo (MC) simulations, provided the MC model has been validated with a clinical system (validation of MC simulation is discussed in Chapter 6, and further discussion on the implementation of perturbation is included in Chapter 8).

This digital phantom simulation study did not investigate other factors which may limit accuracy in the practical application of SPECT quantification. For example, in this work segmentation was performed directly from the generated image and was therefore accurate. Given the relatively large voxels, compared with object size, realistic segmentation would likely involve interpolation to voxel edges, which may impact the accuracy of the correction. The simulation of the anthropomorphic phantoms on the 256 matrix may underestimate this impact, compared with the 128 matrices most often used clinically. In terms of the use of perturbation, the matrix size choice (whether 128 or 256) is not thought to affect the accuracy of the perturbation method - provided that the intensity of the point source is set appropriately.

While noisy datasets were produced, scatter was not modelled and so results here assume perfect scatter correction. Scatter correction methods are commonly accepted to be reasonably accurate for ^{99m}Tc SPECT [Hutton et al., 2011], however may not be perfect as assumed in the current simulation. While an imperfect attenuation correction was applied in the reconstruction, it is acknowledged that other factors which limit the accuracy of attenuation correction in real clinical data are not replicated here. In reality, the accuracy of attenuation correction based on CT images may be limited by issues related to scaling Hounsfield Unit values to the energy of the SPECT photons, mis-registration and image noise. Real-life scatter and attenuation conditions may result in a reduction in the accuracy of the perturbation measurement and PVC applied to clinical data.

Further work testing the perturbation method and PVC algorithm(s) on realistic datasets, utilising Monte Carlo simulation, with synthetically added lesions to provide a ground truth, would be a step closer to the real life clinical scenario.

This is explored further in Chapters 6 and 7.

Note that some contribution to the overall uncertainty of the PVC corrected measurement may be introduced due to variation in the PSF across the diameter of the lesion. Results presented in this chapter assume that, while the PSF may change across the FOV, variation across the local region of the lesion or object of interest would not be large enough to impact accurate application of PVC. This is likely to be a reasonable assumption for small lesions, but may not be for larger objects e.g. organs at risk. However, since larger objects will be less affected by the PVE in the first instance, there may be a trade-off in that the magnitude of the correction required is lower than for small objects.

The work in this chapter did not compare the perturbation method to other techniques proposed for assessing resolution. Previous work using different resolution estimation methods include, for example, Liow & Strother who define measures of Effective Local Gaussian Resolution (ELGR) and Effective Global Gaussian Resolution (EGGR) which were used to investigate object size dependent resolution [Liow and Strother, 1993]. Marquis et al. use the global Gaussian and "ideal" phantom [Marquis et al., 2021], and Tran-Gia et al use a "matched filter analysis" of hot sphere cold background NEMA phantom [Tran-Gia and Lassmann, 2019]. The methods have been compared (albeit for a different application in PET imaging) and were found to be equivalent [Leek et al., 2023].

5.6 Conclusion

Perturbation, using a single voxel point source, was applied to simulated phantoms replicating situations that may be encountered in clinical SPECT oncology imaging. Perturbation reliably estimated PSF values, appropriate for the specific situation, provided that a sufficient number of reconstruction iterations were used.

When PVC was applied using a PSF estimated by perturbation, quantification of regional mean values was more accurate than non-corrected data, and was also more accurate compared with PVC applied using a non-specific PSF. The inaccuracy in regional mean lesion value associated with PVC assuming an invariant

PSF demonstrates that additional processing required for PSF measurement with the perturbation method is justified.

While further study is required to test perturbation with PVC on more realistic datasets, in more realistic simulations, the results in this chapter demonstrate that using the perturbation technique to estimate the PSF and using this information in the application of PVC can improve quantitative accuracy of ^{99m}Tc SPECT images.

Chapter 6

Monte Carlo Simulation of Clinically Relevant Test Datasets

6.1 Aim

The aim of this chapter is to describe the set-up of software and realistic test datasets used for robust testing of Partial Volume Correction (PVC) algorithms in clinically relevant scenarios. Section 5.5.1 notes that the simulation results presented thus far in the thesis have used the same software for both simulation of projection data and reconstructions. Additionally, most testing has been done on relatively simplistic geometric test datasets. Real patient data would be the most relevant datasets to use for testing PVC algorithms, however these datasets are limited due to unknown Ground Truth (GT) activity distribution. The test datasets described in this chapter use real patient data from oncology SPECT studies as a basis for the activity distribution. Synthetic lesions are inserted to ensure a known lesion GT.

This chapter describes the validation, and set-up, of SIMIND Monte Carlo (MC) software. SIMIND is used to simulate acquisition using a real SPECT-CT system. This chapter also describes the requirements for, and design of, test datasets to challenge PVC methods in realistic clinical situations. The foundations of the methods used to test PVC algorithms as described in Chapter 7 will be described in the present chapter.

6.2 Background

6.2.1 Monte Carlo Simulation

The benefits of using MC simulation over performing multiple phantom experiments on a real gamma camera include better reproducibility and speed of image generation. MC simulation also does not incur any radiation dose to the operator who would otherwise be filling, setting up, and scanning phantoms. Stochastic modelling of photon interactions in the collimator and detector simulate emission data with a realistic resolution and noise level, provided that the simulation is set up appropriately. Using MC to simulate projection data for reconstruction with STIR also avoids the limitations associated with using the same system model in the simulation of projection data and in the reconstruction algorithm used to solve the inverse problem [Colton and Kress, 1998].

SIMIND software was selected to perform MC simulation for this project since it is specifically designed for simulation of SPECT data using a conventional gamma camera geometry, and can be configured to model a specific SPECT system. SIMIND was first introduced in 1989 [Ljungberg and Strand, 1989]. Since then, SIMIND and other software systems have facilitated research in PET and SPECT imaging. Recently, amongst other examples of quantitative SPECT research, SIMIND was used to simulate different NEMA sphere configurations to assess the positional dependence of Recovery Coefficients (RCs) [Leube et al., 2024a].

6.2.2 Clinically Realistic Test Data

Digital phantoms, used as input to the MC software and subsequently reconstructed using STIR, can produce images affected by a realistic Partial Volume Effect (PVE). These reconstructed images can then be used to test PVC algorithms. Since the initial input data is known, it is possible to compare the corrected data with a known Ground Truth.

The aim of developing these test datasets, with clinically realistic activity distributions, was to integrate findings from previous chapters; testing PVC, using perturbation (as described in Chapter 5), using realistic test datasets.

6.3 Methods

6.3.1 SIMIND simulation parameter definition

Monte Carlo simulations using SIMIND were run using the command line, using information from an input file which includes parameters which describe the imaging system, and optional control switches. Example command and parameter settings are provided in Appendix C. SIMIND can be run with input activity distribution data defined within SIMIND as an "analytical phantom" (based on internally defined shapes), or using image data as "voxel-based phantoms" (for example images generated using STIR, or other reconstructed image data).

The imaging system defined in this and the following chapter is a Siemens Symbia Intevo Bold SPECT-CT, using LEHR collimators [Siemens, 2017]. This system was selected as it was locally available for acquisition of the data required for validation of the SIMIND simulation, and for the patient data used as a basis for the test datasets in Chapter 7.

Results and data from acceptance testing measurements, alongside specifications given in the equipment manual [Siemens, 2017] were used to inform the choice of parameters defining the hardware components of the imaging system in SIMIND. Key parameters from the equipment manual and acceptance testing report are outlined in Table 6.1.

Specific acquisition settings which were also specified in SIMIND, included SPECT imaging (rather than planar), the width and position of energy windows used, pixel size, number of projections, rotation extent, start angle and rotation direction. The other key simulation option stipulated that Poisson noise was simulated.

6.3.2 SIMIND Set-up Validation

In order to generate realistic and relevant test datasets, it is important that the MC simulation accurately simulates the imaging of a real SPECT-CT system as used in clinical practice.

Previous work validating MC models reviewed the system spatial resolution,

Symbia System Property	SIMIND Setting	SIMIND Index No.
Crystal Material	NaI(Tl)	Main 10
Crystal Thickness	9.5 mm	Index 9
Crystal Dimensions	553 × 387 mm	Indices 8 and 10
Crystal Shape	Rectangular	Index 10
Collimator type	Parallel hole	Index 55
Hole Shape	Hexagonal	Index 54
Hole Diameter	1.11 mm (across the flats)	Indices 46 and 47
Hole Length	24.05 mm	Index 52
Septal Thickness	0.16 mm	Indices 48 and 49
Protective Cover Thickness	1.0 mm	Index 13
Intrinsic Resolution (FWHM)	3.5 mm	Index 23
Energy Resolution for ^{99m} Tc	8.8 %	Index 22

Table 6.1: Key parameters used to define the Siemens Symbia Intevo Bold system with LEHR collimators on SIMIND software. The right hand column references the position within the SIMIND input file used to define a specific feature.

system sensitivity and the energy spectrum [Pells et al., 2023]. This chapter will examine each of these, and also the position and motion of detectors, as these factors are important for SPECT resolution and quantification. In addition to the general validation tests described in this chapter, specific features will be reviewed for each individual simulation in Chapter 7. This will include the appearance of sinograms and projection images, and the detector position for each projection angle.

6.3.2.1 Detector position and motion

Despite the attempt of DICOM conformance statements to remove ambiguity in the descriptions within medical imaging header files, the precise meaning of the "Radial Position" parameter as described in the DICOM image header for Siemens Symbia SPECT data is unclear [DICOM Standards Committee, 2025]. The DICOM conformance statement for the Symbia system states that it is the "Radial distance of the detector from the centre of rotation, in mm". However, this may be interpreted

as either the distance from the centre of rotation to the face of the collimator or from the centre of rotation to the front of the scintillation crystal¹. The Symbia LEHR collimator is 24 mm thick, so the difference in this interpretation could significantly affect the resolution at small radii. In order to clarify this, the physical distance between the collimator surfaces of the two detectors on the Symbia system was measured. These measurements were compared with the radial position as displayed on the Patient Positioning Monitor (PPM) which gives a real time display of the "Radial Distance" parameter as it is recorded in the DICOM header.

The measurements were performed by moving the detectors using the hand controller. Once specific radii were reached for both detectors, the physical distance between the detectors was measured. This was performed for a range of distances between the closest possible setting and furthest possible setting on the Siemens Symbia SPECT/CT system. Measurements were made using the LEHR and the LEGP collimators.

Clarity on the rotation direction is also required in order to ensure appropriate detector positioning at different angles around the patient, and the correct orientation of reconstructed images. It was not clear from the SIMIND manual, or from initial tests, if the definition of rotation direction was the same as the Siemens Symbia definition and/or the STIR definition. To test this, NEMA phantom data, acquired on the Siemens Symbia system and reconstructed in STIR was used as input to SIMIND. Simulations were run with combinations of clockwise and counter-clockwise rotations and start angles set to 0, 90, 180 and 270 degrees. For each simulated dataset the Radius of Rotation (RoR) was reviewed vs detector position for the SIMIND simulation and real data acquisition to assess consistency. Projections at a range of angles were compared with the real Symbia projections. Data were also reconstructed with STIR to check reconstruction orientation.

¹Note that the STIR definition is clear in that it refers to the distance from the collimator (0 cm is collimator face). SIMIND is also clear; "The distance from the origin of the coordinate system to the lowest part of the detector... depending on the defined simulation flags, this can be the collimator lower surface".

6.3.2.2 Planar Spatial Resolution

Since the focus of this thesis is the PVE, it is important that the MC simulation is set up with parameters which represent how resolution changes with distance on a real gamma camera. This was investigated by comparing system resolution measurements from the Siemens Symbia gamma camera to equivalent measurements from SIMIND generated images.

A series of planar acquisitions were made on the Siemens Symbia system using the LEHR collimator, at a range of distances between 20 mm and 300 mm with no additional scattering material. Note that the maximum distance that a detector can be positioned from the centre of the Field of View (FOV) is 36.6 cm, and it is expected that most clinical studies will utilise detector radii between approximately 15 and 30 cm. Five glass capillary tubes with internal bore of 0.5 mm were positioned on a perspex plate which was held level on the gamma camera bed. The perspex was specifically designed with grooves to hold the capillary tubes in place and parallel to one another. A photo of the experimental set up is shown in Figure 6.1.

Each capillary tube was filled with a low volume (approximately 0.2 ml) of $^{99\text{m}}$ Tc. Blue food dye was used as a visual check of uniform filling of the tubes, ensuring no bubbles were present. Total activity was such that the count rate was approximately 4 kcts/s. Images were acquired using an energy window of 129.1 to 150 keV on a $1024 \times 1024 \text{ matrix}$ (pixel size 0.6 mm), with 1000 kcts per acquisition. An initial test acquisition was used to checked the alignment of the line sources relative to the image matrix. The maximum of a fitted Gaussian from profiles taken near the top, middle and bottom of the tube was shown to be within 1 pixel, confirming acceptable alignment.

An equivalent experiment was set up using SIMIND on a 1024×1024 matrix (pixel size 0.6 mm). The imaging system was defined using parameters based on the Symbia system with LEHR collimators. Five, 1 pixel wide, line sources were generated using the internal library of shapes pre-defined in SIMIND. To replicate the Symbia experiment, the sources were positioned with a 6 cm gap between each

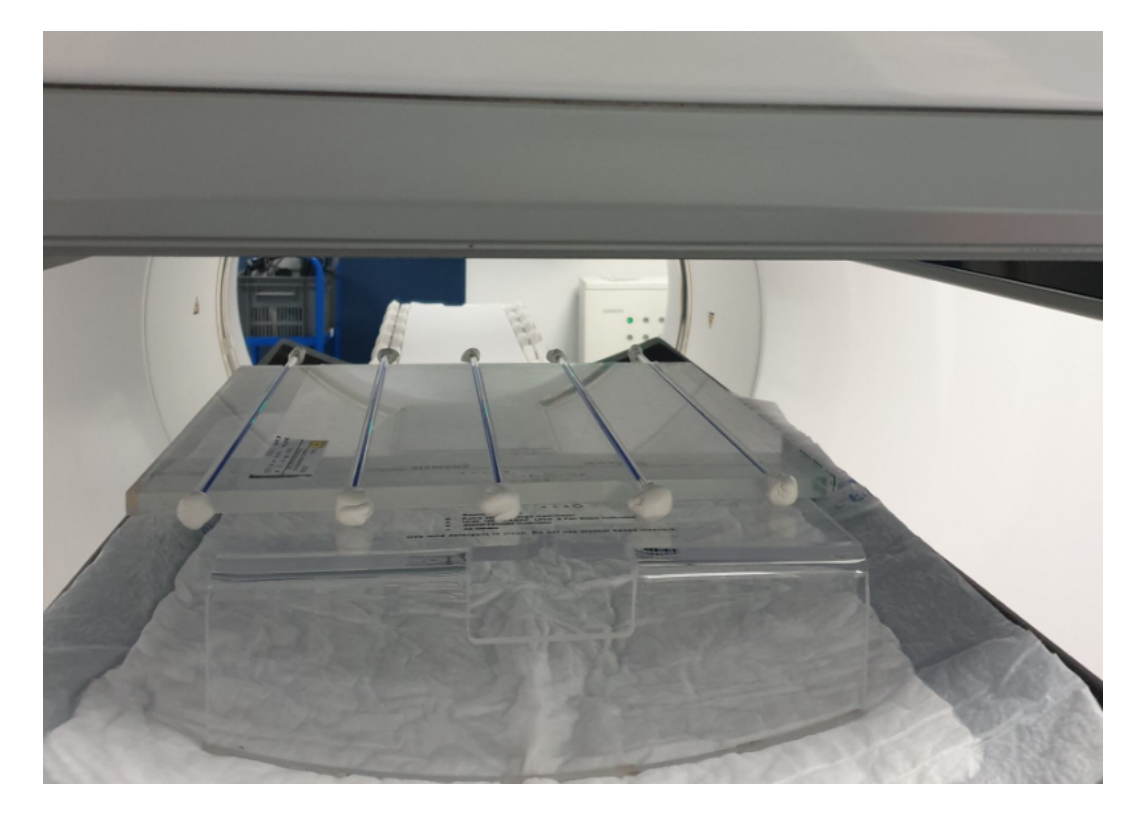


Figure 6.1: Experimental set up for system resolution measurements made using line sources acquired on Siemens Symbia system. The detectors were moved such that acquisitions were made at a range of source to detector distances.

other.

Horizontal profiles were drawn using tools on Hermes (Symbia data) or using ImageJ (SIMIND data) across the five line sources to generate line spread functions. Gaussian profiles were fitted to each line source in turn, using Solver on Excel to find the optimal parameters using a non-linear optimisation. The fitted function allowed calculation of the Full-width at half maximum (FWHM) for each profile, at each distance, for the Symbia and SIMIND data. Results were taken to be the mean of the 5 line source FWHM for each distance. Measurement uncertainty was estimated as 2 × the standard deviation on the mean FWHM.

6.3.2.3 Energy Spectra

SIMIND energy spectra data are automatically acquired for each SPECT simulation. The spectrum from a SIMIND simulation was compared with data from the Siemens Symbia gamma camera to verify that the simulation is producing realistic energy resolution and scatter.

A SIMIND simulation was performed based on a ^{99m}Tc Tektrotyd patient dataset, divided into bins of 0.5 keV. A spectrum, with 1.32 keV bins, acquired from a real ^{99m}Tc Tektrotyd patient was also acquired on the Symbia system.

6.3.2.4 Planar Sensitivity

Data from acceptance testing of the Siemens Symbia system was used for an assessment of the planar sensitivity using LEHR collimators. This acceptance testing was performed by colleagues of the author, prior to the author working locally with the system. Acceptance testing methods and results had been documented for reference. Sensitivity testing data was acquired using a $10 \times 10 \, \mathrm{cm}$ square phantom, with minimal attenuation, filled with $^{99\mathrm{m}}\mathrm{Tc}$. This was positioned 10 cm from the face of the collimator for each detector and a short acquisition was performed.

The phantom was imaged on each detector for a total time, t, of 13 s. The total counts within the image, C, was measured by loading the data as a numpy array in Python and summing all elements. Along with counts and time, information regarding the decay corrected activity, A, was used to calculate the planar sensitivity, S, of each detector using equation 6.1:

$$S = \frac{C}{(t \times A)} \tag{6.1}$$

The acceptance testing imaging was replicated in SIMIND, by setting up a 10×10 cm square phantom, positioned at the centre of the FOV. The phantom was defined using SIMIND's internal library of pre-defined shapes. The activity was set to 30 MBq and the acquisition time set to 60 s. The images, calculated sensitivity values and profiles across the sensitivity phantoms were compared between the Symbia acquisition and the SIMIND simulation.

6.3.3 Use of SIMIND with STIR software

SIMIND software had not previously been used with STIR software in any published research. Due to a number of fundamental differences between the software systems, it was non-trivial to enable STIR and SIMIND to work together.

Documentation developed during this project which summarises requirements for connecting STIR and SIMIND has been made widely available (see Appendix D for details). For this project, it was necessary to convert data which had been defined in STIR to a form which could be used as an input to the SIMIND simulation. In turn, the output from the SIMIND programme needs to be adapted to allow reconstruction in STIR.

Key differences include accepted data types, the definition of coordinate systems, units, naming and header conventions and definition of attenuating material. An overview is provided in Table 6.2.

Software Aspect	STIR	SIMIND
Data types	default is float (others possible)	16 bit integer
Coordinate System	Referenced to imaging system	Referenced to phantom
Units	mm, degrees	cm, radians
Image data filetype	.v	.a00
Header files filetype	.hv	.h00
Units of attenuation	attenuation coefficient (cm ⁻¹)	$1000 \times \text{density (g/cm}^3)$

Table 6.2: Key differences between STIR and SIMIND software conventions.

6.3.3.1 Accepted Data Types

SIMIND is designed primarily for use with emission and density phantoms defined within SIMIND itself (i.e. using pre-set uniform shapes) as this increases computing efficiency. Increased flexibility in input can be accessed by using a voxel based input, at the cost of longer simulations. In addition to more computing, careful definition of input data is also required. In order to utilise the voxel-based phantom input, the data type needs to be 16 bit integers. This means that any floating point data generated in STIR would be affected by rounding errors if input directly. The workaround employed was to multiply input float data by 100 before converting to the integer images required by SIMIND. Note that STIR is flexible with data type and can use; signed integer, unsigned integer, as well as float. STIR can also specify

byte order and number of bytes per pixel.

6.3.3.2 Coordinate Systems and Orientation

The different reference points for the coordinate systems between STIR and SIMIND meant that care needed to be taken to ensure that images were oriented correctly. This also relates to the defined detector position and angle of acquisition. To ensure consistency and that orientation is as expected STIR and SIMIND reconstructions of NEMA phantom data were reviewed, comparing orientation.

Another consideration to note is that SIMIND is limited to simulating data where the dimensions of the input datasets are equal (i.e. x=y=z) This required input images to be padded before SIMIND simulation.

6.3.3.3 Units, Naming Conventions and Header Structure

Units for distance differed by a factor of 10 (mm vs cm) between SIMIND and STIR. This was important for setting radius of rotation, and also required careful checking for setting up phantoms on either software system.

STIR generally follows the Interfile 3.3 format [Todd-Pokropek et al., 1992] (excepting that 'float' rather than 'short float' or 'long float' should be used). SIMIND also allows output to Interfile 3.3 format. This option was always chosen to be TRUE but the header layout still varied from the STIR interfile format.

A script was written to enable reliable conversion of SIMIND output header files to a form that enables STIR to read the data. This included converting units, input of RoR data into the STIR interfile header, and other minor formatting changes to allow STIR to read the header.

6.3.3.4 Definition of Attenuation

In order to simulate the effect of attenuating structures, STIR uses data in the form of the attenuation coefficient (μ), whereas SIMIND uses units of $1000 \times \text{g/cm}^3$.

Converting real CT data for use in STIR was performed using utilities available within the STIR software, including adjustment of voxel sizes using the zoom utility. An executable within STIR allows conversion of CT data in units of Hounsfield Unit (HU) to μ values based on a bilinear slope conversion [Brown et al.,

2008], with the gradient change point at 0 HU (water). The attenuation coefficient is the narrow beam coefficient as scatter will be corrected for separately using the Dual Energy Window method (see Section 2.7.2.1 for further explanation).

Real CT data were also converted into units of $1000 \times \text{g/cm}^3$ for use in SIMIND. Published data were used to estimate conversion factors from HU to density [Brown et al., 2008]. A key reference point is water which has HU = 0, and $\rho = 1 \text{ g/cm}^3$ (i.e. SIMIND input for material with a density of water would consist of voxel values of 1000). Other data used to fit relationships between ρ and HU included bone, perspex, vegetable oil, wood and sawdust [Brown et al., 2008]. This allowed two linear fits to be performed, fixing the intercept at HU = 0 and ρ = 1 for water. Values are demonstrated in Figure 6.2.

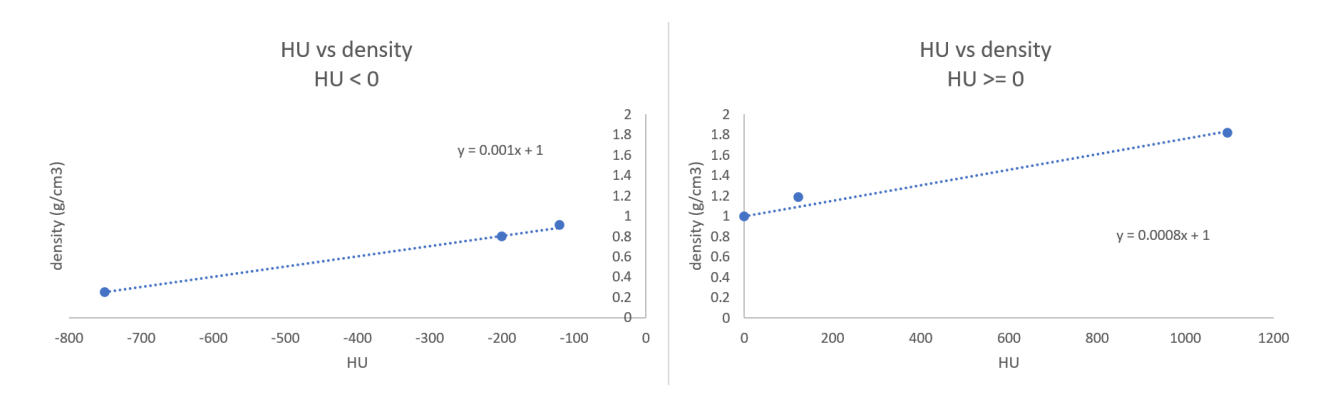


Figure 6.2: Data used and linear fits either side of HU = 0, allowing CT data to be converted to density for use in SIMIND.

SIMIND uses tables of energy dependent cross-sectional values for the photoelectric effect, Compton scattering, coherent scattering and pair production interactions [Ljungberg and Strand, 1989]. There are two tables used depending on the density value of the voxel; the threshold which was pre-defined in the SIMIND parameter file corresponds to a density of 1.17 g.cm³.

Density map use for detector motion in SIMIND

SIMIND has functionality to replicate a non-circular orbit similar to body contouring which is commonly used in clinical imaging. Index 42 can be set to define the distance between the detector and the surface of the phantom. The surface of the patient or phantom is defined based on the density map and a user-

specified density threshold which defines the physical edge (Index 35). The detector positions defined by this set-up are output by SIMIND and were reviewed for each generated dataset, in comparison to the real physical radius of rotation values (further discussion is provided in Section 6.4.3.1).

6.3.4 Development of digital phantoms based on clinical data

It is important to consider which characteristics of images would be challenging to PVC algorithms. Challenges specific to oncology SPECT imaging were discussed in Chapter 3. The criteria developed, based on working around these challenges, are summarised in Section 3.3.9 for ease of reference. Specific aspects relating to the test dataset include that the PVC algorithm should be able to cope with a lesion of interest which is non-uniform, non-spherical, and positioned within a background for which the activity is non-uniform or variable.

A total of 9 digital phantom test datasets were generated with two levels of complexity. The first set of test cases was designed based on Tektrotyd SPECT scans on five different patients, with spherical, uniform lesions added within the liver. The final four test cases used four of the Tektrotyd cases as background activity distribution, with the addition of non-uniform, and non-spherical lesions in variable background conditions. These were designed to test how PVC algorithms perform in realistic situations, with increasing complexity.

These 9 test datasets include a range of situations which will challenge the algorithms, as described above, to illustrate how each method performs in different scenarios. However, this set of test data is not intended to be comprehensive and cannot include every possible clinical activity distribution and lesion type.

6.3.4.1 Clinical source data

Clinical data acquired between 2021 and 2022 at Glasgow Royal Infirmary (GRI) was used as the basis for the test datasets described in this chapter. Following discussion with the NHS Greater Glasgow and Clyde Research and Innovation department, an IRAS form was completed and ethical approval was granted for the use of these data. Relevant documents are included in Appendix E.

A total of 27 patient datasets were reviewed, and five were selected for which the activity distribution and total counts were representative of the overall group. This consisted of 3 males and 2 females, aged between 44 and 77 years old (mean age 55.4 years). Of these, two cases demonstrated physiological Tektrotyd uptake only. The other three demonstrated areas of raised Tektrotyd uptake (Krenning score 3 or 4) indicating somatostatin receptor positive lesions. These five patients were used as background activity distribution for generating the realistic test datasets. Previous research has demonstrated that, despite noise levels and limited resolution, clinical data can be used as an input for MC simulation to produce realistic activity distributions [Stute et al., 2011].

6.3.4.2 Preparation of patient data

On selection of the five anonymised Tektrotyd SPECT/CT datasets, representative of the patient population, several processing steps were required to prepare the datasets for the insertion of synthetic lesions.

Preparation of Projection Data

The raw data consisted of projection data from Siemens Symbia SPECT/CT. The first stage of data preparation was to convert the DICOM projection data to interfile using the STIR executable SPECT_dicom_to_interfile.

Each parameter in the newly created header file was checked and corrected to ensure the parameters such as number of projections, extent of rotation, direction of rotation, start angle, orbit ("non-circular") were correct. The demdump utility (part of the DICOM toolkit; https://support.dcmtk.org) was used to output this information in text form from the DICOM data. However, this utility does not output radial positions which were instead accessed using ImageJ software [Schindelin et al., 2012]. The radial positions for each projection were then copied into the header file for the projection data. Another important manual step was to ensure that two header files were created; one for the photopeak data, and another for the off-peak data. To do this, a copy of the header was made and the number of bits to skip (calculated based on the number of projections, dimensions of projection image and number of bytes per pixel $120 \times 128 \times 128 \times 4 = 7,864,320$) in order to

Clinical Case reference	Total counts in photopeak projections	Total counts in off-peak projections
Patient A	9136800	4371840
Patient B	4791750	2453720
Patient C	6928560	3891870
Patient D	9471580	4354330
Patient E	7021330	3374700
Mean	7470004	3689292

Table 6.3: Summary of total counts in projection data acquired in clinical Tektrotyd cases using the Siemens Symbia SPECT/CT System at Glasgow Royal Infirmary.

point to the data associated with the off-peak energy window.

At this stage, the sinogram data and projections at the anterior and posterior position were viewed visually using Python (by plotting the numpy arrays as figures) to check that the orientation of the projection data was as expected, and that the sinogram appeared as expected. Example images of projection data are shown in Figures 6.3 and 6.4 for photopeak and off-peak data, respectively. In addition, a STIR utility was used to check the total counts in each energy window. In all cases, the total counts of the converted interfiles was identical to the total counts as displayed on the clinical Hermes system [Hermes Medical Solutions, 2024].

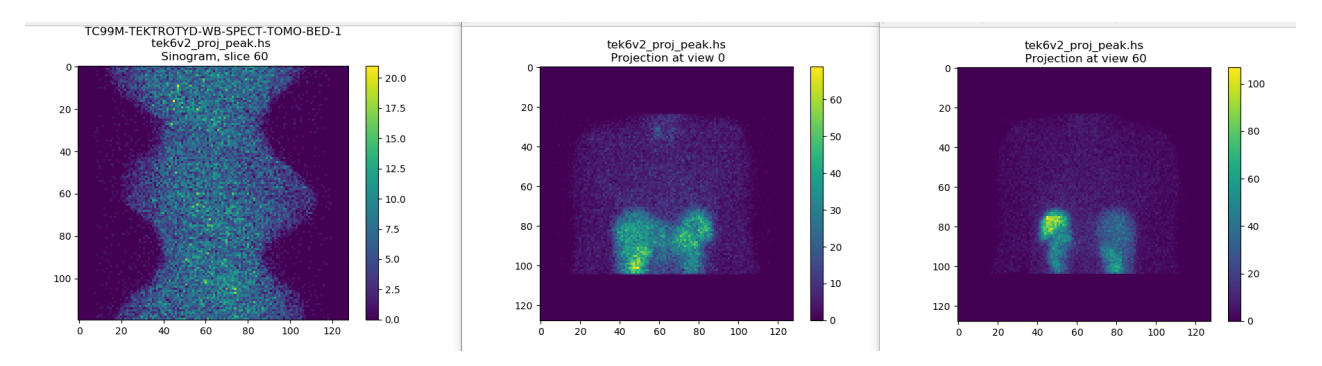


Figure 6.3: From left to right: the interfile sinogram (for a slice in the middle of the body) of clinical Tektrotyd data acquired using an energy window centred on the photopeak with a Symbia SPECT/CT system, the anterior view projection image, the posterior view projection image.

The off-peak energy window was then used to perform a Dual-energy Window

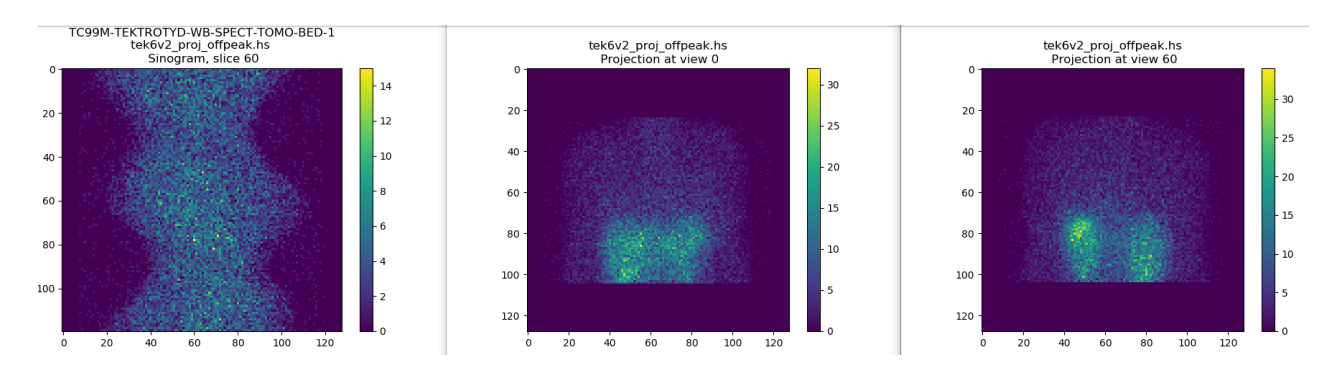


Figure 6.4: From left to right: the interfile sinogram (for a slice in the middle of the body) of clinical Tektrotyd data acquired using an energy window centred 22 keV lower than the photopeak with a Symbia SPECT/CT system, the anterior view projection image, the posterior view projection image.

(DEW) scatter correction on the peak projection data (see Section 2.7.2.1 for description of equation used).

Preparation of CT data

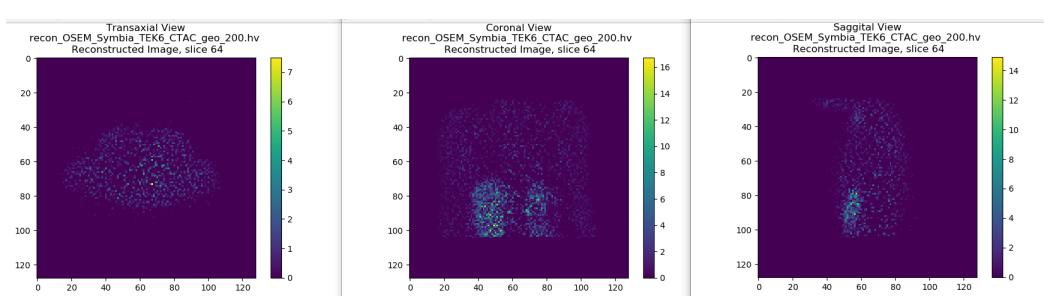
CT DICOM data was converted to interfile using a STIR utility (stir_math) which can take DICOM as input, and output interfile format data. One of the most important steps in the preparation of CT data for use with STIR and SIMIND was to ensure that it was correctly aligned with the SPECT data. To assess this, the photopeak projection data was reconstructed using STIR to give a no-correction reconstruction. This was then overlayed with CT interfile data using AMIDE software, an image viewer which allows fused data to be displayed [Loening and Gambhir, 2003]. For each case, the CT data needed to be flipped in the x- and z-directions, and also shifted by 187.5 mm in the z-direction in order to align with the STIR-reconstructed SPECT data. These manipulations were made to the CT data using the STIR zoom_image utility which also allowed downsampling of the CT data to a 128 × 128 matrix to match the SPECT.

Once the CT data was aligned and downsampled it was converted to the μ map and density data required for STIR and SIMIND, respectively, as described in
Section 6.3.3.4.

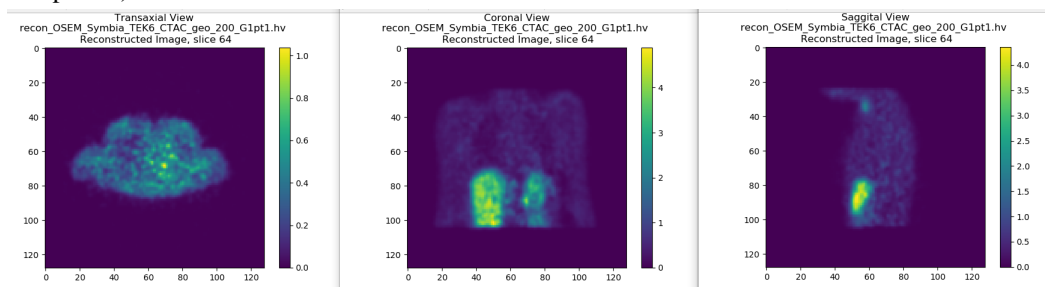
Reconstruction of patient data

The anonymised data were reconstructed using STIR with CT attenuation correction. Reconstruction was performed with OSEM (20 iterations, 10 subsets),

with Resolution Modelling (RM) off and simple Attenuation Correction (AC) (as described in section 4.4.2). These reconstruction parameters were chosen based on work in the previous chapters demonstrating convergence after 200 updates, and without RM to minimise Gibbs artefacts. Selected slices from an illustrative example of the resulting images is shown in Figure 6.5a).



(a) Unsmoothed STIR reconstruction of projection data from Siemens Symbia system (200 OSEM updates)



(b) STIR reconstruction of projection data from Siemens Symbia system (200 OSEM updates), smoothed with a 5.3 cm Gaussian.

Figure 6.5: From left to right: transaxial, coronal and sagittal slices through an example patient dataset showing (a) unsmoothed, and (b) smoothed data.

As the images in Figure 6.5a) are dominated by noise, smoothing was required before input to SIMIND. This was applied by convolving the data with a Gaussian (standard deviation = 1.1 pixels = 5.3 mm) in Python. The resulting smoothed data is shown in Figure 6.5b). A summary of the reconstruction parameters used is included in Table 6.4.

A summary of the process of preparation and use of the realistic test datasets is provided as a flowchart in Figure 6.6.

6.3.4.3 Patient dataset A

The first patient dataset (Patient A) is the activity distribution from the Tektrotyd scan of a 77 year old male patient. The referral for the study noted that the patient

Reconstruction Parameter	Value
Software	STIR
Algorithm	OSEM
No. iterations	20
No. subsets	10
RM	off
AC	Simple
Post filter	Gaussian (sigma = 5.3 mm, FWHM = 12.5 mm)

Table 6.4: Reconstruction parameters used to reconstruct clinical Tektrotyd data, in preparation for inserting synthetic lesions

had a resected small bowel Neuroendocrine tumour (NET), and had known liver metastases. The clinical team were planning for peptide receptor radionuclide therapy (PRRT) and had requested the scan to assess baseline uptake prior to treatment. The report noted several tracer-avid liver deposits. Otherwise there was normal physiological tracer uptake. Representative slices through patient data, reconstructed with STIR as described in Section 6.3.4.2, are shown in Figure 6.7.

6.3.4.4 Patient dataset B

Patient dataset B is a 52 year old male. This patient had an appendiceal NET which had been resected. CT imaging demonstrated possible liver metastasis. The Tektrotyd scan was requested to assess metastatic disease. The Tektrotyd study did not demonstrate any focal tracer uptake to indicate metastases in the liver, or anywhere else in the body. Images of patient B, reconstructed with STIR are shown in Figure 6.8.

6.3.4.5 Patient dataset C

The third patient dataset is also a 52 year old male (Patient C). In this case, the patient had a mass on the head of pancreas, which biopsy proved was a NET. The Tektrotyd scan was recommended by an Multidisciplinary Team meeting (MDT) to assist with planning the further management of this patient. The patient had previously had a CT chest and an MRI of the liver which had not demonstrated any

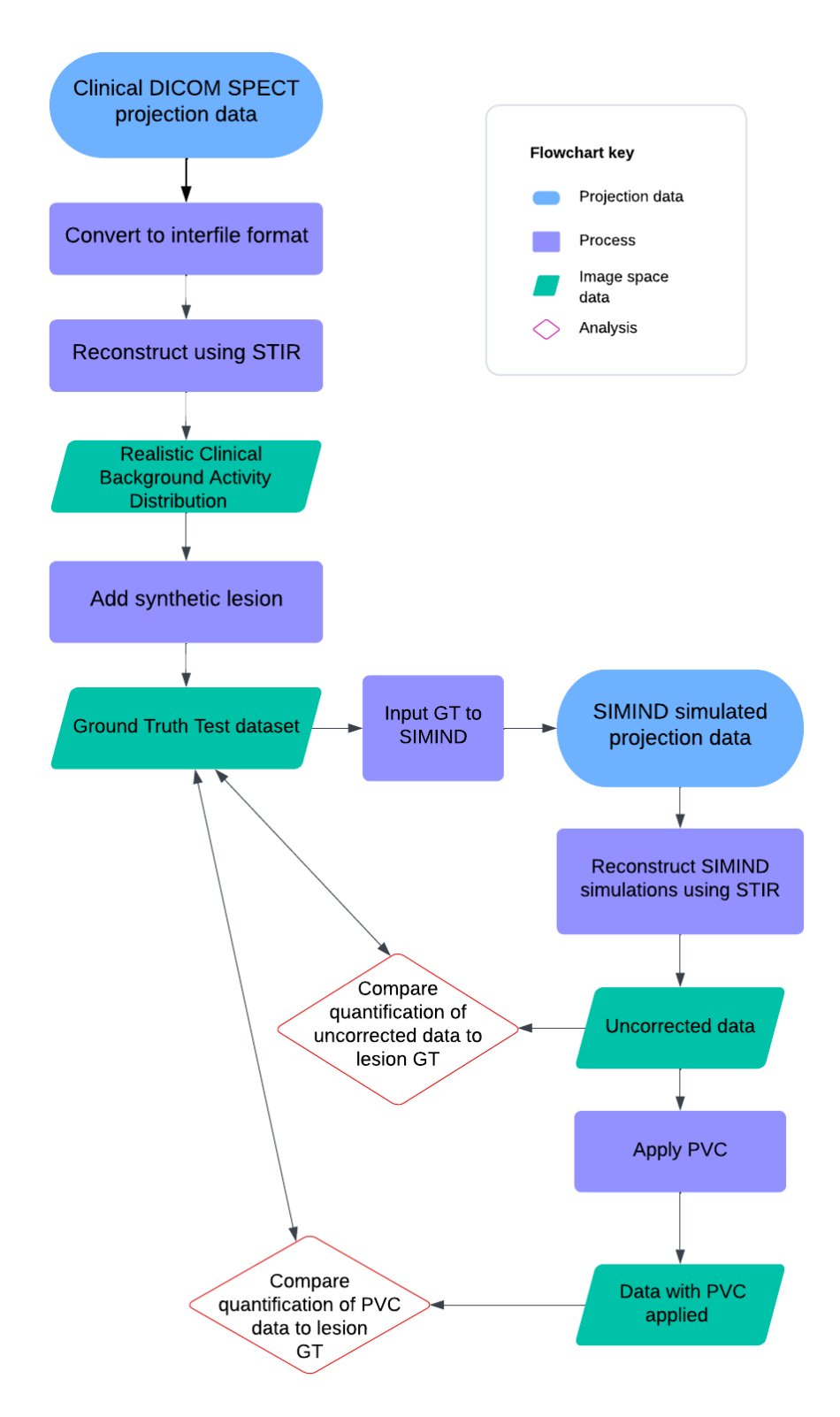


Figure 6.6: Flowchart outlining the steps used for the preparation of GT test datasets, and the subsequent use of these for analysis of PVC methods.

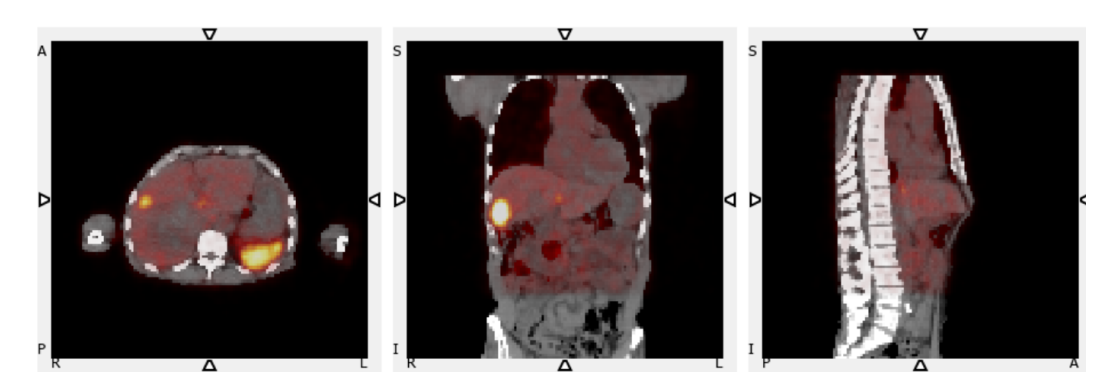


Figure 6.7: STIR reconstruction of Patient Data A, fused with CT, which forms the background for GT dataset Cases 1 and 6.



Figure 6.8: STIR reconstruction of Patient Data B, fused with CT, which forms the background for GT dataset Cases 2 and 7.

metastases. The Tektrotyd scan demonstrated intense tracer uptake at the pancreatic head lesion and portocaval nodes. It was noted that the uptake level was higher than the spleen, giving a Krenning score of 4. In addition to this, a tracer-avid soft tissue nodule on the spleen was thought to be a splenunculus as the avidity was similar to the spleen. Otherwise, there was no abnormal uptake, and no metastatic disease identified in the liver or anywhere else in the body.

6.3.4.6 Patient dataset D

The fourth patient dataset (Patient D) used is a 44 year old female. This patient had been admitted multiple times for severe gastric ulceration and a previous perforated gastric ulcer is noted. The patient had been treated with a high dose proton pump inhibitor, but had not improved despite this treatment. This led the clinical team to suspect gastrinoma, a rare type of NET, and therefore requested a Tektrotyd scan. Physiological activity was noted in the spleen, liver, kidneys and bowel, but no

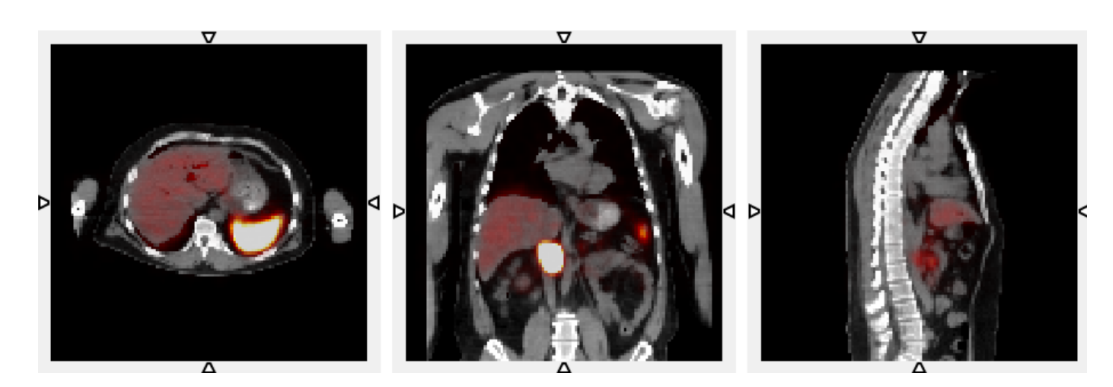


Figure 6.9: STIR reconstruction of Patient Data C, fused with CT, which forms the background for GT dataset Cases 3 and 8.

abnormal activity was noted to suggest any NET.

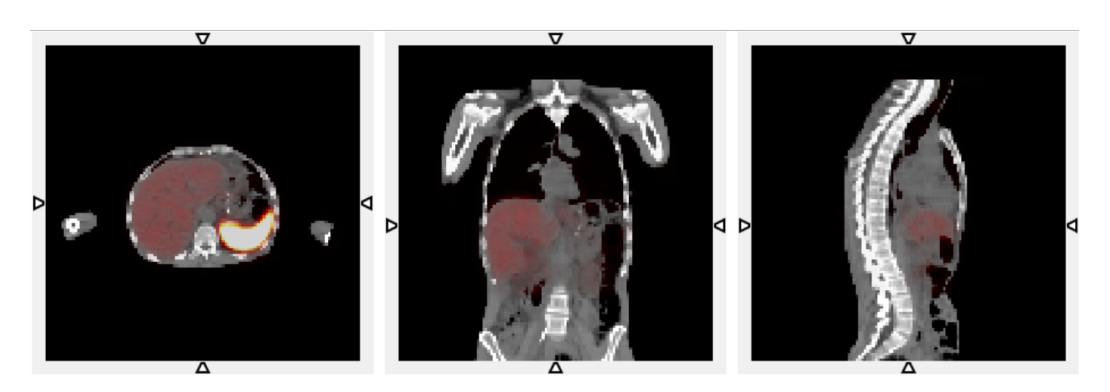


Figure 6.10: STIR reconstruction of Patient Data D, fused with CT, which forms the background for GT dataset Cases 4 and 8.

6.3.4.7 Patient dataset E

The fifth and final patient dataset used (Patient E) is based on a 52 year old female patient who had been admitted to hospital with centralised abdominal pain and vomiting. A CT scan demonstrated a suspicious looking 5 cm nodule in the abdomen. The clinical team suspected that this lesion could be a carcinoid tumour, and requested a Tektrotyd scan to assess the lesion. The Tektrotyd scan demonstrated low intensity uptake in the lower abdomen, but no other areas of abnormal uptake in the liver or elsewhere in the body.

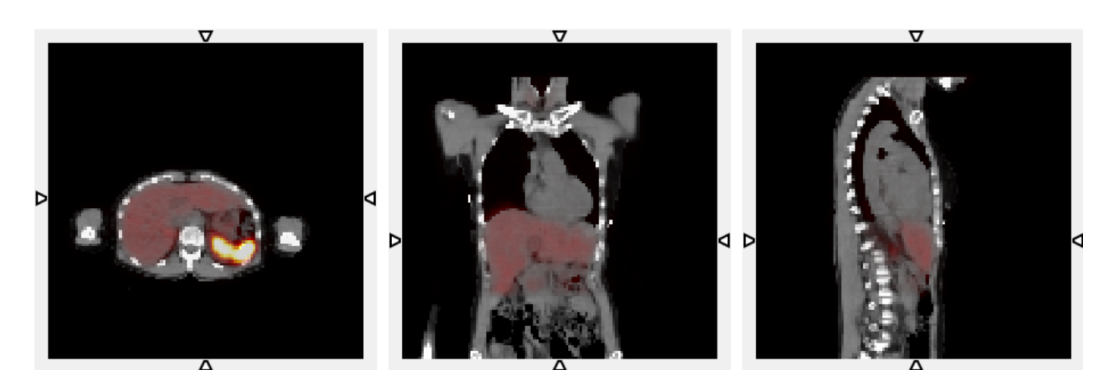


Figure 6.11: STIR reconstruction of Patient Data E, fused with CT, which forms the background for GT dataset Case 5.

6.3.4.8 Insertion of synthetic lesions

STIR was used to generate uniform spherical synthetic lesions. These were positioned at different points in the liver for the five different patient datasets, and were added to the background patient data. The addition of the lesions on top of the patient data, rather than replacing the voxel values, acts to introduce a small amount of non-uniformity which is more realistic than a completely uniform lesion.

For all five test cases with spherical lesions, the synthetic lesions were positioned within the liver. This placement reflects the most common site for NET metastases [Riihimäki et al., 2016]. In addition to this, the normal liver demonstrates physiological tracer uptake which is generally uniform, allowing a relatively homogenous background which is a useful comparison to the apparent lesion avidity (i.e. pre-PVC and post-PVC). The liver is also a clinically relevant organ for comparison to lesion uptake as liver uptake forms part of the Krenning score (described in Section 3.4.5.6).

The intensity of the lesion was compared with a uniform section of normal liver parenchyma, to give a ground truth value for relative activity. The intensity of the lesions to be added was adjusted such that the relative Target to Background Ratio (TBR) compared with normal liver was between 3.8 and 7.9 (based on relative uptake observed in clinical cases and within other research [Reilly et al., 2021]). Each of the spherical lesions had a diameter of 2.9 cm. This single lesion size, and the relatively narrow TBR range, was chosen since the effect of varying lesion size and TBR has been explored in detail in Section 5.4.1.2. The diameter of 2.9 cm

was representative of a sample of eight liver lesions identified in the clinical source SPECT-CT dataset.

6.3. Methods

For the generation of the GT test datasets, it was important to include a range of synthetic lesions, including those which are non-spherical and non-uniform in uptake. A combination of STIR and other software was used for creating non-spherical and non-uniform synthetic lesions. The processes used will be described for individual cases 6 to 9 in the relevant sections below. In addition to two cases with non-spherical synthetic lesions in the liver, test cases with non-spherical lesions in the bowel and lung were generated. These locations were chosen based on sites of possible metastatic spread for NETs.

6.3.5 Generation of GT test datasets

The Ground Truth datasets shown in Figures 6.23, 6.24, 6.25, 6.26, 6.27, 6.28, 6.29, 6.30, 6.31 were input to SIMIND in order to simulate imaging with a gamma camera. This section describes the process of simulation from GT data to reconstructed data, ready for application of PVC.

6.3.5.1 Data preparation for SIMIND

As discussed in Section 6.3.3, data produced in STIR cannot be input to SIMIND directly. A key step for preparing the data for input consisted of converting the binary data to unsigned integer data type (16 bits). Prior to doing this conversion, in order to retain precision which would be otherwise lost by converting float values to integer values, the whole image is multiplied by 100. In addition, as discussed in Section 6.3.3.4, modelling of attenuation in SIMIND is based on each pixel in units of $1000 \times \text{g/cm}^3$.

6.3.5.2 SIMIND simulation

The parameters used for MC simulation with SIMIND, replicating acquisition using a Siemens Symbia gamma camera, are detailed in Appendix C.

The number of photon histories simulated determines the accuracy of the simulation, but also impacts the processing time. The noise level is not impacted by this, instead a parameter within SIMIND (Index 25 in Appendix C) is used to

scale the image to a realistic activity, and therefore an image quality comparable to clinical images. In order to determine an appropriate value for scaling, a number of 'quick' simulations (approximately 30 minutes) were performed with a low number of photon histories, and the total counts in the peak energy window were compared with the total counts recorded in the peak energy window for the clinical data for each test dataset.

Once the appropriate scaling factor was clarified, the MC simulation was run, including Poisson noise. A full simulation of 120 projections around 360° , with appropriate counts took 3-4 hours to run. The number of photon histories was determined by the total counts in the input image and the number of projections. The average number of photon histories used in each simulation was 2.1×10^9 .

6.3.5.3 Reconstruction of Simulated data

Projection data, simulated using SIMIND, were reconstructed using STIR with 20 OSEM iterations (10 subsets). CT based attenuation correction and Dual Energy Window scatter correction were applied. A Gaussian smoothing ($\sigma = 5.3$ cm) was applied to the reconstructed data. Resolution modelling was not applied in the reconstruction following findings discussed in Chapter 4.

6.4 Results

6.4.1 SIMIND Set-up Validation

6.4.1.1 Detector position and motion

The expected distance (based on the sum of the radii shown on the PPM and assuming the "Radial Distance" parameter refers to the distance from the front face of the collimator to the centre of rotation) was compared with the measured distance between collimator faces of the Siemens Symbia system, measured with LEGP and LEHR collimators. Results are shown in Figure 6.12.

Figure 6.12 demonstrates that the physical distance between the front surfaces of collimators was approximately equal to the radius of detector 1 plus the radius of detector 2 as shown on the PPM. A difference of between 1 mm and 3 mm was

6.4. Results 203

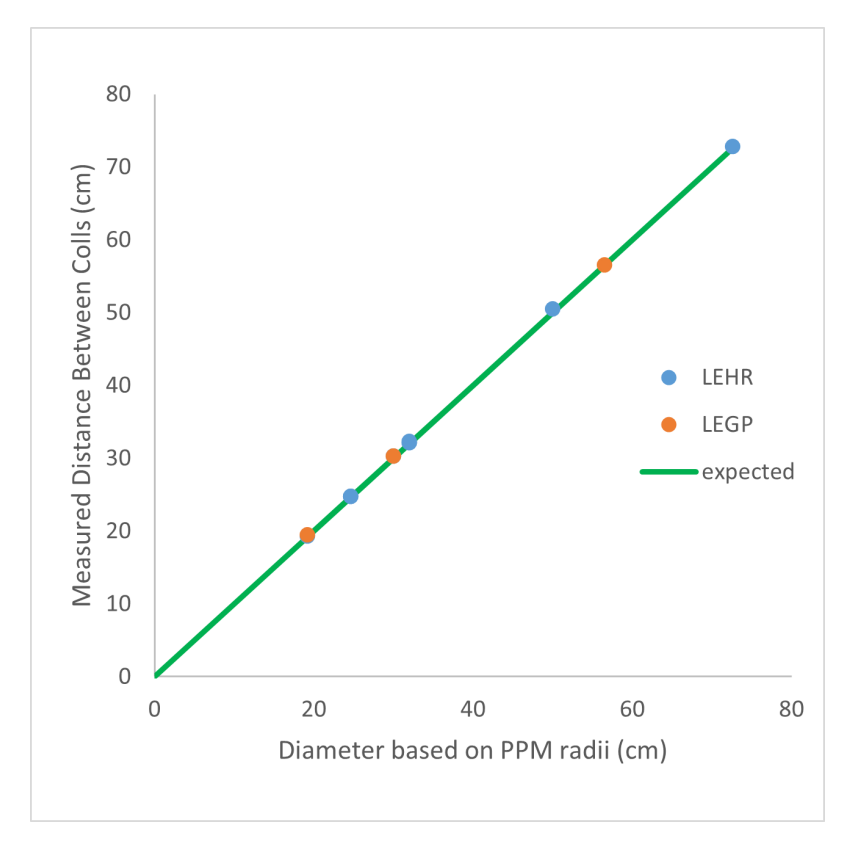


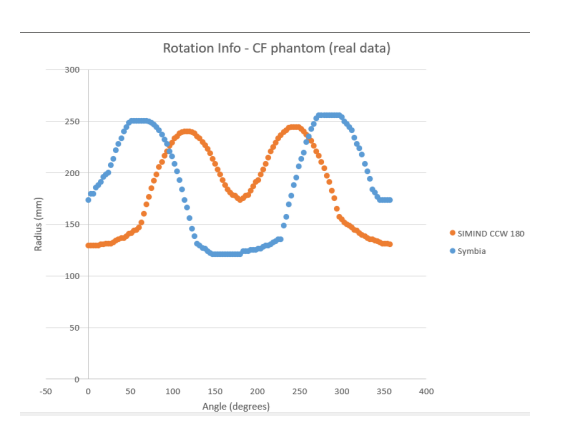
Figure 6.12: Results from measuring the distance for the LEHR and LEGP collimators are shown as points. The green line shows the expected distance based on the sum of the radii shown on the PPM. Approximate measurement error on each point was 3 mm, however error bars are too small to be seen here.

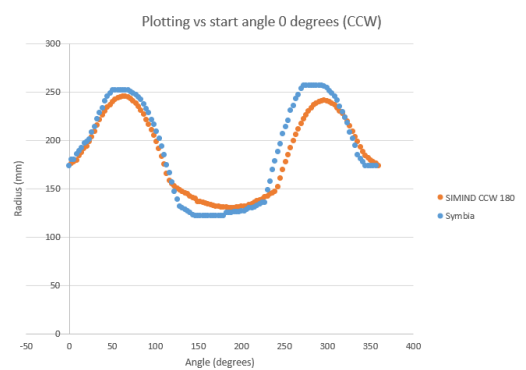
observed such that the measured distance was greater than the expected distance for each position (mean difference of 2.5 mm). Measurement uncertainties were estimated to be 3 mm due to positioning and reading the measuring tape which likely accounts for this difference. Uncertainties of this magnitude were not considered to be significant relative to the radial distances investigated (19.2 to 72.6 cm between detectors).

From these results, it can be concluded that radial distance parameter refers to the distance between the front surface of the collimator and the centre of rotation. If the alternative definition (i.e. referring to the surface of the crystal) was true, then the measured distance could be expected to be (approximately 4.8 cm) less than the PPM as it would not account for the physical distance between the surface of the crystal and the surface of the collimator.

6.4.1.2 Image Orientation

Plots demonstrating the RoR for real Symbia data and SIMIND simulated data with a counter clockwise rotation, and start angle set to 180° are shown in Figure 6.13. Figure 6.13a shows that the rotation simulated by SIMIND appears to be out of phase with the Symbia acquisition. When the start angle is artificially changed to be 0°, as in Figure 6.13b, the RoR plots are in phase. Therefore, for any STIR reconstruction of SIMIND data, the "Start angle" parameter in the header needed to be manually changed by 180 ° to ensure that projections were associated with the correct detector position.





- (a) RoR data for the real Symbia acquisition (blue) and the MC simulated data (orange).
- (b) RoR data with the start angle of the MC simulated data re-set in the header to 0°.

Figure 6.13: Plots of Radius of rotation vs projection angle for acquisition of a NEMA phantom acquired with the Siemens Symbia SPECT-CT, and simulated in SIMIND using a counter clockwise rotation starting at 180°.

Figure 6.14 shows projection data of a NEMA phantom at 180° (first projection angle), 270° , 0° and 90° as acquired by the Symbia gamma camera (top row). The bottom row of this figure shows the equivalent projections, based on the orientation of the shapes within the NEMA phantom. This shows that the equivalent projections are offset by 180° , supporting the conclusion drawn by the RoR analysis above that the "Start angle" parameter in the SIMIND data header should be manually changed by 180° .

These results demonstrate that that STIR reconstruction of SIMIND data is oriented as is expected, provided that a counter clockwise rotation is used and the header is manually edited to change the start angle by 180 °. The requirement for

Symbia vs SIMIND-CCW 180

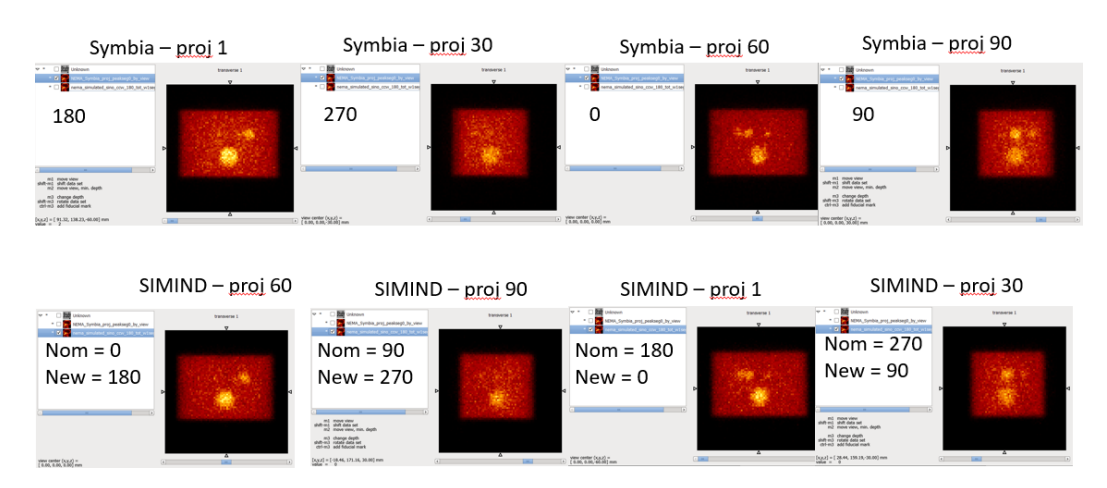


Figure 6.14: Review of projection images, comparing real projection images acquired using the Symbia gamma camera (top row) and the simulated projection images generated using SIMIND with a rotation set to Counter Clockwise, starting at 180 degrees (bottom row).

the change in start angle could be attributed to row-column reading order difference in Fortran vs C (SIMIND uses Fortran, STIR uses C).

6.4.1.3 Planar Spatial Resolution

Example images acquired on the Symbia system using filled capillary tubes are shown in Figure 6.15, and example images used to assess spatial resolution of the SIMIND simulation are shown in Figure 6.16.

Example profiles through the centre rod are shown in Figure 6.17. This Figure demonstrates the shapes of the profiles for both Symbia and SIMIND acquisitions over the range of distances investigated. The Gaussian fits to the data are also shown for each dataset. Using the Gaussian fits, the FWHM was calculated. Five FWHM values were calculated for each distance (one per rod) - allowing a mean FWHM value for the distance to be calculated for both Symbia acquisition and SIMIND simulation.

In addition to good agreement between Symbia and SIMIND data, in terms of the planar spatial resolution, it was also important to establish that the STIR system model used for reconstructing the test datasets was a reasonable representation of the real clinical system. The test datasets (described in Section 6.3.4) are based

6.4. Results 206

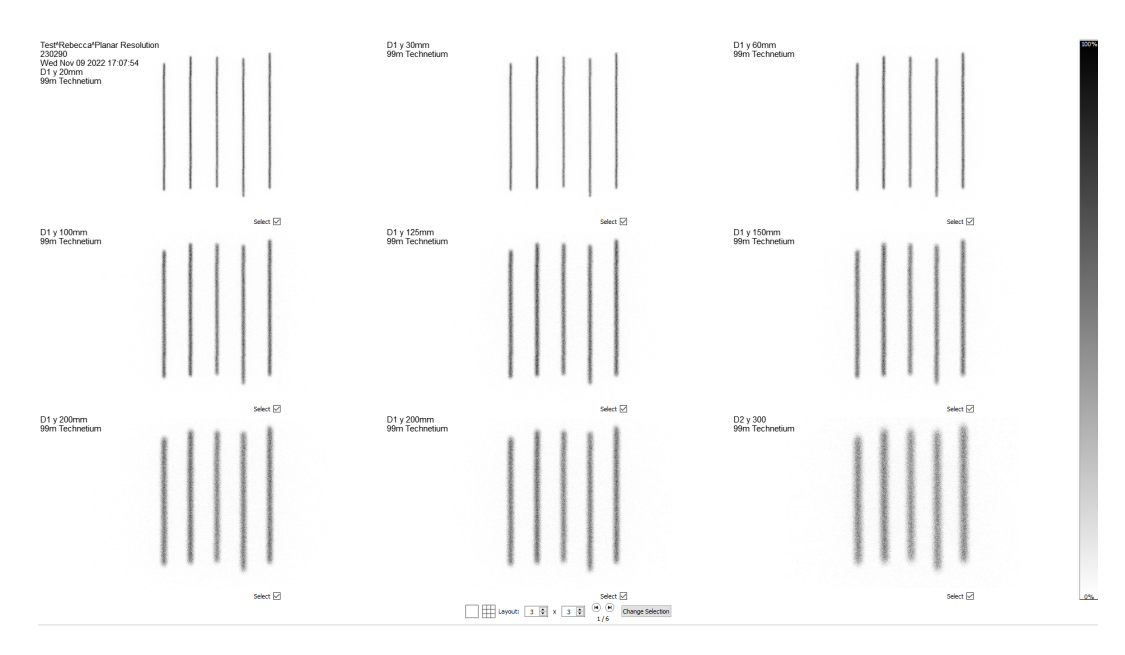
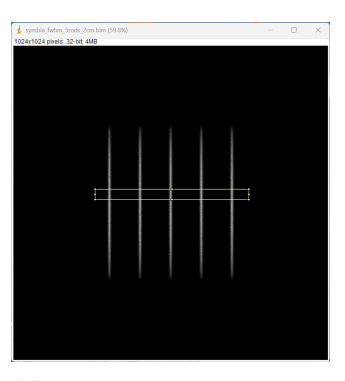


Figure 6.15: Resulting images of the rods used to measure the FWHM at different distances from the detector produced by the Symbia system as viewed on Hermes.



(a) Example SIMIND generated data for thin rods positioned 2 cm from the face of the collimator.



(b) Example SIMIND generated data for thin rods positioned 6 cm from the face of the collimator.



(c) Example SIMIND generated data for thin rods positioned 30 cm from the face of the collimator.

Figure 6.16: Example images generated in SIMIND, used to assess the planar system resolution of MC simulated images. 6.16a also shows region selected on ImageJ used for plotting line spread profiles.

on data acquired on a Siemens Symbia SPECT-CT system, therefore the STIR system model was defined using parameters appropriate to this specific gamma camera using an LEHR collimator. The process of calculating STIR parameters for a specific collimator is described in Section 4.4.2.1. SIMIND, Symbia and STIR planar resolution measurements (in terms of FWHM) are plotted against distance in Figure 6.18.

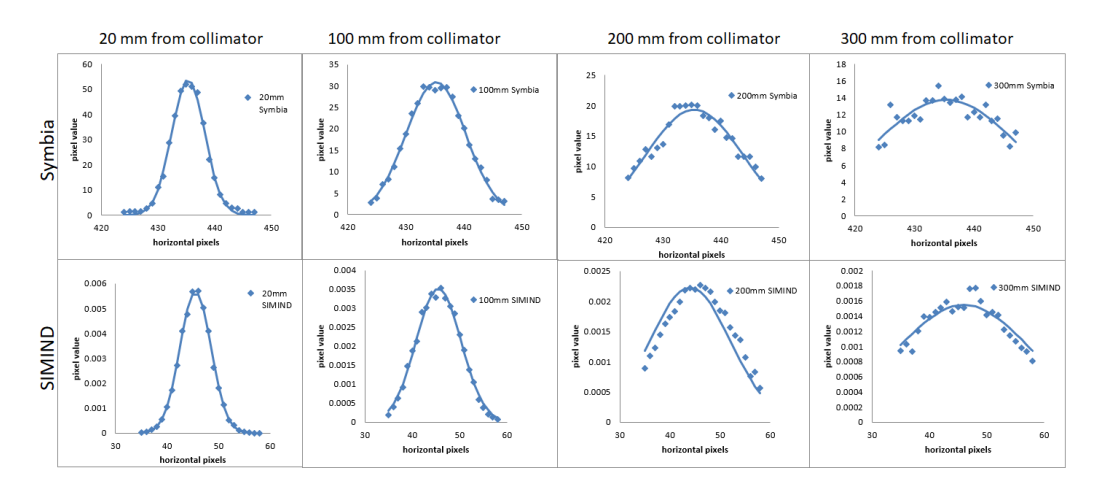


Figure 6.17: Example profiles through the acquired line sources as measured on Symbia and SIMIND, with a range of distances between test object and collimator face. The Gaussian fits based on parameters optimised by Excel Solver are shown as lines in each plot.

To compare the FWHM measurements between the Symbia acquisition and SIMIND simulation, a Bland-Altman plot was generated (Figure 6.19). This demonstrates a small bias in FWHM measurement of 0.4 mm (Symbia higher than SIMIND) which is shown as a solid line intersecting the y-axis. Overall, the differences are spread evenly around this mean value, and all fall within the limits of agreement representing the 95% confidence interval (1.96 \times Standard Deviation) shown as dashed lines at 1.0 and -0.2 mm in Figure 6.19.

Establishing that the planar spatial resolution of the SIMIND simulation agrees well with the Symbia data, to within experimental errors, is an important step in ensuring accurate conclusions about the SPECT resolution and associated PVE can be drawn from MC simulations.

6.4.1.4 Energy Spectra

Figure 6.20 shows the datasets used for comparison of simulated and real energy spectra. Figure 6.20 shows that the position and width of the ^{99m}Tc peak is very similar in both datasets. Both spectra demonstrate a similar magnitude of photons detected within the lower energy window, used for scatter correction. There is some discrepancy with the SIMIND simulation demonstrating higher counts at lower energies, however these would not be expected to contribute to the image. Overall,

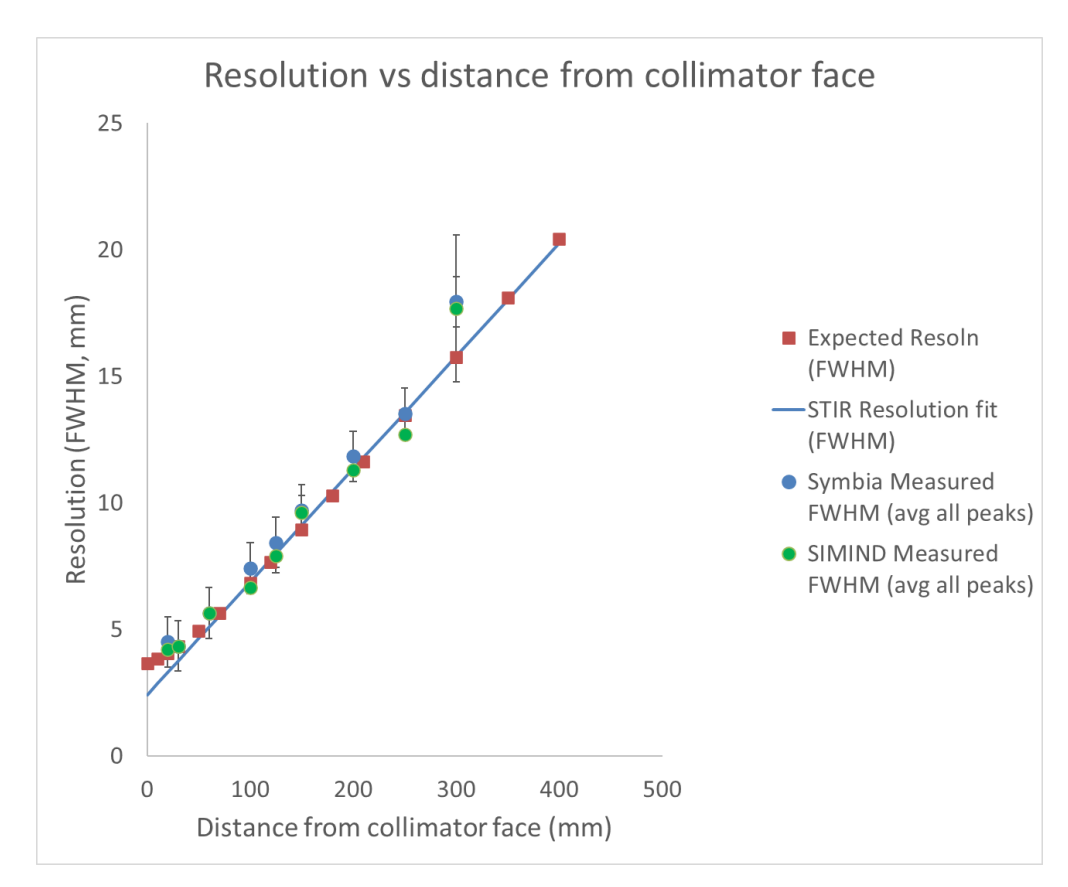


Figure 6.18: System resolution (in FWHM) variation with distance shown for real data, SIMIND data and STIR system model, compared with the expected system resolution (according to equation 2.6). Measurements made at a range of distances, using line sources acquired on Siemens Symbia (blue points) are compared with SIMIND measurements (green points). The linear resolution approximation made by STIR software is shown as a black line (from equation 4.2).

there is good correspondence between the real and simulated energy spectra within the energy windows used to produce the reconstructed SPECT image.

6.4.1.5 Planar Sensitivity

Equation 6.1 resulted in an average system sensitivity of 81.4 cps/MBq for the Symbia system.

The SIMIND simulation used to test the planar sensitivity resulted in the image shown in Figure 6.21. The total counts of the test object in Figure 6.21 was 147405. This resulted in a planar sensitivity measurement of 81.9 cps/MBq.

From these measurements, we can conclude that the sensitivity of a planar SIMIND MC simulation is comparable with the system sensitivity of the Siemens

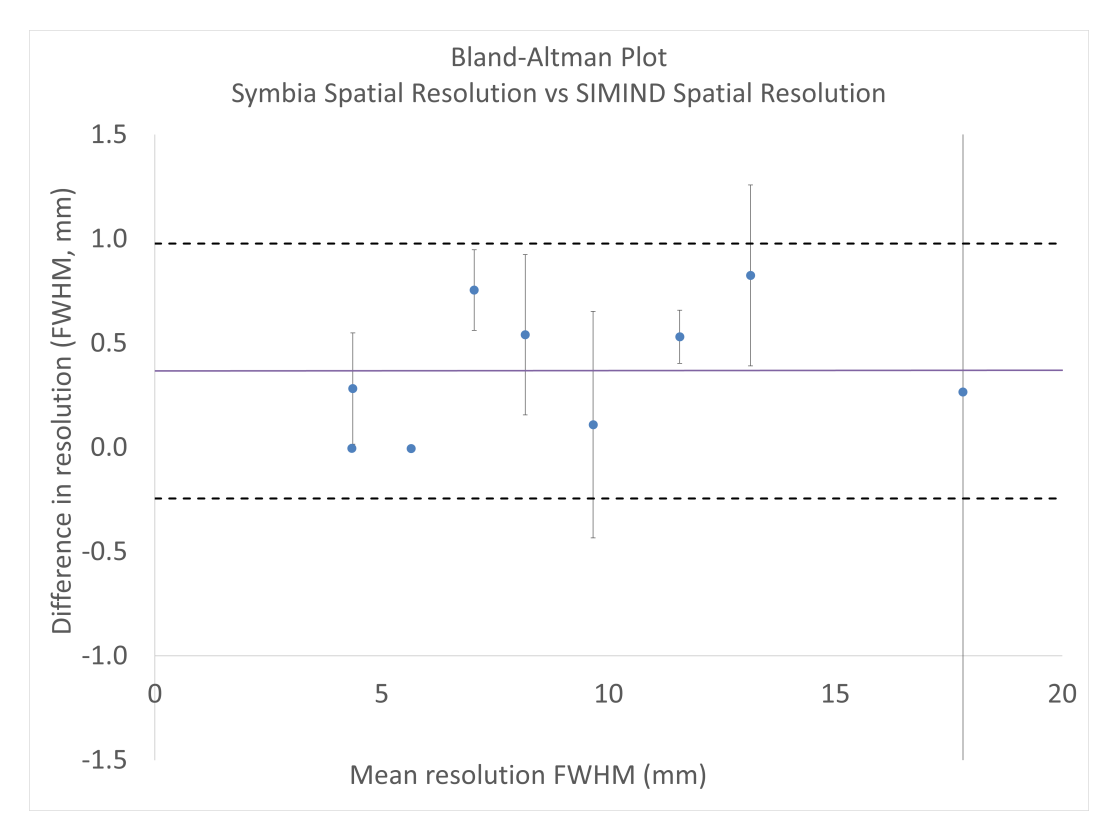


Figure 6.19: Bland-Altman plot showing mean spatial resolution as measured in SIMIND simulations and measurements from a real Symbia gamma camera. Measurements are based on images of five rods. Error bars are derived from the standard deviation of the average FWHM from the five rods.

Symbia gamma camera with LEHR collimators for ^{99m}Tc to within 1 %.

In addition to the images and sensitivity values, the profiles across the sensitivity phantoms are compared in Figure 6.22. Comparing these profiles, which were scaled to the mean count value of the central region, demonstrates that the SIMIND profile is more uniform. This could be expected due to slight imperfections in machining the phantom used to acquire the Symbia sensitivity data. Overall, no significant bias to any specific direction was noted in either profile.

6.4.2 Clinically Realistic Activity Distributions with lesions

6.4.2.1 Case 1: Spherical Lesion in liver (Patient Data A)

A spherical synthetic lesion, diameter of 2.9 cm (volume 12.5 cm³), lesion:liver TBR of 3.75, was added to patient dataset A (images shown in Figure 6.7) to produce input (Ground Truth) data for SIMIND simulation. The resulting GT

6.4. Results 210

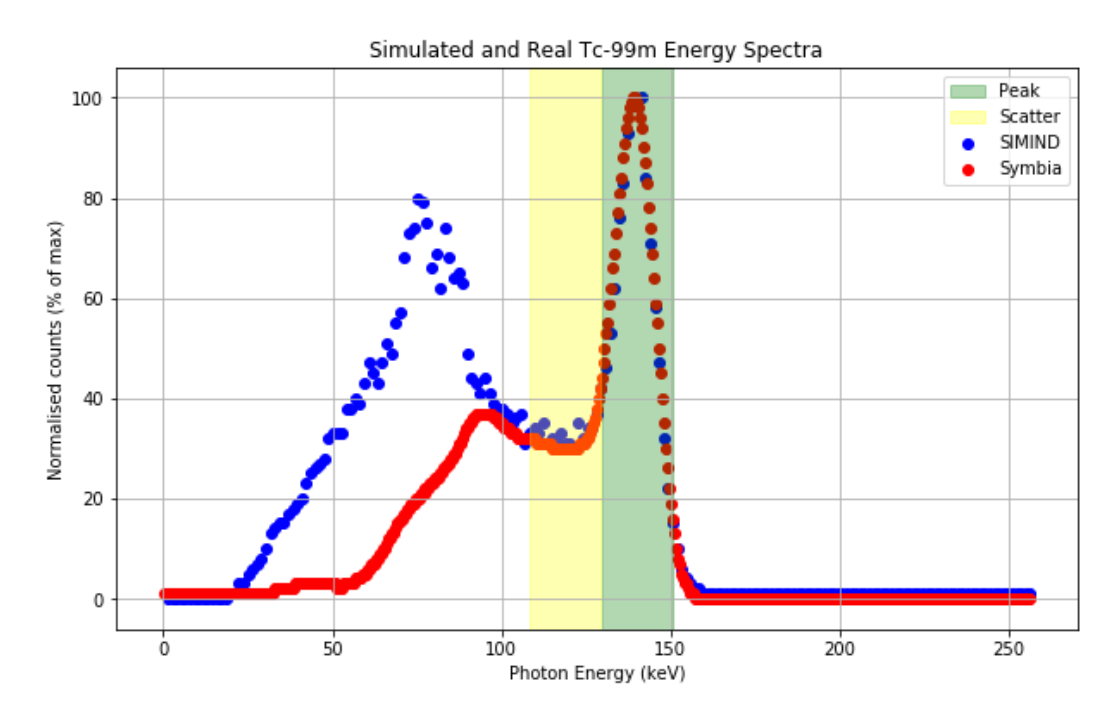


Figure 6.20: Energy spectrum for ^{99m}Tc SIMIND simulation of example dataset 1 of Tektrotyd data, overlayed with a spectrum acquired on the Siemens Symbia gamma camera of a Tektrotyd scan patient. Count data are normalised to the maximum value of each spectrum.

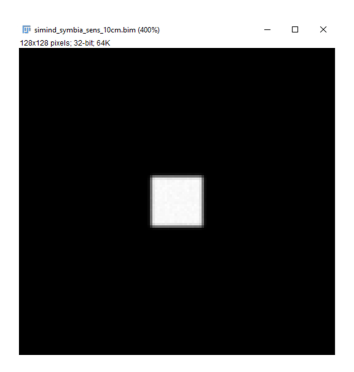


Figure 6.21: SIMIND simulation for the assessment of planar sensitivity.

dataset for test Case 1 is shown in Figure 6.23.

6.4.2.2 Case 2: Spherical Lesion in liver (Patient Data B)

A spherical synthetic lesion, diameter of 2.9 cm (volume 12.5 cm³), lesion:liver TBR of 4.63, was added to patient dataset B (images shown in Figure 6.8) to produce input (Ground Truth) data for SIMIND simulation. The resulting GT dataset for Test Case 2 is shown in Figure 6.24.

6.4. Results 211

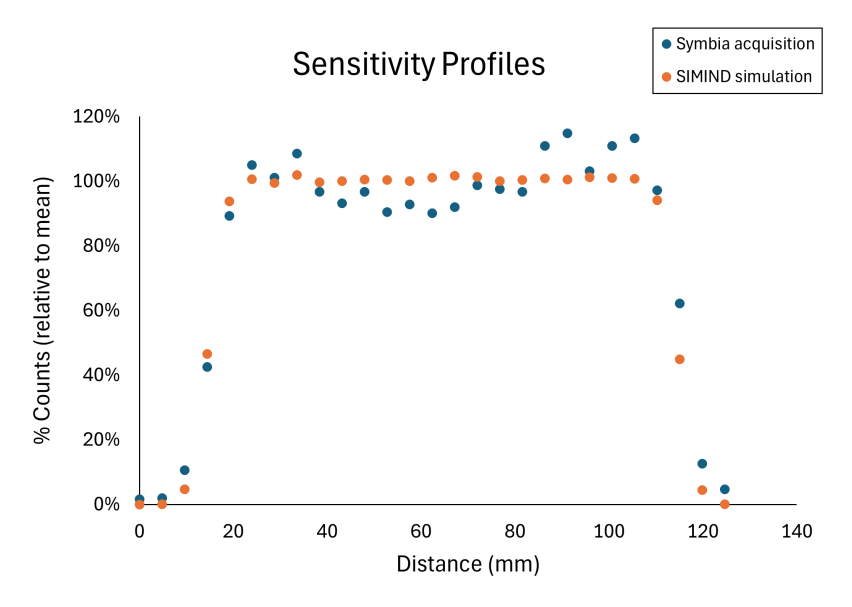


Figure 6.22: Sensitivity profiles.

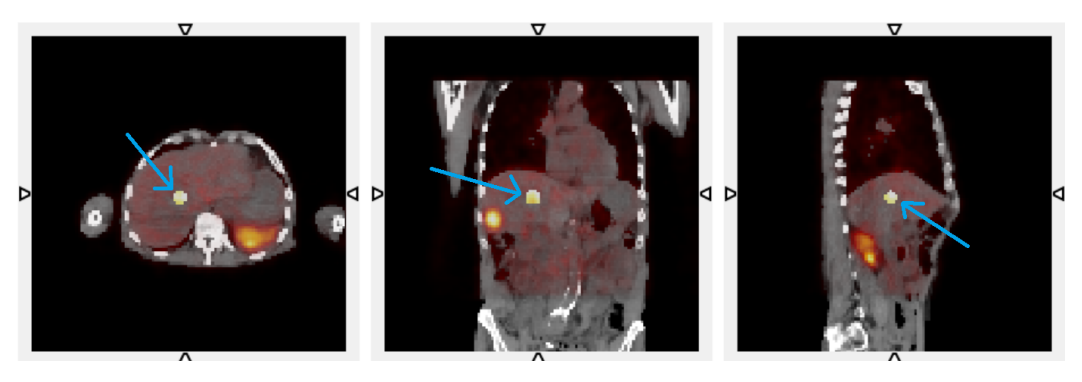


Figure 6.23: Data of test case 1; spherical lesion inserted in the liver of Patient dataset A. These data were used as GT data and were input to SIMIND for simulation. Activity distribution displayed fused with CT.

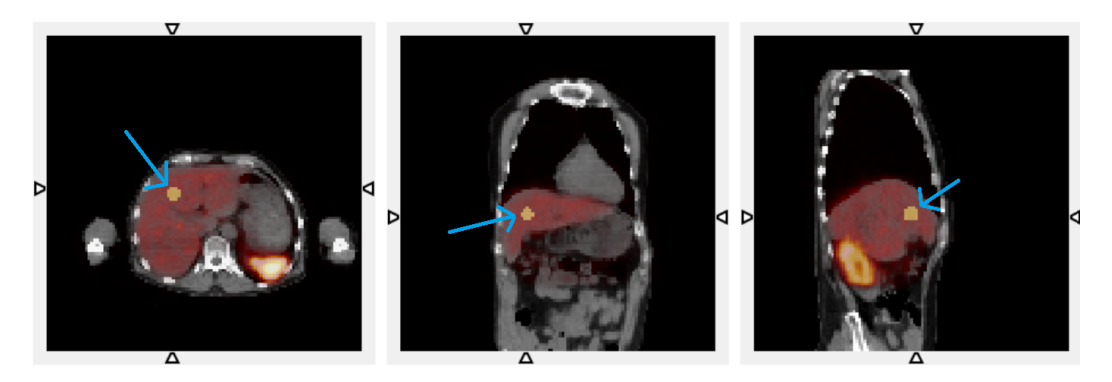


Figure 6.24: Data of test case 2; spherical lesion inserted in the liver of Patient dataset B. These data were used as GT data and were input to SIMIND for simulation. Activity distribution displayed fused with CT.

6.4.2.3 Case 3: Spherical Lesion in liver (Patient Data C)

A spherical synthetic lesion, diameter of 2.9 cm (volume 12.5 cm³), lesion:liver TBR of 5.16, was added to patient dataset C (images shown in Figure 6.9) to produce input (Ground Truth) data for SIMIND simulation. The resulting GT dataset for Test Case 3 is shown in Figure 6.25.

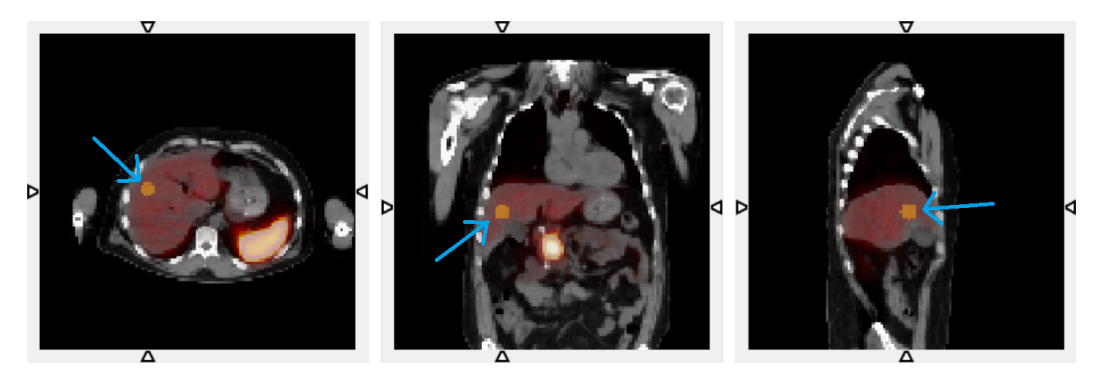


Figure 6.25: Data of test case 3; spherical lesion inserted in the liver of Patient dataset C. These data were used as GT data and were input to SIMIND for simulation. Activity distribution displayed fused with CT.

6.4.2.4 Case 4: Spherical Lesion in liver (Patient Data D)

A spherical synthetic lesion, diameter of 2.9 cm (volume 12.5 cm³), lesion:liver TBR of 4.08, was added to the patient dataset D (images shown in Figure 6.10) to produce input (Ground Truth) data for SIMIND simulation. The resulting GT dataset for Test Case 4 is shown in Figure 6.26.

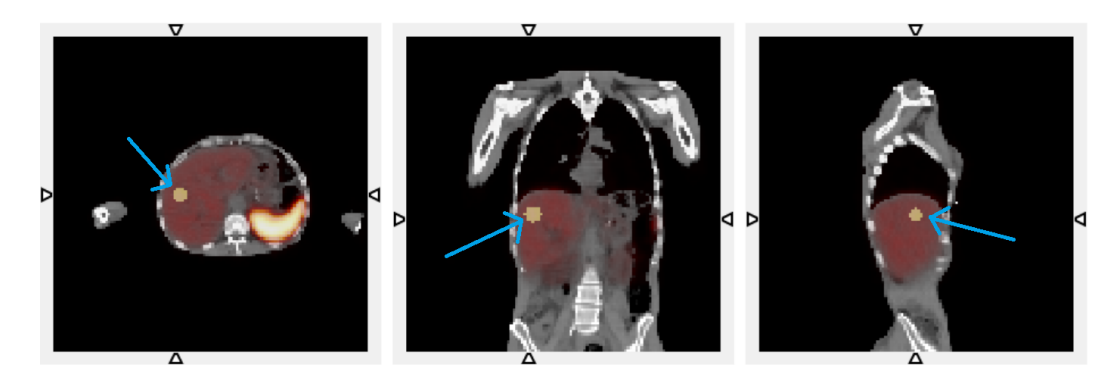


Figure 6.26: Data of test case 4; spherical lesion inserted in the liver of Patient dataset D. These data were used as GT data and were input to SIMIND for simulation. Activity distribution displayed fused with CT.

6.4.2.5 Case 5: Spherical Lesion in liver (Patient Data E)

A spherical synthetic lesion, diameter of 2.9 cm (volume 12.5 cm³), lesion:liver TBR of 4.72, was added to patient dataset E (images shown in Figure 6.11) to produce input (Ground Truth) data for SIMIND simulation. The resulting GT dataset for Test Case 5 is shown in Figure 6.27.

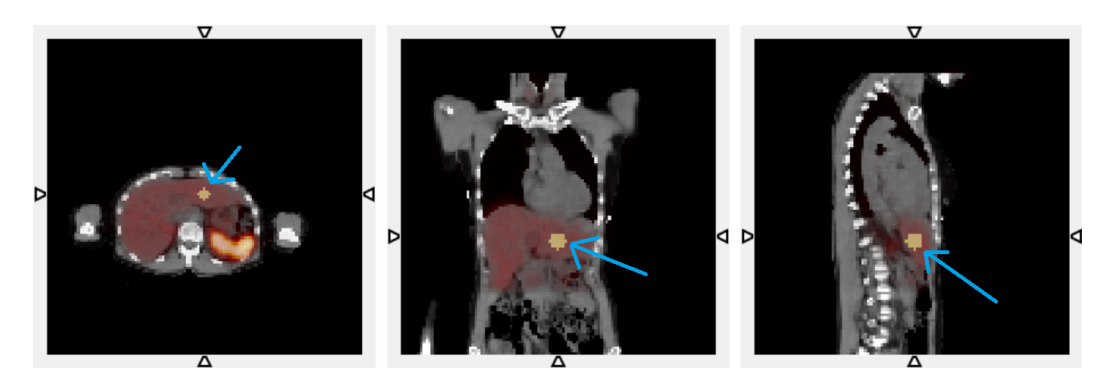


Figure 6.27: Data of test case 5; spherical lesion inserted in the liver of Patient dataset E. These data were used as GT data and were input to SIMIND for simulation. Activity distribution displayed fused with CT.

6.4.2.6 Case 6: Non-Spherical Lesion in Bowel (Patient data A)

The final step of complexity in developing realistic test datasets was to use non-spherical synthetic lesions.

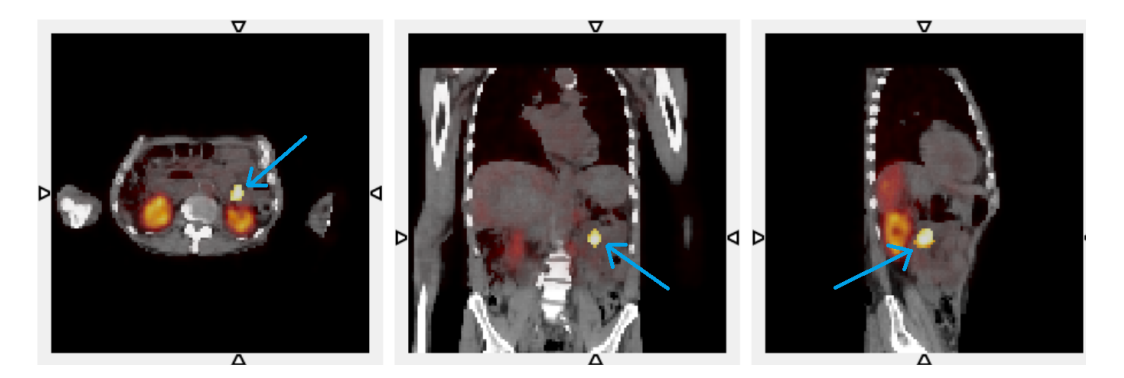


Figure 6.28: Data of test case 6; non-uniform and non-spherical lesion inserted in the bowel area of Patient dataset A. These data were used as GT data and were input to SIMIND for simulation. Activity distribution displayed fused with CT.

To produce test case 6, one of the tracer-avid liver metastases (referred to in Section 6.4.2.1) was manually delineated using ITK-SNAP MIRAS software [Yushkevich et al., 2006]. This produced a non-uniform lesion with a non-spherical

outline. The volume of the synthetic lesion was 18.3 cm³. This lesion was converted into interfile format and added to Patient dataset A, after shifting the position of the lesion. The GT intensity of the lesion was 5 times that of normal liver. The new lesion position was in the bowel; close to the left kidney which demonstrates physiological tracer uptake. This is shown in Figure 6.28.

6.4.2.7 Case 7: Non-Spherical Lesion in liver (Patient data B)

Test case 7 incorporates another non-spherical and highly non-uniform synthetic lesion. For this test case, patient dataset B was used for the background activity distribution. The synthetic lesion was added to the liver, which was known not to contain any existing metastases.

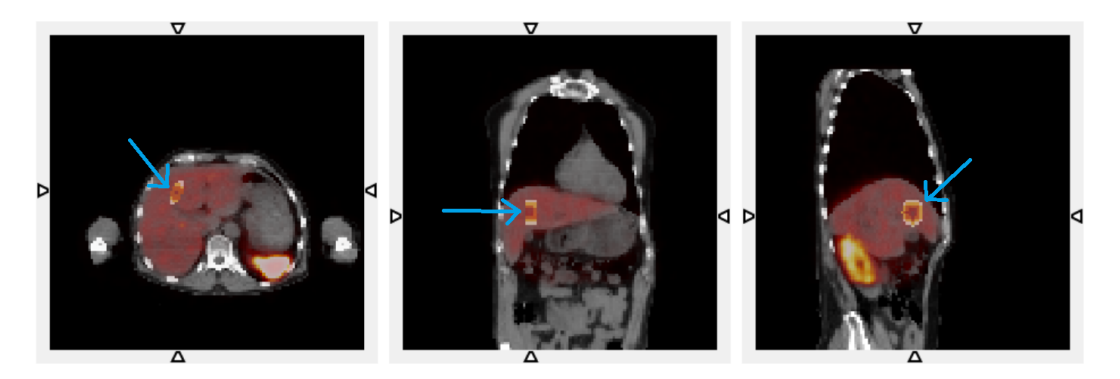


Figure 6.29: Data of test case 7; non-spherical and highly heterogenous lesion inserted in the liver of Patient dataset B. These data were used as GT data and were input to SIMIND for simulation. Activity distribution displayed fused with CT.

The synthetic lesion for test case 7 was produced using a combination of the existing shapes in STIR. Ellipsoids of varying size were defined and combined to produce a non-circular object with an inner volume which was less active than the outer shell. This was designed to represent a lesion with a necrotic and non-active core. The final input GT for test data case 7 is shown in Figure 6.29. In test case 7, the lesion volume was 31.4 cm³, a maximum dimension of 4.9 cm, and with a lesion to normal liver TBR of 6.4.

6.4.2.8 Case 8: Non-Spherical Lesion in liver (Patient data C)

Test data case 8 incorporates the same non-spherical, heterogenous, lesion as defined for case 7. However, for case 8 the lesion is positioned in the liver of patient

dataset C. Voxel values were scaled such that the tumour to background liver ratio was 5.1. The GT data for test case 8 is shown in Figure 6.30.

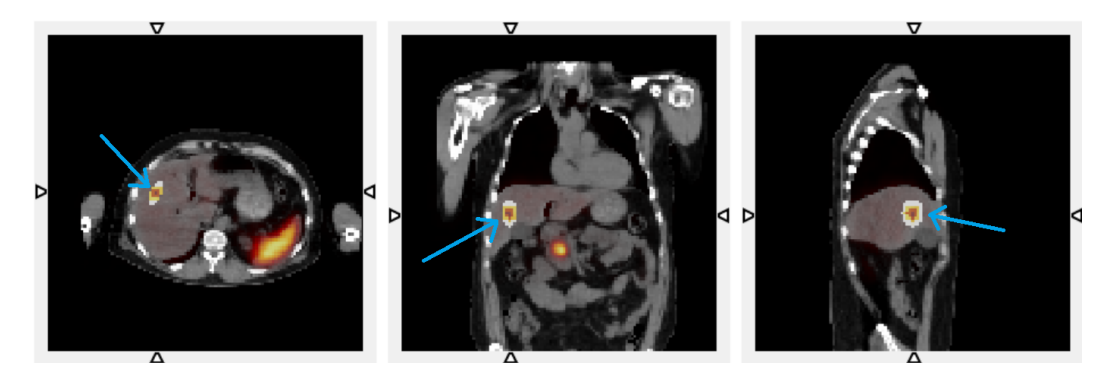


Figure 6.30: Data of test case 8; non-spherical and highly heterogenous lesion inserted in the liver of Patient dataset C. These data were used as GT data and were input to SIMIND for simulation. Activity distribution displayed fused with CT.

6.4.2.9 Case 9: Non-Spherical Lesion in lung (Patient data D)

Test case 9 utilises the background activity distribution from patient D. Case 9 also incorporates a lesion which was segmented from patient A.

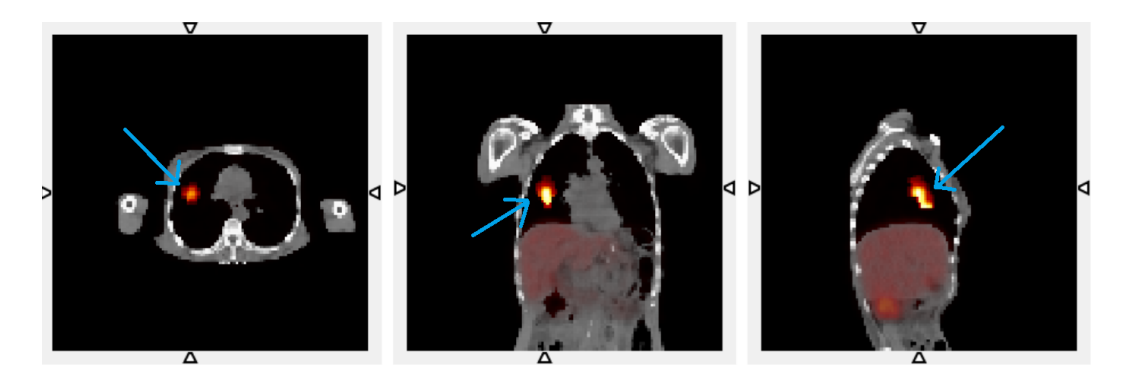


Figure 6.31: Data of test case 9; non-spherical and heterogenous lesion inserted in the right lung of Patient dataset D. These data were used as GT data and were input to SIMIND for simulation. Activity distribution displayed fused with CT.

The lesion was 59.1 cm³ in volume, with a maximum dimension of 6.6 cm. This lesion was subsequently positioned in the lung of patient data D. This test case was designed to examine the effect of a hot lesion in a very low activity background (i.e. a very high contrast situation) which would be challenging for some PVC methods. Around 20 - 30 % of all NETs cases develop in the lungs [Sergieva et al., 2016], so this challenging situation is also clinically relevant. The GT data for test

case 9 is shown in Figure 6.31. The intensity of the lesion was 4.6 times that of normal liver.

6.4.3 SIMIND Simulation of GT test datasets

6.4.3.1 Radius of Rotation review

For each simulation based on clinical cases, the simulated detector position was checked to ensure it was similar to the acquisition of the real data. The detector position (distance from the centre of rotation) for each projection angle for the real clinical case was compared with the equivalent SIMIND simulation (similar to phantom work as shown in Figure 6.13). This is important as the source to detector distance affects the resolution, and the SIMIND simulation should replicate the clinical situation as realistically as possible.

In general, good agreement was demonstrated between simulated and real detector positions. Instances of deviation between clinical and SIMIND detector positions were noted, including some discontinuities in the clinical data. This could be attributed to patient clothing or blankets hanging down and activating the sensor on the detector. Detector position in the SIMIND simulation is based on the outline of the patient, and a defined density threshold. In this case, it is possible that the density of the material was lower than the defined threshold, or that the physical material was not imaged within the CT FOV. Alternatively, the patient could have moved slightly during the scan. These small deviations between clinical and simulated detector positioning are not expected to affect the performance of the PVC algorithms as the simulated Radius of Rotation (RoR) values are in a clinically realistic range.

6.4.3.2 Comparison of SIMIND and Clinical Projection Data

To assess whether SIMIND has produced realistic projection data, the total counts were assessed, along with an evaluation of the Standard Deviation (SD) in a relatively uniform Region of Interest (ROI) in a specific projection. The ROI, 15×28 pixels in size, was positioned in the shoulder area of the posterior projection, as shown in Figure 6.32. SD values are summarised in Table 6.5.

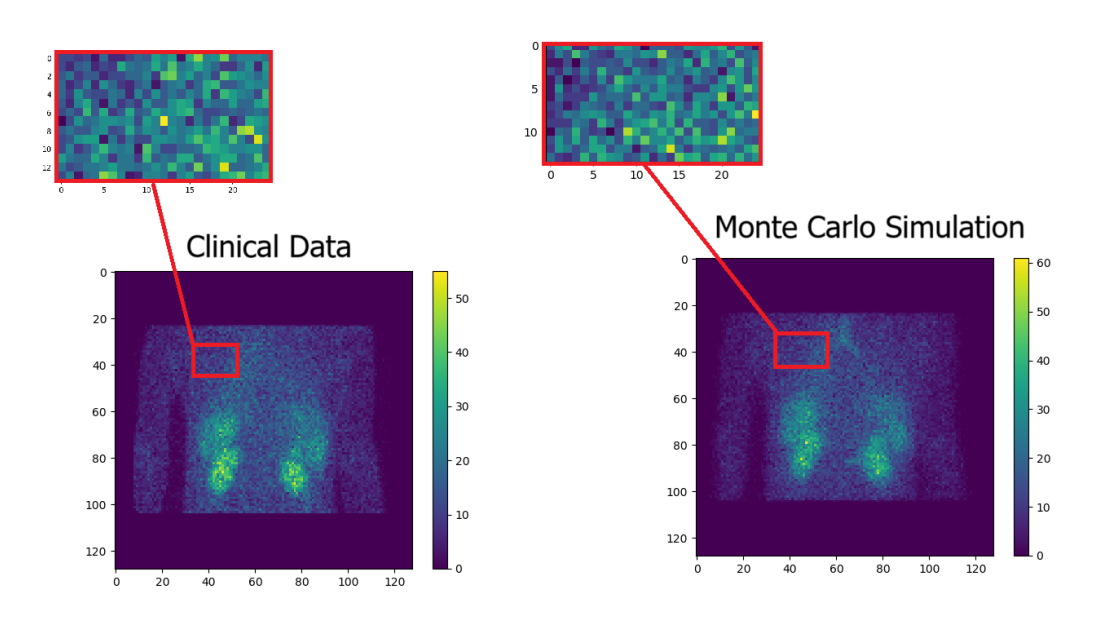


Figure 6.32: Review of standard deviation of voxel values in a uniform area of the same size, comparing clinical acquisition to SIMIND simulation, for patient dataset A.

Case Ref	Clinical proj SD	SIMIND proj SD
Case 1	3.21	3.15
Case 2	1.94	1.57
Case 3	2.04	1.78
Case 4	2.53	2.06
Case 5	2.29	2.08
Case 6	3.21	3.05
Case 7	1.94	1.54
Case 8	1.94	1.59
Case 9	2.04	1.84

Table 6.5: Summary of SD in uniform area of projection data acquired; comparing clinical data and SIMIND simulation.

6.5 Discussion

6.5.1 Monte Carlo Validation

6.5.1.1 Planar Spatial Resolution Validation

Figure 6.18 demonstrates that there is good agreement (within experimental uncertainties) up to around 30 cm from the front face of the collimator between the real clinical gamma camera, the Monte Carlo simulation and the system model used in the reconstruction software. In the datasets used, the RoR was below 30 cm in all cases. Therefore, the system model used for reconstruction is sufficiently accurate for the production of realistic resolution in reconstructed data.

Figure 6.19 shows a small bias between planar resolution measurements on the Symbia gamma camera, compared with the SIMIND simulation. This bias is less than 10% of the smallest FWHM value (measurement made 20 mm from the collimator face) demonstrating that the Monte Carlo simulation agrees well with the real gamma camera in terms of planar spatial resolution.

6.5.1.2 Energy Spectra Comparison

A limitation of the collection of energy spectra datasets for SIMIND and real gamma camera data (as described in Section 6.3.2.3) is that the Symbia data were acquired from an anterior static position over the patient's head and shoulders, whereas the SIMIND data are based on a SPECT acquisition around the torso. This difference is due to a limitation in the Symbia acquisition software which only allows energy spectra calculation during planar image acquisition. In addition to this, SIMIND simulation does not include backscatter from other objects which may be in the room or natural background radiation [Ljungberg and Strand, 1989]. The differences observed at low energies between the shapes of the measured and simulated energy spectra are therefore not unexpected.

The impact of a genuine discrepancy between simulation and measurement energy spectra is expected to be minimal for imaging with ^{99m}Tc. However, this would need to be assessed in more detail for imaging with other radionuclides - in particular for those with multiple photo-peaks, as the scatter correction could be

affected.

6.5.2 Test Dataset Generation

There are multiple examples in previous literature where synthetic lesions have been added digitally to clinical imaging data [Gabrani-Juma et al., 2020, Ahn et al., 2015]. This is most often performed in order to assess visual perception or detectability (e.g. [D'Alessandro et al., 2011, Madsen et al., 2006] in CT and PET, respectively), or segmentation (e.g. [Berthon et al., 2015] in PET) rather than for quantitative evaluation.

It is not possible to define a synthetic lesion which truly captures the boundaries of a real tumour on a digital matrix of a clinically relevant size (i.e. 128×128 or 256×256). These voxel dimensions are too large to contour to true lesion edges. However, it is unclear how the boundary of a lesion could be captured in the digitisation process, even with very high resolution imaging. In addition to this, non-encapsulated lesions would need to consider microscopic spread. In this study, since the emphasis is on quantitative accuracy, rather than visual perception, it was not important for the appearance of the GT datasets (prior to simulation with SIMIND and reconstruction with STIR) to be realistic in appearance. However, following simulation and reconstruction, the resulting images used in this research are visually similar to clinical data, in terms of resolution and noise level, as shown in Figures 7.4 and 7.11.

6.6 Conclusions

This chapter demonstrated validation testing to show that the SIMIND MC simulations used to generate test datasets are a realistic replication of real gamma camera acquisitions. Work was also performed to allow SIMIND to be used with STIR software for reconstruction.

Datasets have been generated which will enable robust testing of PVC algorithms on realistic clinical cases, including scenarios which are challenging for conventional PVC techniques, such as non-spherical, heterogenous lesions. This data will be used in the next chapter.

Chapter 7

Testing of PVC algorithms

7.1 Aim

This chapter aims to draw on the findings and conclusions from previous chapters by testing three Partial Volume Correction (PVC) methods using a set of realistic, clinically relevant, simulated test datasets. Tests will assess the accuracy of the Single Target Correction (STC) and Richardson-Lucy (RL) methods, which incorporate case-specific resolution estimation, compared with the Recovery Coefficient (RC) method which does not. Assessment by visual interpretation will compare both region-based and voxelwise metrics with Ground Truth (GT). Results will give an indication of the suitability of each of the PVC algorithms for application in ^{99m}Tc oncology SPECT imaging.

7.2 Methods

7.2.1 Test Datasets

The set of 9 simulated, realistic, test datasets as described in Section 6.3.4 were used. Each dataset has a known GT lesion value which was compared with measurements uncorrected for the Partial Volume Effect (PVE), and with measurements corrected using different PVC methods as described below.

7.2.2 PVC methods

Chapter 3 explored existing PVC methods in the literature and identified three methods for further study and development (see Section 3.4.5.1 for explanation of

221

the selection). The selected methods of STC with perturbation to estimate the local Point Spread Function (PSF), the RL implementation of iterative Deconvolution (itD) with perturbation (referred to as RL in this chapter for brevity) and phantom-based RC will be examined in detail in the current chapter.

The perturbation technique was performed using the method described in Chapter 5. The noise-free point source was, again, forward projected using STIR.

7.2.2.1 Single Target Correction (STC)

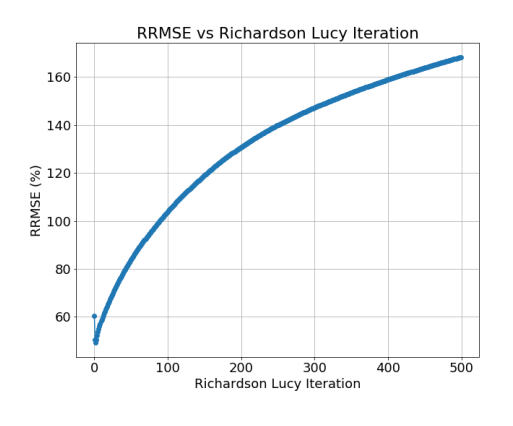
A full description of the STC algorithm can be found in Section 3.4.3.2. STC was implemented in Python. Segmentation was applied using the known GT lesion shape. As described in Section 5.3.7, 10 STC iterations were used, a non-negativity constraint was imposed and the case-specific PSF was estimated using the perturbation method for each individual lesion.

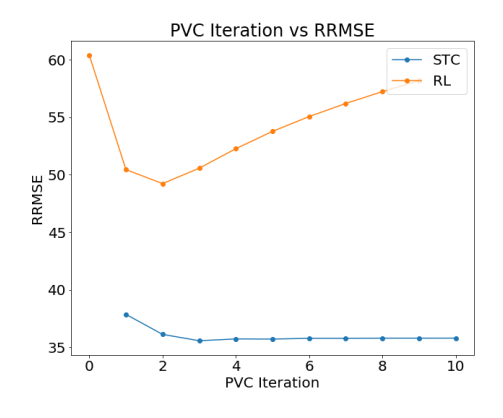
Due to the spatial variation in PSF, the correction was applied to a $30 \times 30 \times 30$ voxel cube around the local volume of the lesion. Corrected images of this local volume were produced by the STC algorithm.

7.2.2.2 Iterative Deconvolution using Richardson-Lucy (RL)

A full description of the RL algorithm can be found in Section 3.4.4.1. RL was implemented in Python. As with STC, the case-specific PSF was estimated using the perturbation method.

Preliminary work reviewing the Relative Root Mean Square Error (RRMSE) was used to determine the optimal number of RL iterations - balancing improvement in accuracy with increased noise (i.e. reduced precision). The algorithm was run to 500 iterations, which demonstrated a steep decrease in RRMSE initially, followed by a rise (see Figure 7.1a), indicating that a high number iterations did not result in a more precisely corrected image. The RRMSE was compared with STC for up to 10 RL iterations (see Figure 7.1b). Cases 1-5 were reviewed in this way and demonstrated a similar pattern. Going forward, 7 RL iterations is used for PVC as this compromised between RRMSE and regional mean accuracy. However, if data with different levels of noise were used, this optimal number of RL iterations would need to be re-evaluated.





- (a) Number of RL iterations vs RRMSE
- (b) Number of PVC iterations vs RRMSE

Figure 7.1: Example RRMSE evaluation for Case 3, for images with PVC using RL applied up to 500 RL iterations (a) and comparing STC and RL for up to 10 iterations (b).

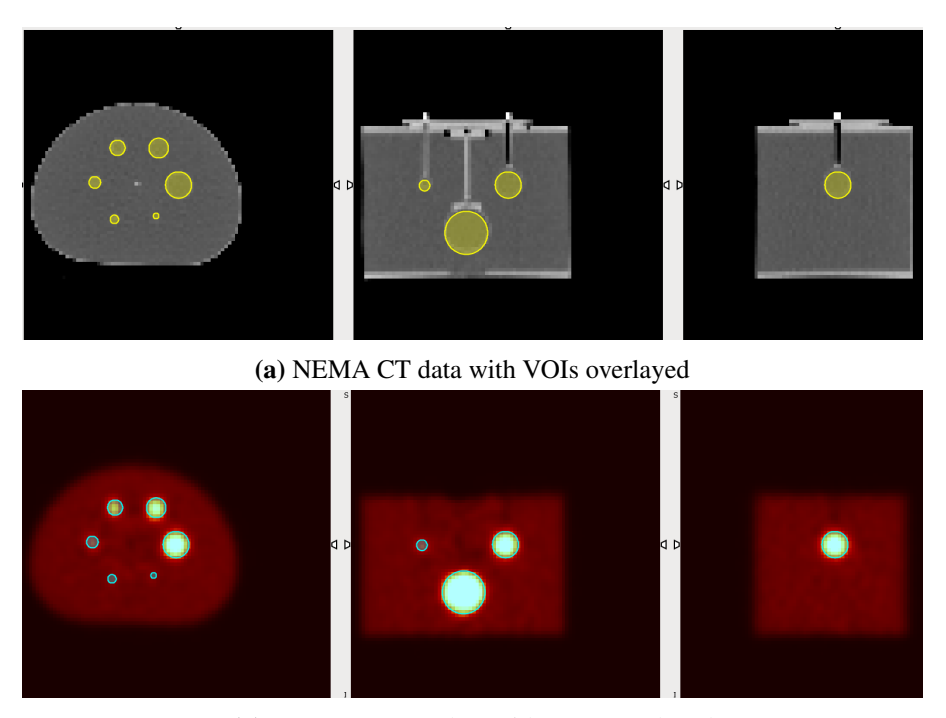
As with STC, the RL correction was applied to a $30\times30\times30$ voxel cube around the local volume of the lesion. Corrected images of this local volume were produced.

7.2.2.3 Recovery Coefficient (RC)

A RC curve was generated using phantom data acquired using the gamma camera system (a Siemens Symbia Intevo Bold) used for the patient datasets, with the same acquisition parameters (see Table 6.4). A standard NEMA phantom was used [National Electrical Manufacturers Association (NEMA), 2001], with a 60 mm diameter sphere added in a central position, on a different plane to the other spheres to avoid unwanted spill-over. A sphere to background activity concentration ratio of 5:1 was used in order to align with the GT TBR values set in the synthetic lesions (see Section 6.4.2). The data were reconstructed using STIR, using the same reconstruction parameters as the clinical Tektrotyd datasets described in Chapter 6.

AMIDE software's segmentation tool was used to position spherical Volumes of Interest (VOIs) of sizes corresponding to the known sphere dimensions to the registered CT dataset over the spheres. The VOIs are shown in yellow in Figure 7.2a. Four 60 mm diameter background VOIs were also defined.

The RC curve was plotted using measurements made of mean voxel value in each spherical VOI, as shown in Figure 7.3. A pseudo calibration factor (pCF) was



(b) NEMA SPECT data with VOIs overlayed

Figure 7.2: Screengrabs from AMIDE showing VOIs positioned on the NEMA phantom used for RC calculation. Left to right: transaxial, coronal and axial planes.

derived from the known background concentration and the average of four 60 mm diameter background sphere mean voxel values, assuming that this was not affected by the PVE. This gave an pCF of 0.0003 Bq/ml per voxel value, from which a measured mean activity concentration was calculated for each sphere. The RC values used to plot the curve were calculated as the measured activity concentration divided by the known activity concentration for each sphere (equation 3.1).

A non-linear least squares fit of the RC values vs sphere volume was performed using SciPy in Python [The SciPy community, 2019] (previously described in Section 4.5.1.2) with the function described in equation 3.3 (reproduced below in equation 7.1 for ease of reading).

$$f_{RC}(v) = \left(1 + \left(\frac{a}{v}\right)^b\right)^{-1} \tag{7.1}$$

where v is the sphere volume in ml, and a and b are fitting parameters.

This gave mean RC fitting parameters for a = 11.2 and b = 0.43.

RC corrected values were calculated by dividing the uncorrected regional mean

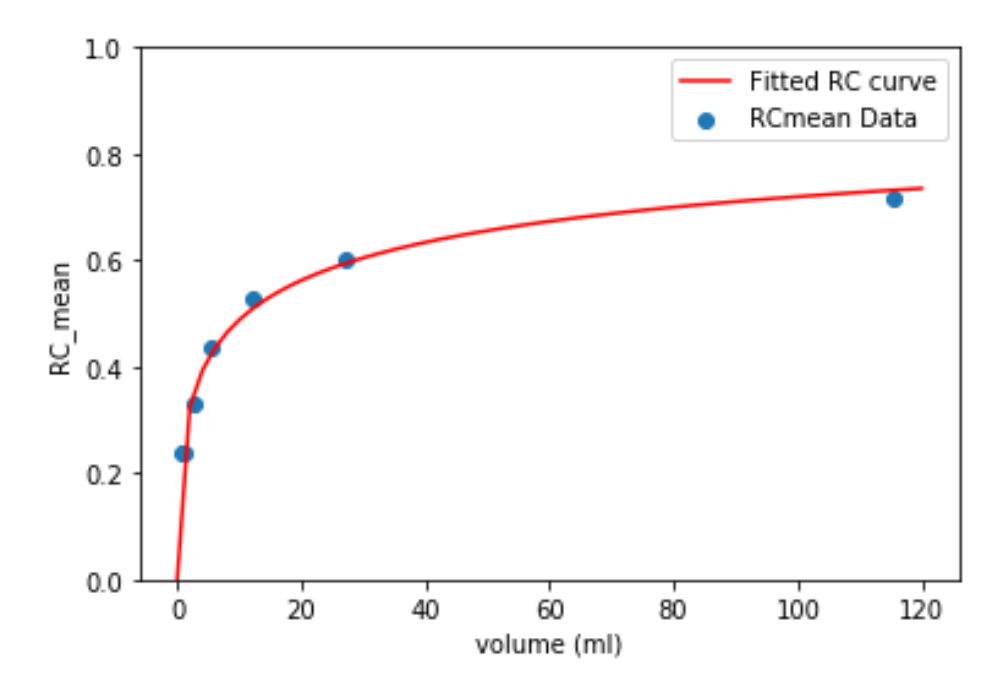


Figure 7.3: Curve fit for NEMA phantom data, using all seven imaged spheres, to produce the mean RC curve.

value by the RC, appropriate for the volume of the lesion to be corrected. No corrected image is produced by the RC method.

7.2.3 Methods for Analysis

7.2.3.1 Visual Assessment

Corrected images of the local area are produced as part of the STC and RL correction algorithms. These locally corrected images were visually compared with local regions of the Ground Truth and uncorrected data for each lesion within each dataset. In particular for the non-uniform activity lesions, activity distribution information may be clinically relevant and so would ideally not be lost due to application of PVC.

Visual assessment was not possible for the RC method.

7.2.3.2 Voxel-based analysis

Comparison of the voxel-by-voxel accuracy of each correction method was performed by assessment of the RRMSE, calculated over voxels within the local lesion volume, compared with ground truth. This metric gives an indication of how

different PVC algorithms account for, and retain, inhomogeneity within a lesion.

A scale factor was determined to scale reconstructed images to GT values. This scale factor was derived by comparing the sum of all counts in the reconstructed image to the sum of counts in the GT image.

Since the RC method does not produce corrected images, a pseudo-corrected image was produced based on the uncorrected data in order to calculate the RC-RRMSE. The pseudo-correction was made by replacing all voxels within the lesion VOI with the RC-corrected regional mean value.

7.2.3.3 Region-based analysis

The known GT was used to delineate a Volume of Interest (VOI) which outlines the lesion. The mean voxel value within this VOI is referred to as the Regional Mean Value (RMV). The ratio between mean voxel value in the lesion and the mean voxel value in an equivalent VOI within normal liver (referred to as the Target to Background Ratio (TBR)) was used for analysis. The corrected TBR, based on correction with each of the PVC algorithms, was compared with the uncorrected TBR and the Ground Truth TBR.

Comparison of corrected TBR with GT over all nine datasets was performed using a Wilcoxon signed-rank test as the data did not follow a normal distribution.

7.3 Results

Representative images for one example spherical lesion, and one example non-spherical lesion have been included to demonstrate features of each lesion type. Quantitative results were obtained for all nine lesions described in Chapter 6.

7.3.1 Spherical Lesions

7.3.1.1 Visual Assessment

Figure 7.4 shows images for visual assessment for the STC and RL algorithms.

Comparing the two images in the left column, which show the full transaxial FOV for the GT and reconstructed (but uncorrected for the PVE) datasets, demonstrates an apparent reduction in contrast between the lesion and normal liver,

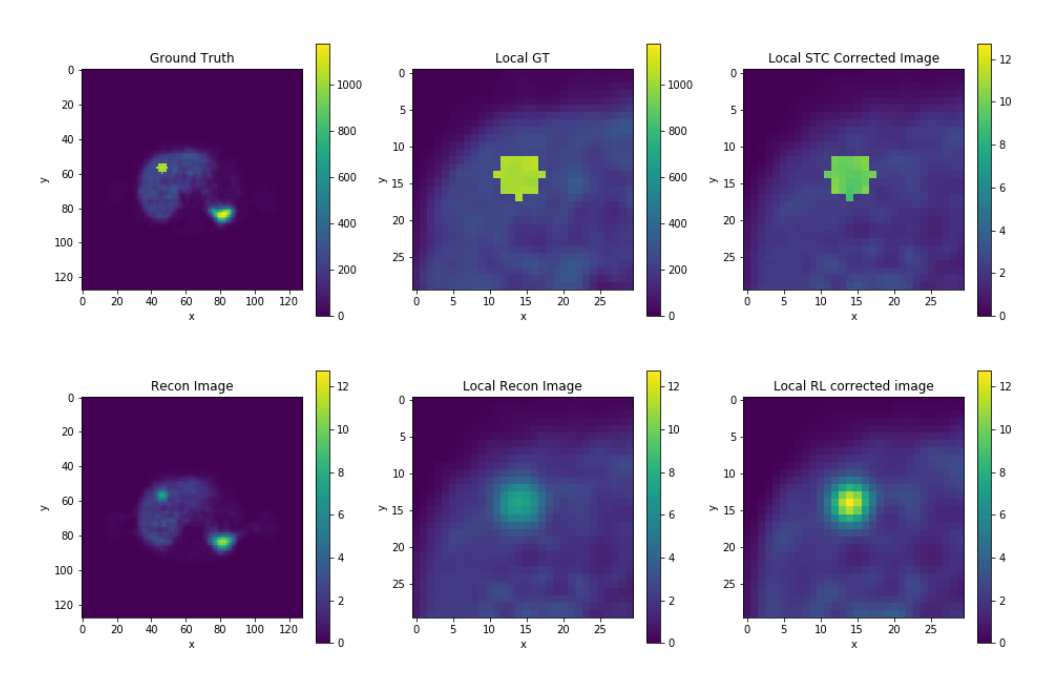


Figure 7.4: Example images for Case 2 including GT, uncorrected, STC corrected and RL corrected spherical lesion. Images in the Left column show transaxial plane of whole image Field of View (FOV). The other images show transaxial plane images of the local region around the lesion.

as expected with the loss of resolution associated with the imaging process. The blurred edges of the reconstructed lesion can be seen clearly when comparing the local region in the GT image (top, centre) to the local region in the reconstructed image (bottom, centre). The partial volume corrected transaxial images which result from STC (top right) and RL (bottom right) are also shown. The main visual difference between these images is the sharp edge introduced by the segmentation aspect of the STC algorithm. The RL correction does not utilise any segmentation information.

Partial volume corrected images in all three planes are shown in Figure 7.5. Observations from the sagittal and coronal planes for STC and RL are similar to that from the transaxial plane shown in the previous figure. The sharp edge is present in the STC corrected images, and not the RL corrected images. The centre of the RL-corrected lesion appears more active, while the voxels within the STC-corrected lesion appear similar when comparing the edge and centre of the lesion. For the pseudo-RC images, the lesion has a uniform pixel value throughout, and visually

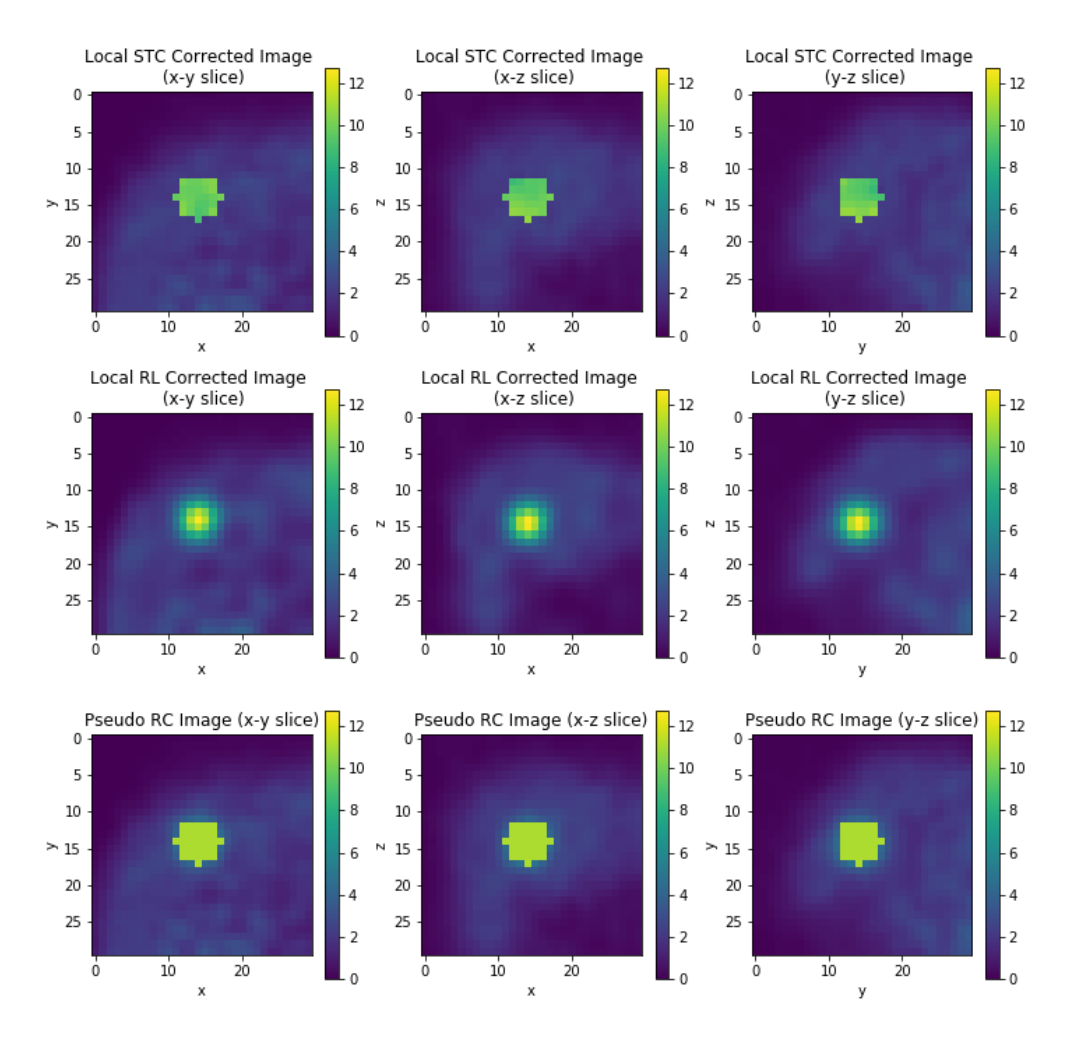


Figure 7.5: PVC corrected lesion images of Case 2, shown in the Axial (left), Coronal (centre) and Sagittal (right) planes. Top row: STC corrected lesion. Middle row: RL corrected lesion, Bottom row: lesion with voxel values replaced by RC-corrected regional mean values to produce pseudo-RC image.

it is also apparent that the spill-out from the lesion to the background has not been corrected for. This can most clearly be seen by comparing the STC corrected and pseudo-RC corrected images.

Residual images (Ground Truth minus PV corrected, relative to lesion GT) were produced for each iteration of both STC and RL corrections. These are presented in Figures 7.6 and 7.7, respectively, using data from Case 2 as an illustrative example.

Figure 7.6 shows that in the first STC iteration, the residual data demonstrate a clear structure; with an area of underestimated voxels positioned at the location of



Figure 7.6: Residual images, in the transaxial plane, comparing the STC-corrected data to the GT for each STC iteration in Case 2. Values are expressed as percentages, relative to the GT lesion value, and the scale ranges from -100% of GT (corrected voxel value overestimates the voxel value by 100%) to 100% (corrected voxel value underestimates the GT voxel value by 100%).

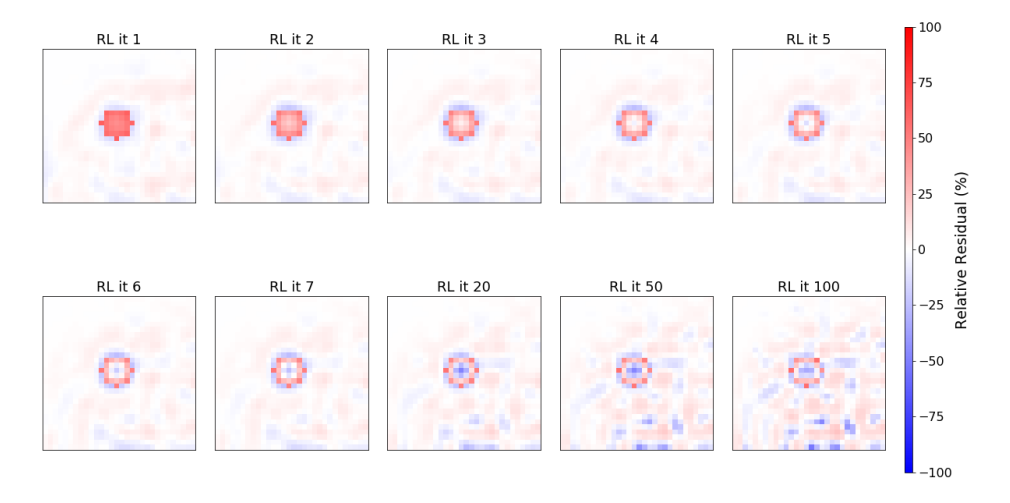


Figure 7.7: Residual images, in the transaxial plane, comparing the RL-corrected data to the GT for RL iterations 1-7 and selected higher RL iterations in Case 2. Values are expressed as percentages, relative to the GT lesion value, and the scale ranges from -100% (corrected voxel value overestimates the voxel value by 100%) to 100% (corrected voxel value underestimates the GT voxel value by 100%).

the spherical lesion. In subsequent iterations, the structure of the residual image disappears and there is very little residual structure by the 10th STC iteration. The first few RL iterations (see Figure 7.7) are structured in a similar way to the early STC residual images. However, increasing RL iterations does not appear to remove this structure. There remain areas of underestimation (red) within the

lesion, surrounded by a concentric ring of overestimated (blue) voxels. In addition, the extent of the over-estimation at the centre of the lesion appears to be increasing with more RL iterations.

7.3.1.2 Quantitative Assessment

As the residual images demonstrate, the extent of the differences between the Ground Truth image and the corrected images, on a voxel-by-voxel basis, depends on the correction method. A comparison of the RRMSE for the three different correction methods is shown in Figure 7.8 for spherical lesion data.

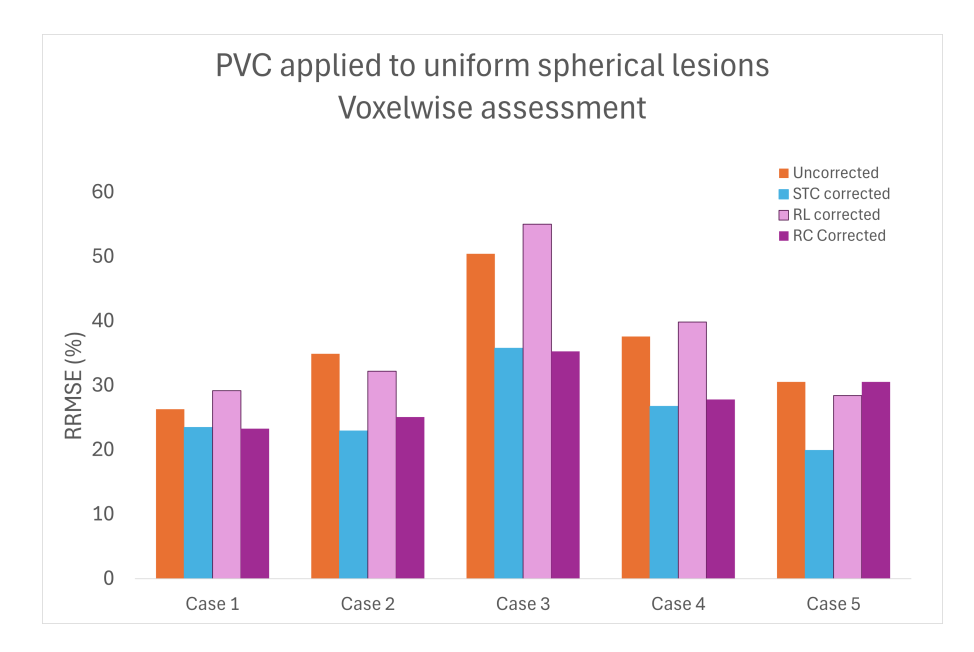


Figure 7.8: Graph showing the RRMSE (in scaled voxel value) for Cases 1-5 (uniform, spherical lesions) for uncorrected data, images produced by STC and RL, and a pseudo-RC-corrected image.

Figure 7.8 gives an indication of the voxelwise difference between the local GT image and the corrected images. Lower RRMSE values indicate a better voxelwise correlation with the Ground Truth. RRMSE values for most of the uniform spherical lesions examined demonstrate similar properties. Both STC and RC methods improve agreement with GT compared with uncorrected data as shown by the lower RMSE values in Cases 1-4. The RL method, however, produces a similar RRMSE to the uncorrected data in all cases. This suggests that, on a voxel-by-voxel basis, the RL correction does not improve on the accuracy of the image.

The relative regional mean values (lesion TBRs) for each of the datasets incorporating uniform spherical lesions are summarised in Figure 7.9.

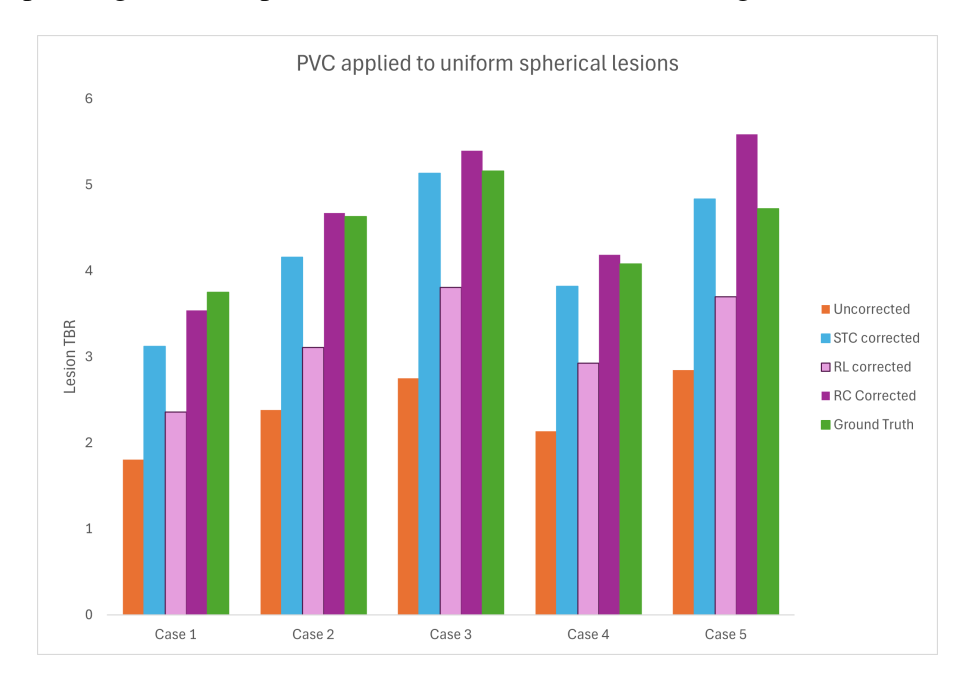


Figure 7.9: Corrected lesion TBR for Cases 1 - 5 (spherical lesions).

Figure 7.9 shows the uncorrected TBR, the GT TBR, and post-correction TBR for the three PVC methods investigated. It is clear from this graph that the uncorrected data consistently underestimates the GT TBR, by around 40 - 50%. For each of the five cases presented here, RL increases the TBR compared with the uncorrected data, but the RL corrected TBR values consistently underestimate the GT by between 22 % and 37 %. STC results in an undercorrection of between 0.5% and 17% in Cases 1 - 4, and over-corrects by 4% in Case 5. RC undercorrects Case 1 by 6% and over-corrects the other cases by between 1% and 18%. A summary of the percentage deviation of the partial volume corrected lesions, compared with GT TBR, is shown in Figure 7.10.

7.3.2 Non-Spherical Lesions

7.3.2.1 Visual Assessment

Figure 7.11 shows the transaxial plane images for visual assessment of PVC applied to Case 7; one of the non-spherical lesions with highly heterogenous uptake.

Several general observations can be made which are similar to the spherical

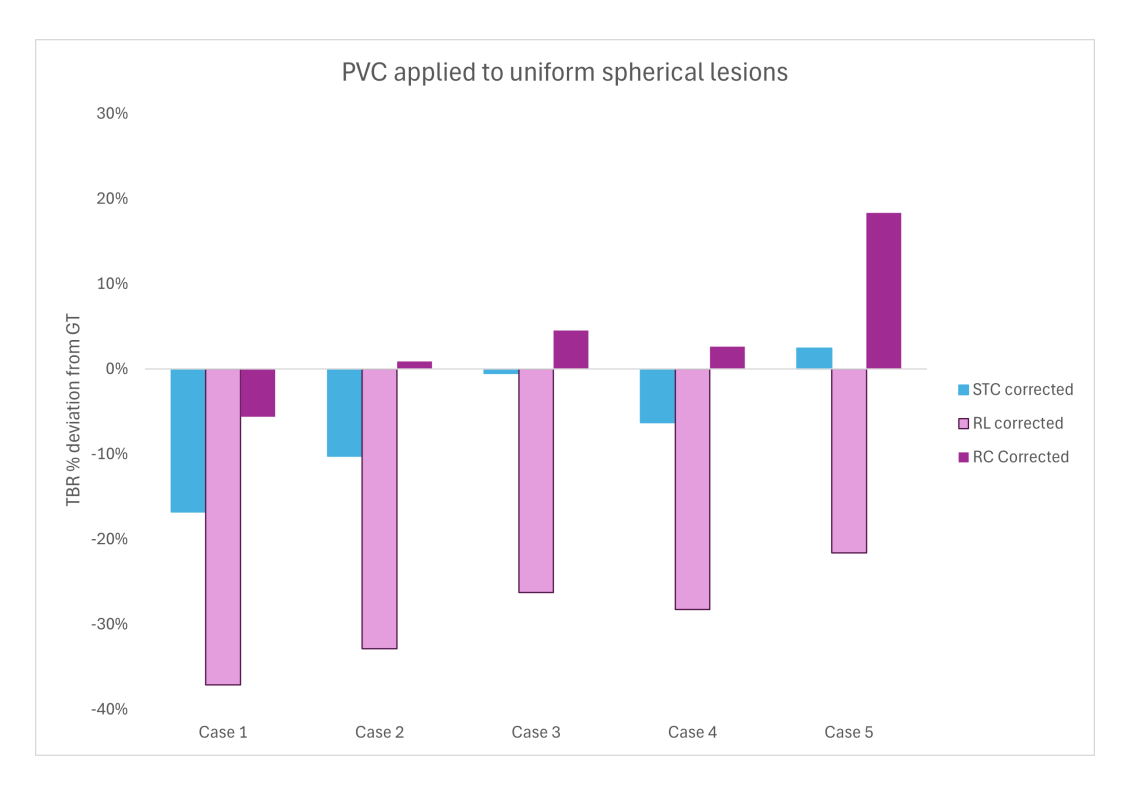


Figure 7.10: Graph showing the percentage deviation from Ground Truth TBR for spherical lesions in Cases 1 - 5 after application of PVC by different methods.

lesion shown in Figure 7.4. These include the blurred edge and loss of contrast in the reconstructed image. The reduction in resolution also results in a loss of the intra-lesion inhomogeneity, in the reconstructed (non-corrected) images. Figure 7.11 demonstrates how the STC method visually recovers this non-uniformity to a greater extent than the RL algorithm. Visual impressions of recovery of blurred edges and inhomogeneity are supported by reviewing profile through the lesion as shown in Figure 7.12. Partial volume corrected images in all three planes are shown in Figure 7.13.

These images demonstrate, again, the recovery of sharp edges at the boundary of the lesion with the STC method. Within the lesion, the less active inner area is recovered in all three planes with STC, whereas with RL it is more subtle on the axial and coronal planes compared with the sagittal plane (the plane through which the lesion appears widest).

Residual images (GT minus corrected data) for Case 7 are shown for STC and RL corrections in Figures 7.14 and 7.15, respectively.

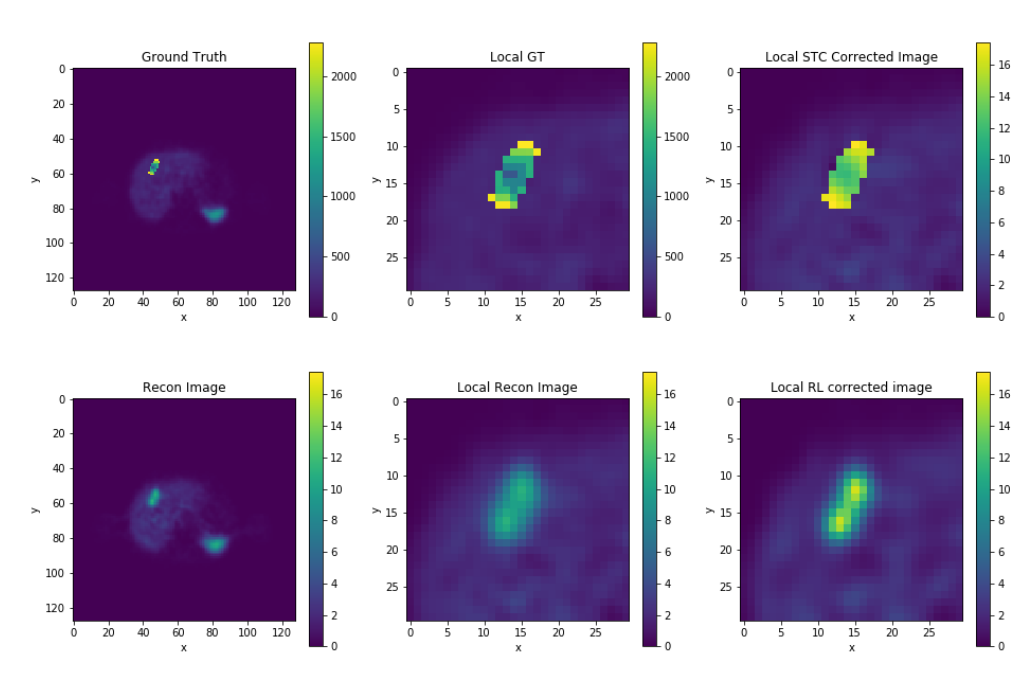


Figure 7.11: Example images for Case 7 including GT, uncorrected, STC corrected and RL corrected non-spherical, heterogenous, lesion. Images in the Left column show transaxial plane of whole image FOV. The other images show transaxial plane images of the local region around the lesion.

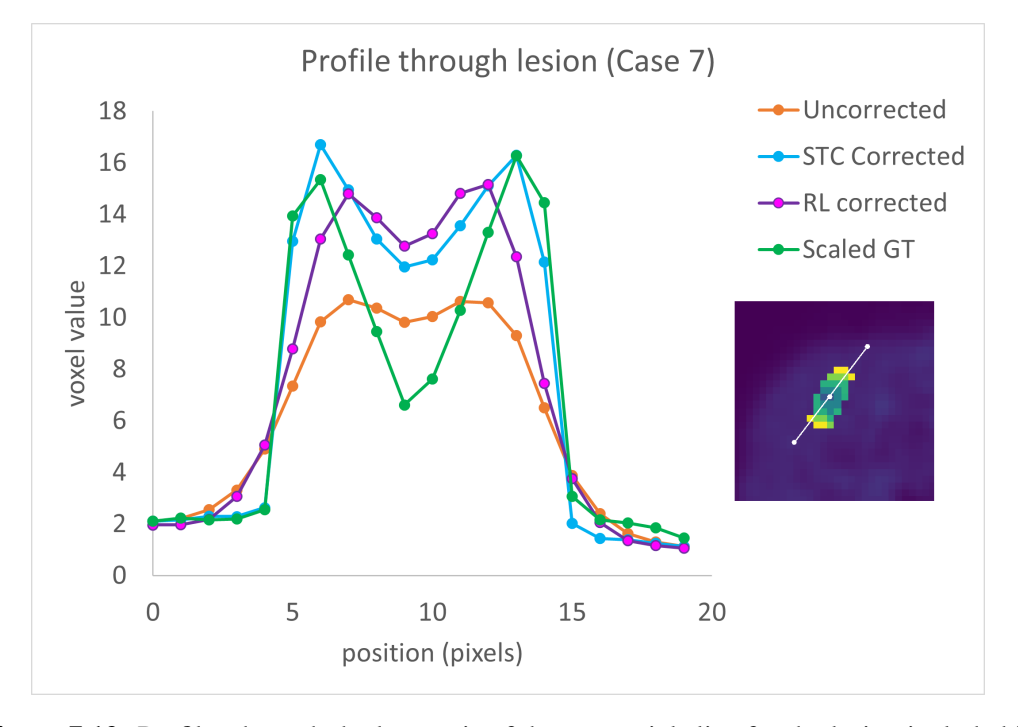


Figure 7.12: Profiles through the long axis of the transaxial slice for the lesion included in Case 7, showing profiles for uncorrected data, scaled ground truth data, data corrected using STC and data corrected using RL.

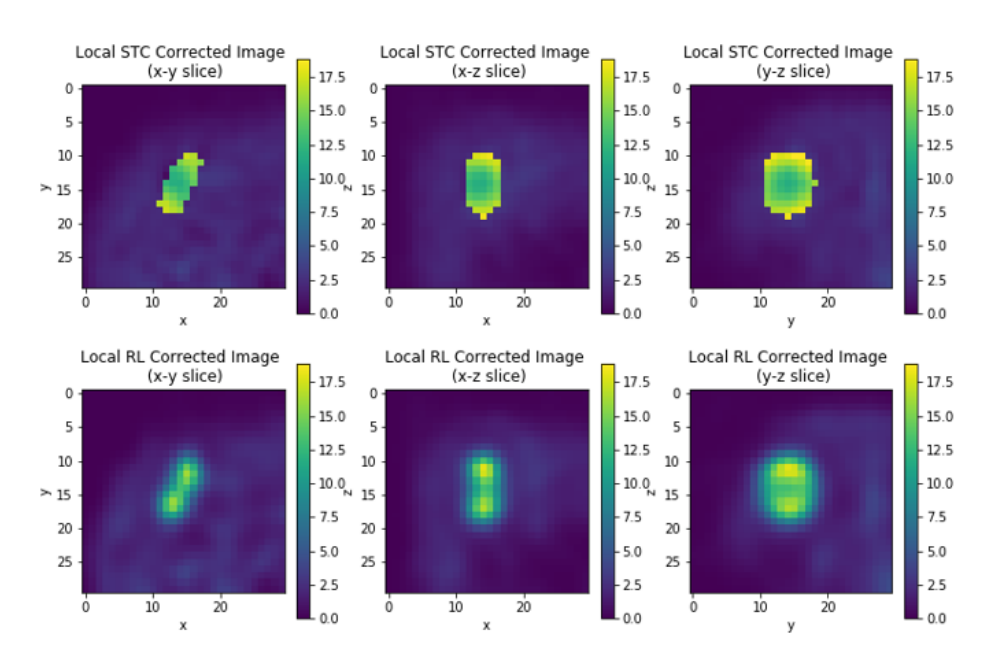


Figure 7.13: PVC corrected lesion images of Case 7, shown in the Axial (left), Coronal (centre) and Sagittal (right) planes. Top row: STC corrected lesion. Bottom row: RL corrected lesion

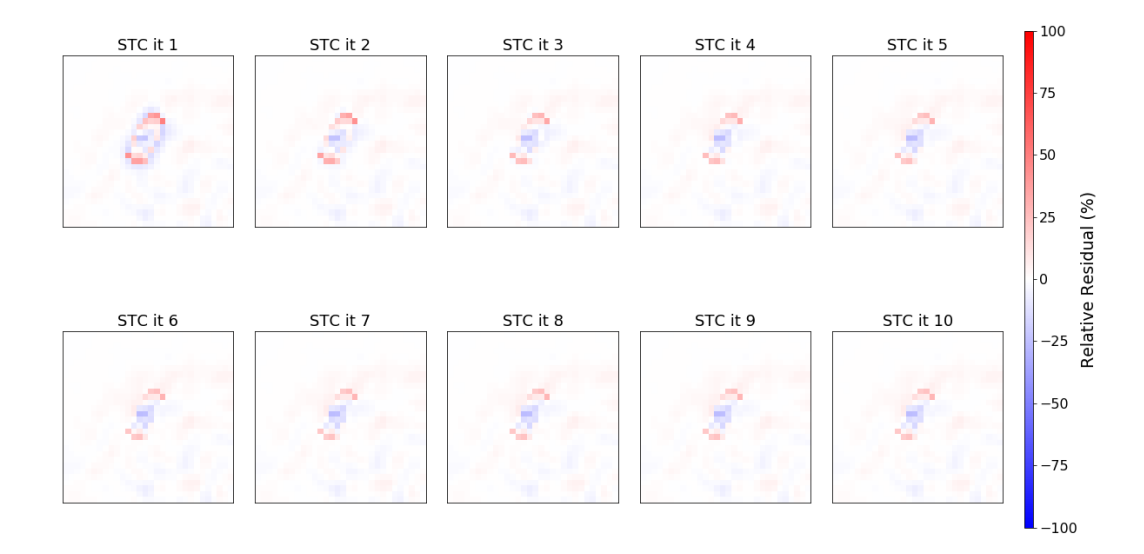


Figure 7.14: Residual images, in the transaxial plane, comparing the STC-corrected data to the GT for each STC iteration in Case 7. Values are expressed as percentages, relative to the GT lesion value, and the scale ranges from -100% (corrected voxel value overestimates the voxel value by 100%) to 100% (corrected voxel value underestimates the GT voxel value by 100%).

Figure 7.14 shows that in the first STC iteration, the structured pattern seen for the uniform, spherical, lesions is still present. With further STC iterations, the magnitude of the residual differences between STC and GT reduce, especially at the

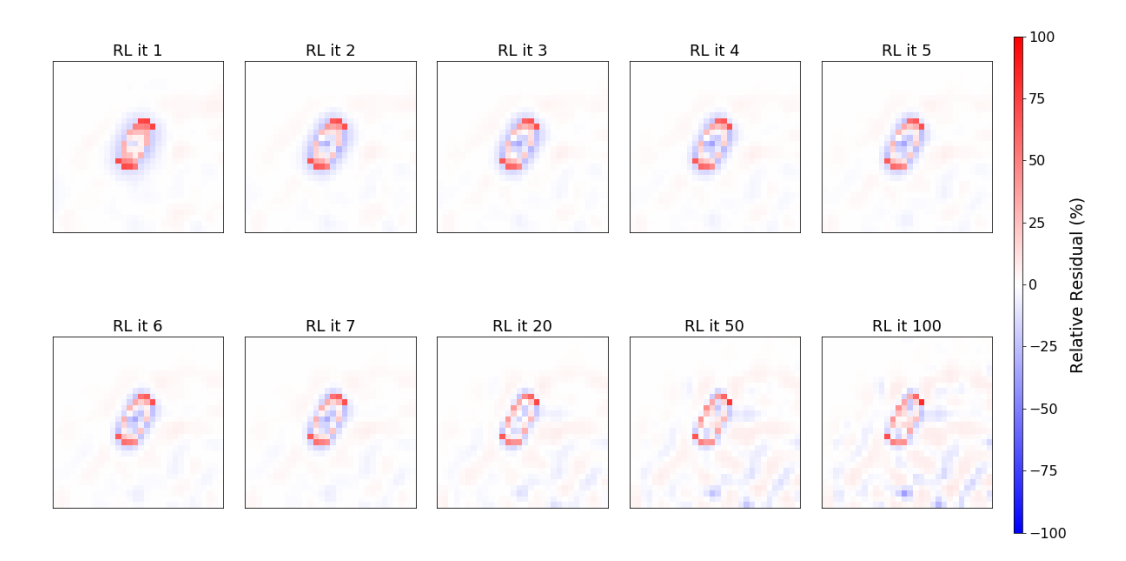


Figure 7.15: Residual images, in the transaxial plane, comparing the RL-corrected data to the GT for RL iterations 1-7, and selected higher RL iterations in Case 7. Values are expressed as percentages, relative to the GT lesion value, and the scale ranges from -100% (corrected voxel value overestimates the voxel value by 100%) to 100% (corrected voxel value underestimates the GT voxel value by 100%).

edge of the lesion. There is a residual overestimate in the centre of the lesion (the colder area in GT) which STC has not removed completely. Reviewing the residual images for the RL correction (Figure 7.15) demonstrate the structured appearance both around edges and in the centre, as before. Similarly to the uniform spherical lesions, increasing the number of RL iterations does not appear to remove this structure - as demonstrated by RL iterations 20, 50 and 100 in Figure 7.15.

7.3.2.2 Quantitative Assessment

A comparison of the RRMSE data for non-spherical lesions is shown in Figure 7.16, which gives an indication of the voxelwise difference between the local GT image and the corrected images.

Comparing the RRMSE results for the non-uniform, non-spherical data to the uniform spherical RRMSE data (in Figure 7.8) shows one outlier. Case 9 demonstrates that the RC correction has failed to improve upon the voxel-by-voxel agreement with the Ground Truth, and has resulted in an estimate which is further from the GT than the uncorrected data. This could be due to the size of the lesion which was the largest volume of all lesions examined. In addition, the heterogeneity

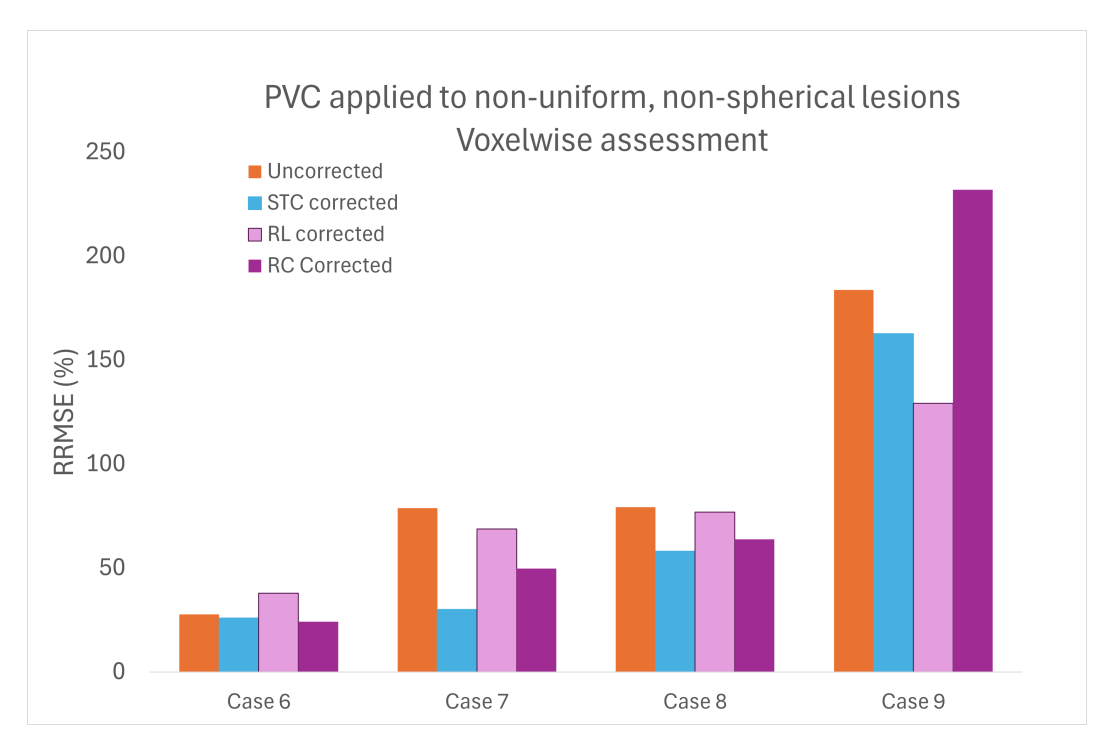


Figure 7.16: Graph showing the RRMSE for Cases 6 - 9 (non-spherical, non-uniform lesions) for uncorrected data, images produced by STC and RL, and a pseudocorrected image for RC.

within this lesion, in particular the more active central area (demonstrated in Figure 6.31), cannot be captured by the simple RC method which returns one value for the entire lesion.

The relative regional mean values (lesion TBRs compared with normal liver) for each of the datasets incorporating non-spherical lesions are summarised in Figure 7.17. This graph shows the uncorrected TBR in orange, the GT TBR in green, and post-correction TBR for the three PVC methods investigated.

Figure 7.17, demonstrates that uncorrected data consistently underestimate the GT TBR, by around 32 - 55%, similar to the underestimate observed for spherical lesions. For each of the four non-spherical cases, RL increases the TBR compared with the uncorrected data, but the corrected TBR values still consistently underestimate the GT by between 15% and 41%. STC results in an undercorrection of 21% for Case 7, but overestimates of between 0.4% and 5% in Cases 6, 8 and 9. RC undercorrects Cases 7 and 8 by 26% and 3% respectively, and overcorrects Cases 6 and 9 by 13% and 2% respectively. The percentage deviation of the partial

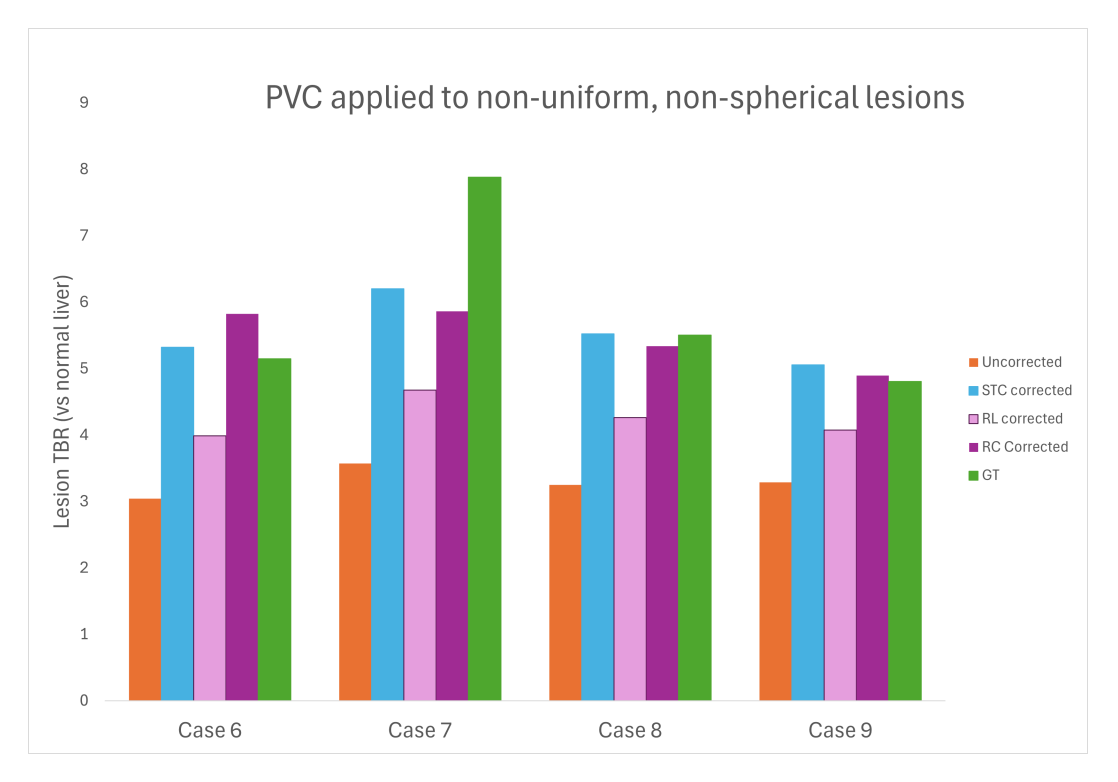


Figure 7.17: Graph showing the corrected lesion TBR for Cases 6 - 9 (non-spherical, non-uniform lesions).

volume corrected lesions, compared with GT TBR, is summarised in Figure 7.18.

7.3.3 Regional Mean Value Results Summary

The corrected TBR values for all 9 datasets are presented in a box plot to compare the performance of each of the PVC methods (Figure 7.19). The boxes show the interquartile range and the median value of the uncorrected TBRs, and TBRs corrected using STC, RL and RC. The green dotted line indicates a TBR value which exactly matches the GT.

The whiskers of the box plot indicate the furthest point lying within $1.5 \times$ the interquartile range from the edge of the box. Only the RC method has data points lying outwith this range (represented by small circles); one due to an overestimate of around 20 % (Case 5) and one due to an underestimate of around 20% (Case 7).

As expected, the uncorrected data demonstrate a significant underestimation of the GT RMV, by at least 30%. The RL correction reduces the extent of this, but still leaves a systematic underestimation of the GT RMV.

Figure 7.19 demonstrates that the median values of the STC and RC corrections

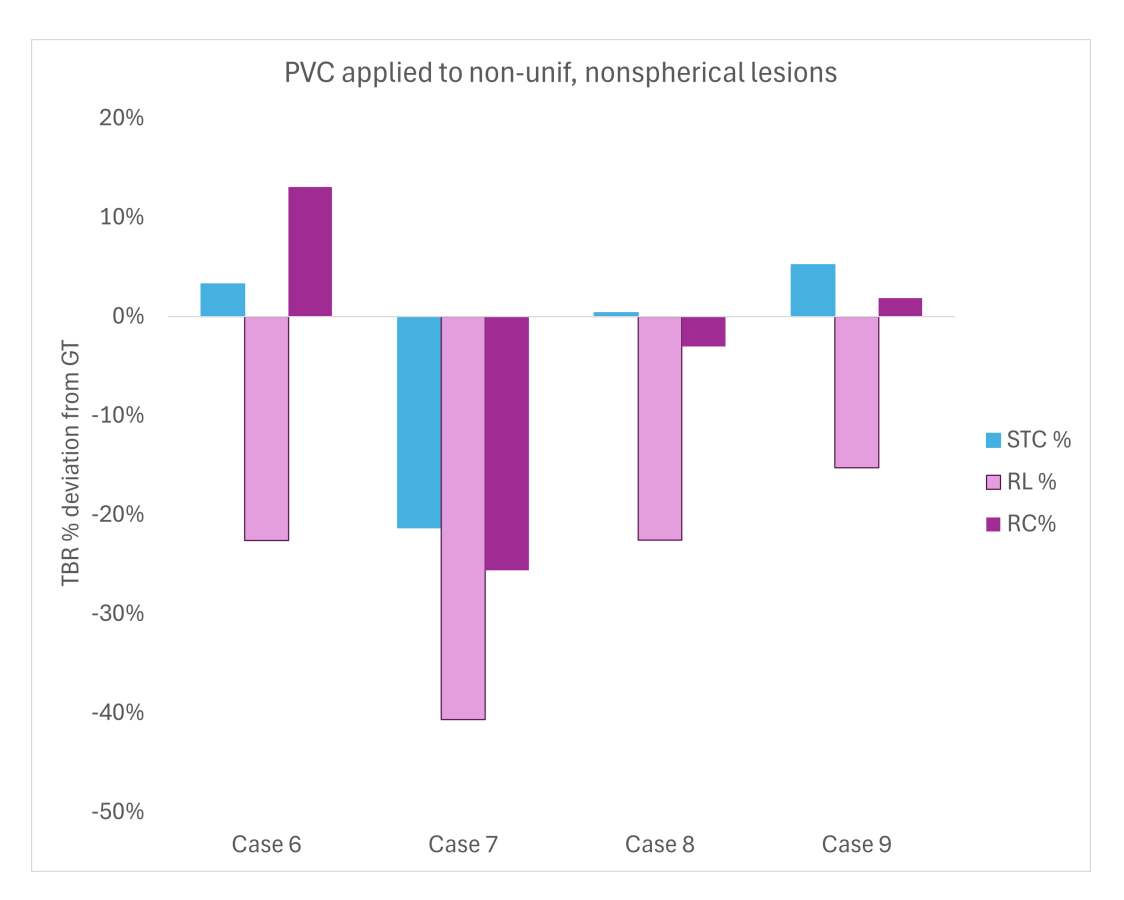


Figure 7.18: Graph showing the percentage deviation from Ground Truth TBR for non-spherical, non-uniform lesions in Cases 6 - 9 after application of PVC by different methods.

are both close to 0 (i.e. good agreement with GT). This agrees with the findings of Wilcoxon signed-rank tests which found no statistically significant difference between the GT and the RC corrected TBR (p = 0.594) or for the GT and the STC corrected TBR (p = 0.260) based on a threshold of p = 0.05.

7.4 Discussion

7.4.1 Recovery Coefficient Performance

A disadvantage of the RC method, compared with RL and STC, is that no corrected image is produced. Therefore visual assessment is not possible, and intra-lesion heterogeneity cannot be reproduced. For uniform lesions in cases 1-4, the RC RRMSE appears to improve on uncorrected RRMSE values to a similar extent as STC. This can reasonably be expected for uniform spherical lesions. However, this

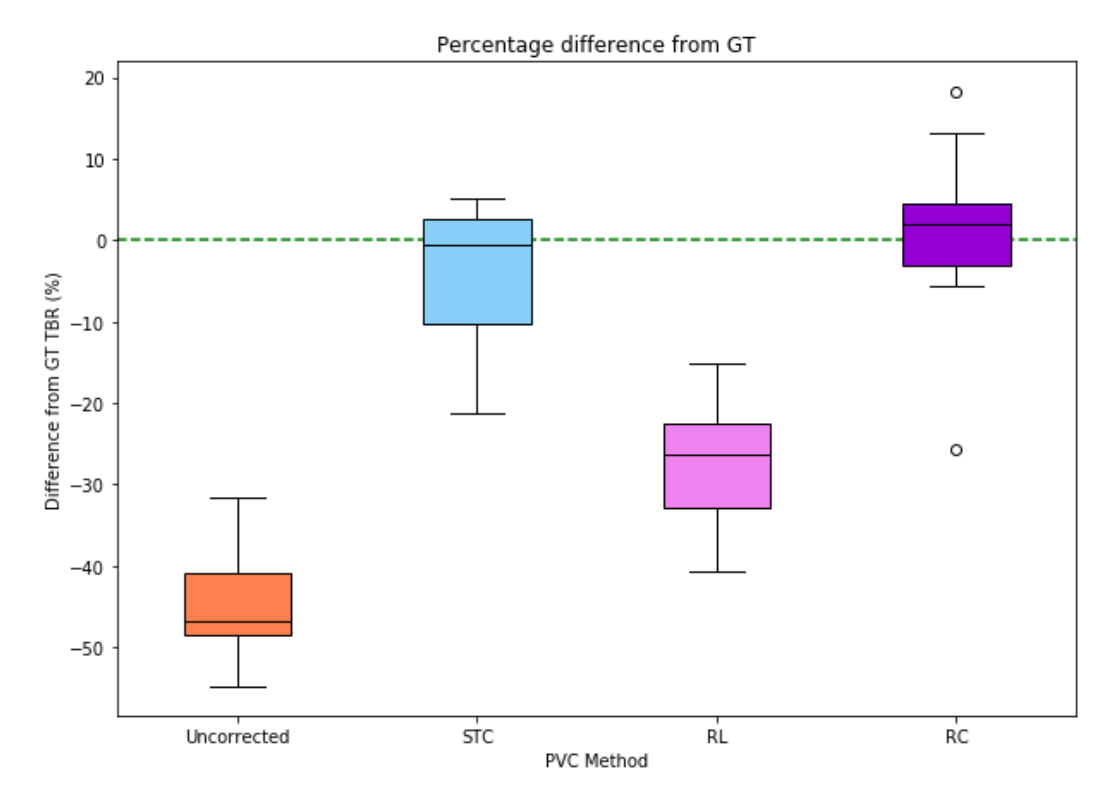


Figure 7.19: Box plot showing the median, minimum, maximum and interquartile range (IQR) of the percentage deviation from Ground Truth TBR for lesions in Cases 1 - 9 after application of PVC by different methods. Points lying outwith 1.5 x IQR are represented by small circles.

was not the case for all datasets, and is not likely to be the case for lesions in clinical practice.

The box plot in figure 7.19 highlights the potential variation in RC accuracy for RMV. While the interquartile range and extent of the whiskers are relatively narrow compared with STC and RL, having two outliers from only nine test cases indicates that there could be features within a patient image which are not accounted for in (or which do not meet the assumptions of) the RC method. It is not clear why the outliers (Case 5 and Case 7) perform badly; in particular Case 7 uses the same lesion as Case 6 but on the background activity distribution from a different patient. This indicates the importance of investigating a range of lesions. Testing on more datasets may help to identify specific features of images for which the RC could not produce an accurate correction (for example, the extent of non-uniformity in lesion, width of PSF due to position in FOV or features which affect convergence in the

reconstruction, and non-uniformity or contrast within the background).

In the cases examined here, the RC correction may have benefitted from the lesion positioning being at a similar radius to the NEMA spheres. This assumption would not always be met in clinical cases. A more comprehensive set of patients including e.g. large patients with more peripheral lesions or paediatric patients where a lesion could be positioned more centrally compared with NEMA spheres, may highlight drawbacks of the implicit assumption in the RC method of static spatial resolution across the FOV.

The example of Case 9 was included within the dataset to include an example of a high lesion to background ratio (lesion was positioned in the lung) compared with the NEMA sphere to background ratio. In one respect this is a challenge to the RC method, as the recovery coefficients are only strictly valid for cases with similar GT TBRs. However in this case, the lesion was relatively large with a high contrast. These factors act to reduce the PVE, outweighing the challenge to the RC method relating to the differing contrast to the NEMA spheres.

Capturing these outliers within the limited dataset examined here is valuable, since without them the confidence in the reliability and accuracy of the RC method, in its current form, may be overestimated. This clinically relevant finding would not have been identified using simplistic phantom data with spherical lesions in a predictable background.

7.4.2 Richardson-Lucy with Perturbation Performance

The RL algorithm consistently underestimated the GT TBR. The underestimate could be reduced by running RL for more iterations, however this would increase the RRMSE, due to the structured areas of over- and under-estimation demonstrated in Figures 7.7 and 7.15. Therefore, the trade-off between the TBR and RRMSE limits the performance of the RL method. The relatively poor RRMSE performance of RL compared with STC was not expected given the advantages described in Chapter 3; specifically that the algorithm provides a voxel based correction. The lack of segmentation information may be a contributing factor.

7.4.3 Single Target Correction with Perturbation Performance

Based on the TBR values, and associated statistical tests, the performance of the STC algorithm is at least as good as the RC method. The STC corrected image captures heterogeneities within the lesion (see Figures 7.4 and 7.11) for visual assessment more accurately than RL. Observations made on corrected images are supported by voxelwise assessment with RRMSE calculation. STC is the only method which does not result in a higher RRMSE, compared with uncorrected data, in all of the 9 examples (RL and RC both have at least one case for which the correction makes the RRMSE higher than uncorrected - see Figures 7.8 and 7.16).

The key disadvantage of STC is the requirement for segmentation. This is a disadvantage shared with RC and is discussed further in Section 8.2.2.1. STC has multiple advantages over RC such as the voxelwise correction, enabling a corrected image to be produced, and the potentially more reliable TBR correction.

7.4.4 Limitations

7.4.4.1 Absolute Quantification of Monte-Carlo Simulated Data

One limitation of the assessment of methods performed in this chapter is the lack of absolute quantification. Absolute quantification is the metric required for dosimetry applications, and would also not be dependent on the selection of a uniform section of normal liver for calculation of the TBR.

7.4.4.2 Recovery coefficient calculation and application

The RC curve was calculated based on each point (i.e. each sphere) being weighted equally. While weighting on ^{99m}Tc data is not likely to make a significant difference to the curve fit, for application to radionuclides with higher energy emissions errors on small spheres could be significant. Uncertainties in sphere size could be incorporated into the weighting of the points for the curve fit. An advantage of the setup used for RC curve fitting is the use of the larger, 60 mm diameter, sphere which is not always used in practice, but is expected to provide a better fit for objects with volume greater than 26.5 ml (the largest of the conventional 6 NEMA spheres).

The accuracy of the RC results may have been overestimated because the lesion

positions were at similar positions to the NEMA spheres. As discussed previously in Section 4.7.5, the recovery curves can vary with position Leube et al. [2024a], which further supports the case for a patient and lesion specific PVC method.

Another well-known limitation of the RC method, in its current form, is the assumption of sphericity - even for objects known to be non-spherical. The RC for each lesion was calculated based on lesion volume. Adaptations to the RC method have been proposed recently; including accounting for non-spherical shapes using the volume to surface area (V/SA) ratio, and accounting for different amounts of spill-in/spill-out depending on the contrast in the image [Marquis et al., 2025]. These adaptations have been shown to improve accuracy and, since they negate the key assumptions of sphericity and contrast matching the phantom, likely reliability. The publication cited here was published during the final write-up stage of this thesis, and therefore the modified RC approach was not tested.

7.4.5 Further work

In terms of the results of this chapter specifically, the conclusions drawn based on the statistical tests would be more robust with a larger dataset including more test cases. It was important to include a range of different test datasets, including realistic variation. Within the nine datasets investigated in the present chapter, a range of properties have been explored including non-sphericity, non-uniformity, and different global activity distributions.

More general areas of further work are discussed in Chapter 8.

7.5 Conclusions

The key conclusions that can be drawn from the work presented in this chapter are:

- STC with perturbation returns corrected values which are at least as accurate as the RC method for both regional (TBR) and voxelwise (RRMSE) metrics
- STC returns a corrected image which includes voxelwise information and retains a degree of non-uniformity from the GT

• RL with perturbation results in either an undercorrection, or an unacceptable amplification of noise

The investigations of the three PVC methods using realistic and varied test datasets have enhanced the understanding of limitations of each method. This is crucial for appropriate application of PVC in clinical practice - in particular for oncology SPECT imaging.

Chapter 8

General Conclusions, Limitations, and Future Directions

8.1 Overall Conclusions

Results throughout Chapters 4, 5, and 7 have consistently demonstrated that Partial Volume Correction (PVC) is required for accurate quantification of SPECT imaging. Reviewing the literature, together with the criteria developed to assess suitability of existing PVC methods in Chapter 3, found no consensus on the optimal method for PVC in oncology SPECT. The criteria identified a shortlist of techniques to be implemented for further investigation; Recovery Coefficient (RC), Single Target Correction (STC), iterative Deconvolution (itD) (using the Richardson-Lucy (RL) method), and Resolution Modelling (RM).

The variation in resolution in SPECT imaging has an impact on the Partial Volume Effect (PVE). Variation can occur due to a range of factors including activity distribution and reconstruction parameters. In particular, Chapter 4 demonstrated that the use of RM introduced greater variability and made assessment of the Point Spread Function (PSF) challenging. Reconstruction was performed without RM for the study of PVC in this thesis. The use of a sufficient number of reconstruction updates gives a more reliable and consistent measure of the PSF.

A case-specific estimate of the PSF, via the perturbation method, was incorporated into the STC and RL PVC algorithms. Testing of these methods,

in comparison with Ground Truth values, and also compared with the conventional RC PVC method was performed for a range of test datasets.

Realistic test datasets, developed as described in Chapter 6, based on patient data with Monte Carlo (MC) simulation were used for comparison of the key PVC methods. The Richardson-Lucy itD method with perturbation-estimated PSF was found to systematically underestimate the Ground Truth and produced region-based and voxel-based results which were consistently less accurate than perturbation-informed STC or than phantom-based RC.

Comparison of STC and RC results using the realistic test data in Chapter 7 found the following:

- Corrected regional mean value accuracy is comparable between STC and RC.
 Across the 9 datasets, both STC and RC were found to be not statistically significantly different to GT. STC may be more reliable due to fewer assumptions.
- STC produces the most reliable voxelwise correction of the three methods examined.
- STC has an advantage over RC in that a corrected local image is produced which could be informative for lesions involving heterogeneity.
- While both STC and RC require segmentation, RC has the drawback of depending on values derived from phantom acquisition and analysis, which could introduce experimental error.

8.2 Discussion

8.2.1 Reconstruction for quantitative assessment

The investigation regarding resolution variation in Chapter 4 resulted in a recommendation to use more reconstruction updates than is currently used in clinical practice. Optimal reconstruction parameters for quantitative accuracy may adversely affect image appearance, which could make interpretation more

challenging for clinicians. To decouple the problem of producing visually good images, for clinical reporting, and quantitatively accurate datasets there is an argument for reconstructing multiple different image sets. For example, one for visual interpretation and another reconstructed using more iterations, which could be used for quantification. However, we must note that an adverse effect of increasing the number of OSEM iterations is an increase in image noise. The optimal reconstruction settings would need to balance the bias and variance for quantification.

8.2.1.1 Matrix Size

A relevant factor regarding typical clinical practice to consider is the matrix or voxel size used for acquisition and reconstruction. The normally accepted limit for sufficient sampling suggests that voxel dimensions should be less than 0.5 times the image resolution [Boellaard et al., 2004]. In the cases studied in Chapter 7 of this work, reflecting typical clinical practice, 4 mm or 4.4 mm voxels were used. Referring back to Figure 5.8, FWHM values as low as approximately 8 mm were measured. These measurements were based on a position 8 cm from the centre of the Field of View (FOV), however for objects positioned closer to the collimator face, the resolution is expected to be superior and therefore voxel sizes may exceed the suggested limit.

A reduced voxel size may also help to reduce the intra-voxel PVE (i.e. the tissue fractionation effect). However, within this work the priority was to use matrix sizes which replicate the clinical situation. In addition, noise would need to be reconsidered in terms of reconstruction and PVC method if voxel size is reduced.

8.2.1.2 Use of Resolution Modelling in Reconstruction

Another important reconstruction parameter to consider is the use of RM. The data presented in Chapters 5 and 7 were reconstructed with OSEM without the use of RM. RM algorithms are commonly used in iterative reconstruction in an attempt to compensate for limited resolution, with the aim of reducing quantitative bias due to the PVE. However, the application of resolution modelling does not provide a complete correction for the effect of limited resolution, therefore some PVC is still

required [Erlandsson et al., 2012b, Alessio et al., 2013]. Even if some reduction in bias is seen by applying RM, the variance has been found to increase, which limits the precision of quantification [Munk et al., 2017]. As shown in Chapter 4, more reconstruction iterations were required than are used in typical clinical practice in order to get a benefit from applying resolution modelling. Chapter 4 also noted that ringing artefacts can add difficulty in accurately characterising the PSF. These ringing artefacts occur when RM is applied in OSEM and are more severe at higher reconstruction iterations. Applying RM does not ensure the resolution in SPECT is consistent across the FOV in all cases, so an estimation of a local PSF may still be required for accurate application of PVC. Due to these limitations of reconstruction using RM, the data presented in this work has been reconstructed without resolution modelling.

Had RM been used in the reconstruction, we may have expected to see some reduction in the underestimation of regional mean value measurements for uncorrected data. However, this reduction in bias would depend on the size and intensity of the lesion and on other reconstruction parameters. Due to Gibbs artefacts, for some smaller lesions, data reconstructed with RM may demonstrate a maximum voxel value of greater than 100 % of the ground truth [Rahmim et al., 2013]. The application of PVC using perturbation to data reconstructed using RM is not guaranteed to be reliably accurate since Gibbs artefacts would also make the assumption of a Gaussian PSF inappropriate. In addition, the assumption of constant PSF across the width of a lesion may no longer be appropriate due to increased enhancement (i.e. improved resolution) at the edges of an object compared with the centre.

It is important to note that, in clinical practice, many vendors are offering quantitative reconstruction solutions which necessitate the use of RM. This may be due to the improvement in visual appearance, however it may detrimentally impact the reliability of quantification. Further work is required in order to explore whether images reconstructed with RM can be quantitatively robust. If evidence is collected to show that the quantification is less reliable on systems forced to reconstruct with

RM, it is possible that vendors could be convinced to adjust their approach. If the evidence shows the opposite, then the robustness of the perturbation method would need to be tested further using data reconstructed with RM.

8.2.2 Limitations and Further Work

A limitation in this work is that for the final testing datasets, it was not possible to generate simulations which allow absolute quantitative metrics to be evaluated. Another practical limitation was the relatively small number of patient-based datasets used for testing. Despite the small number, the datasets were designed to challenge the PVC algorithms in a range of realistic situations in oncology SPECT imaging. The choice of using only OSEM for reconstruction may also be interpreted as a limitation. More advanced reconstruction techniques such as Maximum a Posteriori (MAP) are available, however the motivation for choosing OSEM was to match the most commonly used reconstruction algorithm in clinical practice. More work would be required to investigate whether perturbation can reliably characterise the PSF of MAP reconstructions, or other advanced reconstruction algorithms.

As noted in Section 2.7.8.1, more 'compact' objects suffer less from the PVE. It has recently been suggested that this 'compactness' can be described in terms of the volume to surface area (V/SA) ratio [Mínguez Gabiña et al., 2023, Marquis et al., 2025]. It is possible that implementing the RC method using this metric rather than volume, as suggested in these recent publications, would improve the performance. However, the purpose of including the RC method in the assessment was as a comparator reflecting the conventional, most common, PVC method. In most cases, and the vast majority of publications which use the RC method, the spherical assumption is made and compactness is not taken into account. Investigating the method of RC, accounting for shape, may be worth evaluation in future work.

Areas of further work around the subject of this thesis include, but are not limited to, an assessment of precision (i.e. evaluating uncertainties), and error propagation - including an assessment of the required accuracy of the system model used for sinogram generation/reconstruction.

In addition to these areas, as mentioned in Section 3.4.5.2, further work involving different combinations of PVC techniques could be informative. In particular, utilising perturbation to estimate the PSF for application with combined PVC methods would build on the work of this thesis.

8.2.2.1 Influence of registration and segmentation

Translation of any PVC technique involving segmentation based on anatomical data to clinical practice should involve an assessment of the impact of segmentation and registration on the accuracy of the PVC, and therefore overall quantification. Uncertainties and errors introduced in the process of segmentation could potentially be significant. Further work on error propagation within SPECT quantification, and estimation of the resulting uncertainty, would be important for the appropriate use of the resulting PV corrected data. For clinical data, uncertainty analysis could be performed by following the EANM guidelines [Gear et al., 2018].

Due to the possibility for introducing errors, the criteria developed in Section 3.3 specified that 'The PVC method should not depend on segmentation based on anatomical images'. The RC and STC methods do not explicitly require registered anatomical datasets, except perhaps for application of corrections within the reconstruction.

Further work would be beneficial to explore the effect on PVC from imperfect segmentation due to deviation from Ground Truth segmentation. The segmentation used for both the RC and STC algorithms could be systematically varied to explore the effect of different extents of segmentation error including; larger than Ground Truth (GT), smaller than GT, offset from GT.

8.2.2.2 Application to other radionuclides

Further investigation would be required to test whether the application of the perturbation method can be generalised to other radionuclides such as those used for imaging in the context of theranostics (¹²³I or ¹¹¹In), or those used with therapeutic intent (⁹⁰Y, ¹³¹I or ¹⁷⁷Lu). The PSF of these radionuclides is likely to be wider and may include star artefacts due to high energy emissions and septal penetration. The perturbation method could potentially account for this, provided

that the implementation does not make the assumption of a Gaussian PSF.

Further investigation towards implementing perturbation on radionuclides other than ^{99m}Tc would be informative, perhaps utilising Monte-Carlo modelling to explore shapes and position-dependence of the PSF.

8.2.3 Practicalities of implementing PVC on clinical data

One of the key criteria developed in Chapter 3 is that the PVC method of choice for oncology should be 'simple and practical to implement'. The current PVC method most commonly used is the RC method, based on phantom measurements. While this method is conceptually simple, the practical implementation involves multiple stages - each of which could introduce error or variation.

While not utilised as commonly as RC, the STC method could potentially be implemented in a practical and simple manner, which would not be time consuming for the operator. Perturbation could be easily incorporated provided that an accurate system model (for example, this could be the same model used by the vendor for reconstruction) was available for use in the forward projection of the point source. The only user input required would be to select the position within the reconstructed image for which the PSF should be measured (i.e. somewhere within the lesion). Optional user input for segmentation of the object of interest could also be used. The rest of the algorithm could be automated; reconstruction of the perturbed image, cropping the image to the local area around the object of interest, fitting a Gaussian to the PSF, and applying the STC algorithm. An even more accurate solution could involve using a (validated) MC simulation to generate the point source. This could incorporate scatter and attenuation based on a registered CT dataset, and could be more realistic than an analytical simulation.

A quality control check of the implementation of the STC method could be performed using the IEC NEMA phantom. In particular, checking different collimators, reconstruction settings and different positions within the phantom would be worthwhile.

8.3 Summary

PVC using RC is likely to improve accuracy in most cases, however there will be clinical scenarios where a number of the underlying assumptions are not met, and RC will therefore produce inaccurate results. Applying PVC using STC with perturbation has been shown to produce corrected regional mean data which is at least as accurate as RC, with fewer assumptions. STC also has the benefit of producing a corrected local image, and allows for voxel-by-voxel analysis which could be useful for certain applications in oncology SPECT imaging.

Further testing on a larger, and more varied, set of realistic oncology test datasets would be of benefit, including images produced using radiopharmaceuticals used for Molecular Radiotherapy (MRT). Robust segmentation techniques and a more complete assessment of measurement uncertainties would also be important for the conclusions of this thesis to be applied more widely. In the future, with cooperation from system vendors, it would be possible to implement STC with perturbation as a practical method for PVC of oncology SPECT imaging in the clinical setting. The work performed in this thesis can help to guide further research towards improving the accuracy of quantitative SPECT, via PVC, for the benefit of patients.

Appendix A

Detail of PVC Method Scoring Based on Novel Criteria

The following pages contain brief explanations for scoring the PVC methods discussed in Chapter 3 using the oncology-SPECT specific criteria. The summarised results are presented in Figure 3.4.

Method	Criteria	Score	Explanation
	Assumption of VOI shape?	0	Usually assumes spherical VOI
(e.g. CT or MRI)? Robust to small changes/ segmentation or registr Assumes uniformity in re Assumes zero backgro Assumes known and invar Amplifies Noise or Intro Artefacts? Produces voxelwise corr Evaluate uncertainty on final	Requires use of higher resolution data (e.g. CT or MRI)?	5	No other image data required
	Robust to small changes/errors in segmentation or registration?	3	Extent of errors will depend on segmentation method
	Assumes uniformity in region(s)?	0	Assumes uniform regions and background
	Assumes zero background?	1	Assumes zero background unless CRC used, and unless phantoms acquired at a range of TBRs
	Assumes known and invariant PSF?	1	Implicitly assumes all organs will have the same PSF as the spheres in the phantom, under the conditions that the phantom was imaged with
	Amplifies Noise or Introduces Artefacts?	5	No artefacts or additional noise introduced
	Produces voxelwise correction?	0	Not evaluated for mean value based methods
	Evaluate uncertainty on final value(s)?	5	EANM guidance suggests evaluating uncertainty based on RC curve fit parameters and volume estimation
	Easy/simple implementation?	4	Currently the most commonly implemented in clinical practice
	Segmentation of entire image required?	5	Segmentation of region of interest only required
Geometric Transfer Matrix (GTM)	Assumption of VOI shape?	5	No spherical assumption made
	Requires use of higher resolution data (e.g. CT or MRI)?	2	Generally required for segmentation
	Robust to small changes/errors in segmentation or registration?	2	Not likely to be particularly robust since errors in segmentation of one compartment will affect others
	Assumes uniformity in region(s)?	0	Assumes uniform regions
	Assumes zero background?	5	Doesn't assume zero background
nsfer	Assumes known and invariant PSF?	1	Implicitly assumes all regions and positions will have the same PSF (size and shape)
Amplifies Noise Artefa	Amplifies Noise or Introduces Artefacts?	5	No artefacts or additional noise introduced
netric	Produces voxelwise correction?	0	Not evaluated for mean value based methods
Eva	Evaluate uncertainty on final value(s)?	0	Unsure how uncertainty analysis would be done
	Easy/simple implementation?	1	Ease of implementation limited by requirement to segment the whole image
	Segmentation of entire image required?	0	Segmentation of entire region always required
R	Assumption of VOI shape?	5	No spherical assumption made
	Requires use of higher resolution data (e.g. CT or MRI)?	2	Generally required for segmentation
	Robust to small changes/errors in segmentation or registration?	3	May be more robust to mis-registration errors than standard GTM since matrix is based on Regional Spread Function (rather than VOI)
	Assumes uniformity in region(s)?	0	Assumes uniform regions
N (sG	Assumes zero background?	5	Doesn't assume zero background
symmetric	Assumes known and invariant PSF?	1	Implicitly assumes all regions and positions will have the same PSF (size and shape)
	Amplifies Noise or Introduces Artefacts?	5	No artefacts or additional noise introduced
	Produces voxelwise correction?	0	Not evaluated for mean value based methods
	Evaluate uncertainty on final value(s)?	0	Unsure how uncertainty analysis would be done; note that noise properties are likely to be different to standard GTM.
	Easy/simple implementation?	1	Ease of implementation limited by requirement to segment the whole image
	Segmentation of entire image required?	0	Segmentation of entire region always required

Method	Criteria	Score	Explanation
	Assumption of VOI shape?	5	No spherical assumption made
	Requires use of higher resolution data (e.g. CT or MRI)?	2	Generally required for segmentation
<u> </u>	Robust to small changes/errors in segmentation or registration?	2	Not likely to be particularly robust since errors in segmentation of one compartment will affect others
GTN	Assumes uniformity in region(s)?	0	Assumes uniform regions
<u>y</u>	Assumes zero background?	5	Doesn't assume zero background
n GT	Assumes known and invariant PSF?	1	Implicitly assumes all regions and positions will have the same PSF (size and shape)
perturbation GTM (pGTM)	Amplifies Noise or Introduces Artefacts?	5	No artefacts or additional noise introduced
ertur	Produces voxelwise correction?	0	Not evaluated for mean value based methods
ă	Evaluate uncertainty on final value(s)?	0	Unsure how uncertainty analysis would be done
	Easy/simple implementation?	1	Ease of implementation limited by requirement to segment the whole image
	Segmentation of entire image required?	0	Segmentation of entire region always required
	Assumption of VOI shape?	5	No assumption made on shape
	Requires use of higher resolution data (e.g. CT or MRI)?	3	Segmentation currently based on CT image, but this is not strictly necessary for algorithm
	Robust to small changes/errors in segmentation or registration?	3	Robustness to moderate inaccuracies investigated (Southekal 2011). Magnitude of uncertainties have slight dependence on iteration number.
(P)	Assumes uniformity in region(s)?	1	Assumes uniformity in all regions, unless non-uniform model is used
ion (Assumes zero background?	5	Doesn't assume zero background
oject	Assumes known and invariant PSF?	5	No knowledge of PSF required (system model used)
Local Projection (LP)	Amplifies Noise or Introduces Artefacts?	4	for recon introduce artefacts?). Moore paper notes Gibbs artefacts but this may be
Loc	Produces voxelwise correction?	0	Not evaluated for mean value based methods
	Evaluate uncertainty on final value(s)?	3	Poisson stats (Noise properties known and spatially uncorrelated in projection domain
	Easy/simple implementation?	4	Relatively straightforward implementation if System Model is known
	Segmentation of entire image required?	4	Segmentation only required for small region
	Assumption of VOI shape?	5	No assumption made on shape
	Requires use of higher resolution data (e.g. CT or MRI)?	4	Originally implemented with CT-based segmentation, but could be used with emission data
	Robust to small changes/errors in segmentation or registration?	3	Not demonstrated
(LB)	Assumes uniformity in region(s)?	2	Hofheinz method computes local background separately for each voxel in the spill-out region, but this is based on a mean of the local background
pun	Assumes zero background?	5	Doesn't assume zero background; computes local background separately for each voxel in the spill-out region
kgro	Assumes known and invariant PSF?	1	Assumes known FWHM to define size of regions
Local Background (LB)	Amplifies Noise or Introduces Artefacts?	3	Not demonstrated
	Produces voxelwise correction?	0	Not evaluated for mean value based methods
	Evaluate uncertainty on final value(s)?	0	Uncertainty calculations not demonstrated in publications
	Easy/simple implementation?	4	Relatively straightforward implementation if PSF is known
	Segmentation of entire image required?	4	Segmentation derives boundaries from PET data (Hofheinz) or combination of CT and PET

Method	Criteria	Score	Explanation
	Assumption of VOI shape?	5	No assumption made on shape
	Requires use of higher resolution data (e.g. CT or MRI)?	5	Not required
	Robust to small changes/errors in segmentation or registration?	3	Depends on segmentation method
	Assumes uniformity in region(s)?	2	Gives voxelwise correction, but assumes small fluctuations about overall mean. Assumes background uniformly zero.
(OIN	Assumes zero background?	0	Background assumed zero; corrects for spill-out only
Videen (VID)	Assumes known and invariant PSF?	0	Convolves with known PSF
Vide	Amplifies Noise or Introduces Artefacts?	5	No noise or artefacts introduced
	Produces voxelwise correction?	4	Voxelwise correction for region of interest only
	Evaluate uncertainty on final value(s)?	0	Uncertainty calculations not demonstrated in publications
	Easy/simple implementation?	4	Relatively straightforward implementation if PSF is known
	Segmentation of entire image required?	4	Only ROI segmented
	Assumption of VOI shape?	5	No assumption made on shape
	Requires use of higher resolution data (e.g. CT or MRI)?	2	Segmentation usually demonstrated using higher resolution data
(Mg	Robust to small changes/errors in segmentation or registration?	3	Not demonstrated
Σ Σ	Assumes uniformity in region(s)?	2	As per Videen, assumes small variation about mean and assumes that relative regional means are known
Muller-Gartner Method (MGM)	Assumes zero background?	3	Background not assumed zero, but assumed that relative regional means are known and that variation about means in background is small.
Ž Ž	Assumes known and invariant PSF?	0	Convolves with known PSF
artne	Amplifies Noise or Introduces Artefacts?	5	No noise or artefacts introduced
er-G	Produces voxelwise correction?	4	Voxelwise correction for region of interest only
Mul	Evaluate uncertainty on final value(s)?	0	Uncertainty calculations not demonstrated in publications
	Easy/simple implementation?	4	Relatively straightforward implementation if segmentation is possible
	Segmentation of entire image required?	3	Examples usually segment entire image, but maybe not required for regions outwith brain
	Assumption of VOI shape?	5	No assumption made on shape
Single Target Correction (STC)	Requires use of higher resolution data (e.g. CT or MRI)?	5	Higher resolution data not required
	Robust to small changes/errors in segmentation or registration?	3	Depends on segmentation method
	Assumes uniformity in region(s)?	4	Only assumes uniformity for the spill-out correction
	Assumes zero background?	5	Doesn't assume zero background
	Assumes known and invariant PSF?	0	Convolves with known PSF
	Amplifies Noise or Introduces Artefacts?	5	No noise or artefacts introduced
	Produces voxelwise correction?	5	Voxelwise correction for region and local background
	Evaluate uncertainty on final value(s)?	0	Uncertainty calculations not demonstrated in publications
	Easy/simple implementation?	4	Relatively straightforward implementation if segmentation is possible
	Segmentation of entire image required?	5	Segmentation of entire image not required

Method	Criteria	Score	Explanation
	Assumption of VOI shape?	5	No assumption made on shape
	Requires use of higher resolution data (e.g. CT or MRI)?	2	Segmentation of whole image required - usually demonstrated with anatomical imaging
	Robust to small changes/errors in segmentation or registration?	3	Depends on segmentation method
	Assumes uniformity in region(s)?	2	Produces voxelwise correction but need to know relative regional means
	Assumes zero background?	4	Doesn't assume zero background but knowledge of relative regional means is strong prior
Yang	Assumes known and invariant PSF?	1	Yes (unless projection of regions is done)
,	Amplifies Noise or Introduces Artefacts?	5	No noise or artefacts introduced
	Produces voxelwise correction?	5	Voxelwise correction of entire image
	Evaluate uncertainty on final value(s)?	0	Uncertainty calculations not demonstrated in publications
	Easy/simple implementation?	2	Knowledge of relative regional mean values required
	Segmentation of entire image required?	0	Segmentation of entire image is required
	Assumption of VOI shape?	5	No assumption made on shape
	Requires use of higher resolution data (e.g. CT or MRI)?	2	Segmentation of whole image required - usually demonstrated with anatomical imaging
BV)	Robust to small changes/errors in segmentation or registration?	3	Depends on segmentation method
se (R	Assumes uniformity in region(s)?	3	Gets relative regional mean values from GTM
elwis	Assumes zero background?	5	Doesn't assume zero background
×o > F	Assumes known and invariant PSF?	1	Yes (unless projection of regions is done)
Region-based Voxelwise (RBV)	Amplifies Noise or Introduces Artefacts?	5	No noise or artefacts introduced
d-noi	Produces voxelwise correction?	5	Voxelwise correction of entire image
Reg	Evaluate uncertainty on final value(s)?	0	Uncertainty calculations not demonstrated in publications
	Easy/simple implementation?	3	Segmentation of entire image required
	Segmentation of entire image required?	0	Segmentation of entire image is required
	Assumption of VOI shape?	5	No assumption made on shape
	Requires use of higher resolution data (e.g. CT or MRI)?	2	Segmentation of whole image required - usually demonstrated with anatomical imaging
	Robust to small changes/errors in segmentation or registration?	3	Depends on segmentation method
(Assumes uniformity in region(s)?	3	correction and repeat for a number of iterations. But assumes uniformity about this
i) gu	Assumes zero background?	5	Doesn't assume zero background
iterative Yang (iY)	Assumes known and invariant PSF?	1	Yes (unless projection of regions is done)
	Amplifies Noise or Introduces Artefacts?	5	No noise or artefacts introduced
	Produces voxelwise correction?	5	Voxelwise correction of entire image
	Evaluate uncertainty on final value(s)?	0	Uncertainty calculations not demonstrated in publications
	Easy/simple implementation?	3	Segmentation of entire image required
	Segmentation of entire image required?	0	Segmentation of entire image is required

Method	Criteria	Score	Explanation
	Assumption of VOI shape?	5	No assumption made on shape
	Requires use of higher resolution data (e.g. CT or MRI)?	5	Not required
£	Robust to small changes/errors in segmentation or registration?	5	No registration or segmentation required
li) no	Assumes uniformity in region(s)?	5	No assumption on uniformity
olutic	Assumes zero background?	5	Doesn't assume zero background
Sonve	Assumes known and invariant PSF?	0	Need to know PSF, usually assumed to be spatially invariant
iterative Deconvolution (itD)	Amplifies Noise or Introduces Artefacts?	1	Noise amplified at higher iterations
rativ	Produces voxelwise correction?	5	Voxelwise correction of entire image
ite	Evaluate uncertainty on final value(s)?	0	Uncertainty calculations not demonstrated in publications
	Easy/simple implementation?	5	No user input required
	Segmentation of entire image required?	5	No segmentation required
	Assumption of VOI shape?	5	No assumption made on shape
	Requires use of higher resolution data (e.g. CT or MRI)?	4	Not necessarily required but CT or MRI may be used as regulariser
reg)	Robust to small changes/errors in segmentation or registration?	4	May depend on regulariser
itD with regularisation (itD + reg)	Assumes uniformity in region(s)?	4	No assumption on uniformity, but may be implicit assumption of a small variation about a mean activity within regions of segmented anatomical image
ion (Assumes zero background?	5	Doesn't assume zero background
risat	Assumes known and invariant PSF?	0	Need to know PSF, usually assumed to be spatially invariant
elnga	Amplifies Noise or Introduces Artefacts?	3	Noise limited by regulariser
ith re	Produces voxelwise correction?	5	Voxelwise correction of entire image
tΟw	Evaluate uncertainty on final value(s)?	0	Uncertainty calculations not demonstrated in publications
	Easy/simple implementation?	4	No user input required, except from choosing regularisation factor
	Segmentation of entire image required?	3	Segmentation of anatomical image may be required if regulariser is CT or MRI
	Assumption of VOI shape?	5	No assumption made on shape
blind iterative Deconvolution (blind itD)	Requires use of higher resolution data (e.g. CT or MRI)?	2	Publications demonstrating blind itD use anatomical data either for segmentation (Mignotte 2000) or anatomical based filtering (Wu 2017)
	Robust to small changes/errors in segmentation or registration?	3	No manual segmentation required, but some implementations may need anatomical data
	Assumes uniformity in region(s)?	5	No assumption on uniformity
	Assumes zero background?	5	Doesn't assume zero background
	Assumes known and invariant PSF?	3	No knowledge of PSF required (semi-blind deconvolution needs to know shape of PSF only), but probably assumed to be spatially invariant
	Amplifies Noise or Introduces Artefacts?	1	Noise amplified at higher iterations
	Produces voxelwise correction?	5	Voxelwise correction of entire image
	Evaluate uncertainty on final value(s)?	0	Uncertainty calculations not demonstrated in publications
	Easy/simple implementation?	3	No user input required, except from possible choice of regularisation factor
	Segmentation of entire image required?	5	No segmentation required

Method	Criteria	Score	Explanation
	Assumption of VOI shape?	5	No assumption made on shape
	Requires use of higher resolution data (e.g. CT or MRI)?	0	Method fundamentally relies on higher resolution data from another image set
(9	Robust to small changes/errors in segmentation or registration?	2	can introduce artefacts if there's a mismatch between high res and functional image, but can use 'local analysis' to reduce likelihood of this
ltire	Assumes uniformity in region(s)?	5	Doesn't assume uniformity
nw)	Assumes zero background?	5	Doesn't assume zero background
ition	Assumes known and invariant PSF?	0	Need to know PSF, and assumes spatial resolution is the same throughout the image
multiresolution (multires)	Amplifies Noise or Introduces Artefacts?	1	Amplifies noise and can introduce artefacts if there's a mismatch between high res and functional image
Jultir	Produces voxelwise correction?	5	Voxelwise correction of entire image
	Evaluate uncertainty on final value(s)?	0	Uncertainty calculations not demonstrated in publications
	Easy/simple implementation?	4	No segmentation or other user input required, except if images need to be registered
	Segmentation of entire image required?	5	No segmentation required
	Assumption of VOI shape?	5	No assumption made on shape
	Requires use of higher resolution data (e.g. CT or MRI)?	5	No other image data required
-	Robust to small changes/errors in segmentation or registration?	5	No segmentation required
g (RN	Assumes uniformity in region(s)?	5	No assumption made on uniformity
Resolution Modelling (RM)	Assumes zero background?	5	Doesn't assume zero background
Mod	Assumes known and invariant PSF?	5	No knowledge of PSF required (depends on system model)
tion	Amplifies Noise or Introduces Artefacts?	1	Introduces Gibbs artefacts
nlos	Produces voxelwise correction?	5	Voxelwise correction of entire image
Re	Evaluate uncertainty on final value(s)?	0	residual PVE can be hard to estimate due to non-linear nature of iterative recon and RM
	Easy/simple implementation?	4	Needs a good estimate of system model but currently available in clinical reconstruction software so applicable immediately
	Segmentation of entire image required?	5	No segmentation required
	Assumption of VOI shape?	5	No assumption made on shape
iors)	Requires use of higher resolution data (e.g. CT or MRI)?	0	Method relies on higher resolution data from another image set
+ pr	Robust to small changes/errors in segmentation or registration?	2	Unclear how these methods would react to mis-match
econ	Assumes uniformity in region(s)?	4	may assume areas of constant CT or MR intensity have same radiopharmaceutical uptake
ors (r	Assumes zero background?	5	Doesn't assume zero background
Reconstruction with priors (recon + priors)	Assumes known and invariant PSF?	5	No assumption of PSF required
	Amplifies Noise or Introduces Artefacts?	3	unsure of potential for introducing noise or artefacts
	Produces voxelwise correction?	5	Voxelwise correction of entire image
	Evaluate uncertainty on final value(s)?	0	Uncertainty calculations not demonstrated in publications
ecor	Easy/simple implementation?	1	Little user input required, but may need to select penalisation parameters
~	Segmentation of entire image required?	3	Segmentation of anatomical image may be required if prior is CT or MRI, but may be based on purely CT or MRI values

Method	Criteria	Score	Explanation
	Assumption of VOI shape?	5	No assumption made on shape
	Requires use of higher resolution data (e.g. CT or MRI)?	0	Method relies on higher resolution data from another image set
oriors	Robust to small changes/errors in segmentation or registration?	3	Unclear how these methods would react to mis-match, but kernel should make them more robust than pure anatomical priors
nel	Assumes uniformity in region(s)?	4	may assume areas of constant CT or MR intensity have same radiopharmaceutical uptake
h ker	Assumes zero background?	5	Doesn't assume zero background
wit	Assumes known and invariant PSF?	5	No assumption of PSF required
reconstruction with kernel priors	Amplifies Noise or Introduces Artefacts?	3	unsure of potential for introducing noise or artefacts
	Produces voxelwise correction?	5	Voxelwise correction of entire image
recor	Evaluate uncertainty on final value(s)?	0	Uncertainty calculations not demonstrated in publications
	Easy/simple implementation?	2	No user input required, but may be difficult to introduce clinically
	Segmentation of entire image required?	3	Segmentation of anatomical image may be required if prior is CT or MRI, but may be based on purely CT or MRI values
	Assumption of VOI shape?	5	No assumption made on shape
	Requires use of higher resolution data (e.g. CT or MRI)?	1	Higher resolution data intrinsic to the method (could be CT/MRI or PET)
Σ	Robust to small changes/errors in segmentation or registration?	3	Kernel method should be robust, depending on parameters used
H H	Assumes uniformity in region(s)?	4	Assumes MR or CT edges are related to PET/SPECT edges
ethoc	Assumes zero background?	5	Doesn't assume zero background
Hybrid Kernel Method (HKM)	Assumes known and invariant PSF?	4	No assumption made on PSF (?) although parameters may need optimised
	Amplifies Noise or Introduces Artefacts?	2	May suppress details which are not present in anatomical image
	Produces voxelwise correction?	5	Voxelwise correction of entire image
	Evaluate uncertainty on final value(s)?	0	Uncertainty calculations not demonstrated in publications
	Easy/simple implementation?	4	No user input required, currently available in STIR, but may be difficult to introduce clinically
	Segmentation of entire image required?	5	No segmentation required

Appendix B

Use of STIR Software

STIR is open-source software which has multiple useful tools for image generation, simulation and reconstruction used throughout this project. Instructions for STIR can be adjusted using parameter (.par) files. Use of STIR software in this project has included the use of the following tools:

- defining images based on pre-set shapes
 - generate_image generate_image.par
- adding pre-set shapes to existing datasets
 - stir_math --add combined_image.hv bkg_image.hv
 lesion_image.hv
- forward projecting through a SPECT system model (see Chapter 4.4) to produce sinogram or projection datasets, incorporating effect of collimators and attenuation
 - forward_project output_sino_filename.hs
 emission_image template_sino
 fwd_proj_parfile.par
- applying mathematical operations on projection data
 - stir_math.exe -s --including-first --timesscalar 10 output_sino_x10.hs input_sino.hs
- reconstructing projection data using FBP or OSEM, with corrections for AC and options for RM (2D and 3D)
 - OSMAPOSL reconstruction_settings.par

Example parameter files used to generate images, forward project and reconstruct with OSEM are reproduced below for reference:

```
generate image Parameters :=
 3
 4
     imaging modality:=nucmed
     patient orientation := feet in
     patient rotation := supine
 8
     output filename:=emission_image.smi
output file format type:= Interfile
9
10
11
       interfile Output File Format Parameters:=
12
         number format := unsigned integer
13
         number of bytes per pixel:=2
         scale_to_write_data:= 1
14
15
       End Interfile Output File Format Parameters:=
16
17
     X output image size (in pixels) := 64
18
     Y output image size (in pixels) := 64
19
     Z output image size (in pixels) := 64
20
     X voxel size (in mm) := 4
21
     Y voxel size (in mm) := 4
22
     Z voxel size (in mm) := 4
23
24
       Z number of samples to take per voxel := 1
25
       Y number of samples to take per voxel := 1
       {\tt X} number of samples to take per voxel := 1
26
28
29
    ; body-like shape
     shape type:= ellipsoidal cylinder
3.0
     Ellipsoidal Cylinder Parameters:=
32
        radius-x (in mm) := 96
33
        radius-y (in mm) := 84
34
        length-z (in mm) := 200
35
        origin (in mm):=\{128, 0, 0\}
36
        ; z, y, x
37
        END:=
38
    value := 5
39
40
     ; central point
41
    ;next shape :=
42
    ;shape type:= Ellipsoid
43
    ;Ellipsoid Parameters:=
44
         radius-x (in mm) := 1
    ;
4.5
         radius-y (in mm) := 1
46
         radius-z (in mm):= 1
    ;
47
         origin (in mm):=\{128, 0, 0\}
48
         END:=
49
     ;value := 5
50
51
    ; lung like shapes
52
53
54
    ; lung 1
55
     next shape :=
56
     shape type:= ellipsoidal cylinder
57
     Ellipsoidal Cylinder Parameters:=
58
        radius-x (in mm) := 32
59
        radius-y (in mm) := 64
60
        length-z (in mm) := 180
        origin (in mm):=\{128, 0, 40\}; z, y, x
61
62
        END:=
63
     value := -5
64
65
66
     ; lung 2
67
     next shape :=
68
     shape type:= ellipsoidal cylinder
69
     Ellipsoidal Cylinder Parameters:=
```

```
70
          radius-x (in mm) := 32
 71
         radius-y (in mm) := 64
 72
          length-z (in mm) := 180
 73
          origin (in mm):=\{128, 0, -40\}; z, y, x
 74
          END:=
 75
      value := -5
 76
 77
 78
      ; lung lesion-like shape
 79
      next shape :=
      shape type:= Ellipsoid
 81
      Ellipsoid Parameters:=
         radius-x (in mm) := 12
radius-y (in mm) := 12
radius-z (in mm) := 12
 82
 83
 84
          origin (in mm):=\{128, -24, 32\}; z, y, x
 85
          END:=
 86
 87
      value := 3
 88
 89
 90
 91
      ; spine like shape
 92
      next shape :=
 93
      shape type:= ellipsoidal cylinder
 94
      Ellipsoidal Cylinder Parameters:=
 95
         radius-x (in mm) := 12
         radius-y (in mm) := 12
length-z (in mm) := 200
 96
 97
 98
         origin (in mm):=\{128, 64, 0\}; z, y, x
 99
        END:=
100
      value := 3
101
102
103
      END:=
104
```

```
Forward Projector parameters:=
    ; example par file for specifying the forward projector for e.g. fwdtest
3
    type:=Matrix
 4
       Forward Projector Using Matrix Parameters :=
 5
          Matrix type := SPECT UB
 6
7
          Projection Matrix By Bin SPECT UB Parameters:=
8
9
             maximum number of sigmas:= 4.0
10
11
            psf type:= 3D
12
             ; sigma at depth = collimator slope * depth in cm + collimator sigma 0(cm)
13
                 collimator slope := 0.018\overline{3}
14
                 collimator sigma 0(cm) := 0.1
15
             ;Attenuation correction { Simple // Full // No }
16
17
             attenuation type := Simple
18
             ; Values in attenuation map in cm-1 (float file)
19
             attenuation map := atten_128.hv
20
             ;Mask properties { Cylinder // Attenuation Map // Explicit Mask // No}
21
22
             mask type := Attenuation Map
23
24
          End Projection Matrix By Bin SPECT UB Parameters:=
25
26
       End Forward Projector Using Matrix Parameters :=
27
    end:=
```

```
1
     OSMAPOSLParameters :=
 2
 3
       objective function type:= PoissonLogLikelihoodWithLinearModelForMeanAndProjData
 4
 5
       PoissonLogLikelihoodWithLinearModelForMeanAndProjData Parameters:=
 6
7
         input file := projection data.hs
8
 9
         ; output image parameters
10
         zoom := 1
11
         ; image size defaults to whole FOV
12
         xy output image size (in pixels) := 128
13
14
         ; you NEED to set this to the number of z-position in your data.
15
         ; otherwise, the current projector will abort
16
         Z output image size (in pixels):= 128
17
         ; currently NEED to set this to 0.5 to get same z-spacing as in the data
         z \text{ zoom } := 0.5
18
19
         projector pair type := Matrix
21
           Projector Pair Using Matrix Parameters :=
22
             Matrix type := SPECT UB
             Projection Matrix By Bin SPECT UB Parameters:=
23
24
                 ; width of PSF
                 maximum number of sigmas:= 2.0
25
26
                 ;PSF type of correction { 2D // 3D // Geometrical }
28
                 psf type:= Geometrical
29
                 ; next 2 parameters define the PSF. They are ignored if psf type is
                 "Geometrical"
30
                 ; These values are mostly dependent on your collimator.
31
                 ; the PSF is modelled as a Gaussian with sigma dependent on the distance
                 from the collimator
                 ; sigma_at_depth = collimator_slope * depth_in_cm + collimator sigma 0(cm)
32
33
                 collimator slope := 0.0183
34
                 collimator sigma 0(cm) := 0.1
35
36
                 ;Attenuation correction { Simple // Full // No }
37
                 attenuation type := Simple
38
                 ; Values in attenuation map in cm-1
39
                 attenuation map := atten_128.hv
40
                 ;Mask properties { Cylinder // Attenuation Map // Explicit Mask // No}
41
                 mask type := No
42
43
                ; if next variable is set to 0, only a single view is kept in memory
44
45
                keep all views in cache:= 0
46
             End Projection Matrix By Bin SPECT UB Parameters:=
47
48
49
          End Projector Pair Using Matrix Parameters :=
50
51
         subset sensitivity filenames := ssens %d.hv
         recompute sensitivity := 1
52
53
         use subset sensitivities := 1
54
55
       end PoissonLogLikelihoodWithLinearModelForMeanAndProjData Parameters:=
56
57
       initial estimate:= 1
58
       output filename prefix := recon OSEM geo
59
60
       number of subsets:= 10
61
       number of subiterations:= 200
62
       Save estimates at subiteration intervals:= 10
63
64
    END :=
65
```

Appendix C

Use of SIMIND Software

SIMIND software Version 7 was used for Monte Carlo simulation in this thesis.

An example command used to run the SIMIND simulation using an .smc file defined based on a Siemens Symbia gamma camera using LEHR collimators was:

```
simind.exe symbia_LEHR_CCW_180.smc outputfilename/FD:
density_filename.dmi/FS:input_filename.smi/PX:0.4/NN:1/I2-1/25:1330
```

Screenshots from the Change programme used to set the parameters for the simulation are included below for reference.

```
:\simind>change symbia_LEHR_for_TEK_CCW_180.smc
[2J←[H
     C H A N G E: Main page for SIMIND version V7.0
     1 - Comment sentence..... Test simulation
     2 - Change general data ....:
     3 - Change simulation flags....:
     4 - SMC file export .....: symbia_LEHR_for_TEK_CCW_18
     5 - SMC file import....:
     6 - Transfer changes to SMC files..:
     7 - Phantom soft tissue..... h2o
     8 - Phantom bone tissue....: bone
      - Cover material..... al
    10 - Crystal material..... nai
    11 - Image file - phantom .....: dens
12 - Image file - source .....: emis
    13 - Backscatter material..... pmt
    14 - Energy-resolution file....: none
    ←[22;07H←[K
                 Option number....:
```

```
C H A N G E: Scintillation camera parameters
1 - Photon energy.....keV:
                                                 140.0000
30.6890
                                                   0.0000
                                                  0.0000
5 - Phantom: half-length .....cm:
                                                  30.6890
6 - Phantom: half-width ......cm:
7 - Phantom: half-height .....cm:
                                                   0.0000
                                                   0.0000
8 - Crystal: half-length/Radius.....cm:
                                                  19.3500
9 - Crystal: thickness.....cm:
10 - Crystal: half-width.[0=circular]....cm:
11 - Backscattering material: thickness....cm:
                                                  0.9500
                                                  27.6500
                                                  10.0000
12 - Height to detector surface.....cm:
                                                  26.0000
13 - Cover: thickness.....cm:
                                                   0.1000
14 - Phantom type....:
                                                  -1.0000
                                                  -1.0000
15 - Source type....:
←[22;07H←[K
             Index number....:
```

```
C H A N G E: Scintillation camera parameters
16 - Shift source in x-direction.....cm:
                                               0.0000
17 - Shift source in y-direction.....cm:
                                                0.0000
18 - Shift source in z-direction.....cm:
                                                0.0000
                                                2.0000
19 - Photon direction.....deg:
20 - Upper window threshold.....keV:
                                               -15.0000
21 - Lower window threshold.....keV:
                                              -15.0000
22 - Energy resolution ...[140 keV]...... %:
                                                8.8000
23 - Intrinsic resolution [140 keV].....cm:
                                                0.3500
24 - Emitted photons per decay....:
                                                0.8900
25 - Source activity.....MBq:
                                              2250.0000
26 - Number of photon histories * 1E6.....
                                                0.5000
27 - keV/channel.....keV:
                                                0.5000
28 - Pixel size in simulated image.....cm:
                                                0.4795
29 - SPECT: No of projections....:
                                              120.0000
30 - SPECT: Rotation [0=-360,1=-180,2=360,3=180] :
                                                0.0000
←[22;07H←[K
            Index number....:
```

C H A N G E: Non-homogeneous phantom and SPECT parameters 31 - Pixel size in density maps..... cm: 0.4795 32 - Orientation of the density map phantom....: 0.0000 33 - Start image when reading density maps.....: 1.0000 34 - Number of CT-images....: 128.0000 35 - Density limit defining the border..... g/cm3: 0.1000 36 - Shift density map relative origin (y-dir).cm: 0.0000 37 - Shift density map relative origin (z-dir).cm: 0.0000 38 - Step size for photon path simulation.....cm: 0.1000 39 - Shift density map relative origin.(x-dir).cm: 0.0000 40 - Density threshold between soft & bone..g/cm3: 0.0000 41 - SPECT: Starting angle..... degree: 180.0000 -2.0000 42 - SPECT: Orbital rotation fraction.....: 0.0000 0.0000 45 - Code definitions in generic Zubal phantom...: 1.0000 Index number....:

```
C H A N G E: Collimator parameters ge-legp
0.1110
47 - Hole Size Y...... cm:
                                            0.1282
48 - Distance between holes in x-direction....cm:
                                            0.0160
49 - Distance between holes in y-direction....cm:
                                            0.0918
50 - Displacement center hole in x-direction...cm:
                                            0.0635
51 - Displacement center hole in y-direction...cm:
                                            0.1100
52 - Collimator thickness.....cm:
                                            2.4050
53 - Collimator routine .....:
                                            0.0000
54 - Hole shape:2=Cir,3=Hex,4=Rect....:
                                            3.0000
55 - Type: 0=PA,1=PI,2=CO,3=FB,4=DV,5=SH .....:
                                            0.0000
56 - Distance from collimator to detector.....cm:
                                            0.0000
                                            0.0000
58 - .....:
                                            0.0000
                                            0.0000
59 - Random collimator movement (0=no).....
0.0000
```

```
C H A N G E: Imaging parameters and other settings
76 - Matrix size image I .....:
                                            128.0000
77 - Matrix size image J .....:
                                            128.0000
78 - Matrix size density map I .....:
                                            128.0000
79 - Matrix size source map I .....:
                                            128.0000
80 - Energy spectra channels .....:
                                            1024.0000
                                            128.0000
81 - Matrix size Density map J .....:
82 - Matrix size source map J .....:
                                            128.0000
83 - Cut-off energy to terminate photon history..:
                                              0.0000
84 - Scoring routine .....:
                                              1.0000
85 - CSV file content .....:
                                              0.0000
←[22;07H←[K
            Index number....:
```

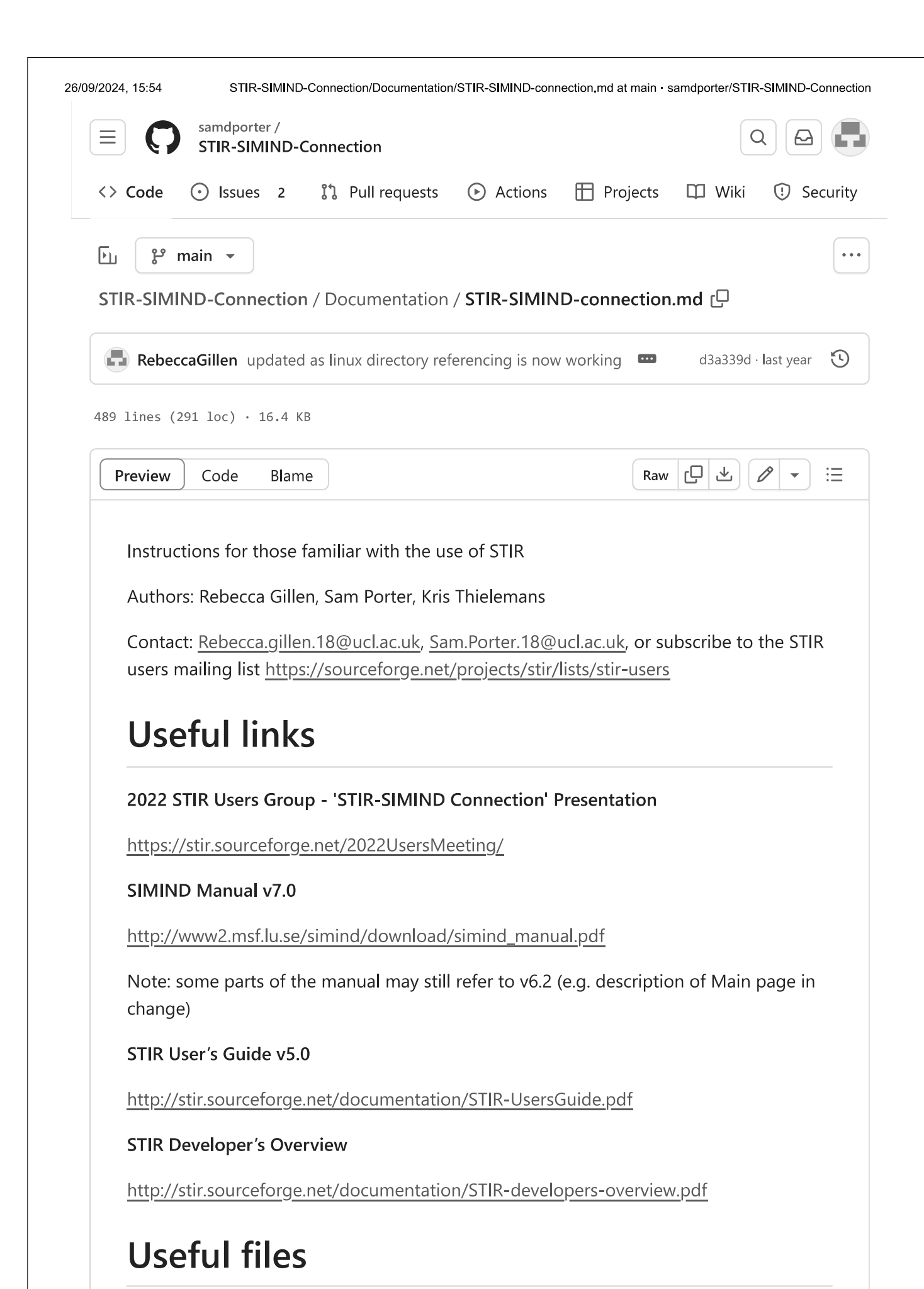
Appendix D

SIMIND STIR connection

Work in this thesis depended on utilising STIR software and SIMIND software together. This was not trivial and instructions for doing this had not been produced before. A significant amount of work was required in order to enable this. In order to make this information available to other researchers, our work was presented at the STIR user's group at the MIC conference in 2022.

Together with Sam Porter and Kris Thielemans, I published this information on GitHub as a reference for other users.https://github.com/samdporter/STIR-SIMIND-Connection/tree/main.

As well as highlighting useful software reference manuals, and key parameter files required for setting up simulations the documentation on GitHub explains how to use SIMIND for a user who is familiar with STIR. This includes the information that must be input to SIMIND (including specific format requirements) and key commands for defining the system and simulation parameters. Some of the parameters need to be defined specifically to allow SIMIND to run with STIR input data (and to allow STIR to reconstruct SIMIND simulated data). Screengrabs from the GitHub page written by myself, Sam and Kris are reproduced below:



Jupyter notebook demo and example python script [1]

Jupyter notebook STIR_simind.ipynb

Python script STIR_simind.py

Other useful STIR and SIMIND files

SIMIND:

Example .smc file input.smc

Example file for specifying energy windows input.win

STIR: example parameter files for generating data

generate_emission_image.par

generate_attenuation_image.par

example parameter file for forward projection of SPECT data

forward_project_SPECT.par

Combining STIR and SIMIND:

scripts to convert SIMIND headers to STIR-friendly format (.awk file should be in the same directory as .sh file):

Circular orbit convertSIMINDToSTIR.sh and convertSIMINDToSTIR.awk

Non-circular orbit <u>convertSIMINDToSTIR_noncirc.sh</u> and convertSIMINDToSTIR_noncirc.awk

Getting started with SIMIND

Follow the instructions for download and install from https://simind.blogg.lu.se/downloads/

(V7.0 available at 06/09/2022 / updated v7 with linux directory referencing available from 23/01/23)

There are two key programs within SIMIND:

- **change** (defines SPECT system and other simulation parameters)
- simind (performs the Monte Carlo simulation)

more detail on each will be given below

Minimum required input files for SIMIND

- Emission data (extension *.smi)
 - o Must be in 16 bit integer form
- Density data (extension *.dmi)
 - Must be in 16 bit integer form
 - Units of 1000*density (e.g. water density = 1.0 g/cm³, pixel value should be 1000)
- *.smc file
 - File created in/edited with the **change** program
 - Contains parameters used to define the imaging system

Basic SIMIND instructions; defining parameters for the system (change)

change is the program that allows configuration of simulation (i.e. defines the system) **change** is an interface for editing the *.smc file

Usage:

> change

Opens "Main" page in order to edit simind.smc file

- simind.smc initially holds all the default parameters, but is updated whenever you close the "change" program after making changes, even if you output to a different *.smc file
- Should be considered a temporary file

```
C:\simind>change
[2J+[H
     C H A N G E: Main page for SIMIND version V7.0
     1 - Comment sentence..... Test simulation
     2 - Change general data ....:
     3 - Change simulation flags....:
       - SMC file export ..... simind.smc
       - SMC file import.....
        Transfer changes to SMC files..:
       - Phantom soft tissue..... h2o
     8 - Phantom bone tissue....: bone
     9 - Cover material..... al
    10 - Crystal material...... nai
    11 - Image file - phantom ..... dens
    12 - Image file - source .....: emis
    13 - Backscatter material..... pmt
    14 - Energy-resolution file....: none
    +[22;07H+[K
                  Option number...:
```

> change filename.smc

Opens "Main" page in order to edit a specific *.smc file

Once this menu is opened, you can:

- review and edit system and simulation parameters (option 2)
- review simulation flags [T/F] (option 3)
- choose to export changes to a different *.smc file (option 4)

This creates a new file, but be aware that changes will ALSO be made to whatever *.smc file that **change** was initially opened with

• load in a different previously saved .smc file (option 5)

Note that if you pick option 1, this will force you to enter a value for all 101 parameters (and if you keep hitting return, it will overwrite each parameter with zero). $\frac{[2]}{}$

• In this case, to exit out of the change programme without saving, use CTRL+C

Usually best to pick option 2 – change general data

This allows you to specify which parameters you want to edit

A series of pages with 10-15 parameters on each page is displayed as follows:

- Indices 1 15: Scintillation Camera Parameters
- Indices 16 30: Scintillation Camera Parameters

- Indices 31 45: Non-homogeneous phantom and SPECT parameters
- Indices 46 60: Collimator parameters
- Indices 76 85: Imaging parameters and other settings
- Indices 91 101: Solid-state detector settings

If you're happy with the parameters on one page, hit return to move on to the next page

On the relevant page, enter the index number of the parameter you want to change and hit return

Enter the value you want to change that parameter to and hit return

The new value should be displayed for the relevant parameter

See SIMIND manual for detailed descriptions of all parameters for each index number.

See section below for specific parameters required to configure your simulation with voxelwise input from STIR.

When satisfied with all parameters, exit the **change** program (by hitting return on the 'home' page), then the *.smc file will be overwritten by the parameters you've just used.

Note certain parameters can also be specified using switches when you run your simind simulation (see below)

To exit **change** at any time, without saving, use CTRL+C

Parameters required to configure simulation to be compatible with voxelwise input (generated in STIR)

- Set Index-14 (type of phantom) to -1
 - density distribution map
- Set Index-15 (type of source distribution to be simulated) to -1
 - source distribution map
- Set Index-41 (SPECT: Starting angle) to 90 degrees
 - This corresponds with a STIR simulation start angle of 180 degrees

- Index 12 corresponds to radius of rotation
 - Note that units are in cm throughout (important for defining pixel sizes and radius of rotation)

Note that indices 79 and 82 (source map dimensions) must be equal

Recommend setting indices 2, 3, 4, 5, 6, and 7 as appropriate to encompass entire relevant part of the data (note that units are in cm)

Basic SIMIND instructions; performing the Monte Carlo simulation (simind)

Basic usage:

> simind param_filename.smc output_filename

Usage including switches (example):

> simind param_filename.smc output_filename/FD:dens_file/FS:emiss_file/PX:0.4

Switches are useful for performing multiple simulations using the same basic *.smc file, but varying one parameter at a time

For example, the number of photons simulated (i.e. statistical noise) can be controlled with switch /NN

The larger number chosen for switch /NN, the longer the simulation will take and the better the image statistics will be (note that total sum of events in the image will remain the same)

In addition, when using voxelwise phantoms, a switch specifying pixel size must be used /PX:

We recommend that the input files for density and emission maps are specified using switches rather than in **change** since there is a character limit of 11 characters stored using **change**

See simind manual for full list of possible runtime switches.

See simind manual for how to use switches in addition to directory referencing (note that the description in the SIMIND manual will only work for Linux systems for simind software downloaded after 23rd Jan 2023. Otherwise input and output files should be saved in the same directory - or see Sam Porter's example Jupyter notebook STIR_simind.ipynb or Python script STIR_simind.py which include use of symlink).

Output files from SIMIND

- Output files comparable to those produced with STIR:
 - *.h00 (header file)
 - o * .a00 (data)
- If setting Index 84 (scoring routine) to 1 ("scattwin")
 - 3 different sets of *.h00 and *.a00 files are produced for each energy window defined: air, scatter and "total"
 - "Total" data takes attenuation and other interactions into account
 - "Air" data is simulation without interactions in the phantom (no attenuation or scatter). Useful for comparing corrections as this corresponds to perfect corrections.
- .res file summarises simulation (how it was set up, energy windows, time taken, sensitivity etc. and all the information that is output to terminal while simind is running)

See simind manual for full list of possible output files.

Reconstructing SIMIND Data using STIR

SIMIND output data can be reconstructed with STIR. First, a few tweaks need to be made to the header file to convert it to a STIR-friendly form. Steps are included below, but note that this can be done quickly and efficiently using the convertSIMINDToSTIR.sh script, note that you will also need the corresponding .awk file in the same folder)

- make a copy of the .h00 file, and rename it with extension *.hs
- Edit *.hs file as follows:
 - Comment out, or delete the following:
 - Program author
 - Program version
 - Original institution
 - Contact person
 - Patient name

STIR-SIMIND-Connection/Documentation/STIR-SIMIND-connection, at main · samdporter/STIR-SIMIND-Connection

- Study ID
- Data description
- Exam type
- Patient ID
- Total number of images
- Number of detector heads
- Number of images/energy window
- Energy window upper and lower level
- Time per projection (sec)
- Image duration (sec) [throws STIR error]
- Change number format from "short float" to "float"
- Ensure !matrix size [2] := value corresponds to number of STIR z-slices (it probably won't by default)
- o Change radius value to mm (currently in cm) and uncomment Radius line

For attenuation correction; use STIR-appropriate attenuation values in the reconstruction (ie. Values of approx. 0.15 rather than 1000 for water). Use STIR utility ctac_to_mu_values to convert from CT HU to STIR- appropriate attenuation values.

Data Types

- SIMIND requires 16-bit integer data when dealing with voxelwise inputs
 - o Can specify this filetype in the generate image .par file in STIR
 - When using voxelwise input (e.g. as generated in STIR), SIMIND expects the activity file to have extension *.smi, and the density map to have extension *.dmi
 - Rename the binary (*.v) files generated by STIR with the relevant extension
- SIMIND outputs results of simulated SPECT projections as a binary file, consisting of projection data in 32-bit float format (*.a00 files). Header files in interfile format are also produced (*.h00)
- STIR uses Interfile version 3.3 "(with a few small changes)"

- SIMIND also uses Interfile type headers but note that units are in cm rather than mm
- Naming data types: STIR is OK with reference to "integer", but SIMIND needs "signed integer" [3]

Defining attenuation maps

- STIR uses attenuation coefficient values (e.g. 0.15cm^-1^ for water)
- SIMIND uses density x 1000 (e.g. 1000 for water, where density of water = 1.0 g/cm³)
- Remember when simulating in SIMIND to use SIMIND attenuation map
 - If reconstructing in STIR, remember to use STIR-appropriate attenuation values

Simulation with a non-circular orbit

- An elliptical orbit can be defined using Index-42 to define the ratio between major and minor axes. Index-12 defines the horizontal radius (z-axis in the SIMIND coordinate system)
- Non-circular orbits based on the edge of the objects in the density map can be defined by setting Index-42 to <0. The absolute value of Index-42 adds an airgap between the defined border and the surface of the detector (the detector here meaning the overall device so could be collimator surface, Al cover or crystal depending on how simulation is set-up). The edge of objects in the density map is defined by Index-35 this should be <1 for water (i.e. lower than the g/cm value which defines the relevant border). A value of 0.1 has worked well for a test datset.

Note that the .h00 file produced by simind states "orbit:=noncircular", but STIR headers need "orbit:=Non-circular". Also radii values are in cm rather than mm. These aspects can be resolved by running the convertSIMINDToSTIR_noncirc.sh script (this copies radii values from the .cor output file into a separate text file, and then reads them in to the STIR header in an appropriate format).

Other key differences & things to be aware of

• An apparent limitation of SIMIND is that the dimensions of the input datasets should be equal (i.e. x=y=z)

- \circ If, for example z=/=x or y, the simulation will run, but the .h00 file will not contain any information regarding the number of z-slices
- If specifying input emission and attenuation filenames via the main menu (options 11 and 12, there is a character limit (not including the file extension) of 11 characters
 - Suggested workaround: specifying filenames as switches OR editing the .smc file in a text editor after using the change program
- Due to the use of switches in SIMIND, referring to files in different directories does not seem to be possible - recommend that all input data files are stored in the same directory as simind is run from
- Units of ROR
 - o SIMIND = cm
 - Note that this applies to both setting parameters, and in the interfile header
 - STIR = mm [as per interfile standard]
- Coordinate systems
 - STIR

x-axis: horizontal axis, pointing right when looking from the bed into the gantry

y-axis: vertical axis, pointing downwards

z-axis: the scanner axis, pointing from the gantry towards the bed

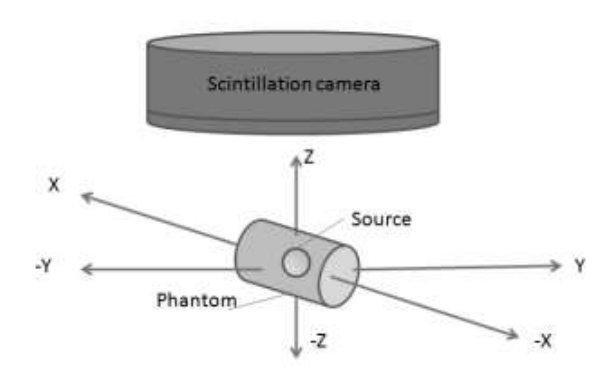
The origin of the X and Y axes are located on the central axis of the PET scanner and the Z origin (z=0) is located in the middle of the first ring (i.e at the opposite side of the bed). Note that for images with an even size in x and y, the axis of the scanner does coincide with the centre of a pixel. In particular, for range of 2n, the (internal) image coordinates would run from -n to (n-1).

http://stir.sourceforge.net/wiki/index.php/STIR_FAQ#How_does_the_STIR_coor dinate_system_work_.28e.g._for_generate_image.29

- Coordinates relate to the scanner (not the patient/phantom)
- STIR coordinates are ordered (z,y,x) (with z along the scanner axis, y vertical and x horizontal)
- Recommend to use odd-sided images in all directions
- SIMIND
 - When simulating voxel-based phantoms, the first density/activity image is located towards +X and the last one is located towards -X. When

26/09/2024, 15:54

STIR-SIMIND-Connection/Documentation/STIR-SIMIND-connection.md at main · samdporter/STIR-SIMIND-Connection simulating SPECT, the camera rotates in the ZY plane either clockwise or counter-clockwise (controlled by index 30)



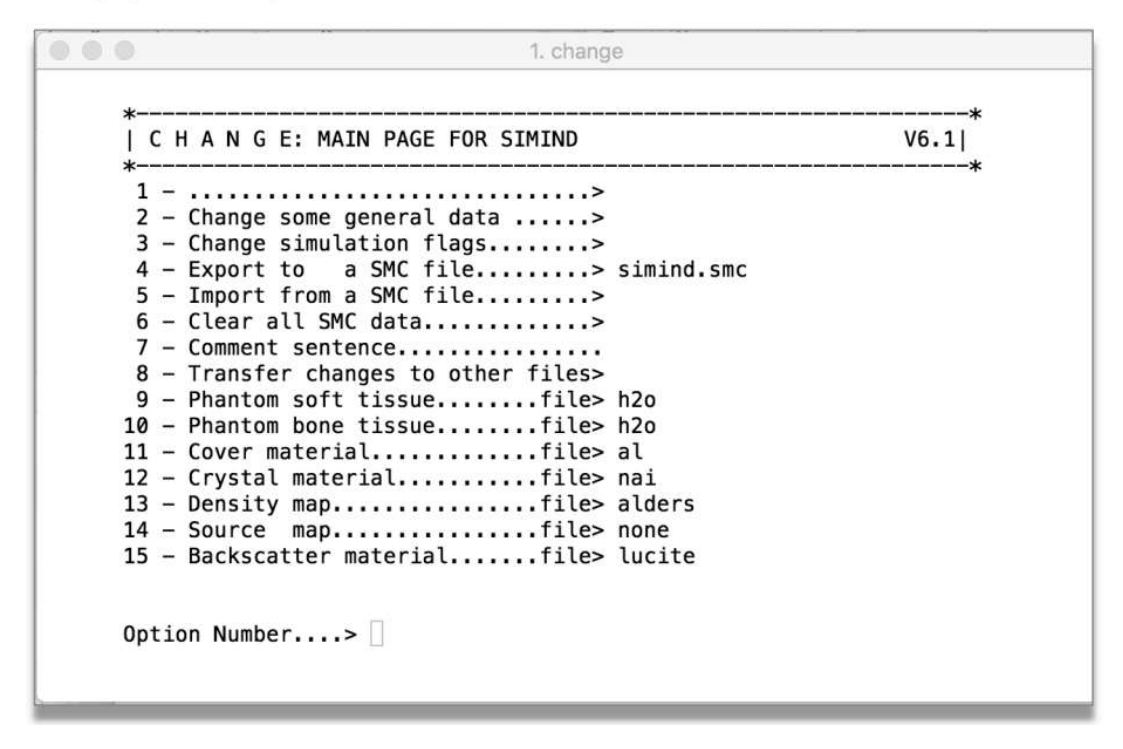
Disclaimer:

This crib sheet and associated test data/tutorials/Jupyter notebook is a work in progress and does not claim to be entirely complete or accurate.

The authors welcome any additions/corrections.

Appendix 1 – old Main page in change for SIMIND v6.1

Main page in Change



26/09/2024, 15:54 STIR-SIMIND-Connection/Documentation/STIR-SIMIND-connection.md at main · samdporter/STIR-SIMIND-Connection

- 1. These may be added to STIR examples at a later date **2**
- 2. In v6.2, it was possible to update comment sentence, but don't seem to be able to do this with V7 (manual says you can change using Index-9 of the main menu. On v6.2 it was option 7: see appendix)
- 3. RG to look into this to clarify which files this is important for; think it throws up an error or warning <a>[<a>[

Appendix E

IRAS Application and Ethical Approval

Following discussion with the NHS Greater Glasgow and Clyde Research and Innovation department, an IRAS application was required to use retrospective patient data for this work.

This appendix reproduces the letter from the Research and Innovation department at NHS Greater Glasgow and Clyde confirming that the study has been approved.



Research & Innovation Dykebar Hospital, Ward 11 Grahamston Road Paisley, PA2 7DE Scotland, UK

Coordinator/administrator: Rozanne Suarez Telephone Number: NA E-Mail: Rozanne.Suarez2@ggc.scot.nhs.uk

Website: https://www.nhsggc.org.uk/aboutus/professional-support-sites/research-innovation

06/03/2023

Rebecca Gillen NHS Greater Glasgow and Clyde

NHS GG&C Board Approval

Dear Rebecca Gillen

Study Title: Partial Volume Correction in Oncology SPECT

Principal Investigator: Rebecca Gillen

GG&C HB site Glasgow Royal Infirmary

Sponsor NHS Greater Glasgow and Clyde

 R&I reference:
 GN23ON023

 REC reference:
 23/NRS/0017

 Protocol no:
 V1.2 – 17.02.2023

(including version and

date)

I am pleased to confirm that Greater Glasgow & Clyde Health Board is now able to grant Approval for the above study.

Conditions of Approval

- 1. For Clinical Trials as defined by the Medicines for Human Use Clinical Trial Regulations, 2004
 - a. During the life span of the study GGHB requires the following information relating to this site
 - i. Notification of any potential serious breaches.
 - ii. Notification of any regulatory inspections.

It is your responsibility to ensure that all staff involved in the study at this site have the appropriate GCP training according to the GGHB GCP policy (www.nhsggc.org.uk/content/default.asp?page=s1411), evidence of such training to be filed in the site file. Researchers must follow NHS GG&C local policies, including incident reporting.

- 2. For all studies the following information is required during their lifespan.
 - a. First study participant should be recruited within 30 days of approval date.
 - b. Recruitment Numbers on a monthly basis
 - c. Any change to local research team staff should be notified to R&I team
 - d. Any amendments Substantial or Non Substantial
 - e. Notification of Trial/study end including final recruitment figures
 - f. Final Report & Copies of Publications/Abstracts



g. You must work in accordance with the current NHS GG&C COVID19 guidelines and principles.

Please add this approval to your study file as this letter may be subject to audit and monitoring.

Your personal information will be held on a secure national web-based NHS database.

I wish you every success with this research study

Yours sincerely,

Rozanne Suarez Research Co-ordinator

Bibliography

- Sangtae Ahn, Steven G Ross, Evren Asma, Jun Miao, Xiao Jin, Lishui Cheng, Scott D Wollenweber, and Ravindra M Manjeshwar. Quantitative comparison of OSEM and penalized likelihood image reconstruction using relative difference penalties for clinical PET. *Physics in Medicine & Biology Phys. Med. Biol*, 60: 5733–5751, 2015. doi: 10.1088/0031-9155/60/15/5733.
- Mercy I. Akerele, Steven Sourbron, Charalampos Tsoumpas, Nicolas A.
 Karakatsanis, Daniel Deidda, Jacobo Cal-Gonzalez, Rachael O. Forsythe,
 Marc R. Dweck, Maaz Syed, David E. Newby, and Robert G. Aykroyd.
 Comparison of Correction Techniques for the Spill in Effect in Emission
 Tomography. *IEEE Transactions on Radiation and Plasma Medical Sciences*,
 Early Acce:1–1, 2020. ISSN 2469-7311. doi: 10.1109/TRPMS.2020.2980443.
- Abass Alavi, Thomas J. Werner, Poul Flemming Høilund-Carlsen, and Habib Zaidi. Correction for Partial Volume Effect Is a Must, Not a Luxury, to Fully Exploit the Potential of Quantitative PET Imaging in Clinical Oncology. *Molecular Imaging and Biology*, 20(1):1–3, feb 2018. ISSN 1536-1632. doi: 10.1007/s11307-017-1146-y.
- Adam M. Alessio, Paul M. Kinahan, and Thomas Lewellen. Improved quantitation for PET/CT image reconstruction with system modeling and anatomical priors. In *Medical Imaging 2005: Image Processing*, volume 5747, page 695. SPIE, apr 2005. doi: 10.1117/12.595372.
- Adam M. Alessio, Arman Rahmim, and Colin G. Orton. Point/counterpoint.

- Resolution modeling enhances PET imaging. *Medical physics*, 40(12), 2013. doi: 10.1118/1.4821088.
- Hossein Arabi, Azadeh Akhavan Allaf, Amirhossein Sanaat, Isaac Shiri, and Habib Zaidi. The promise of artificial intelligence and deep learning in PET and SPECT imaging. *Physica medica: PM: an international journal devoted to the applications of physics to medicine and biology: official journal of the Italian Association of Biomedical Physics (AIFB)*, 83:122–137, 3 2021. ISSN 1724-191X. doi: 10.1016/J.EJMP.2021.03.008.
- Ian S. Armstrong. Spatial dependence of activity concentration recovery for a conjugate gradient (Siemens xSPECT) algorithm using manufacturer-defined reconstruction presets. *Nuclear Medicine Communications*, 40(3):287–293, mar 2019. ISSN 14735628. doi: 10.1097/MNM.00000000000000060.
- Samuli Arvola, Ivan Jambor, Anna Kuisma, Jukka Kemppainen, Sami Kajander, Marko Seppänen, and Tommi Noponen. Comparison of standardized uptake values between 99m tc-hdp spect/ct and 18 f-naf pet/ct in bone metastases of breast and prostate cancer. *EJNMMI Research*, 9, 2019. doi: 10.1186/s13550-019-0475-z.
- Steffie M B Peters, Niels R van der Werf, Marcel Segbers, Floris H P van Velden, Roel Wierts, Koos A K Blokland, Mark W Konijnenberg, Sergiy V Lazarenko, Eric P Visser, Martin Gotthardt, and Al EJNMMI Physics. Towards standardization of absolute SPECT/ CT quantification: a multi-center and multi-vendor phantom study EJNMMI Physics. *EJNMMI Physics*, 6(29), 2019. doi: 10.1186/s40658-019-0268-5.
- Daniel Badger and Leighton Barnden. Spatial resolution is dependent on image content for SPECT with iterative reconstruction incorporating distance dependent resolution (DDR) correction. *Australasian Physical and Engineering Sciences in Medicine*, 37(3):551–557, sep 2014.
- Dale L. Bailey and Kathy P. Willowson. Quantitative SPECT/CT: SPECT joins PET

- as a quantitative imaging modality. *European Journal of Nuclear Medicine and Molecular Imaging*, 41(S1):17–25, may 2014. ISSN 1619-7070. doi: 10.1007/s00259-013-2542-4.
- David L. Barbee, Ryan T. Flynn, James E. Holden, Robert J. Nickles, and Robert Jeraj. A method for partial volume correction of PET-imaged tumor heterogeneity using expectation maximization with a spatially varying point spread function. *Physics in Medicine and Biology*, 55(1):221–36, jan 2010. ISSN 1361-6560. doi: 10.1088/0031-9155/55/1/013.
- Beatrice Berthon, Ida Häggström, Aditya Apte, Bradley J. Beattie, Assen S. Kirov, John L. Humm, Christopher Marshall, Emiliano Spezi, Anne Larsson, and C. Ross Schmidtlein. PETSTEP: Generation of synthetic PET lesions for fast evaluation of segmentation methods. *Physica Medica*, 31(8):969–980, dec 2015. ISSN 1724191X. doi: 10.1016/j.ejmp.2015.07.139.
- V. Bettinardi, Isabella Castiglioni, Elisabetta De Bernardi, and M. C. Gilardi. PET quantification: strategies for partial volume correction. *Clinical and Translational Imaging*, 2(3):199–218, jun 2014. ISSN 2281-5872. doi: 10.1007/s40336-014-0066-y.
- Jan Biemond, Reginald L Lagendi, and Russell M Mersereau. Iterative Methods for Image Deblurring. In *Proceedings of the IEEE*, volume 78, pages 856–883, 1990. URL https://pdfs.semanticscholar.org/05fd/12610f341ef0ea389081ae5b83aa57479bbe.pdf.
- James Bland, Abolfazl Mehranian, Martin A. Belzunce, Sam Ellis, Casper Costa-Luis, Colm J. McGinnity, Alexander Hammers, and Andrew J. Reader. Intercomparison of MR-informed PET image reconstruction methods. *Medical Physics*, page mp.13812, oct 2019. ISSN 0094-2405. doi: 10.1002/mp.13812.
- Ronald Boellaard, Nanda C Krak, Otto S Hoekstra, and Adriaan A Lammertsma. Effects of noise, image resolution, and ROI definition on the accuracy of standard

- uptake values: a simulation study. *Journal of Nuclear Medicine*, 45(9):1519–27, sep 2004. ISSN 0161-5505.
- N. Boussion, C. Cheze Le Rest, M. Hatt, and D. Visvikis. Incorporation of wavelet-based denoising in iterative deconvolution for partial volume correction in whole-body PET imaging. *European Journal of Nuclear Medicine and Molecular Imaging*, 36(7):1064–1075, jul 2009. ISSN 1619-7070. doi: 10.1007/s00259-009-1065-5.
- James E. Bowsher, Hong Yuan, Laurence W. Hedlund, Timothy G. Turkington, Gamal Akabani, Alexandra Badea, William C. Kurylo, C. Ted Wheeler, Gary P. Cofer, Mark W. Dewhirst, and G. Allan Johnson. Utilizing MRI information to estimate F18-FDG distributions in rat flank tumors. In *IEEE Nuclear Science Symposium Conference Record*, volume 4, pages 2488–2492, 2004. doi: 10. 1109/nssmic.2004.1462760.
- Winfried Brenner, Karl Heinz Bohuslavizki, Nicole Sieweke, Stephan Tinnemeyer, Malte Clausen, and Eberhard Henze. Quantification of diphosphonate uptake based on conventional bone scanning. *European Journal of Nuclear Medicine*, 24, 10 1997.
- Saxby Brown, Dale L. Bailey, Kathy P. Willowson, and Clive Baldock. Investigation of the relationship between linear attenuation coefficients and CT Hounsfield units using radionuclides for SPECT. *Applied Radiation and Isotopes*, 66(9): 1206–1212, sep 2008. ISSN 0969-8043. doi: 10.1016/J.APRADISO.2008.01. 002.
- Ralph A Bundschuh, Markus Essler, Julia Dinges, Christian Berchtenbreiter, Jan Mariss, Axel Martínez-Möller, Gaspar Delso, Melanie Hohberg, Stephan G Nekolla, Dominik Schulz, Sibylle I Ziegler, and Markus Schwaiger. Semiautomatic Algorithm for Lymph Node Analysis Corrected for Partial Volume Effects in Combined Positron Emission Tomography-Computed

- Tomography. *Medical Imaging*, 9(6):319–328, 2010. doi: 10.2310/7290.2010. 00019.
- Michal Cachovan, Alexander Hans Vija, Joachim Hornegger, and Torsten Kuwert. Quantification of 99m tc-dpd concentration in the lumbar spine with spect/ct. *EJNMMI Research*, 2013.
- Jacobo Cal-González, Stephen C. Moore, M-A Park, J L Herraiz, J J Vaquero, M Desco, and J M Udias. Improved quantification for local regions of interest in preclinical PET imaging. *Physics in Medicine and Biology*, 60:7127–7149, 2015. doi: 10.1088/0031-9155/60/18/7127.
- Jacobo Cal-González, Xiang Li, Daniel Heber, Ivo Rausch, Stephen C. Moore, Klaus Schäfers, Marcus Hacker, and Thomas Beyer. Partial volume correction for improved PET quantification in 18F-NaF imaging of atherosclerotic plaques. *Journal of Nuclear Cardiology*, 25(5):1742–1756, oct 2018a. ISSN 1071-3581. doi: 10.1007/s12350-017-0778-2.
- Jacobo Cal-González, Charalampos Tsoumpas, M L Lassen, S Rasul, L Koller, M Hacker, Klaus Schäfers, and Thomas Beyer. Impact of motion compensation and partial volume correction for 18 F-NaF PET/CT imaging of coronary plaque. *Physics in Medicine and Biology*, 63(1):015005, dec 2018b. ISSN 1361-6560. doi: 10.1088/1361-6560/aa97c8.
- Alfred S. Carasso. Linear and nonlinear image deblurring: A documented study. *Society for Industrial and Applied Mathematics Journal on Numerical Analysis*, 36(6):1659–1689, 1999. ISSN 00361429. doi: 10.1137/S0036142997320413.
- Lily Carnegie-Peake, Jan Taprogge, Iain Murray, Glenn D Flux, and Jonathan Gear. Quantification and dosimetry of small volumes including associated uncertainty estimation. *EJNMMI Physics*, 86(9), 2022. doi: 10.1186/s40658-022-00512-9.
- Lee Tzuu Chang. A method for attenuation correction in radionuclide computed tomography. *IEEE Transactions on Nuclear Science*, 25(1):638–643, 1978. ISSN 15581578. doi: 10.1109/TNS.1978.4329385.

- Zhibiao Cheng, Junhai Wen, Gang Huang, and Jianhua Yan. Applications of artificial intelligence in nuclear medicine image generation. *Quantitative Imaging in Medicine and Surgery*, 11(6):2792822–2792822, jun 2021. ISSN 2223-4306. doi: 10.21037/QIMS-20-1078.
- Simon R. Cherry, James A. Sorenson, and Michael E. Phelps. *Physics in Nuclear Medicine*. Elsevier, jan 2012. ISBN 9781416051985. doi: 10.2967/jnumed.113. 123125.
- Carlo Chiesa, Manuel Bardiès, and Habib Zaidi. Voxel-based dosimetry is superior to mean-absorbed dose approach for establishing dose-effect relationship in targeted radionuclide therapy. *Medical Physics*, 46(12):5403–5406, oct 2019. ISSN 0094-2405. doi: 10.1002/mp.13851.
- D L Colton and R Kress. *Inverse acoustic and electromagnetic scattering theory*, volume 93. Springer, 4 edition, 1998.
- Matthijs C F Cysouw, Gerbrand Maria Kramer, Otto S Hoekstra, Virginie Frings, Adrianus Johannes de Langen, Egbert F Smit, Alfons J M van den Eertwegh, Daniela E Oprea-Lager, and Ronald Boellaard. Accuracy and Precision of Partial-Volume Correction in Oncological PET/CT Studies. *Journal of Nuclear Medicine*, 57(10):1642–1649, oct 2016. ISSN 1535-5667. doi: 10.2967/jnumed. 116.173831.
- Matthijs C F Cysouw, Gerbrand M Kramer, Linda J Schoonmade, Ronald Boellaard, Henrica C W de Vet, and Otto S Hoekstra. Impact of partial-volume correction in oncological PET studies: a systematic review and meta-analysis. *European Journal of Nuclear Medicine and Molecular Imaging*, 44(12):2105–2116, nov 2017. ISSN 1619-7089. doi: 10.1007/s00259-017-3775-4.
- Matthijs C F Cysouw, S. V. S. Golla, V. Frings, E. F. Smit, Otto S Hoekstra, G. M. Kramer, Ronald Boellaard, and On behalf of the QuIC-ConCePT Consortium. Partial-volume correction in dynamic PET-CT: effect on tumor kinetic parameter estimation and validation of simplified metrics.

- EJNMMI Research, 9(1):12, dec 2019. ISSN 2191-219X. doi: 10.1186/s13550-019-0483-z. URL https://ejnmmires.springeropen.com/articles/10.1186/s13550-019-0483-z.
- Brian D'Alessandro, Mark Madsen, Ehsan Samei, Xiang Li, Jin Wooitan, Kevin S. Berbaum, Kevin Schartz, Robert Caldwell, and Lionel S. Zuckier. Synthetic Positron Emission Tomography-Computed Tomography Images for Use in Perceptual Studies. *Seminars in Nuclear Medicine*, 41(6):437–448, nov 2011. ISSN 0001-2998. doi: 10.1053/J.SEMNUCLMED.2011.06.007.
- Data Spectrum. Elliptical Jaszczak Phantom, 2025. URL https://www.spect.com/our-products/elliptical-jaszczak-phantom.
- Stijn De Schepper, Philipp Ritt, Tim Van Den Wyngaert, and Torsten Kuwert. Quantitative radionuclide imaging of bone metastases. *The quarterly journal of nuclear medicine and molecular imaging: official publication of the Italian Association of Nuclear Medicine (AIMN) [and] the International Association of Radiopharmacology (IAR), [and] Section of the Society of..., 63(2):129–135, jun 2019. ISSN 1827-1936. doi: 10.23736/S1824-4785.19.03204-7. URL https://pubmed.ncbi.nlm.nih.gov/31298016/.*
- Milan Decuyper, Jens Maebe, Roel Van Holen, and Stefaan Vandenberghe. Artificial intelligence with deep learning in nuclear medicine and radiology. *EJNMMI Physics 2021 8:1*, 8(1):1–46, dec 2021. ISSN 2197-7364. doi: 10.1186/S40658-021-00426-Y.
- Daniel Deidda, Nicolas A Karakatsanis, Philip M Robson, Yu-Jung Tsai, Nikos Efthimiou, Kris Thielemans, Zahi A Fayad, Robert G Aykroyd, and Charalampos Tsoumpas. Hybrid PET-MR list-mode kernelized expectation maximization reconstruction. *Inverse Problems*, 35(4):044001, apr 2019. ISSN 0266-5611. doi: 10.1088/1361-6420/ab013f.
- Robert A. Dekemp, R. Glenn Wells, and Rob S. B. Beanlands. Lesion contrast recovery for partial-volume averaging: Quantitative correction or qualitative

- enhancement? *Journal of Nuclear Cardiology*, 25:1757–9, 2018. doi: 10.1007/s12350-017-0869-0.
- Cedric Desmonts, Mohammed Abdeldjalil Bouthiba, Blandine Enilorac, Catherine Nganoa, Denis Agostini, and Nicolas Aide. Evaluation of a new multipurpose whole-body czt-based camera: comparison with a dual-head anger camera and first clinical images. *EJNMMI Physics*, 7, 3 2020. doi: https://doi.org/10.1186/s40658-020-0284-5.
- Yuni K. Dewaraja, Michael Ljungberg, and K. F. Koral. Monte Carlo evaluation of object shape effects in iodine-131 SPET tumor activity quantification. *European Journal of Nuclear Medicine and Molecular Imaging*, 28(7):900–6, jul 2001. ISSN 0340-6997.
- Yuni K. Dewaraja, Eric C. Frey, George Sgouros, A. Bertrand Brill, Peter Roberson, Pat B. Zanzonico, and Michael Ljungberg. MIRD pamphlet No. 23: quantitative SPECT for patient-specific 3-dimensional dosimetry in internal radionuclide therapy. *Journal of Nuclear Medicine*, 53(8):1310–25, aug 2012. ISSN 1535-5667. doi: 10.2967/jnumed.111.100123.
- John Dickson, James Ross, and Stefan Vöö. Quantitative SPECT: the time is now. *EJNMMI Physics*, 6(1):4, dec 2019. ISSN 2197-7364. doi: 10.1186/s40658-019-0241-3.
- John C. Dickson, Ian S. Armstrong, Pablo Minguez Gabiña, Ana M. Denis-Bacelar, Aron K. Krizsan, Jonathan M. Gear, Tim Van den Wyngaert, Lioe-Fee de Geus-Oei, and Ken Herrmann. EANM practice guideline for quantitative SPECT-CT. European Journal of Nuclear Medicine and Molecular Imaging 2022, 8:1–16, dec 2022. ISSN 1619-7089. doi: 10.1007/S00259-022-06028-9.
- DICOM Standards Committee. DICOM Conformance Statement, 2025. URL https://dicom.nema.org/medical/dicom/current/output/html/part03.html{#}sect{_}C.8.4.12.

- Yong Du, B. M. W. Tsui, and E.C. Frey. Partial volume effect compensation for quantitative brain SPECT imaging. *IEEE Transactions on Medical Imaging*, 24 (8):969–976, aug 2005. ISSN 0278-0062. doi: 10.1109/TMI.2005.850547.
- EARL and EANM. Lu-177 SPECT/CT Accreditation, 2022. URL https://earl.eanm.org/177lu-spect-ct/.
- Kjell Erlandsson and Brian F. Hutton. A novel voxel-based partial volume correction method for single regions of interest. *Journal of Nuclear Medicine*, 55(supplement 1):2123–2123, may 2014.
- Kjell Erlandsson, A.T. Wong, R. van Heertum, J.J. Mann, and R.V. Parsey. An improved method for voxel-based partial volume correction in PET and SPECT. *NeuroImage*, 31:T84, jan 2006. ISSN 10538119. doi: 10.1016/j.neuroimage. 2006.04.072.
- Kjell Erlandsson, Krzysztof Kacperski, Dean van Gramberg, and Brian F. Hutton. Performance evaluation of D-SPECT: a novel SPECT system for nuclear cardiology. *Physics in Medicine and Biology*, 54(9):2635–2649, may 2009. doi: 10.1088/0031-9155/54/9/003.
- Kjell Erlandsson, Irène Buvat, P Hendrik Pretorius, Benjamin A Thomas, and Brian F Hutton. A review of partial volume correction techniques for emission tomography and their applications in neurology, cardiology and oncology. *Physics in Medicine and Biology*, 57(21):R119–R159, nov 2012a. ISSN 0031-9155. doi: 10.1088/0031-9155/57/21/R119.
- Kjell Erlandsson, Irène Buvat, P. Hendrik Pretorius, Benjamin A. Thomas, and Brian F. Hutton. A review of partial volume correction techniques for emission tomography and their applications in neurology, cardiology and oncology. *Physics in Medicine and Biology*, 57(21):R119–R159, nov 2012b. ISSN 0031-9155. doi: 10.1088/0031-9155/57/21/R119.
- Domenico Finocchiaro, Salvatore Berenato, Elisa Grassi, Valentina Bertolini, Gastone Castellani, Nico Lanconelli, Annibale Versari, Emiliano Spezi, Mauro

- Iori, and Federica Fioroni. Partial volume effect of SPECT images in PRRT with 177Lu labelled somatostatin analogues: A practical solution. *Physica Medica*, 57:153–159, jan 2019. ISSN 1120-1797. doi: 10.1016/J.EJMP.2018.12.029.
- Brent Foster, Ulas Bagci, Awais Mansoor, Ziyue Xu, and Daniel J. Mollura. A review on segmentation of positron emission tomography images. *Computers in Biology and Medicine*, 50:76–96, jul 2014. ISSN 0010-4825. doi: 10.1016/J. COMPBIOMED.2014.04.014.
- Russell Frood, Garry McDermott, and Andrew Scarsbrook. Respiratory-gated PET/CT for pulmonary lesion characterisation—promises and problems. *The British Journal of Radiology*, 91(1086):20170640, 2018. ISSN 1748880X. doi: 10.1259/BJR.20170640.
- Hanif Gabrani-Juma, Zamzam Al Bimani, Lionel S. Zuckier, and Ran Klein. Development and validation of the Lesion Synthesis Toolbox and the Perception Study Tool for quantifying observer limits of detection of lesions in positron emission tomography. *Journal of medical imaging (Bellingham, Wash.)*, 7(2): 1, apr 2020. ISSN 2329-4302. doi: 10.1117/1.JMI.7.2.022412. URL https://pubmed.ncbi.nlm.nih.gov/32341935/.
- R Gadd, M Baker, K S Nirjan, S Owens, W Thomson, and M J Woo. Protocol for establishing and maintaining the calibration of medical radionuclide calibrators and their quality control. measurement good practice guide no.93. Technical report, National Physical Laboratory, 5 2006. URL https://www.npl.co.uk/resources/gpgs/maintaining-the-calibration-medical-radionuclide.
- J. Gear, F. Leek, and G. Flux. Improving resolution recovery factors using 3D printed phantoms and Monte Carlo for quantitative imaging and dosimetry. In *Annual Congress of the European Association of Nuclear Medicine October 12* 16, 2019 Barcelona, Spain, volume 46, page \$135. NLM (Medline), oct 2019. doi: 10.1007/s00259-019-04486-2.

- Jonathan I. Gear, Maurice G. Cox, Johan Gustafsson, Katarina Sjögreen Gleisner, Iain Murray, Gerhard Glatting, Mark W. Konijnenberg, and Glenn D. Flux. EANM practical guidance on uncertainty analysis for molecular radiotherapy absorbed dose calculations. *European Journal of Nuclear Medicine and Molecular Imaging*, 45(13):2456–2474, dec 2018. ISSN 1619-7070. doi: 10.1007/s00259-018-4136-7.
- Mirela Gherghe, Mario Demian Mutuleanu, Adina Elena Stanciu, Ionela Irimescu, Alexandra Maria Lazar, Radu Valeriu Toma, Oana Gabriela Trifanescu, and Rodica Maricela Anghel. Quantitative assessment of treatment response in metastatic breast cancer patients by spect-ct bone imaging—getting closer to pet-ct. *Cancers*, 15:696, 2 2023. ISSN 20726694. doi: 10.3390/CANCERS15030696.
- H. B. Giap, D. J. Macey, J. E. Bayouth, and A. L. Boyer. Validation of a dose-point kernel convolution technique for internal dosimetry. *Physics in medicine and biology*, 40(3):365–381, 1995. ISSN 0031-9155. doi: 10.1088/0031-9155/40/3/003.
- R. Gillen, M.J. Firbank, J. Lloyd, and J.T. O'brien. CT-based attenuation and scatter correction compared with uniform attenuation correction in brain perfusion SPECT imaging for dementia. *Physics in Medicine and Biology*, 60(17), 2015. ISSN 13616560. doi: 10.1088/0031-9155/60/17/6775.
- Rebecca Gillen. Assessing the potential extent of spatial dependence of the Partial Volume Effect in SPECT. In *British Nuclear Medicine Society Spring Meeting* 2022, volume 43, pages 577–623. NLM (Medline), May 2022. doi: 10.1097/MNM.000000000001555.
- Rebecca Gillen, Ana M. Denis-Bacelar, Sarah J. McQuaid, Kjell Erlandsson, Kris Thielemans, and Brian F. Hutton. Can SPECT Resolution Be Considered Invariant in Partial Volume Correction? In Annual Congress of the European Association of Nuclear Medicine October 12 16, 2019 Barcelona,

- *Spain*, volume 46, page S771. NLM (Medline), oct 2019. doi: 10.1007/s00259-019-04486-2.
- Rebecca Gillen, Kjell Erlandsson, Ana M. Denis-Bacelar, Kris Thielemans, Brian F. Hutton, and Sarah J. McQuaid. Towards accurate partial volume correction in tc-99m oncology spect: perturbation for case-specific resolution estimation. *EJNMMI Physics*, 9:1–22, 12 2022. ISSN 21977364. doi: 10.1186/S40658-022-00489-5/FIGURES/10.
- Katarina Sjögreen Gleisner, Nicolas Chouin, Pablo Minguez Gabina, Francesco Cicone, Silvano Gnesin, Caroline Stokke, Mark Konijnenberg, Marta Cremonesi, Frederik A. Verburg, Peter Bernhardt, Uta Eberlein, and Jonathan Gear. Eanm dosimetry committee recommendations for dosimetry of 177lu-labelled somatostatin-receptor- and psma-targeting ligands. *European Journal of Nuclear Medicine and Molecular Imaging*, 49:1778, 5 2022. ISSN 16197089. doi: 10.1007/S00259-022-05727-7.
- Silvano Gnesin, Paulo Leite Ferreira, Jerome Malterre, Priscille Laub, John O. Prior, and Francis R. Verdun. Phantom Validation of Tc-99m Absolute Quantification in a SPECT/CT Commercial Device. *Computational and Mathematical Methods in Medicine*, 2016:6, 2016. ISSN 17486718. doi: 10.1155/2016/4360371.
- Stanley J. Goldsmith. Targeted Radionuclide Therapy: A Historical and Personal Review, 2019. ISSN 15584623.
- Sandeep S. V. Golla, Mark Lubberink, Bart N. M. van Berckel, Adriaan A. Lammertsma, and Ronald Boellaard. Partial volume correction of brain PET studies using iterative deconvolution in combination with HYPR denoising. *EJNMMI Research*, 7(1):36, dec 2017. ISSN 2191-219X. doi: 10.1186/s13550-017-0284-1.
- Kuang Gong, Simon R. Cherry, and Jinyi Qi. On the assessment of spatial resolution of PET systems with iterative image reconstruction. *Physics in Medicine and*

- Biology, 61(5):N193–N202, feb 2016. ISSN 13616560. doi: 10.1088/0031-9155/61/5/N193.
- Stephen A. Graves, Ryan T. Flynn, and Daniel E. Hyer. Dose point kernels for 2,174 radionuclides. *Medical Physics*, 46(11):5284–5293, nov 2019. ISSN 2473-4209. doi: 10.1002/MP.13789.
- Johan Gustafsson and Jan Taprogge. Future trends for patient-specific dosimetry methodology in molecular radiotherapy. *Physica Medica*, 115:103165, nov 2023. ISSN 1120-1797. doi: 10.1016/J.EJMP.2023.103165.
- Johan Gustafsson, Gustav Brolin, Maurice G. Cox, Michael Ljungberg, Lena Johansson, and Katarina Sjögreen Gleisner. Uncertainty propagation for SPECT/CT-based renal dosimetry in 177 Lu peptide receptor radionuclide therapy. *Physics in Medicine and Biology*, 60(21):8329–8346, nov 2015. doi: 10.1088/0031-9155/60/21/8329.
- M. Hatt. PS-66 Functional Volume Segmentation State of the Art. In *Annual Congress of the European Association of Nuclear Medicine October 12 16*, 2019 Barcelona, Spain, volume 46, page S771. NLM (Medline), oct 2019. doi: 10.1007/s00259-019-04486-2.
- Mathieu Hatt, Catherine Cheze Le Rest, Nidal Albarghach, Olivier Pradier, and Dimitris Visvikis. PET functional volume delineation: a robustness and repeatability study. *European Journal of Nuclear Medicine and Molecular Imaging*, 38(4):663–672, apr 2011. ISSN 1619-7070. doi: 10.1007/s00259-010-1688-6.
- Mathieu Hatt, John A. Lee, Charles R. Schmidtlein, Issam El Naqa, Curtis Caldwell, Elisabetta De Bernardi, Wei Lu, Shiva Das, Xavier Geets, Vincent Gregoire, Robert Jeraj, Michael P. MacManus, Osama R. Mawlawi, Ursula Nestle, Andrei B. Pugachev, Heiko Schöder, Tony Shepherd, Emiliano Spezi, Dimitris Visvikis, Habib Zaidi, and Assen S. Kirov. Classification and evaluation strategies of auto-segmentation approaches

- for PET: Report of AAPM task group No. 211. *Medical Physics*, 44 (6):e1-e42, jun 2017. ISSN 00942405. doi: 10.1002/mp.12124. URL http://www.ncbi.nlm.nih.gov/pubmed/28120467http://www.pubmedcentral.nih.gov/articlerender.fcgi?artid=PMC5902038http://doi.wiley.com/10.1002/mp.12124.
- Hermes Medical Solutions. Hermes Hybrid Viewer Software, 2024. URL https://www.hermesmedical.com/ifu/products/hybrid-viewer/.
- Marc Hickeson, Mijin Yun, Alexander Matthies, Hongming Zhuang, Lars Eric Adam, Lester Lacorte, and Abass Alavi. Use of a corrected standardized uptake value based on the lesion size on CT permits accurate characterization of lung nodules on FDG-PET. *European Journal of Nuclear Medicine and Molecular Imaging*, 29(12):1639–1647, 2002. ISSN 03406997. doi: 10.1007/s00259-002-0924-0.
- Nikie J Hoetjes, Floris H P van Velden, Otto S Hoekstra, Corneline J Hoekstra, Nanda C Krak, Adriaan A Lammertsma, and Ronald Boellaard. Partial volume correction strategies for quantitative FDG PET in oncology. *European Journal of Nuclear Medicine and Molecular Imaging*, 37(9):1679–87, aug 2010. doi: 10.1007/s00259-010-1472-7.
- E. J. Hoffman, S.C. Huang, and M. E. Phelps. Quantitation in positron emission computed tomography: 1. Effect of object size. *Journal of Computer Assisted Tomography*, 3(3):299–308, jun 1979. ISSN 0363-8715. URL http://www.ncbi.nlm.nih.gov/pubmed/438372.
- Frank Hofheinz, S Dittrich, C Potzsch, and Jörg van den Hoff. Effects of cold sphere walls in PET phantom measurements on the volume reproducing threshold. *Physics in Medicine and Biology*, 55:1099, 2010. doi: 10.1088/0031-9155/55/4/013.
- Frank Hofheinz, Jens Langner, Jan Petr, Bettina Beuthien-Baumann, Liane Oehme, Jörg Steinbach, Jörg Kotzerke, and Jörg van den Hoff. A

- method for model-free partial volume correction in oncological PET. *EJNMMI Research*, 2(1):16, apr 2012. ISSN 2191-219X. doi: 10. 1186/2191-219X-2-16. URL http://ejnmmires.springeropen.com/articles/10.1186/2191-219X-2-16.
- Thomas A. Hope, Jeremie Calais, Li Zhang, William Dieckmann, and Corina Millo. 111In-Pentetreotide Scintigraphy Versus 68Ga-DOTATATE PET: Impact on Krenning Scores and Effect of Tumor Burden. *Journal of Nuclear Medicine*, 60(9):1266–1269, sep 2019. ISSN 0161-5505. doi: 10.2967/JNUMED.118. 223016.
- J. H. Hubbell and S. M. Seltzer. X-Ray Mass Attenuation Coefficients NIST, 1996. URL https://www.nist.gov/pml/x-ray-mass-attenuation-coefficients.
- H.M. Hudson and R.S. Larkin. Accelerated image reconstruction using ordered subsets of projection data. *IEEE Transactions on Medical Imaging*, 13(4):601– 609, 1994. ISSN 02780062. doi: 10.1109/42.363108.
- R H Huesman. A new fast algorithm for the evaluation of regions of interest and statistical uncertainty in computed tomography. *Physics in Medicine and Biology*, 29(5):543–552, 1984.
- Brian F. Hutton. Spect imaging: Basics and new trends. *Handbook of Particle Detection and Imaging: Second Edition*, pages 1217–1236, 1 2021. doi: 10.1007/978-3-319-93785-4_37/FIGURES/8. URL https://link.springer.com/referenceworkentry/10.1007/978-3-319-93785-4_37.
- Brian F. Hutton and A Osiecki. Correction of partial volume effects in myocardial SPECT. *Journal of Nuclear Cardiology*, 5(4):402–13, 1998. ISSN 1071-3581.
- Brian F. Hutton, H. Malcolm Hudson, and Freek J. Beekman. A clinical perspective of accelerated statistical reconstruction. *European Journal of Nuclear Medicine*, 24(7):797–808, 1997. ISSN 03406997. doi: 10.1007/BF00879671/METRICS.

- Brian F. Hutton, A. Olsson, S. Som, Kjell Erlandsson, and M. Braun. Reducing the influence of spatial resolution to improve quantitative accuracy in emission tomography: A comparison of potential strategies. *Nuclear Instruments and Methods in Physics Research Section A*, 569(2):462–466, dec 2006. ISSN 01689002. doi: 10.1016/j.nima.2006.08.143.
- Brian F. Hutton, Irène Buvat, and Freek J Beekman. Review and current status of SPECT scatter correction. *Physics in Medicine and Biology*, 56(14):R85–R112, jul 2011. ISSN 0031-9155. doi: 10.1088/0031-9155/56/14/R01.
- IAEA. IAEA HUMAN HEALTH Report 9: Quantitative Nuclear Medicine Imaging: Concepts, Requirements and Methods. Technical report, IAEA, Vienna, 2014.
- Zacharie Irace, Anthonin Reilhac, Bruno Mendez de Vigo, Hadj Batatia, and Nicolas Costes. PCA-based approach for inhomogeneous PSF estimation and partial volume correction in PET. In 2016 IEEE Nuclear Science Symposium, Medical Imaging Conference and Room-Temperature Semiconductor Detector Workshop (NSS/MIC/RTSD), pages 1–3. IEEE, oct 2016. ISBN 978-1-5090-1642-6. doi: 10.1109/NSSMIC.2016.8069439.
- Price A. Jackson, Michael S. Hofman, Rodney J. Hicks, Mark Scalzo, and John Violet. Radiation dosimetry in 177lu-psma-617 therapy using a single posttreatment spect/ct scan: A novel methodology to generate time- and tissue-specific dose factors. *Journal of nuclear medicine : official publication, Society of Nuclear Medicine*, 61:1030–1038, 7 2020. ISSN 1535-5667. doi: 10.2967/JNUMED.119.233411.
- Hajer Jomaa, Rostom Mabrouk, and Nawres Khlifa. Post-reconstruction-based partial volume correction methods: A comprehensive review. *Biomedical Signal Processing and Control*, 46:131–144, sep 2018. ISSN 17468094. doi: 10.1016/j.bspc.2018.05.029.
- Andres Kaalep, Terez Sera, Wim Oyen, Bernd J. Krause, Arturo Chiti, Yan Liu, and

- Ronald Boellaard. EANM/EARL FDG-PET/CT accreditation summary results from the first 200 accredited imaging systems. *European journal of nuclear medicine and molecular imaging*, 45(3):412–422, mar 2018. ISSN 1619-7089. doi: 10.1007/S00259-017-3853-7.
- S. Cheenu Kappadath. Effects of voxel size and iterative reconstruction parameters on the spatial resolution of Tc-99m SPECT/CT. *Journal of Applied Clinical Medical Physics*, 12(4):210–220, sep 2011. doi: 10.1120/jacmp.v12i4.3459.
- E. P. Krenning, M. De Jong, P. P.M. Kooij, W. A.P. Breeman, W. H. Bakker, W. W. De Herder, C. H.J. Van Eijck, D. J. Kwekkeboom, F. Jamar, S. Pauwels, and R. Valkema. Radiolabelled somatostatin analogue(s) for peptide receptor scintigraphy and radionuclide therapy. *Annals of oncology : official journal of the European Society for Medical Oncology*, 10 Suppl 2(SUPPL. 2), 1999. ISSN 0923-7534. doi: 10.1093/ANNONC/10.SUPPL_2.S23.
- Ichiei Kuji, Tomohiko Yamane, Akira Seto, Yota Yasumizu, Suguru Shirotake, and Masafumi Oyama. Skeletal standardized uptake values obtained by quantitative SPECT/CT as an osteoblastic biomarker for the discrimination of active bone metastasis in prostate cancer. *European Journal of Hybrid Imaging*, 1(1):2, 2017. ISSN 2510-3636. doi: 10.1186/s41824-017-0006-y.
- Thomas Langbein, Wolfgang A Weber, and Matthias Eiber. Future of Theranostics: An Outlook on Precision Oncology in Nuclear Medicine. *Journal of Nuclear Medicine*, 60:13S–19S, 2019. doi: 10.2967/jnumed.118.220566.
- Richard .S. Lawson. *The Gamma Camera: A Comprehensive Guide*. Institute of Physics and Engineering in Medicine, 2013. ISBN 9781903613535. URL https://books.google.co.uk/books?id=bJWUnQEACAAJ.
- Francesca Leek, Cameron Anderson, Andrew P. Robinson, Robert M. Moss, Joanna C. Porter, Helen S. Garthwaite, Ashley M. Groves, Brian F. Hutton, and Kris Thielemans. Optimisation of the air fraction correction for lung pet/ct:

- addressing resolution mismatch. *EJNMMI Physics*, 10:1–22, 12 2023. ISSN 21977364. doi: 10.1186/S40658-023-00595-Y/TABLES/6.
- Julian Leube, Wies Claeys, Johan Gustafsson, Maikol Salas-Ramirez, Michael Lassmann, Michel Koole, and Johannes Tran-Gia. Position dependence of recovery coefficients in 177 Lu-SPECT/CT reconstructions-phantom simulations and measurements. *EJNMMI Physics*, 11(52), 2024a. doi: 10.1186/s40658-024-00662-y. URL http://creativecommons.org/licenses/by/4.0/.Leubeetal.EJNMMIPhysics.
- Julian Leube, Johan Gustafsson, Michael Lassmann, Maikol Salas-Ramirez, and Johannes Tran-Gia. A Deep-Learning–Based Partial-Volume Correction Method for Quantitative 177Lu SPECT/CT Imaging. *Journal of Nuclear Medicine*, 65 (6):980–987, 6 2024b. ISSN 0161-5505. doi: 10.2967/JNUMED.123.266889.
- Laquan Li, Jian Wang, Wei Lu, and Shan Tan. Simultaneous Tumor Segmentation, Image Restoration, and Blur Kernel Estimation in PET Using Multiple Regularizations. *Computer Vision and Image Understanding*, 155:173–194, feb 2017a. ISSN 1077-3142. doi: 10.1016/j.cviu.2016.10.002.
- Yusheng Li, Margaret E Daube-Witherspoon, Samuel Matej, and Scott D Metzler. Lesion Quantification Using the Local Impulse Response from Embedded Point Source. In *The 14th International Meeting on Fully Three-Dimensional Image Reconstruction in Radiology and Nuclear Medicine source*, pages 272–275, 2017b. doi: 10.12059/Fully3D.2017-11-3202022.
- Jeih-S Liow and S C Strother. The convergence of object dependent resolution in maximum likelihood based tomographic image reconstruction. *Physics in Medicine and Biology*, 38(1):55–70, jan 1993. ISSN 0031-9155. doi: 10.1088/0031-9155/38/1/005.
- Shaoying Liu, Michael A. King, Aaron B. Brill, Michael G. Stabin, and Troy H. Farncombe. Convolution-based forced detection Monte Carlo simulation incorporating septal penetration modeling. *IEEE Transactions on Nuclear*

- Science, 55(3):967–974, jun 2008. ISSN 00189499. doi: 10.1109/TNS.2008. 924079.
- Michael Ljungberg. Absolute Quantitation of SPECT Studies. *Seminars in Nuclear Medicine*, 48(4):348–358, jul 2018. ISSN 0001-2998. doi: 10.1053/J.SEMNUCLMED.2018.02.009.
- Michael Ljungberg and Sven-Erik Strand. A Monte Carlo program for the simulation of scintillation camera characteristics. *Computer Methods and Programs in Biomedicine*, 29:257–272, 1989.
- R Loeevinger and M Berman. A schema for absorbed-dose calculations for biologically-distributed radionuclides. *Journal of Nuclear Medicine*, Suppl 1: 9–14, 2 1968.
- Andreas Markus Loening and Sanjiv Sam Gambhir. AMIDE: A Free Software Tool for Multimodality Medical Image Analysis. *Molecular Imaging*, 2(3), jul 2003. ISSN 1536-0121. doi: 10.1162/15353500200303133.
- Leonor Lopes, Alejandro Lopez-Montes, Yizhou Chen, Pia Koller, Narendra Rathod, August Blomgren, Federico Caobelli, Axel Rominger, Kuangyu Shi, and Robert Seifert. The Evolution of Artificial Intelligence in Nuclear Medicine. *Seminars in Nuclear Medicine*, 2 2025. ISSN 0001-2998. doi: 10.1053/J. SEMNUCLMED.2025.01.006.
- L B Lucy. An iterative technique for the rectification of observed distributions. *The Astronomical Journal*, 79(6), 1974.
- Mark T. Madsen, Kevin S. Berbaum, Andrew N. Ellingson, Brad H. Thompson, Brian F. Mullan, and Robert T. Caldwell. A new software tool for removing, storing, and adding abnormalities to medical images for perception research studies. *Academic radiology*, 13(3):305–312, mar 2006. ISSN 1076-6332. doi: 10.1016/J.ACRA.2005.11.041. URL https://pubmed.ncbi.nlm.nih.gov/16488842/.

- H. Marquis, D. Deidda, A. Gillman, K. P. Willowson, Y. Gholami, T. Hioki, E. Eslick, K. Thielemans, and D. L. Bailey. Theranostic SPECT reconstruction for improved resolution: application to radionuclide therapy dosimetry. *EJNMMI Physics*, 8(1):16, dec 2021. ISSN 21977364. doi: 10.1186/s40658-021-00362-x.
- Harry Marquis, Kathy P. Willowson, and Dale L. Bailey. Partial volume effect in spect and pet imaging and impact on radionuclide dosimetry estimates. *Asia Oceania Journal of Nuclear Medicine and Biology*, 11:44, 1 2023. ISSN 23225726. doi: 10.22038/AOJNMB.2022.63827.1448.
- Harry Marquis, C. Ross Schmidtlein, Robin de Nijs, Pablo Mínguez Gabiña, Johan Gustafsson, Gunjan Kayal, Juan C. Ocampo Ramos, Lukas M. Carter, Dale L. Bailey, and Adam L. Kesner. MIRD Pamphlet No. 32: A MIRD Recovery Coefficient Model for Resolution Characterization and Shape-Specific Partial-Volume Correction. *Journal of Nuclear Medicine*, 66(2), jan 2025. ISSN 0161-5505. doi: 10.2967/JNUMED.124.268520.
- Berta Marti-Fuster, Kjell Erlandsson, Carles Falcon, Charalampos Tsoumpas, Lefteris Livieratos, Domenec Ros, and Kris Thielemans. Evaluation of the novel 3D SPECT modelling algorithm in the STIR reconstruction framework: Simple vs. full attenuation correction. In 2013 IEEE Nuclear Science Symposium and Medical Imaging Conference (2013 NSS/MIC), pages 1–3. IEEE, oct 2013a. ISBN 978-1-4799-0534-8. doi: 10.1109/NSSMIC.2013.6829258.
- Berta Marti-Fuster, Carles Falcon, Charalampos Tsoumpas, Lefteris Livieratos, Pablo Aguiar, Albert Cot, Domenec Ros, and Kris Thielemans. Integration of advanced 3D SPECT modeling into the open-source STIR framework. *Medical Physics*, 40(9):092502, aug 2013b. ISSN 00942405. doi: 10.1118/1.4816676.
- Sarah J. McQuaid, Sudeepti Southekal, Marie Foley Kijewski, and Stephen C. Moore. Joint optimization of collimator and reconstruction parameters in SPECT imaging for lesion quantification. *Physics in Medicine and Biology*, 56:6983–7000, 2011. doi: 10.1088/0031-9155/56/21/014.

- Mediso. AnyScan TRIO SPECT/CT/PET. URL https://mediso.com/
 global/en/product/integrated-spectctpet-systems/
 anyscan-trio-spectctpet.
- C C Meltzer, P E Kinahan, P J Greer, T E Nichols, C Comtat, M N Cantwell, M P Lin, and J C Price. Comparative evaluation of MR-based partial-volume correction schemes for PET. *Journal of Nuclear Medicine*, 40(12):2053–65, dec 1999. ISSN 0161-5505.
- Carolyn Cidis Meltzer, Jeffrey P. Leal, Helen S. Mayberg, Henry N. Wagner, and J. Janies Frost. Correction of PET data for partial volume effects in human cerebral cortex by MR imaging. *Journal of Computer Assisted Tomography*, 14 (4):561–570, 1990. ISSN 15323145. doi: 10.1097/00004728-199007000-00011.
- Max Mignotte and Jean Meunier. Threedimensional blind deconvolution of SPECT images. *IEEE Transactions on Biomedical Engineering*, 47(2):274280, 2000. ISSN 00189294. doi: 10.1109/10.821781.
- Pablo Mínguez Gabiña, Teresa Monserrat Fuertes, Inés Jauregui, Cristina del Amo, Emilia Rodeño Ortiz de Zarate, and Johan Gustafsson. Activity recovery for differently shaped objects in quantitative SPECT. *Physics in Medicine & Biology*, 68(12):125012, jun 2023. ISSN 0031-9155. doi: 10.1088/1361-6560/ACD982.
- Azimi Mohammad-Saber, Alireza Kamali-Asl, Ay Mohammad-Reza, Navid Zeraatkar, Hosseini Mahboubeh-Sadat, Amirhossein Sanaat, Habibollah Dadgar, and Hossein Arabi. Deep learning-based partial volume correction in standard and low-dose positron emission tomography-computed tomography imaging. *Quantitative Imaging in Medicine and Surgery*, 14(3):2146–2166, mar 2024. ISSN 22234306. doi: 10.21037/QIMS-23-871/COIF.
- Stephen C. Moore, Sudeepti Southekal, Mi-Ae Mi-Ae Park, Sarah J. McQuaid, Marie Foley Kijewski, and Stefan P. Müller. Improved Regional Activity Quantitation in Nuclear Medicine Using a New Approach to Correct for Tissue

- Partial Volume and Spillover Effects. *IEEE Transactions on Medical Imaging*, 31(2):405–416, feb 2012. ISSN 0278-0062. doi: 10.1109/TMI.2011.2169981.
- Hans W. Müller-Gärtner, Jonathan M. Links, Jerry L. Prince, R. Nick Bryan, Elliot McVeigh, Jeffrey P. Leal, Christos Davatzikos, and J. James Frost. Measurement of Radiotracer Concentration in Brain Gray Matter Using Positron Emission Tomography: MRI-Based Correction for Partial Volume Effects. *Journal of Cerebral Blood Flow & Metabolism*, 12(4):571–583, jul 1992. ISSN 0271-678X. doi: 10.1038/jcbfm.1992.81.
- O L Munk, L P Tolbod, S B Hansen, and T V Bogsrud. Point-spread function reconstructed PET images of sub-centimeter lesions are not quantitative. *EJNMMI Physics*, 5(5), 2017. doi: 10.1186/s40658-016-0169-9.
- National Electrical Manufacturers Association (NEMA). Performance Measurements of Positron Emission Tomographs. NEMA Standards Publication NU 2- 2001. Technical report, National Electrical Manufacturers Association, Washington, D.C., 2001.
- Johan Nuyts. Unconstrained image reconstruction with resolution modelling does not have a unique solution. *EJNMMI physics*, 1(1):98, dec 2014. ISSN 2197-7364. doi: 10.1186/s40658-014-0098-4.
- Sonya Park, Ashwin Singh Parihar, Lisa Bodei, Thomas A. Hope, Nadine Mallak, Corina Millo, Kalpna Prasad, Don Wilson, Katherine Zukotynski, and Erik Mittra. Somatostatin receptor imaging and theranostics: Current practice and future prospects. *Journal of Nuclear Medicine*, 62:1323–1329, 10 2021. ISSN 0161-5505. doi: 10.2967/JNUMED.120.251512.
- C. Parker, S. Nilsson, D. Heinrich, S.I. Helle, J.M. O'Sullivan, S.D. Fosså, A. Chodacki, P. Wiechno, J. Logue, M. Seke, A. Widmark, D.C. Johannessen, P. Hoskin, D. Bottomley, N.D. James, A. Solberg, I. Syndikus, J. Kliment, S. Wedel, S. Boehmer, M. Dall'Oglio, L. Franzén, R. Coleman, N.J. Vogelzang, C.G. O'Bryan-Tear, K. Staudacher, J. Garcia-Vargas, M. Shan, Ø.S. Bruland, and

- O. Sartor. Alpha Emitter Radium-223 and Survival in Metastatic Prostate Cancer. *New England Journal of Medicine*, 369(3):213–223, jul 2013. ISSN 0028-4793. doi: 10.1056/NEJMoa1213755.
- Sophia Pells, David M Cullen, Daniel Deidda, Ana M Denis-Bacelar, Andrew Fenwick, Kelley M Ferreira, David Hamilton, Warda Heetun, Peter Julyan, George Needham, Ben Pietras, Emlyn Price, James Scuffham, Jill Tipping, and Andrew P Robinson. Quantitative validation of Monte Carlo SPECT simulation: application to a Mediso AnyScan GATE simulation. *EJNMMI physics*, 10(60), 2023. doi: 10.1186/s40658-023-00581-4.
- Steffie Peters, Johannes Tran-Gia, Sam Agius, Oleksandra V. Ivashchenko, Jean Noël Badel, Marta Cremonesi, Jens Kurth, Pablo Minguez Gabiña, Elisa Richetta, Katarina Sjögreen Gleisner, Jill Tipping, Manuel Bardiès, and Caroline Stokke. Implementation of dosimetry for molecular radiotherapy; results from a European survey. *Physica Medica*, page 103196, dec 2023. ISSN 1724-191X. doi: 10.1016/J.EJMP.2023.103196.
- Steffie M Peters, Sebastiaan L Meyer Viol, Niels R van der Werf, Nick de Jong, Floris H P van Velden, Antoi Meeuwis, Mark W Konijnenberg, Martin Gotthardt, Hugo W A M de Jong, and Marcel Segbers. Variability in lutetium-177 SPECT quantification between different state-of-the-art SPECT/CT systems. *EJNMMI Physics*, 7(9), 2020. doi: 10.1186/s40658-020-0278-3.
- Giulia Poletto, Diego Cecchin, Stefania Sperti, Luca Filippi, Nicola Realdon, and Laura Evangelista. Head-to-Head Comparison between Peptide-Based Radiopharmaceutical for PET and SPECT in the Evaluation of Neuroendocrine Tumors: A Systematic Review. *Current issues in molecular biology*, 44:5516–5530, 2022. doi: 10.3390/cimb44110373.
- Michela Del Prete, François Alexandre Buteau, and Jean Mathieu Beauregard. Personalized 177lu-octreotate peptide receptor radionuclide therapy of neuroendocrine tumours: a simulation study. *European Journal of Nuclear*

Medicine and Molecular Imaging, 44:1490–1500, 8 2017. ISSN 16197089. doi: 10.1007/S00259-017-3688-2/FIGURES/5.

Jinyi Qi and Richard M. Leahy. Iterative reconstruction techniques in emission computed tomography. *Physics in Medicine and Biology*, 51(15):R541–R578, aug 2006. ISSN 0031-9155. doi: 10.1088/0031-9155/51/15/R01.

Kambiz Rahbar, Hojjat Ahmadzadehfar, Clemens Kratochwil, Uwe Haberkorn, Michael Schafers, Markus Essler, Richard P. Baum, Harshad R. Kulkarni, Matthias Schmidt, Alexander Drzezga, Peter Bartenstein, Andreas Pfestroff, Markus Luster, Ulf Lutzen, Marlies Marx, Vikas Prasad, Winfried Brenner, Alexander Heinzel, Felix M. Mottaghy, Juri Ruf, Philipp Tobias Meyer, Martin Heuschkel, Maria Eveslage, Martin Bögemann, Wolfgang Peter Fendler, and Bernd Joachim Krause. German multicenter study investigating 177 Lu-PSMA-617 Radioligand therapy in advanced prostate cancer patients. *Journal of Nuclear Medicine*, 58(1):85–90, jan 2017. ISSN 2159662X. doi: 10.2967/jnumed.116. 183194.

Arman Rahmim and Habib Zaidi. PET versus SPECT: strengths, limitations and challenges. *Nuclear Medicine Communications*, 29(3):193–207, mar 2008. ISSN 0143-3636. doi: 10.1097/MNM.0b013e3282f3a515.

Arman Rahmim, Jinyi Qi, and Vesna Sossi. Resolution modeling in PET imaging: theory, practice, benefits, and pitfalls. *Medical physics*, 40(6):064301, jun 2013. ISSN 2473-4209. doi: 10.1118/1.4800806.

Caitlin Reilly, Alastair J. Gemmell, Ian M. McLaughlin, Robert Fleming, Nicholas Reed, David McIntosh, and Alice Nicol. Characterisation of Tc-99m EDDA/HYNIC-TOC (Tektrotyd) physiological and neuroendocrine tumour uptake using SPECT/CT standardised uptake values: Initial experience. *Nuclear Medicine Communications*, pages 935–939, 2021. ISSN 14735628. doi: 10.1097/MNM.0000000000001416.

William Hadley Richardson. Bayesian-Based Iterative Method of Image

- Restoration. *Journal of the Optical Society of America*, 62(1):55, jan 1972. ISSN 0030-3941. doi: 10.1364/josa.62.000055.
- Matias Riihimäki, Akseli Hemminki, Kristina Sundquist, Jan Sundquist, and Kari Hemminki. The epidemiology of metastases in neuroendocrine tumors. *International journal of cancer*, 139:2679–2686, 12 2016. ISSN 1097-0215. doi: 10.1002/IJC.30400.
- Andrew P. Robinson, Jill Tipping, David M. Cullen, David Hamilton, Richard Brown, Alex Flynn, Christopher Oldfield, Emma Page, Emlyn Price, Andrew Smith, and Richard Snee. Organ-specific SPECT activity calibration using 3D printed phantoms for molecular radiotherapy dosimetry. *EJNMMI physics*, 3(1): 12, dec 2016. ISSN 2197-7364. doi: 10.1186/s40658-016-0148-1.
- Bruno Rojas, Daniel R. McGowan, Jonathan Gear, April-Louise Smith, Catherine Scott, Allison J. Craig, James Scuffham, David Towey, Matthew Aldridge, and Jill Tipping. Nearly double the patients and dramatic changes over 14 years of UK MRT: Internal Dosimetry Users Group survey results from 2007 to 2021. Nuclear Medicine Communications, October 2023. ISSN 0143-3636. doi: 10.1097/MNM.0000000000001780. URL https://journals.lww.com/nuclearmedicinecomm/fulltext/9900/nearly{_}double{_}the{_}patients{_}and{_}dramatic{_}changes. 226.aspx.
- James C. Ross, Dijana Vilić, Tom Sanderson, Stefan Vöö, and John Dickson. Does quantification have a role to play in the future of bone SPECT? *European Journal of Hybrid Imaging*, 3(1):1–18, dec 2019. ISSN 2510-3636. doi: 10.1186/s41824-019-0054-6.
- O G Rousset, Y Ma, and Alan C Evans. Correction for partial volume effects in PET: principle and validation. *Journal of Nuclear Medicine*, 39(5):904–11, may 1998.
- HyunJu Ryu, Steven R. Meikle, Kathy P. Willowson, Enid M. Eslick, and Dale L.

- Bailey. Performance evaluation of quantitative SPECT/CT using NEMA NU 2 PET methodology. *Physics in Medicine and Biology*, 64(14):145017, jul 2019. ISSN 1361-6560. doi: 10.1088/1361-6560/ab2a22.
- Ali Salavati, Samuel Borofsky, Teo K Boon-Keng, Sina Houshmand, Benjapa Khiewvan, Babak Saboury, Ion Codreanu, Drew A Torigian, Habib Zaidi, and Abass Alavi. Application of Partial Volume Effect Correction and 4D PET in the Quantification of FDG Avid Lung Lesions. *Molecular Imaging and Biology*, 17: 140–148, 2015. doi: 10.1007/s11307-014-0776-6.
- M Samim, W Prevoo, B J De Wit-Van Der Veen, K F Kuhlmann, T Ruers, R van Hillegersberg, M A A J van den Bosch, H M Verkooijen, M G E H Lam, and M P M Stokkel. 18F-FDG PET as novel imaging biomarker for disease progression after ablation therapy in colorectal liver metastases. *European Journal of Nuclear Medicine and Molecular Imaging*, 44:1165–1175, 2017. doi: 10.1007/s00259-017-3637-0.
- Marcelo Tatit Sapienza and José Willegaignon. Radionuclide therapy: current status and prospects for internal dosimetry in individualized therapeutic planning. *Clinics*, 74:e835, 2019. ISSN 19805322. doi: 10.6061/clinics/2019/e835.
- Jelena Saponjski, Djuro Macut, Nebojsa Petrovic, Sanja Ognjanovic, Bojana Popovic, Zoran Bukumiric, and Dragana Sobic Saranovic. Clinical research Diagnostic and prognostic value of 99m Tc-Tektrotyd scintigraphy and 18 F-FDG PET/CT in a single-center cohort of neuroendocrine tumors. *Archives of Medical Science*, 2021. doi: 10.5114/aoms/130996.
- Hasan Sari, Kjell Erlandsson, Ian Law, Henrik Bw Larsson, Sebastien Ourselin, Simon Arridge, David Atkinson, and Brian F. Hutton. Estimation of an image derived input function with MR-defined carotid arteries in FDG-PET human studies using a novel partial volume correction method. *Journal of Cerebral Blood Flow and Metabolism*, 37(4):1398–1409, 2017. doi: 10.1177/0271678X16656197.

- Mike Sattarivand, Maggie Kusano, Ian Poon, and Curtis Caldwell. Symmetric geometric transfer matrix partial volume correction for PET imaging: principle, validation and robustness. *Physics in Medicine and Biology*, 57(21):7101–7116, nov 2012. ISSN 0031-9155. doi: 10.1088/0031-9155/57/21/7101.
- Johannes Schindelin, Ignacio Arganda-Carreras, Erwin Frise, Verena Kaynig, Mark Longair, Tobias Pietzsch, Stephan Preibisch, Curtis Rueden, Stephan Saalfeld, Benjamin Schmid, Jean Yves Tinevez, Daniel James White, Volker Hartenstein, Kevin Eliceiri, Pavel Tomancak, and Albert Cardona. Fiji: an open-source platform for biological-image analysis. *Nature Methods*, 9(7):676–682, jun 2012. ISSN 1548-7105. doi: 10.1038/nmeth.2019. URL https://www.nature.com/articles/nmeth.2019.
- W. Paul Segars, B. M.W. Tsui, Jing Cai, Fang Fang Yin, George S.K. Fung, and Ehsan Samei. Application of the 4-D XCAT Phantoms in Biomedical Imaging and beyond. *IEEE Transactions on Medical Imaging*, 37(3):680–692, mar 2018. doi: 10.1109/TMI.2017.2738448.
- S. M. Seidlin, L. D. Marinelli, and E. Oshry. RADIOACTIVE IODINE THERAPY: effect on functioning metastases of adenocarcinoma of the thyroid. *Journal of the American Medical Association*, 132(14):838, dec 1946. ISSN 0002-9955. doi: 10.1001/jama.1946.02870490016004. URL http://jama.jamanetwork.com/article.aspx?doi=10.1001/jama.1946.02870490016004.
- Robert Seifert, Manuel Weber, Emre Kocakavuk, Christoph Rischpler, and David Kersting. Artificial Intelligence and Machine Learning in Nuclear Medicine: Future Perspectives. *Seminars in nuclear medicine*, 51(2):170–177, mar 2021. ISSN 1558-4623. doi: 10.1053/J.SEMNUCLMED.2020.08.003.
- Sonya Sergieva, Bozhil Robev, Milena Dimcheva, Albena Fakirova, and Radka Hristoskova. Clinical application of spect-ct with tc-99m-tektrotyd in bronchial and thymic neuroendocrine tumors (nets). *Nuclear medicine review. Central and*

- Eastern Europe, 19:81–87, 7 2016. ISSN 1644-4345. doi: 10.5603/NMR.2016. 0017.
- S Shcherbinin and Anna Celler. Assessment of the severity of partial volume effects and the performance of two template-based correction methods in a SPECT/CT phantom experiment. *Physics in Medicine and Biology*, 56(16):5355–5371, aug 2011. ISSN 0031-9155. doi: 10.1088/0031-9155/56/16/018.
- S. Shcherbinin, A. Celler, T. Belhocine, R. Vanderwerf, and A. Driedger. Accuracy of quantitative reconstructions in spect/ct imaging. *Physics in Medicine and Biology*, 53:4595, 8 2008. ISSN 0031-9155. doi: 10.1088/0031-9155/53/17/009.
- Sarah Shearer, Alastair Gemmell, Rebecca Gillen, Caitlin Reilly, and Hugh Wallace. Multi-site comparison of imaging protocols for quantitative tc-99m spect-ct. In *European Journal of Nuclear Medicine and Molecular Imaging*, 2024.
- L. A. Shepp and Y. Vardi. Maximum Likelihood Reconstruction for Emission Tomography. *IEEE Transactions on Medical Imaging*, 1(2):113–122, oct 1982. ISSN 0278-0062. doi: 10.1109/TMI.1982.4307558.
- Siemens. Symbia Intevo Bold, 2017. URL https://www.siemens-healthineers.com/molecular-imaging/xspect/symbia-intevo-bold.
- Antti O Sohlberg and Markus T Kajaste. Fast monte carlo-simulator with full collimator and detector response modelling for spect. *Annals of Nuclear Medicine*, 26:92–98, 2012. doi: 10.1007/s12149-011-0550-7.
- Marine Soret, Stephen L Bacharach, and Irène Buvat. Partial-volume effect in PET tumor imaging. *Journal of Nuclear Medicine*, 48(6):932–45, jun 2007. doi: 10.2967/jnumed.106.035774.
- Sudeepti Southekal, Sarah J. McQuaid, and Stephen C. Moore. Activity estimation in small volumes with non-uniform radiotracer uptake using a local projection-

- based fitting approach. In 2011 IEEE Nuclear Science Symposium Conference Record, pages 3777–3779. IEEE, oct 2011. ISBN 978-1-4673-0120-6. doi: 10. 1109/NSSMIC.2011.6153714.
- Sudeepti Southekal, Sarah J. Mcquaid, Marie Foley Kijewski, and Stephen C. Moore. Evaluation of a method for projection-based tissue-activity estimation within small volumes of interest. *Physics in Medicine and Biology*, 57:685–701, 2012. doi: 10.1088/0031-9155/57/3/685.
- J. A. Stamos, W. L. Rogers, N. H. Clinthorne, and K. F. Koral. Object-dependent performance comparison of two iterative reconstruction algorithms. *IEEE Transactions on Nuclear Science*, 35(1):611–614, 1988. doi: 10.1109/23.12797.
- Caroline Stokke, Silvano Gnesin, Johannes Tran-Gia, Francesco Cicone, Søren Holm, Marta Cremonesi, Johan Blakkisrud, Thomas Wendler, Nic Gillings, Ken Herrmann, Felix M. Mottaghy, and Jonathan Gear. Eanm guidance document: dosimetry for first-in-human studies and early phase clinical trials. *European Journal of Nuclear Medicine and Molecular Imaging*, 51:1268–1286, 4 2024. ISSN 16197089. doi: 10.1007/S00259-024-06640-X/TABLES/4.
- S. Stute, T. Carlier, K. Cristina, C. Noblet, A. Martineau, B. Hutton, L. Barnden, and I. Buvat. Monte carlo simulations of clinical pet and spect scans: impact of the input data on the simulated images. *Physics in medicine and biology*, 56: 6441–6457, 2011. ISSN 1361-6560. doi: 10.1088/0031-9155/56/19/017.
- The SciPy community. scipy.optimize.curve_fit SciPy v1.3.0 Reference Guide, 2019. URL https://docs.scipy.org/doc/scipy/reference/generated/scipy.optimize.curve{_}}fit.html.
- Kris Thielemans, Charalampos Tsoumpas, Sanida Mustafovic, Tobias Beisel, Pablo Aguiar, Nikolaos Dikaios, and Matthew W Jacobson. STIR: software for tomographic image reconstruction release 2. *Physics in Medicine and Biology*, 57(4):867–883, feb 2012. ISSN 0031-9155. doi: 10.1088/0031-9155/57/4/867.

- Kris Thielemans, Charalampos Tsoumpas, D. Suage, C Labbé, C Morel, M Jacobson, A Zverovich, T Beisel, Carles Falcon, R. Twyman, D. Deidda, and M Strugari. STIR User's Guide v5.2, 2023. URL https://stir.sourceforge.net/documentation/STIR-UsersGuide.pdf.
- Benjamin A. Thomas, Kjell Erlandsson, Marc Modat, Lennart Thurfjell, Rik Vandenberghe, Sebastien Ourselin, and Brian F. Hutton. The importance of appropriate partial volume correction for PET quantification in Alzheimer's disease. *European Journal of Nuclear Medicine and Molecular Imaging*, 38(6): 1104–1119, jun 2011. ISSN 1619-7070. doi: 10.1007/s00259-011-1745-9.
- Benjamin A. Thomas, Vesna Cuplov, Alexandre Bousse, Adriana Mendes, Kris Thielemans, Brian F. Hutton, and Kjell Erlandsson. PETPVC: a toolbox for performing partial volume correction techniques in positron emission tomography. *Physics in Medicine and Biology*, 61(22):7975–7993, nov 2016. ISSN 0031-9155. doi: 10.1088/0031-9155/61/22/7975.
- A. Todd-Pokropek, T. D. Cradduck, and F. Deconinck. A file format for the exchange of nuclear medicine image data: a specification of Interfile version 3.3. *Nuclear medicine communications*, 13(9):673–699, 1992. ISSN 0143-3636. doi: 10.1097/00006231-199209000-00007. URL https://pubmed.ncbi.nlm.nih.gov/1448241/.
- Jussi Tohka and Anthonin Reilhac. A Monte Carlo study of deconvolution algorithms for partial volume correction in quantitative PET. In *2006 IEEE Nuclear Science Symposium Conference Record*, pages 3339–3345. IEEE, 2006. ISBN 1-4244-0560-2. doi: 10.1109/NSSMIC.2006.353719.
- Jussi Tohka and Anthonin Reilhac. Deconvolution-based partial volume correction in Raclopride-PET and Monte Carlo comparison to MR-based method. *NeuroImage*, 39(4):1570–1584, feb 2008. ISSN 10538119. doi: 10.1016/j. neuroimage.2007.10.038.

Johannes Tran-Gia and Michael Lassmann. Characterization of noise and resolution

- for quantitative 177 lu spect/ct with xspect quant. *Journal of Nuclear Medicine*, 60:50–59, 1 2019. ISSN 2159662X. doi: 10.2967/jnumed.118.211094. Line phantom used to obtain centre and off-centre resolution values.
- Johannes Tran-Gia, Maikol Salas-Ramirez, and Michael Lassmann. What you see is not what you get: On the accuracy of voxel-based dosimetry in molecular radiotherapy. *Journal of nuclear medicine : official publication, Society of Nuclear Medicine*, 61:1178–1186, 8 2020. ISSN 15355667. doi: 10.2967/jnumed.119.231480.
- B. M. W. Tsui, E. C. Frey, Xide Zhao, D. S. Lalush, R. E. Johnston, and W. H. McCartney. The importance and implementation of accurate 3D compensation methods for quantitative SPECT. *Physics in Medicine and Biology*, 39(3):509–530, mar 1994. ISSN 0031-9155. doi: 10.1088/0031-9155/39/3/015.
- J Harvey Turner. An introduction to the clinical practice of theranostics in oncology. *The British Journal of Radiology*, 91(1091):20180440, nov 2018. ISSN 0007-1285. doi: 10.1259/bjr.20180440.
- Robert Twyman, Simon Arridge, Brian F. Hutton, Elise C. Emond, Ludovica Brusaferri, Sangtae Ahn, and Kris Thielemans. Iterative pet image reconstruction using adaptive adjustment of subset size and random subset sampling. In *2019 IEEE Nuclear Science Symposium and Medical Imaging Conference (NSS/MIC)*, pages 1–3, 2019. doi: 10.1109/NSS/MIC42101.2019.9059799.
- Andor F. Van Den Hoven, Charlotte E.N.M. Rosenbaum, Sjoerd G. Elias, Hugo W.A.M. De Jong, Miriam Koopman, Helena M. Verkooijen, Abass Alavi, Maurice A.A.J. Van Den Bosch, and Marnix G.E.H. Lam. Insights into the dose-response relationship of radioembolization with Resin 90Y-Microspheres: A prospective cohort study in patients with colorectal cancer liver metastases. *Journal of Nuclear Medicine*, 57(7):1014–1019, jul 2016. ISSN 2159662X. doi: 10.2967/jnumed.115.166942.
- T Van Den Wyngaert, & K Strobel, W U Kampen, & T Kuwert, & W Van Der

- Bruggen, H K Mohan, G Gnanasegaran, & R Delgado-Bolton, W A Weber, & M Beheshti, & W Langsteger, F Giammarile, F M Mottaghy, & F Paycha, and F Paycha. The EANM practice guidelines for bone scintigraphy On behalf of the EANM Bone & Joint Committee and the Oncology Committee. *Eur J Nucl Med Mol Imaging*, 43:1723–1738, 2016. doi: 10.1007/s00259-016-3415-4.
- Tim Van den Wyngaert, Filipe Elvas, Stijn De Schepper, John A. Kennedy, and Ora Israel. SPECT/CT: Standing on the Shoulders of Giants, It Is Time to Reach for the Sky! *Journal of Nuclear Medicine*, 61(9):1284–1291, sep 2020. ISSN 0161-5505. doi: 10.2967/JNUMED.119.236943.
- Matt Vanderhoek, Scott B Perlman, and Robert Jeraj. Impact of the Definition of Peak Standardized Uptake Value on Quantification of Treatment Response. *J Nucl Med*, 53:4–11, 2012. doi: 10.2967/jnumed.111.093443.
- Tom O. Videen, Joel S. Perlmutter, Mark A. Mintun, and Marcus E. Raichle. Regional Correction of Positron Emission Tomography Data for the Effects of Cerebral Atrophy. *Journal of Cerebral Blood Flow & Metabolism*, 8(5):662–670, oct 1988. ISSN 0271-678X. doi: 10.1038/jcbfm.1988.113.
- Dimitris Visvikis, · Philippe Lambin, · Kim, Beuschau Mauridsen, Roland Hustinx, Michael Lassmann, Christoph Rischpler, Kuangyu Shi, and Jan Pruim. Application of artificial intelligence in nuclear medicine and molecular imaging: a review of current status and future perspectives for clinical translation. *European Journal of Nuclear Medicine and Molecular Imaging*, 49:4452–4463, 2022. doi: 10.1007/s00259-022-05891-w.
- Matthew D. Walker, Andrew J. Morgan, Kevin M. Bradley, and Daniel R. McGowan. Data-Driven Respiratory Gating Outperforms Device-Based Gating for Clinical 18F-FDG PET/CT. *Journal of Nuclear Medicine*, 61(11):1678–1683, nov 2020. ISSN 0161-5505. doi: 10.2967/JNUMED.120.242248.
- Kathy P. Willowson, Enid M. Eslick, Hyunju Ryu, Aurora Poon, Elizabeth J. Bernard, and Dale L. Bailey. Feasibility and accuracy of single time point

- imaging for renal dosimetry following Lu-DOTATATE ('Lutate') therapy. *EJNMMI Physics*, 5(33):1–9, 2018. doi: 10.1186/s40658-018-0232-9.
- Jing Wu, Hui Liu, Taraneh Hashemi Zonouz, Veronica M. Sandoval, Hassan Mohyud Din, Rachel J. Lampert, Albert J. Sinusas, Chi Liu, and Yi-Hwa Liu. A blind deconvolution method incorporated with anatomical-based filtering for partial volume correction: Validations with 123-mIBG cardiac SPECT/CT. *Medical Physics*, 44(12):6435–6446, dec 2017. doi: 10.1002/mp.12622. URL http://doi.wiley.com/10.1002/mp.12622.
- J. Yang, S C Huang, M. Mega, K.P. Lin, A.W. Toga, G.W. Small, and M. E. Phelps. Investigation of partial volume correction methods for brain FDG PET studies. *IEEE Transactions on Nuclear Science*, 43(6):3322–3327, 1996. ISSN 00189499. doi: 10.1109/23.552745.
- Paul A. Yushkevich, Joseph Piven, Heather Cody Hazlett, Rachel Gimpel Smith, Sean Ho, James C. Gee, and Guido Gerig. User-guided 3D active contour segmentation of anatomical structures: Significantly improved efficiency and reliability. *NeuroImage*, 31(3):1116–1128, jul 2006. ISSN 1053-8119. doi: 10.1016/J.NEUROIMAGE.2006.01.015.
- Habib Zaidi, M'hamed Bentourkia, Abdel Ouahab Boudraa, Michael Braun,
 A Bertrand Brill, Eric C. Frey, Guido Germano, Bruce H Hasegawa, Brian F.
 Hutton, Kenneth F. Koral, David A. Mankoff, Mark Muzi, Johan Nuyts,
 Olivier G. Rousset, Piotr Slomka, Michael G. Stabin, Benjamin M. W. Tsui,
 and Koenraad Van Laere. *Quantitative Analysis in Nuclear Medicine Imaging*.
 Springer US, Boston, MA, 2006. ISBN 978-0-387-23854-8. doi: 10.1007/b107410.
- Wei Zhao, Pedro L. Esquinas, Xinchi Hou, Carlos F. Uribe, Marjorie Gonzalez, Jean-Mathieu Beauregard, Yuni K. Dewaraja, and Anna Celler. Determination of gamma camera calibration factors for quantitation of therapeutic radioisotopes. *EJNMMI Physics*, 5(1):8, dec 2018. doi: 10.1186/s40658-018-0208-9.